Title
Computational Studies of Organic Electronic Materials

Author
Lin, Janice

Publication Date
2018

Peer reviewed|Thesis/dissertation

UNIVERSITY OF CALIFORNIA

Los Angeles

Computational Studies of Organic Electronic Materials

A dissertation submitted in partial satisfaction of the requirements for the degree

Doctor of Philosophy in Chemistry

by

Janice Biay Lin

2018

ABSTRACT OF THE DISSERTATION

Computational Studies of Organic Electronic Materials

by

Janice Biay Lin

Doctor of Philosophy in Chemistry

University of California, Los Angeles, 2018

Professor Kendall N. Houk, Chair

The sun produces 1020 W m^{-2} of energy per day; that is, in one hour, the earth receives enough energy to power the earth for an entire year. This energy can be harvested for a range of processes, including water splitting, photocatalysis, and electricity. Photovoltaic technologies, in particular, harness the energy of the sun to produce electrical energy. Organic solar cells, or organic photovoltaics (OPVs), hold advantages over inorganic cells in scalability, range of functionalization, and potential in flexible applications. While the power conversion efficiency (PCE) of this relatively new type of solar cell has made tremendous progress over the last decade, OPVs must continue to improve over 15% PCE in order to become a viable competitor to inorganic cells.

Several factors in the active layer (donor and acceptor layers) of a solar cell can lead to low efficiency, including low carrier mobility, inadequate absorption of the electromagnetic

spectrum, and disordered morphology. Therefore, control of morphology in the active layer and tuning of electronic levels of the donors and acceptors in organic photovoltaics are important parameters that need to be controlled for favorable device performance. One approach to improving efficiency is designing molecules that pack closely together to allow for efficient charge transport. These types of systems offer significant possibilities for controlled morphologies, high charge transport, and high efficiencies in solar cells. Towards these types of materials, this work aims to:

1. Understand the effect of torsional behavior in organic materials on the morphology of the active layer to guide the design of materials with low disorder.

2. Determine the effect of crystal packing on charge transport of organic small-molecules and oligomers to lend insight into mechanisms that govern high mobility, and

3. Characterize optical properties of trimeric oligomers to lend insight into potential electronic applications.

Motivated by the potential of new organic photovoltaic materials, this thesis begins with a focus on using computational methods to understand systems of relevance to organic electronics (Chapters 1-7). Early projects aim to use an iterative computational-experimental scheme to understand morphology and charge transport as relevant in organic electronic devices (Chapters 1-3). Molecular properties are calculated and correlated to bulk properties observed experimentally to derive design principles for new molecules that would give rise to interesting packing in solid state. Excited state calculations are used to understand the underlying properties that give rise to optical transitions and to predict new molecules that would absorb strongly in the visible light region (Chapters 4). Mechanistic studies of the degradation pathways of small molecules will also be discussed, and functional handles that would lead to more stable structures are identified (Chapter 5). Calculations are employed to understand the transformation of polydiacetylene polymers to graphene nanoribbons, which lends insight into tuning this reaction

for other *N*-doped materials (Chapter 6). Later in the thesis, the focus diverges to the use of computations to understand the reactivity of a class of ruthenium-based olefin metathesis catalysts towards the design of a stable, *E*-selective catalyst (Chapter 7-8).

Various methods are employed in the chapters described in this dissertation. Density functional theory is used to characterize ground state geometry, conformational analysis, transition state geometry, molecular orbitals, reorganization energies. Time-dependent density functional theory is used to characterize excited state properties, including bandgap, absorption, emission, excited state geometry, charge transfer properties. ZINDO is used for other excited state properties such as charge transfer, electronic coupling. Molecular dynamics is used for time-scale properties, including electronic disorder, energetic disorder, ordered and disordered morphology. Kinetic Monte Carlo as implemented in the VOTCA program is used for charge transport calculations.

The dissertation of Janice Biay Lin is approved.

Yves F. Rubin

Yang Yang

Kendall N. Houk, Committee Chair

University of California, Los Angeles

2018

Table of Contents

List of Schemes

List of Figures

List of Tables

Acknowledgements

I must first thank my PhD advisor, Professor Ken Houk. Over the last four years, he has steadily guided my research projects, through which I have learned an immense amount. He is an advisor from and with whom I have learned, and I am grateful for all the times when we would sit down and think through problems together. He took a chance on a first-year graduate student, and I would not be in this place today without his support, guidance, and advising. In the Houk lab, I have been fortunate to have been able to branch out to various research areas, including bulk materials, photoactive materials, catalyst design, and mechanistic elucidation, touching upon many aspects of computational organic chemistry. I thank Prof. Houk for his open-mindedness and for his investment in me.

I would also like to acknowledge the professors who comprise my thesis committee. Prof. Heather Maynard was my first research advisor at UCLA. The summer I spent working on polymer chemistry in her lab was a challenging but highly rewarding time, which set up a foundation for the rest of my time at UCLA. I thank the members of the Maynard lab who graciously welcomed me, taught me, and challenged me. Prof. Yang Yang was an integral part of my decision to invest my PhD in researching solar materials. Prof. Yves Rubin has been an excellent collaborator and soundboard with whom I have enjoyed brainstorming ideas and lively discussions of organic materials. I thank these committee members for the part each played in the creation of this volume of work blended from several disciplines.

My mentors throughout my undergraduate research career are many. George Rhoderick taught me at the bench, explained gas valves and the importance of standards and calibration. He entrusted a fresh-faced teenager straight out of her first year of college with not only an independent project but also with his time. Dr. Shelby Ellery patiently walked with me side-by-side up and down the halls of the Beckman building to get anhydrous solvent, run NMRs, and guided me through my first research seminar and my first group meeting. She is an example of a strong

female scientist who selflessly gave to the next generation. Dr. Yi Zhang reached out and took me under her wing and taught me not only science but of the trials and tribulation of graduate life. Dr. Mahmut Tosun showed me by example what hard work looks like, yet he always bore a smile and was never short of encouraging words. Prof. Rehan Kapadia was a mentor who challenged me with hard questions, a mentor who stood me at the board and asked me to explain concepts to him, one who never let me slide by. He constantly reminded me of the importance of grit and to always ask, “How can I improve?”

The older lab members in the Houk group welcomed me with lots of laughter, sarcasm, and real talk. Dr. Hung Pham was a guiding light in what was a windy, toilsome first year of graduate school, an encourager, and a great source of laughter throughout my early years. Dr. Blanton Martin served as an unofficial mentor and in this capacity also challenged me to not be afraid to explore things outside the three walls of our cubicles. Prof. Steven Lopez was a mentor who taught me from the beginning, through each line of command and the setup of each calculation. I am grateful that throughout the years, we have been aligned in our ideologies, our desire to advocate and invest into the next generation of scientists that we hope will be made up of all walks of life and colors. Dr. Ilhan Yavuz was a pioneer in the early days of the OPV subgroup, and his work laid the foundation of several chapters in this thesis. I thank him for his continual patience in teaching me all things in device physics. Dr. Jiyong Park held down the OPV subgroup with me, and I learned from him how tools can be widely applicable in so many fields. Dr. Ashay Patel was my cubicle neighbor, a computational encyclopedia of sort, and an unofficial mentor who challenged me to learn, to be always candid and honest, and served as a bantering partner. I always enjoyed our matches from across the room. My friend and unofficial mentor, Dr. Jessie Grandner, took me under her wing from day one, and I am proud to be referred to as her “mini-me.” She taught me things before I even knew that I would need them, and I am grateful that she equipped me with that readiness. Dr. Cyndi He was a constant support in lab, a dear friend, and

fellow coffee addict. I will always remember our cozy cubicle days together fondly. My friend Dr. Marc Garcia Borràs is a great coffee buddy and encourager, as well as a brilliant labmate who I could always bounce ideas off of and have stimulating discussion with.

I am grateful for many friends who I began and continue this journey with. Leibniz Hang, my work wife, my partner in the trenches of pre-first year, first year, and the years after. Terri Lin, my kindhearted friend and fellow woman who has been my soundboard for so much. Dalton Steele, someone who has challenged me in ways beyond scholastic. Patty Tran, who has been my co-operator in life for the past 4.5 years. We have shared an apartment and two lives that have meshed into sometimes one. Abigail Yusam, forever my study partner and a fellow child at heart who always encourages and laughs at my antics. Cam Luu, who has relentlessly supported me both from near and afar. Will Zheng, whose calming presence is always felt, whichever coast he may be on. Elisa Shieh, a friend with whom I never stop laughing but can also share the deepest thoughts and conversations. Christopher Joseph Fung, a person who is so much, my code writer, solver, (outdated) Webster's dictionary, to name just a few. He is someone I have learned from and with, side by side, in and through all things.

My older sister Dorothy, who has reached down to the dark places and pulled me up, who has since young inspired me with her creativity. My younger sister Grace, who has unwaveringly supported me, playing into the hours of the night despite a lack of endurance, who keeps me young at heart. My brother Timothy, a young academic in his own right, whose drive to learn and for thought has also inspired a deeper, more layered thinking in myself. My mother and father, each of whom are different in every single way, but each who has helped shape the person I am today. Mama, from mother to close friend, who over the years I have learned much about medicine, cleanliness, and strength. Baba, who has always taught me be at peace, to not worry, and to venture outside normality. And to the one who has led me through it all, who has danced over me even when I was unaware, my God and Savior, the most important part of my being.

Finally, my bash directory, which over the years has taken on more and more aliases. Words cannot express how grateful I am.

Chapter 1 is a modified version of the publication "Torsional Barriers to Rotation and Planarization in Heterocyclic Oligomers of Value in Organic Electronics." Lin, J. B.; Jin, Y.; Lopez, S. A.; Druckerman, N.; Wheeler, S. E.; Houk, K. N. *J. Chem. Theory Comput.* **2017**, *13*, 5624. This is a collaboration with Prof. Steven Wheeler (at the time at Texas A&M University), who carried out high-level calculations to which we compared our DFT results. Prof. Steven Lopez laid the foundation for this work with his mentorship. I performed extensive calculations using DFT and carried out the analysis for this work. Nathan Druckerman contributed to the benchmark, and Yu Jin performed calculations of the conformational library.

Chapter 2 is a modified version of the publication "Quantitative Prediction of Morphology and Electron Transport in Crystal and Disordered Organic Semiconductors." Yavuz, I.; Lopez, S. A.; Lin, J. B.; Houk, K. N. *J. Mater. Chem. C.* **2016**, *4*, 11238. This work was led by Dr. Ilhan Yavuz, and along with Prof. Steven Lopez, together we performed calculations to predict the mobility of test sets of electron acceptors.

Chapter 3 is a modified version of the manuscript "Impact of Morphology, Side-chain, and Crystallinity on Charge Transport Properties" which is undergoing submission. This is a collaboration with the Itami group at Nagoya University. Dr. Ilhan Yavuz and I performed mobility calculations for the double helicene molecules.

Chapter 4 is a modified version of the publication "Conjugated Trimeric Scaffolds Accessible From Indolyne Cyclotrimerizations: Synthesis, Structures, and Electronic Properties." Lin, J. B.; Shah, T. K.; Goetz, A. E.; Garg, N. K.; Houk, K. N. *J. Am. Chem. Soc.* **2017**, *139*, 10447. This is a collaboration with the Garg lab at UCLA. Dr. Adam Goetz performed the first cyclotrimerization reaction, and Dr. Tejas Shah synthesized the trimer molecules. I performed all

DFT and TD-DFT calculations described in this chapter. Drs. Blanton Martin and Steven Lopez provided valuable discussion for this project.

Chapter 5 is modified version of the publication “Oxidation of Rubrene, and Implications for Device Stability.” Ly, J. T.; Lopez, S. A.; Lin, J. B.; Zhang, L.; Aspuru-Guzik, A.; Houk, K. N.; Briseno, A. L. *J. Mat. Chem. C.* **2018**, *6*, 3757. This is a collaboration with the Briseno group at University of Massachusetts Amherst. The Briseno performed all experiments. Prof. Steven Lopez and I performed calculations discussed for the stage 2 oxidation product. This chapter also discusses unpublished work, calculations performed to explore the regioselectivity of rubrene derivatives synthesized by the Briseno group. I performed the DFT calculations, and Dr. Lopez performed higher-level DLNPO calculations.

Chapter 6 is a modified version of the publication “Synthesis of N=8 Armchair Graphene Nanoribbons from Four Distinct Polydiacetylene.” Jordan, R. S.; Li, Y. L.; Lin, C.-W.; McCurdy, R. D.; Lin, J. B.; Brosmer, J.; Marsh, K.; Houk, K. N.; Kaner, R. B.; Rubin, Y*. J. Am. Chem. Soc.* **2017**, *139*, 15878. This is a collaboration with the Rubin group at UCLA. Dr. Rob Jordan led the experimental synthesis and characterization of the GNRs. I performed DFT calculations to elucidate the regioselectivity of the Hopf cyclization in the gas phase and further predictive calculations on unpublished systems.

Chapters 7 and **8** discuss computational studies undertaken toward a stable, *E*-selective Ru-based olefin metathesis catalyst. This is a collaboration with the Grubbs group at Caltech. Experimental work was carried out by members of the Grubbs group, Dr. Chen Xu, Dr. Patrick Montgomery, and Dr. Tonia Ahmed. I carried out DFT calculations discussed here, which are a continuation of work by Dr. Jessica Grander.

I would like to acknowledge funding for this research from various sources, including the National Science Foundation (DMR-1335645 and CHE-1254897) and the University of California Los Angeles. This work used computational and storage services associated with the Hoffman2

cluster provided by the UCLA Institute for Digital Research and Education's Research Technology Group, the NSF-supported Extreme Science and Engineering Discovery Environment (XSEDE)'s Gordon and Comet supercomputers (OCI-1053575) at the San Diego Supercomputing Center. I am grateful for the support of the Graduate Dean's Scholar Award and Dissertation Year Fellowship for the completion of this dissertation.

Vita

Education

University of California, Los Angeles
Ph.D. Candidate 9/2016
M.S. Chemistry- GPA: 3.84 12/2015
University of Maryland, College Park
B.S. Chemistry- GPA: 3.89 12/2013
- Magna Cum Laude, with Honors citation

National Taiwan University
Mandarin language study- GPA: 3.72 Fall 2012
- Boren Scholar, National Security Education Program

Teaching

Graduate Teaching Assistantships: Chemistry and Biochemistry Department, UCLA (Fall 2014 – present)
- Courses taught: CHEM14CL (3 quarters), CHEM14D (2 quarters), CHEM30A (2 quarters)

Academic Tutor: Academic Support and Career Development Unit, University of Maryland (Spring 2014)
- Subjects tutored: biochemistry, physics, computer science

Undergraduate Teaching Assistantships: Department of Chemistry and Biochemistry, University of Maryland (Fall 2011, Fall 2013)
- Course taught: Organic Chemistry Laboratory II: Synthesis and Characterization (2 semesters)

Publications

1. Rhoderick, G. C.; Lin, J. Stability Assessment of Gas Mixtures Containing Monoterpenes in Varying Cylinder Materials and Treatments. Anal. Chem. **2013**, *85*, 4675.
2. Yavuz, I.; Lopez, S. A.; Lin, J. B.; Houk, K. N. Quantitative Prediction of Morphology and Electron Transport in Crystal and Disordered Organic Semiconductors. *J. Mater. Chem. C.* **2016**, *4*, 11238.
3. Lin, J. B.; Shah, T. K.; Goetz, A. E.; Garg, N. K.; Houk, K. N. Conjugated Trimeric Scaffolds Accessible from Indolyne Cyclotrimerizations: Synthesis, Structures, and Electronic Properties. *J. Am. Chem. Soc.* **2017**, *139*, 10447.
4. Jordan, R. S.; Li, Y. L.; Lin, C.-W.; McCurdy, R. D.; Lin, J. B.; Brosmer, J.; Marsh, K.; Houk, K. N.; Kaner, R. B.; Rubin, Y. Synthesis of N=8 Armchair Graphene Nanoribbons from Four Distinct Polydiacetylene. *J. Am. Chem. Soc.* **2017***, 139*, 15878.
5. Lin, J. B.; Jin, Y.; Lopez, S. A.; Druckerman, N.; Wheeler, S. E.; Houk, K. N. Torsional Barriers to Rotation and Planarization in Heterocyclic Oligomers of Value in Organic Electronics, *J. Chem. Theory Comput*. **2017**, *13*, 5624.
6. Ly, J. T.; Lopez, S. A.; Lin, J. B.; Kim, J. J.; Lee, H.; Burnett, E.; Zhang, L.; Aspuru-Guzik, A.; Houk, K. N.; Briseno, A. L. Oxidation of Rubrene and Implications for Device Stability, *J. Mat. Chem. C.* **2018**, *6*, 3757.

7. Yavuz, I.; Lin, J. B.; Houk, K. N. Impact of Morphology, Side-chains, and Crystallinity on Charge-Transport Properties of π-Extended Double Helicenes, *Phys. Chem. Chem. Phys.*, accepted.
8. Lin, J. B.; Darzi, E. D.; Jasti, R. Yavuz, I.; Houk, K. N. Size Scaling of Solid-State Order and Charge Mobility in Cycloparaphenylenes, submitted.
9. Stappenbeck, F.; Jorda, J.; Khan, S.; Dong, X.; Lin, J. B.; Yang, S.; Houk, K. N. Sterol Binding to the Smoothened Protein: Molecular Modeling and Computational Docking Studies Offer Structure-Based Clues with Implications for Hedgehog Signaling and Osteogenesis, in preparation.
10. Lin, J. B.; Lopez, S. A.; Kocasoy, V.; Xie, S.; Ramstroöf, O.; Yan, M.; Houk, K. N. Mechanistic Investigation of Perfluorophenyl Azide Cycloadditions to Enamines and Enolates: Mechanism of N_2 Extrusion from Triazolines, in preparation.
11. Jiang, X.; Jellen, M.; Yang, S.; Lin, J. B.; Houk, K. N.; Garcia-Garibay, M. A. Solvent Dynamics in Molecular Rotor Systems, in preparation.

Select Presentations

- Lin, J. B.; Yavuz, I.; Houk, K. N. Impact of Morphology, Side-chains, and Crystallinity on Charge-Transport Properties of π-Extended Double Helicenes. Poster at the Materials Research Society Spring Meeting, Phoenix, AZ, April 5, 2018.
- Lin, J. B.; Shah, T. K.; Goetz, A. E.; Houk, K. N.; Garg, N. K. Conjugated Trimeric Scaffolds Accessible Using Indolyne Cyclotrimerizations. Talk presented at the American Chemical Society National Meeting, San Francisco, CA, April 6, 2017.
- Lin, J. B.; Shah, T. K.; Goetz, A. E.; Houk, K. N.; Garg, N. K. Conjugated Trimeric Scaffolds Accessible Using Indolyne Cyclotrimerizations. Talk presented at the University of California Chemical Symposium, Lake Arrowhead, CA, March 28, 2017.
- Lin, J. B.; Jin, Y.; Lopez, S. A.; Druckerman, N.; Wheeler, S. E.; Houk, K. N. Conformational Studies of Organic Photovoltaic Oligomers: Torsional Barriers to Planarization in Crystal Structure. Poster presented at the American Chemical Society National Meeting, San Diego, CA, March 15, 2016.
- Lin, J. B.; Lopez, S. A.; Xie, S.; Ramström, O.; Yan, M.; Houk, K. N. Mechanistic Investigation of Perfluorophenyl Azide Cycloadditions to Enols and Enolates: Origins of N_2 Extrusion from Triazolines. Poster presented at the National Organic Symposium, College Park, MD, July 1, 2015.

Chapter 1. Torsional Barriers to Rotation and Planarization in Heterocyclic Oligomers of Value in Organic Electronics

1.1 Background

Morphology and electronic levels in organic devices are both contributing factors to the device performance of organic field-effect transistors (OFETs), organic light-emitting diodes (OLEDs), and organic photovoltaics (OPVs).[1] Both properties are influenced by the conformational behavior of the organic components, and these effects have been described by various experimental and computational groups.[2-6] It is well established that planar polymers and oligomers have been shown to exhibit lower bandgaps, less structural disorder, and lower reorganization energies via cation delocalization.[2] Beenken *et al.*[3] have also used density functional theory (DFT) to demonstrate the influence of torsional motion on spectral broadening in biphenyl and bithiophene. More recently, Vezie *et al.*[4] have shown that high light absorption in organic semiconducting polymers can be explained by high persistence length, which is affected by the ratio of *cis-trans* conformations. Collini and Scholes used two-dimensional photo echo experiments to show how conformational disorder plays an important role in introducing quantum effects in electronic energy transfer dynamics.[5] Jackson *et al*.[6] have also studied the validity of considering a single conformational isomer as respresentative of an entire conformational distribution in an oligomer or polymer and have determined that different conformations play a role in electronic properties, including ionization potential, electron affinity, and bandgap. However, despite the breadth of work on effects conformational disorder, achieving control over polymorphism to maintain a highly ordered crystal remains a current challenge when designing and evaluating new materials for organic electronics.[6,7]

The effects of molecular structure on solid-state packing behavior and device performance have been studied by many groups.[8,9,10] Molecular dynamics (MD) has been employed to

understand conformational order in the aggregation of polymers.[11,12] Huang *et al*.[13] have also shown how the backbone conformation, as influenced by side-chain substitution, of a linear π-conjugated system affects the packing style (herringbone or lamellar) of the molecule in the solid-state. Stabilizing interactions between subunits in organic semiconducting molecules have been studied by various experimental and computational groups[14] and applied as conformational locks.[15] Noteably, Jackson *et al.*14[a] previously studied intramolecular non-covalent interactions in dimers as a mechanism for conformational control in conjugated oligomers and polymer, showing that with hydrogen-bonding interactions (i.e., CH—O and CH—N interactions) are stronger than noncovalent interactions between heteroatoms (i.e., S—S) on adjacent units. More recently, Conboy *et al.*14[b] conducted a similar study on the interactions between dimers with hydrogen-bonding possibilities and find that intermolecular interactions between heteroatoms still play a role in dictating planarity within poly(3,4-ethylenedioxythiophene) (PEDOT) and derivatives. Planarity is not the only means to tune electronics, as non-planar systems can be found in transition metal dyes,[16] subphthalocyanine derivatives,[17] and contorted hexabenzocornonene derivatives,[18] which also display interesting optical properties that can be tuned by ligand optimization, covalent functionalization, and structural tuning, respectively. However, planarity still does serve as an important component in dictating packing properties, and we focus our attention to correlation of gas-phase energetics to solid-state behavior in thiophene-based materials.

It is well known that conformers such as biphenyl and bithiophene are non-planar in the gas phase;[19,20] however, when incorporated into organic oligomers and polymers, torsional disorder along the backbone of the molecules is low in the solid state, as planarization is achieved due to stabilizing non-covalent interactions between molecules that reduce the conformational flexibility in the system.[21] In this study, we place our focus on the influence of molecular structure and barriers to planarization on solid-state packing properties in organic thiophene-based

materials, which are of interest in OFETs and OPVs.[22] We seek to answer this question: how difficult is it to planarize these types of torsions?

1.2 Aims

In line with previous work,[23] we first benchmarked a series of density functionals for a series of BTTT (2,5-bis(3-tetradecylthiophen-2-yl)thieno[3,2-*b*]-thiophene) oligomers (Scheme 1.1) against high-level focal point analysis (FPA). FPA involves a systematic increase of basis set size and inclusion of electron correlation effects, which allows for extrapolation to the complete basis set (CBS) limit and a systematic approach toward the *ab initio* limit.[24] FPA is similar to the Weizmann-*n* (*i.e.* W3, W4, *etc*.) methods[25] and Feller-Peterson-Dixon approach.[26] BTTT was chosen as the model system as these systems are currently being pursued by experimental and theoretical groups as new semiconducting materials.[27,28,29,30] The presence of rotatable SCCS dihedrals introduces polymorphisms in crystal structures, which affects the performance of polymeric and oligomeric BTTTs in OFETs[27] and OPVs.[29] Due to the known torsional disorder of these materials, we decided to explore the conformational space of BTTT derivatives shown in Scheme 1.1. Next, to establish a set of trends in regards to conformational preferences and barriers to planarization, we performed conformational analysis on a library comprised of common fragments found in the backbones of organic electronic materials. Transition states of planarization and rotation were computed in order to obtain free energy barriers to these transformations in the gas phase (Figure 1.1a). We then compare these gas-phase energetics to experimental crystal structures of oligomers and approximate the planarization barriers to achieve the conformation found in the solid state. Using this approach, we study the structure of **DERDTS-TBDT**, a hole transport material used in perovskite solar cells,[31] and design a new oligomer likely to be planar in the solid state.

Scheme 1.1. Three conformations of BTTT used to benchmark DFT methods against FPA

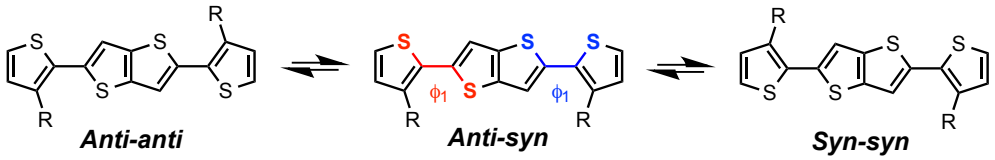

BTTT-H (R = H)
BTTT-Me (R = Me)

1.3 Computational Methods

All DFT computations were performed with Gaussian 09.[32] We assessed the performance of 11 popular DFT functionals, which include B3LYP[33,34,35,36] (hybrid GGA), M06[37] (hybrid meta-GGA), M06-HF[36] (hybrid meta-GGA), M06-2X[36] (hybrid meta-GGA), M06L,[38] B97D[39,40] (GGA), ωB97X[41] (range-corrected), ωB97X-D[42] (range-corrected), PBE1PBE[43] (GGA), BLYP[39], and BLYP-25HF[39]. Each of these functionals were tested with three Pople-style basis sets (6-31+G(d,p), 6-31++G(d), 6-311++G(d)). M06-2X is known to be sensitive to DFT integration grids; thus, we used an ultrafine grid consisting of 590 radial shells and 99 grid points per shell and tight convergence criteria for all DFT computations.[44] A highly-accurate energy difference between the *anti-anti* and *syn-syn* conformations of BTTT-H was computed within the focal point approach based on geometries optimized using MP2/aug-cc-pVTZ. In FPA,[24] valence energies are computed via systematic extrapolations using the correlation consistent hierarchy of basis sets.[24c] In this work, Hartree-Fock energies were extrapolated to the CBS limit using an exponential form[24d] based on energies computed with the cc-pVXZ (X = T, Q, 5) basis sets, while electron correlation energies (within the frozen-core approximation) were extrapolated using the functional form of Helgaker *et al*.[24e] based on CCSD/cc-pVTZ and CCSD/cc-pVQZ energies. Finally, an additive correction of –0.07 kcal/mol for higher-order electron correlation effects was appended to this energy, based on the difference in CCSD(T)/cc-pVTZ and CCSD/cc-pVTZ energies. The reported FPA energy difference is well-converged (< 0.1 kcal/mol) to both the CBS and full configuration interaction (FCI) limit. Conformational analysis of the subunits was performed by

computing the ground state structures (minima) and transition structures of planarization and rotation (maxima) using ωB97X-D/6-31+G(d,p) with an ultrafine grid and tight convergence criteria. This conformational analysis was performed on conformational library subunits and subunits of experimental oligomers. Vibrational analysis was used to confirm stationary points as minima (no imaginary frequencies) or first-order saddle points (one imaginary frequency). All graphics of optimized structures were generated with CYLview.[45]

1.4 Benchmark

There is a need for economical density functionals that capture the conformational preferences of thiophene-based materials to facilitate rapid screening of many candidates using common density functional methods. Toward this goal, we first use FPA to extrapolate accurate relative energies of the ***anti-anti*** and ***syn-syn*** conformers of BTTT-H. Reference geometries of the ***anti-anti*** and ***syn-syn*** conformers of BTTT-H used for FPA were optimized using MP2/cc-aug-pVTZ (see Figure 1.1b). In the ***anti-anti*** conformer, both S-C-C-S dihedral angles are 155° (25° out of plane), and in the ***syn-syn*** conformer, both dihedrals are 32°. Extrapolations of coupled cluster energies to the CBS limit indicate that ***anti-anti*** is preferred over ***syn-syn*** by 0.99±0.1 kcal mol^{-1}. Although the energy of the ***anti-syn*** conformer was not extrapolated using the FPA method, we expect the energetic preference to be ~0.5 kcal mol^{-1} relative to ***syn-syn***, a value half of that of the ***anti-anti*** conformer. The assumption that one dihedral has no impact on the other is validated in our DFT calculations of oligothiophenes, which are discussed in a later section.

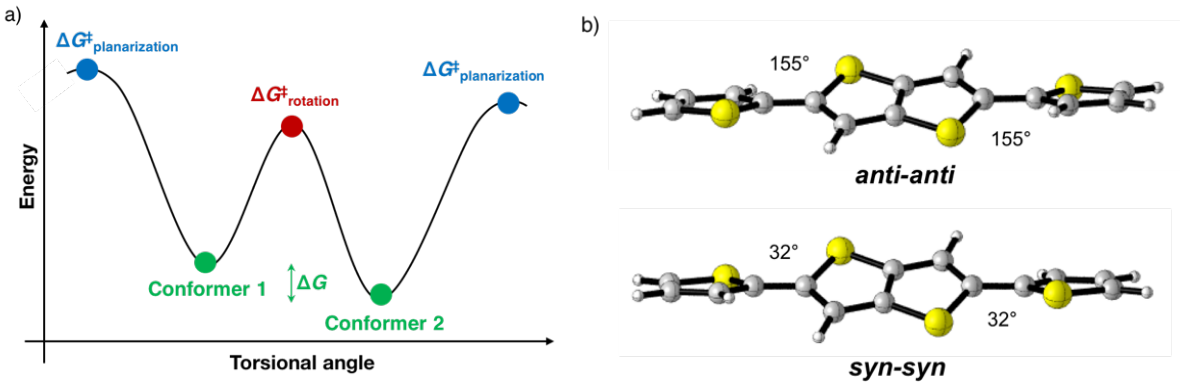

Figure 1.1. Schematic overview of this work.
(a) Schematic torsional potential indicating the computed structures in this work. (b) Geometries of ***anti-anti*** and ***syn-syn*** conformers of **BTTT-H** optimized using MP2/cc-aug-pVTZ. These geometries were used for subsequent FPA analysis.

Next, 11 DFT methods were used for geometry optimizations of the three different conformers of BTTT-H. Angles ϕ_1 or ϕ_2 in ***anti-anti*** and ϕ_1 in ***anti-syn*** (referred to as *anti*) were found to be the same in the optimized geometries, and angles ϕ_1 or ϕ_2 in ***syn-syn*** and ϕ_2 in ***anti-syn*** (referred to as *syn*) are the same in the optimized geometries. Thus, in our analysis, we treated each dihedral, whether it was ϕ_1 or ϕ_2, independently of the other dihedral in BTTT-H. The independence of each within oligomeric chains is further studied and discussed in a later section. Figure 1.2a shows the torsional behavior of the *syn* and *anti* dihedrals in BTTT-H across the different methods, and Figure 1.2b shows the energetic preference of the ***anti-anti*** conformer over the ***syn-syn*** conformer across the different methods. Dihedrals range from ~20-35° out of plane, with little variation across all methods. However, the energetic preference for the ***anti-anti*** conformer varies across the methods, ranging from 0.0 to 2.0 kcal mol^{-1}.

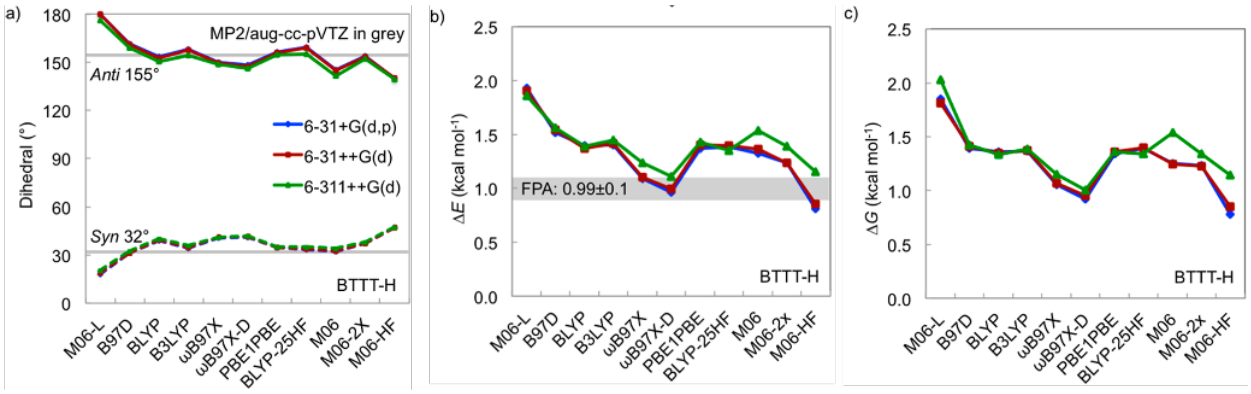

Figure 1.2. Benchmark results for BTTT-H.
(a) Deviation of DFT-calculated geometries from MP2/cc-aug-pVTZ geometries for the ***anti-anti*** (solid) and ***syn-syn*** (dashed) conformers of BTTT-H. (b) Relative electronic energy difference in BTTT-H, where $\Delta E = E_{syn\text{-}syn} - E_{anti\text{-}anti}$. DFT functionals are plotted with increasing HF-exchange, and extrapolated value is indicated in grey. (c) Relative free energy difference in BTTT-H, where $\Delta G = G_{syn\text{-}syn} - G_{anti\text{-}anti}$.

We compared DFT-calculated energies to the FPA-extrapolated energy, and ωB97X-D shows the smallest error relative to the FPA benchmark, falling well within error for all basis sets tested. This finding is in line with the findings of Bloom and Wheeler, who found that B2PLYP, ωB97X, and ωB97X-D provide reliable conformational energies for bithiophene.[23b] M06-HF slightly underestimates the energy, while ωB97X overestimates. However, both of those functionals fall within the margin of computational error. Other functionals overestimate the energy by up to 1 kcal mol^{-1}. In general, thermal corrections for free energies did not change the values considerably from electronic energies (see Figure 1.2c). Thus, ωB97X-D/6-31+G(d,p) was chosen as the most computationally efficient method and basis set pair for the development of the conformational library, as presented in the next section.

The electronic energies calculated using M06, M06-2X, and M06-HF are more strongly influenced by the choice of basis set than the other functionals tested, which may be due to the high percentage of HF exchange in these functionals. For M06-HF, the energy differs by a slightly higher value of 0.2 kcal mol^{-1} for the ***anti-anti*** conformer. Within the M06 family (M06, M06-HF, M06-L), energies vary between double-ζ and triple-ζ basis sets, with triple-ζ basis sets

overestimating energies. Across all the methods, the energies of the double-ζ basis sets 6-31+G(d,p) and 6-31++G(d) do not differ substantially. For BLYP, B3LYP, ωB97X, ωB97X-D, PBE1PBE, BLYP-25HF, and M06-2X, the energies calculated using triple-ζ basis sets varied by 0.1 kcal mol^{-1} or less.

Due to the high computational cost of FPA, only BTTT-H was subjected to the FPA method. However, the three conformers of BTTT-Me were thoroughly investigated using DFT methods. Figure 1.3a shows the torsional behavior of the *syn* and *anti* dihedral angles in BTTT-Me across the different methods. The torsional behavior varies little across the methods. *Anti* dihedrals range from 10 to 60° out of plane (though generally about 45°), and *syn* dihedrals are 30 to 60° out of plane (also generally about 45°). These dihedrals are a bit further from planar than those of BTTT-H (~35°). The optimized ground state structures of BTTT-Me showed that peripheral 3-methylthiophenes cause an increase in deviation from planarity, as expected because of unfavorable steric clashes upon planarization.

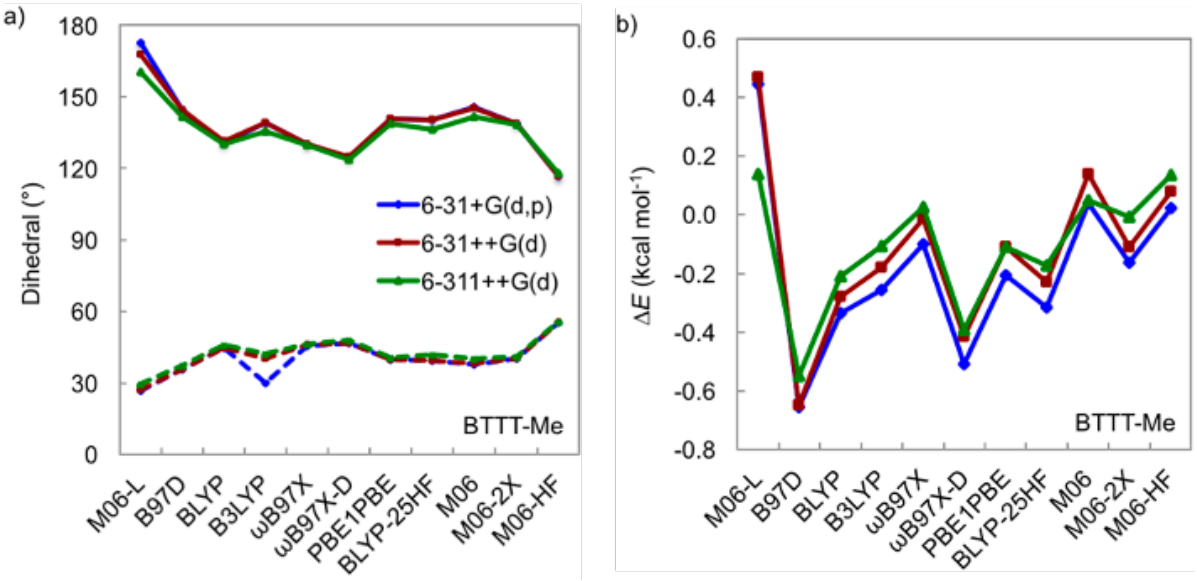

Figure 1.3. Benchmark results for BTTT-Me.
(a) Dihedrals for DFT-calculated geometries of the ***anti-anti*** (solid) and ***syn-syn*** (dashed) conformers of BTTT-Me. (b) Relative electronic energy difference in BTTT-Me, where $\Delta E = E_{syn\text{-}syn} - E_{anti\text{-}anti}$.

Whereas BTTT-H favors the ***anti-anti*** conformer by 1 kcal mol^{-1}, there is little or no preference in BTTT-Me (see Figure 1.3b). Regardless of basis set size, M06-L, M06, and M06-HF show a slight energetic preference for the ***anti-anti*** conformer, while B97D, BLYP, B3LYP, ωB97X, ωB97X-D, PBE1PBE, BLYP-25HF, and M06-2X show a slight energetic preference for the ***syn-syn*** conformer. As the basis size is increased, the energy difference between the two conformers decreases, except for M06-HF. In general, methyl substitution results in conformers that are close in energy, with relative energies of less than 0.7 kcal mol^{-1}. We conclude that the lack of preference for the ***anti-anti*** conformer is a result of the unfavorable CH_3—S interaction, and in many methods, including ωB97X-D, the ***syn-syn*** conformer is slightly more stable than the ***anti-anti***.

Although ωB97X-D has been shown (both in our benchmark and in previous studies[23a,b]) to be highly accurate for thiophene-based materials, it was not found to be as accurate for other dimeric species. Bloom *et al.*[23a] previously studied the full torsional potentials of bithiophene, bifuran, and biselenophene using FPA and several DFT methods, including 8 out of the 11 used in our benchmark. According to this study, ωB97X-D performs for bithiophene and bifuran, although less well for biselenophene. With this in mind, we further benchmarked bipyrrole and biphenyl. Compared to previous experimental and computational studies of biphenyl, ωB97XD does not perform as well as Becke functionals such as B3LYP and BLYP.[46,47] On the other hand, the energetics of bipyrrole are best described using ωb97X-D when compared to previously calculated energies using SCF and MP2/CCSD(T).[48]

1.5 Conformational Library

To establish a set of design rules regarding conformational preferences and barriers to planarization, we performed conformational analysis on a library comprised of common subunits found in the backbones of organic electronic materials. We performed conformational analysis on a wide range of dimers, particularly thiophene-based materials (see Scheme 1.2) using ωB97X-

D/6-31+G(d,p). The ground state structures and energetic preferences (*anti* or *syn*) of each dimer were compared, and rotational and planarization transition states were computed in order to obtain free energy barriers to rotation and planarization (see Figure 1.1a). We modeled the effect of long alkyl chains (usually added to polymers and oligomers for solubility) as methyl groups, as we find that an increase in alkyl chain length does not significantly affect planarization and rotational barriers for **1-Me**, **3-Me**, and **6-Me** ($\Delta\Delta G^{\ddagger}$ < 2.0 kcal mol^{-1}).

Scheme 1.2. Common subunits in conjugated polymers and oligomers used in organic electronics

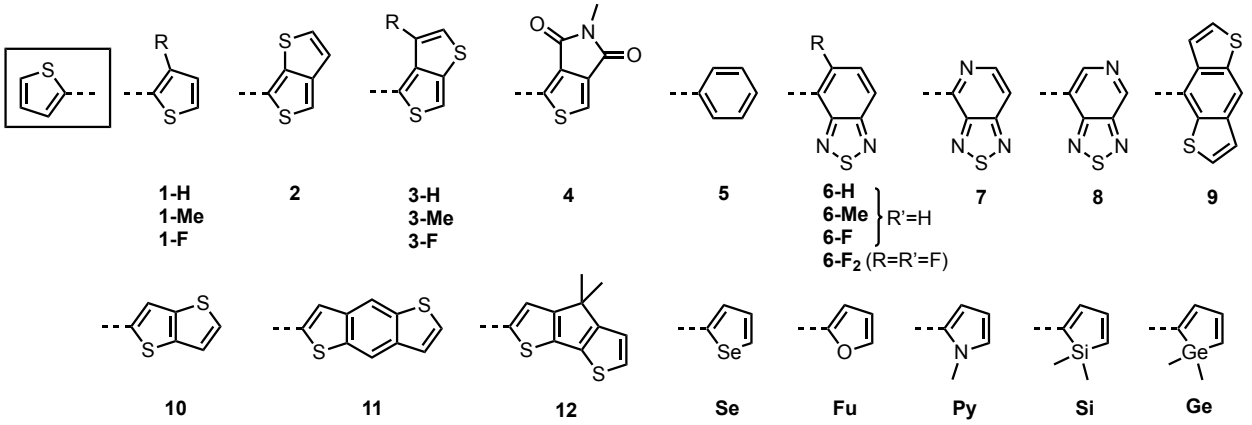

All units used in calculations were 2-thiophenyl (in box) and a second aryl or heterocyclic subunit (unboxed). The *anti* conformers are shown.

Table 1.1 gives a summary of the general trends observed in various subsets of the dimers studied. We compare a number of factors that influence planarity and conformational preferences of different subunits, including the effects of substituents (hydrogen, methyl, and fluorine), heteroatom substitution, and extent of conjugation. The effect of fluorine substitution is of interest due to recent studies showing that fluorination of polymers results in an increase in charge transport due to a conformationally restricted backbone and ordered aggregates.[49] Structures with fused rings attached are also promising photovoltaic materials due to a stable backbone conformation,[50] and thus subunits with such moieties are of interest in this study. In polycyclic heterocycles, we define *endo* and *exo* to mean that the unsymmetrically substituted sulfur or nitrogen heteroatom in the fused ring is near or away from, respectively, the parent thiophene

ring. The effect of using heterocycles other than thiophene was explored as well, as the substitution allows for electronic tuning. Although less prevalent in the literature, selenophene-based oligomers have reduced optical band gaps and enhanced photostability compared to their thiophene counterparts.[51]

Table 1.1. Effects studied in conformational library test set

effect studied	comparative subunits	observed trends
substitution of thiophene (**1**) and thieno[3,4-*b*]thiophene (**3**) with hydrogen, methyl, and fluorine	**1-H, 1-Me, 1-F** **3-H, 3-Me, 3-F**	Methyl substitution results in a lower energetic preference for the *anti* conformer due to stronger Me−S repulsion than H−S repulsion in hydrogen-substituted units. Fluorine substitution results in a *syn* preference due to favorable H−F interactions.
endo vs *exo* nature of thieno[3,4-*b*] thiophene	**2, 3-H**	*Syn* is preferred when sulfur is *endo* (**2**) and *anti* is preferred when sulfur is *exo* (**3-H**), as the 1,5 S−S interaction is unfavorable while the 1,6 S−H interaction is favorable.[a]
substitution of 2,1,3-benzothiadiazole (**6**) with hydrogen, methyl, and fluorine	**6-H, 6-Me, 6-F, 6-F_2**	*Anti* is always preferred due to a strong unfavorable S−N repulsion, which dominates over stabilizing H−F interactions in **6-F** and **6-F_2**.
endo vs *exo* nature of pyridothiadiazole	**7, 8**	**7** (*endo*) is completely planar in both *anti* and *syn* conformations, while **8** (*exo*) is ∼20−30° out of plane in both conformations. This is due to the ability of **7** to delocalize electron density onto the pyridino nitrogen.
increase in conjugation due to fused ring systems	**10, 11, 12**	When the second subunit in the dimer is thieno[3,2-*b*]thiophene, benzodithiophene, or cyclopentadithiophene, the conformational behavior does not change greatly. As would be expected, the HOMO−LUMO gap decreases slightly with each fused ring that is added due to the increase in electron delocalization across the fragment.
heterocyclic rings	**Se, Fu, Py, Si, Ge**	Except for **Py**, heteroatom substitution results in more planar conformations compared to **1-H**. With increasing heteroatom size, HOMO−LUMO gaps decrease.[b]

[a]This observation supports the findings of Jackson *et al.*[14]
[b]This observation is in line with DFT calculations reported by Dou *et al.*[49d] The HOMO level increases and the LUMO levels drops due to electron-stabilizing effects from the increased polarizability of selenium compared to oxygen and sulfur.

Table 1.2 relates the preferred conformations, as well as barriers to rotational and planarization for all 24 dimers or heterodimers studied here. The energy difference between *anti* and *syn* conformations (Δ*G*, Table 1.2) serves as a measure of the relative disorder in polymer chains.[52] In general, for the conformers studied in this work, the *anti* conformers are preferred over the *syn* conformers by less than 1 kcal mol^{-1}, and the preferred dihedral angles range from 0 to 70° out of plane. Subunit **4**, featuring maleimide as the second unit, is the only structure in this study that substantially prefers the *syn* conformer, exhibiting a 1.3 kcal mol^{-1} preference. We attribute this preference to the destabilizing carbonyl O—S interaction and stabilizing CH—O hydrogen bonding. These types of favorable interactions have previously been explored by Jackson *et al*.[14] in other dimer units, with the oxygen-hydrogen interactions stabilizing these units by 0.8 to 2.4 kcal mol^{-1} at optimal distances where binding energy is maximum.

Table 1.2. Conformational preferences, energetics, and electronics conformational library test set

subunit	conformer	|⟨SCCX⟩|, deg	ΔG[a] (kcal mol^{-1})	$\Delta G^{\ddagger}_{\text{planarization}}$[a] (kcal mol^{-1})	$\Delta G^{\ddagger}_{\text{rotation}}$[a] (kcal mol^{-1})	HOMO (eV)	LUMO (eV)	HOMO−LUMO gap (eV)
				Thiophene and Thienothiophene Derivatives				
1-H	*anti*	33	0.0	1.9	2.5	−7.8	0.4	8.2
	syn	42	0.7	2.7		−7.8	0.5	8.3
1-Me	*anti*	56	0.0	3.0	1.3	−7.9	0.7	8.6
	syn	47	0.1	1.3		−7.8	0.6	8.4
1-F	*anti*	27	0.1	1.5	2.3	−7.8	0.3	8.1
	syn	34	0.0	1.7		−7.9	0.3	8.2
2	*anti*	34	0.2	1.7	2.2	−7.6	0.0	7.6
	syn	36	0.0	1.7		−7.4	0.0	7.4
3-H	*anti*	39	0.0	1.9	2.0	−7.5	−0.2	7.3
	syn	44	0.2	2.7		−7.6	0.1	7.7
3-Me[b]	*anti*	75	0.2	6.6	0.7	−7.5	0.4	7.9
	syn	70	0.0	7.3		−7.5	0.4	7.9
3-F	*anti*	51	0.1	2.8	1.7	−7.6	0.0	7.6
	syn	43	0.0	2.3		−7.5	−0.1	7.4
4	*anti*	14	1.3	2.7	4.6	−8.6	−0.9	7.7
	syn	1	0.0			−8.6	−0.8	7.8
				Benzenoid Derivatives				
5		36		1.8	2.5	−8.0	0.6	8.6
6-H	*anti*	20	0.0	1.1	3.3	−7.9	−1.0	6.9
	syn	32	0.6	2.1		−8.0	−1.0	7.0
6-Me[b]	*anti*	66	0.0	5.0	1.3	−8.2	−0.8	7.4
	syn	57	0.1	5.4		−8.1	−0.8	7.3
6-F	*anti*	7	0.0	1.6	3.0	−7.9	−1.1	6.8
	syn	20	0.4	2.0		−8.0	−1.1	6.9
6-F$_2$	*anti*	0	0.0		3.6	−8.1	−1.2	6.9
	syn	22	1.0	1.5		−8.1	−1.2	6.9
7[c]	*anti*	0	0.0		7.8	−8.2	−1.4	6.8
	syn	0	1.3			−8.1	−1.3	6.8
8	*anti*	17	0.0	1.4	3.6	−8.2	−1.4	6.8
	syn	33	0.8	2.2		−8.2	−1.3	6.9
9[b]	*anti*	68	0.4	9.1	1.4	−7.5	0.2	7.7
	syn	68	0.0	10.9		−7.5	0.2	7.7
				Fused Rings				
10	*anti*	33	0.0	1.4	2.6	−7.6	0.1	7.7
	syn	41	0.6	2.5		−7.6	0.2	7.8
11	*anti*	28	0.0	1.2	3.0	−7.4	−0.1	7.3
	syn	38	0.7	2.4		−7.4	0.0	7.4
12	*anti*	32	0.0	1.4	2.7	−7.1	0.0	7.1
	syn	41	0.4	2.2		−7.1	0.1	7.2
				Heteroatom Substitution				
Se	*anti*	25	0.0	1.7	3.6	−7.7	0.2	7.9
	syn	0	1.1			−7.6	0.1	7.7
Fu	*anti*	0	0.0		4.1	−7.6	0.5	8.1
	syn	10	0.3	1.5		−7.6	0.5	8.1
Py	*anti*	45	0.0	3.2	1.3	−7.4	1.0	8.4
	syn	62	0.3	3.3		−7.6	1.0	8.6
Si	*anti*	0	0.0		3.8	−7.4	−0.1	7.3
	syn	24	0.8	2.5		−7.5	0.0	7.5
Ge	*anti*	0	0.0		4.0	−7.4	0.0	7.4
	syn	0	1.1			−7.4	0.0	7.4

[a]Free energies are relative to lowest energy conformer (*anti* or *syn*) in the ground state for each dimer.
[b]Subunits have high planarization barriers.
[c]Subunit has a high rotational barrier.

Figure 1.4a shows the free energy for rotation or planarization versus the minimum out-of-plane angle. Rotational and planarization barriers are usually low ($\Delta G^{\ddagger}$ <4 kcal mol^{-1} and <3 kcal mol^{-1}, respectively), and rotation will be rapid at room temperature. In general, as the ground state dihedral increases, the rotational barrier decreases and the planarization barrier increases. The exceptions are >4 kcal mol^{-1}. Subunit **7** has the highest rotational barrier (7.8 kcal mol^{-1}), although both *anti* and *syn* conformers are completely planar due to electron delocalization onto the benzenoid nitrogen. High planarization barriers were found for both conformers of **3-Me**, **6-Me**, and **9**. These three conformers are highly nonplanar in the ground state, ranging from about 60 to 70° out of plane, and there is very large steric hindrance in the planar conformers. In particular, both conformers of subunit **9** are highly out of plane as indicated by large torsional angles (68° for both) and high planarization barriers (9.1 and 10.9 kcal mol^{-1} for *anti* and *syn*). The *syn* conformer exhibits 1,5 S—S repulsion and the *anti* conformer exhibits 1,7 S—H interactions, both of which are unfavorable. Although this dimer, unlike the others the set, is unlikely to planarize readily, its three-dimensional nature can be useful, as benzodithiophene is often employed in oligomers as a means for grid-type π-overlap in the solid state, which can lead to high charge transport.[53]

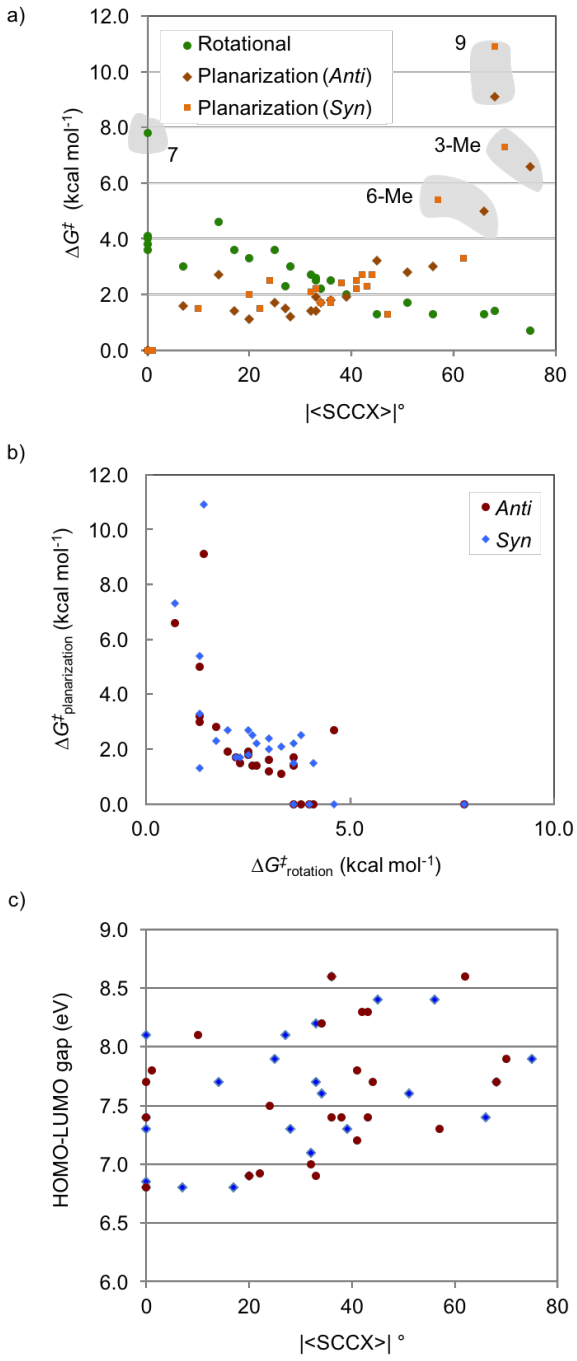

Figure 1.4. Conformational library results.
(a) Free energy barriers for rotation and planarization versus degrees out of plane about the SCCX dihedral in each dimer. (b) Free energy barrier for planarization versus free energy barrier for planarization for *syn* and *anti* conformers, high planarization barriers correlate with lower rotational barriers. (c) HOMO- LUMO gaps of dimers versus degrees out of plane.

Figure 1.4b shows the free energy barrier for planarization versus the free energy barrier for rotation. In general, subunits with high planarization barriers have low rotational barriers, and subunits with low planarization barriers have high rotational barriers. Ground state geometries that are highly out of plane (e.g., **3-Me** or **9**) have higher planarization barriers but low rotational barriers. On the other hand, planar ground states (e.g., *syn* conformer of **Fu**) have low planarization barriers but higher rotational barriers. The lowest energy conformer of **3-Me** is 70° out of plane; this results in a high planarization barrier of 7.3 kcal mol^{-1} but a low rotational barrier of 0.7 kcal mol^{-1}. We conclude that out-of-plane geometries are pre-distorted to easily undergo rotation, while planar geometries are pre-distorted to easily undergo planarization. This pre-distortion argument has been made previously by our group[54] and various other groups for a variety of transformations.[55]

Across the test set, we find no correlation between the HOMO-LUMO gap and planarity of the ground state (Figure 1.4c), although increased conjugation and heteroatom substitution leads to narrowing of the gap (further described in Table 1.2), also reported previously by the Bendikov group.[56] Fluorine substitution does not lower the gap significantly, although it leads to more planar ground states.

Our calculations on these thiophene-based dimers correlate with previous DFT studies and experimental work. Previous DFT calculations of the ground state of **1** have shown that its dihedral angles range from 23 to 27° using CAM-B3LYP, PBE0, and BHLYP with 6-31G(d).[57] This non-planar structure of bithiophene has also been characterized experimentally. In independent studies, the S-C-C-S dihedral angle in gas phase at room temperature was measured by electron diffraction and found to be 146 and 144° (34 and 36° out of plane) for the *anti* conformation of bithiophene.[20a,20b] Our computed value for **1-H** *anti* using ωB97X-D/6-31+G(d,p) is 33°, which falls within range of the previously measured and computed dihedrals.

We propose that the conformational behavior of thiophene-based oligomers and polymers can be generalized using the results of our conformational analysis in an additive manner. This generalization assumes that the behavior of individual dihedrals in a chain is independent of the rest of the molecule. To validate this line of thinking, we present a twofold analysis of (1) the optimized structures of di-, tri-, tetra-, penta-, and hexathiophene and (2) a comparative study of the additive model (using bithiophene as the additive unit) and calculated model (using hexathiophene).

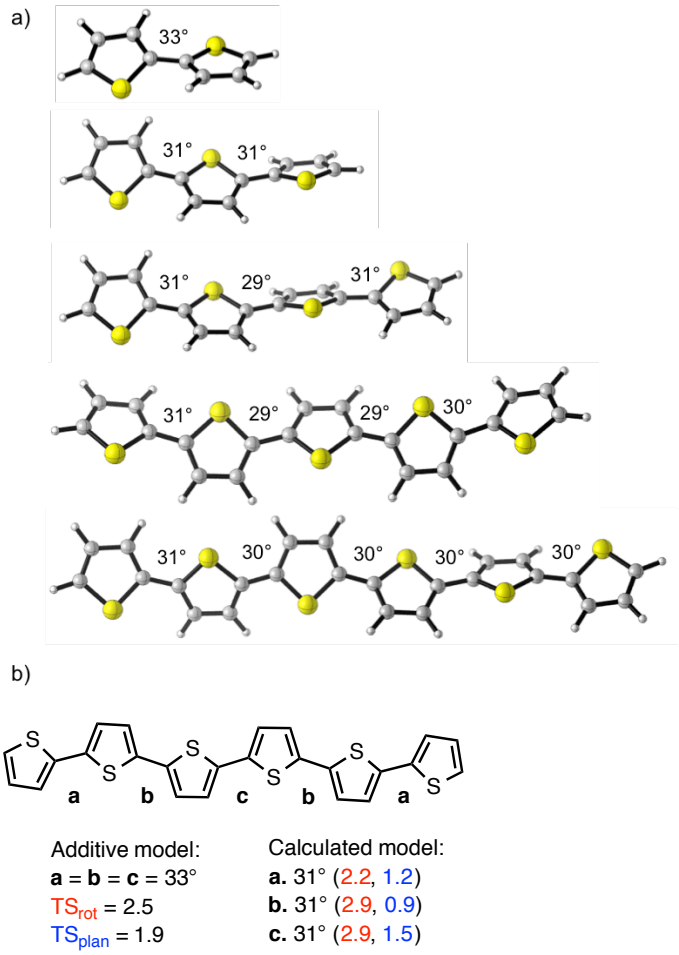

Figure 1.5. Additive vs. calculated model.
(a) Dihedral angles in structures of bithiophene, trithiophene, tetrathiophene, pentathiophene, and hexathiophene optimized with ωB97X-D/6-31+G(d,p) (b) Dihedral angles and rotation and planarization barriers (kcal mol^{-1}) from the additive model and from ωB97X-D/6-31+G(d,p) calculations.

Each of the structures in Figure 1.5 was optimized using ωB97X-D/6-31+G(d,p). The ground state of bithiophene is 33° out of plane, as described in the conformational library study. As the number of appended thiophenyl units is increased (up to *n*=6), the S-C-C-S dihedrals change insignificantly (Figure 1.5a). Notably, each of the S-C-C-S dihedrals in the ground state of hexathiophene are 31° out of plane. Previous work by Zade *et al.*[2] has shown that as conjugation length increases, oligothiophenes become more planar in the gas phase. The increase in conjugation favors a slightly more planar overall structure in hexathiophene compared to bithiophene, but the change in planarity with extension is insignificant. A full conformational search was performed for hexathiophene, and the all-*anti* conformer (shown in Figure 1.5a) is preferred by 0.3 kcal mol^{-1}. This indicates that the conformational preference of a ground state structure of an oligomeric chain can be predicted using its dimeric subunits.

We next compare the planarization and rotational barriers of bithiophene against those calculated using hexathiophene using ωB97X-D/6-31+G(d,p) (Figure 1.5b). The rotational barrier for bithiophene is 2.5 kcal mol^{-1}, and the planarization barrier is 1.9 kcal mol^{-1}. Rotational and planarization barriers were also found to have approximate additivity for hexathiophene, with rotational barriers and planarization barriers falling in the range of 2.2—2.9 and 0.9—1.5 kcal mol^{-1}, respectively. The terminating thiophene units have slightly lower rotational barriers (2.2 kcal mol^{-1}) than that of the internal dihedrals (2.9 kcal mol^{-1}), though all values fall within 0.4 kcal mol^{-1} of that for bithiophene. On the other hand, planarization barriers for hexathiophene in the calculated model are slightly lower than those for bithiophene. The differences in barriers are likely due to the favorable orbital overlap in the extended structure, though all differences are less than 0.7 kcal mol^{-1}. Thus, this additive model is useful to describe the inherent conformational behavior of complex systems without the need to perform calculations on entire oligo- and polymeric chains. However, we note that this model does not account for external intermolecular

interactions in crystals that also play a part in influencing conformation, as those in hexathiophene dimers and higher order clusters described by Vujanovich *et al.*[21d]

1.6 Gas phase vs. solid state

Thiophene-based oligomers are typically nearly planar in the solid-state due to stabilizing non-covalent interactions.[20b] In some instances, there are non-planar torsionals, likely due to face-to-edge interactions that dominate over face-to-face stacking, resulting in non-planar conformations. To understand the barriers to planarization of such oligomers in solid state, gas phase energetics were compared to experimental crystal structures. We performed conformational analysis on the subunits of 8 thiophene-based oligomers (**FPDT**,[58] **FPTT**,[58] **FPQT**,[58] **TFPTP**,[59] **BPFT**,[60] **HPT**,[61] **TFAPT**,[62] and **DC4VT**[63]) (Scheme 1.3) and compared the gas phase geometries to conformations found in solid state. Unfortunately, the subunits for which we computed high barriers to planarization (i.e., **3-Me**, **6-Me**, and **9**) are typically used in amorphous polymer films[64] and thus we were not able to obtain experimental crystal data for comparison.

Scheme 1.3. Oligomer test set

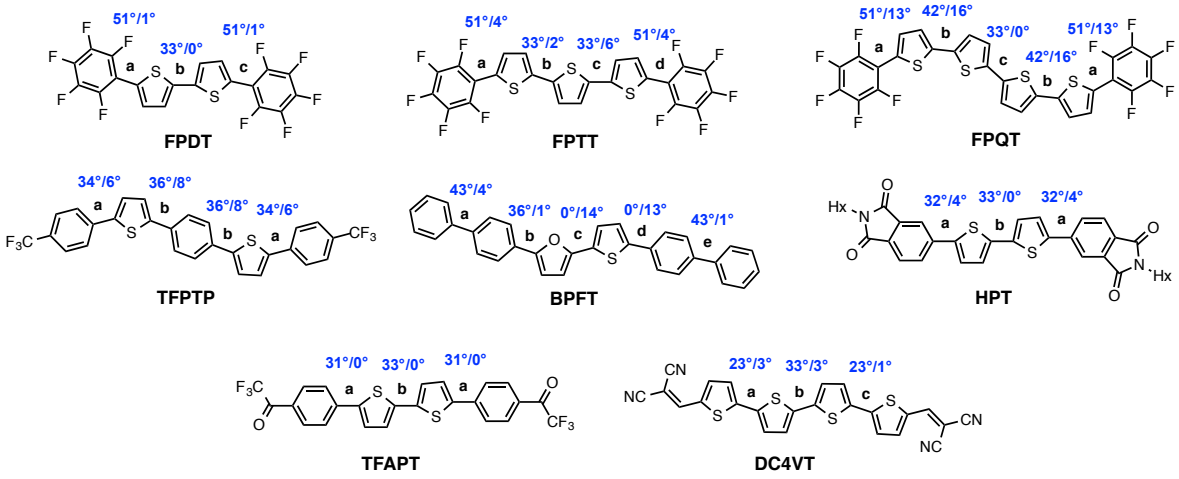

Labels in blue are dihedrals from gas phase ωB97X-D/6-31+G(d,p) optimizations/crystal structures.

For each of the structures in Scheme 1.3, the ground state conformation, free energy barrier to planarization, and electronic energy difference to achieve the dihedral found in crystal

structure was computed for each dimer subunit (dihedrals are labeled). These results are presented in Table 1.3. We present an analysis of the packing motifs of **FPTT**, **FPDT**, and **HPT**, and relate the conformations in solid state to computed gas-phase energetics. Gas phase optimizations show that dimeric dihedrals range from 20 to 50° out of plane (average 34°). Dihedrals in crystal are 0 to 16° out of plane, with an average dihedral of 4° out of plane. The energetic cost to achieve the dihedral found in the crystal is less than 1 kcal mol^{-1} (except for **BPFT**, due to T-shaped stacking in the crystal structure), and the average cost to completely planarize is 2.1 kcal mol^{-1}.

FPTT molecules pack in a mixed packing mode, where the adjacent molecules in the same phase form π-stacked structures. In the gas phase, the dihedrals of the exterior diaryl units (*a* and *d*) are 51° out of plane and dihedrals of the interior bithiophene units (*b* and *c*) are 33° out of plane. In the crystal structure, all four dihedrals are relatively planar, none exceeding 6° out of plane, having overcome free energy barriers of 1.9 and 2.6 kcal mol^{-1} for the internal and external dihedrals, respectively. These noncovalent π-stacking interactions serve as stabilizing interactions to assist in the planarization of these dihedrals.

FPDT molecules pack in a cofacial π-stacking motif, with one external dihedral rotated 36° (*c*) out of plane in order to form face-to-edge interactions with adjacent molecules. Other dihedrals are completely planar in the crystal structure. Similar to **FPTT**, gas phase calculations show that internal dihedrals are 33° out of plane, and external dihedrals are 51° out of plane. Planarization in the crystal of dihedrals *a* and *b* is achieved by overcoming free energy barriers of 1.9 and 2.6 kcal mol^{-1}, respectively.

In the case of **HPT**, the molecules pack in a π-stacking motif with planar dihedrals varying from 0 to 4°. The barriers for planarization of each dihedral from gas phase structure (~30° for each) are low (< 2 kcal mol^{-1}). In our calculations, we used methyl groups in place of the hexyl

chains on each end of the molecule. Even with long alkyl chains, planarization of dihedrals is achieved in crystals.

Table 1.3. Energetic barriers to planarization of oligomer test set

		|⟨XCCX⟩|, deg		energy barrier (kcal mol^{-1})	
	angle	gas[a]	crystal	ΔE^b	$\Delta G^{\ddagger}_{\text{planarization}}$
FPDT	*a*	51	1	0.9	2.6
	b	33	0	0.4	1.9
	c	51	1	0.1	2.6
FPTT	*a*	51	4	0.9	2.6
	b	33	2	0.4	1.9
	c	33	6	0.4	1.9
	d	51	4	0.9	2.6
FPQT	*a*	51	13	0.7	2.6
	b	42	16	0.6	2.1
	c	33	0	0.4	1.9
TFPTP	*a*	34	6	0.6	1.6
	b	36	8	0.4	1.8
BPFT	*a*	43	4	2.8	4.2
	b	36	1	0.8	1.8
	c	0	13	0.1	
	d	0	14	0.0	
	e	43	1	2.8	4.2
HPT	*a*	32	4	0.5	0.3
	b	33	0	0.4	1.9
TFAPT	*a*	31	0	0.5	1.5
	b	33	0	0.4	1.9
DCV4T	*a*	23	3	0.2	1.2
	b	33	3	0.4	1.9
	c	23	1	0.2	1.2
average		34	4	0.7	2.1
SD		14	5	0.7	0.9

[a]Ground state geometries were optimized using ωB97X-D/6-31+G(d,p).
[b]Electronic energy difference between ground state geometry and that found in experimental crystal structure.

Over the eight structures analyzed, the average electronic energy barrier to planarization to the conformation observed in the crystal is only 0.6±0.6 kcal mol^{-1} per unit, and the average free energy barrier to complete planarization is 1.9±1.1 kcal mol^{-1} per unit. These numbers correlate well with those computed using the conformational library test set, where free energies

to planarization were less than 4 kcal mol^{-1} per unit. The low average energies per subunit indicate that planarization is readily achieved in these materials and further demonstrate the applicability of our conformational library model to these types of materials.

1.7 Analysis of HTMs

Recently, thiophene-based oligomers have been shown to have excellent properties as hole transport materials for perovskite solar cells.[65] In particular, **DERDTS-TBDT** (Scheme 1.4) was used as an efficient hole transport material with lead halide perovskite active layers, achieving efficiency of 16.2% with $CH_3NH_3PbI_{3-x}Cl_x$ due to favorable energy alignment.[31] We subjected the subunits in **DERDTS-TBDT** to conformational analysis and predict that these subunits can readily achieve planarization due to the low torsional barriers to planarization (Table 1.4).

Scheme 1.4. Structure of DERDTS-TBDT

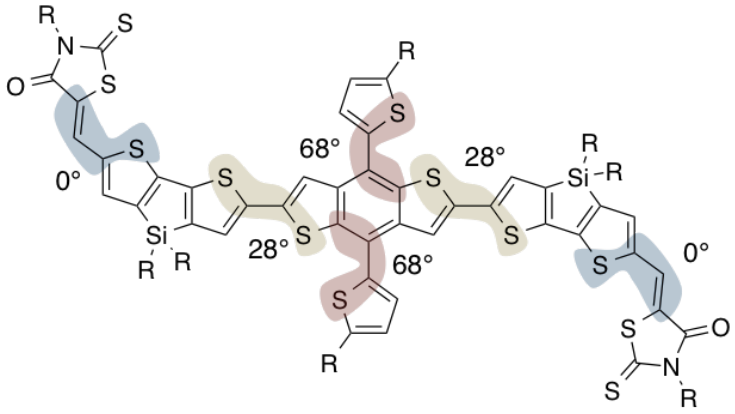

Studied dihedrals are highlighted. R groups represent ethylhexyl groups, which were modeled with methyl groups in calculations for computational efficiency. Dihedrals from gas phase optimizations of dimeric analogues using ωB97X-D/6-31+G(d,p) are shown.

Energetics for the dihedrals highlighted in red and gold were extracted from the conformational library results (subunits **9** and **11**). The red dihedral favors the *syn* conformer by 0.4 kcal mol^{-1}. Since the planarization barrier is high (10.9 kcal mol^{-1}), it is unlikely that the conformer will planarize, even in the crystal structure. The gold dihedral is slightly out of plane in

the gas phase, favoring the *anti* conformation by 0.7 kcal mol^{-1}. This dihedral is likely to planarize in the solid state, as the planarization barrier is low (1.2 kcal mol^{-1}). The blue conformer was found to be completely planar both in the *anti* and *syn* conformations, with no energetic preference for either, though the rotational barrier is on the upper end (5.7 kcal mol^{-1}), indicating that it is unlikely for the dihedral to rotate easily from one conformer to another. Based on this conformational analysis, we conclude that in the solid state, **DERDTS-TBDT** is planar across the backbone of the oligomer, with thiophene units highlighted in red coming out of plane, since those are not readily planarized unlike the rest of the backbone. Crystal packing of this structure likely results in close π-π stacking in two directions, allowing for multi-dimensional charge transport. Previous studies have shown that molecules that have highly dimensional (2D, 3D) π-systems (e.g., tetrahedral spiral and cruciform structures) pack in a manner that maximizes π-stacking in both directions, maximizing the dimensionality of the available charge transport pathways.[66]

Table 1.4. Calculated energetics for DERDTS-TBDT dihedrals

subunit	conformer	|⟨SCCX⟩|, deg	ΔG^a (kcal mol^{-1})	$\Delta G^{\ddagger}_{\text{planarization}}{}^a$ (kcal mol^{-1})	$\Delta G^{\ddagger}_{\text{rotation}}{}^a$ (kcal mol^{-1})
red (**9**)	*anti*	68	0.4	9.1	1.4
	syn	68	0.0	10.9	
gold (**11**)	*anti*	28	0.0	1.2	3.0
	syn	38	0.7	2.4	
blue	*anti*	0	0.1		5.7
	syn	0	0.0		

[a]Free energies are relative to lowest energy conformer (anti or syn) in the ground state for each dimer.

1.8 Prediction of a new oligomer

Finally, we designed a new oligomer **BDT-1** with a benzodithiophene core (Figure 1.6) that should be easily planarized in the crystal structure due to low planarization barriers and stabilizing interactions. For computational efficiency, we use *N*-methyl maleimide, although longer alkyl chains would be used in place of methyl for solubility. The gas-phase optimized geometry shows that thiophene-phenyl dihedrals are each about 20°out of plane in the gas phase.

According to the conformational library study, subunit **5** is 36° out of plane in its optimized geometry. The two dihedral values are not very different, though the slightly enhanced planarity of **BDT-1** is likely due to the extended electron delocalization within the backbone of the molecule. Due to the low planarization barrier of the out-of-plane dihedrals (planarization barrier is 1.8 kcal mol^{-1} for **5**) and favorable π-π interactions, the backbone of the molecule is expected to planarize in the dimer. Synthesis of this compound can be achieved through reactions found in the literature. The synthesis of the 2,5-diphenylbenzodithiophene core can be achieved via intramolecular cyclization of 1,4-dibromo-2,5-bis(phenylethynyl)benzene.[67] This benzene precursor can be prepared in two-steps from 1,4-dibromobenzene,[68] and the phenyl groups can be furnished with boron-containing groups to allow for subsequent Suzuki cross-coupling to attach additional thiophene groups.[69] This simple synthetic procedure allows for the synthesis of **BDT-1** with several different chalcogenophenes. Experimental studies are currently underway to validate these predictions.

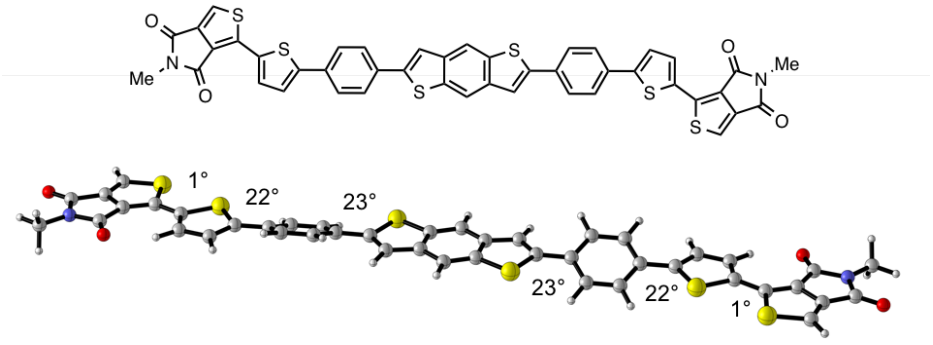

Figure 1.6. New predicted oligomer.
Gas-phase optimized geometry of **BDT-1** using ωB97X-D/6-31+G(d,p). Values indicate degrees out of plane.

1.9 Conclusions

We have computationally investigated the planarization barriers of small conjugated organic molecules and polymers in solid state. In a benchmarking study of DFT energetics against data extrapolated *ab initio* values, we find that ωB97X-D gives the most accurate values, which

was then used to perform conformational analysis of 24 thiophene-based subunits. Results were compared to a test set of experimental crystal structures, and planarization barriers of crystal dihedral angles correlated with those of individual subunits. We applied the results of our conformational study in an analysis of **DERDTS-TBDT** and in the design of a new oligomer. Based on these data, we summarize a set of general rules regarding the conformational preferences and planarization barriers of common fragments of organic materials:

- The dimers studied in this work are easily planarized at room temperature in solution-processing due to low gas-phase energy barriers of planarization (less than 3 kcal mol^{-1}). Rotational barriers are also low (less than 4 kcal mol^{-1}), indicating fast interconversion between *anti* and *syn* ground state conformers.
- Torsional angles, planarization barriers, and rotational barrers are additive.
- Analysis of experimental crystal structures indicate that in the absence of other stabilizing interactions between molecules such as T-shaped interactions, molecular torsions are planar.
- The torsional potentials of these dimers can also further applied in force field parametrizations.[23c]

While these gas-phase calculations rooted in DFT provide a foundation to understand planarity, one of the many influences in molecular conformations in the solid-state, we acknowledge that a holistic picture can only be obtained by further development of theoretical solid-state methods. Bridging the discrepancy between gas-phase calculations and prediction of bulk materials properties by employing dynamics or QM/MM methods is indeed a challenge; nevertheless, this approach is a launching point for molecular design of future organic electronic materials on which we can build an understanding of molecular conformations of organic semiconductors in the solid state, particularly as relevant in subsequent work discussed in later chapters.

1.10 References

[1] (a) Dang, M. T.; Hirsch, L.; Wantz, G.; Wuest, J. D. *Chem. Rev.* **2013**, *113*, 3734-3765. (b) Huang, Y.; Kramer, E. J.; Heeger, A. J.; Bazan, G. C. *Chem. Rev.* **2014**, *114*, 7006-7043. (c) Dou, L.; Liu, Y.; Hong, Z.; Li, G.; Yang, Y. *Chem. Rev.* **2015,** *115*, 12633-12665.

[2] Zade, S. S.; Bendikov, M. *Chem. Eur. J.* **2007**, *13*, 3688-3700.

[3] (a) Beenken, W. J. D.; Lischka, H. *J. Chem. Phys.* **2005**, *123*, 144311. (b) Beenken, W. J. D. *Chem. Phys.* **2008**, *349*, 250-255.

[4] Vezie, M. S.; Few, S.; Meager, I.; Pieridou, G.; Dörling, B.; Ashraf, R. S.; Goñi, A. R.; Bronstein, H.; McCulloch, I.; Hayes, S. C.; Campoy-Quiles, M.; Nelson, J. *Nat. Mat.* **2016**, *15*, 746-753.

[5] (a) Collini, E.; Scholes, G. D. *Science* **2009**, *323*, 369-373. (b) Hwang, I.; Scholes, G. D. *Chem. Mater.* **2011**, *23*, 610-620.

[6] Jackson, N. E.; Savoie, B. M.; Kohlstedt, K. L.; Marks, T. J.; Chen, L. X.; Ratner, M. A. *Macromolecules* **2014***, 47,* 987-992.

[7] For a recent review on conformational and phase behavior of conjugated polymers, see: Kuei, B.; Gomez, E. D. *Soft Matter* **2017**, *13,* 49-67.

[8] For select studies of the influence of molecular structures on molecular packing in organic materials: (a) Fei, Z.; Pattanasattayavong, P.; Han, Y.; Schroeder, B. C.; Yan, F.; Kline, R. J.; Anthopoulos, T. D.; Heeney, M. *J. Am. Chem. Soc.* **2014**, *136*, 15154-15157. (b) Yao, J.; Yu, C.; Liu, Z.; Luo, H.; Yang, Y.; Zhang, G.; Zhang, D. *J. Am. Chem. Soc.* **2015**, *138*, 173-185. (c) MacLachlan, A. J.; Rath, T.; Cappel, U. B.; Dowland, S. A.; Amenitsch, H.; Knall, A.-C.; Buchmaier, C.; Trimmel, G.; Nelson, J.; Haque, S. A. *Adv. Funct. Mater.* **2015**, *25*, 409-420. (d) Li, S.; Ye, L.; Zhao, W.; Zhang, S.; Ade, H.; Hou, J. *Adv. Energy Mater.* **2017**, DOI: 10.1002/aenm.201700183.

[9] Fei, Z.; Pattanasattayavong, P.; Han, Y.; Schroeder, B. C.; Yan, F.; Kline, R. J.; Anthopoulos, T. D.; Heeney, M. *J. Am. Chem. Soc.* **2014**, *136*, 15154-15157.

[10] For a perspective on strategies employed in design and structural organization of organic conjugated materials, see: Beaujuge, P. M.; Fréchet, J. M. J. *J. Am. Chem. Soc.* **2011**, *133,* 20009-20029.

[11] Noriega, R.; Rivnay, J.; Vandewal, K.; Koch, F. P. V.; Stingelin, N.; Smith, P.; Toney, M. F.; Salleo, A. *Nat. Mat.* **2013**, *12*, 1038-1044.

[12] For examples of MD simulations of organic materials, see: (a) Muccioli, L.; D'Avino, G.; Zannoni, C. *Adv. Mater.* **2011**, *23*, 4532-4536. (b) Jackson, N. E.; Kohlstedt, K. L.; Savoie, B. M.; Olvera de la Cruz, M.; Schatz, G. C.; Chen, L. X.; Ratner, M. A.. *Am. Chem. Soc.* **2015**, *137*, 6254-6262. (c) Yavuz, I.; Martin, B. N.; Park, J.; Houk, K. N. *J. Am. Chem. Soc.* **2015,** *137*, 2856-2866. (d) Yavuz, I.; Zhang, L.; Briseno, A. L.; Houk, K. N. *J. Phys. Chem. C* **2015,** *119*, 158-165. (e) Yavuz, I.; Lopez, S. A.; Lin, J. B.; Houk, K. N. *J. Mater. Chem. C.* **2016***, 4*, 11238-11243. (f) Yavuz, I.; Houk, K. N. *J. Phys. Chem. C* **2017**, *121*, 993–999. (g) Root, S. E.; Jackson, N. E.; Savagutrup, S.; Arya, G.; Lipomi, D. J. *Energy Environ. Sci.* **2017**, *10*, 558-569.

[13] Huang, C.-F.; Wu, S.-L.; Huang, Y.-F.; Chen, Y.-C.; Chang, S.-T.; Wu, T.-Y.; Wu, K.-Y.; Chuang, W.-T.; Wang, C.-L. *Chem. Mater.* **2016**, *28,* 5175-5190.

[14] For computational studies of non-covalent interactions in conjugated materials, see: (a) Jackson, N. E.; Savoie, B. M.; Kohlstedt, K. L.; de la Cruz, M. O.; Schatz, G.; Chen, L. X.; Ratner, M. A. *J. Am. Chem. Soc.* **2013**, *135*, 10475-10483. (b) Coughlin, J. E.; Zhugayevych, A.; Bakus, R. C., II.; van der Poll, T. S.; Welch, G. C.; Teat, S. J.; Bazan, G. C.; Tretiak, S. *J. Phys. Chem. C* **2014**, *118,* 15610-15623. (c) Conboy, G.; Spencer, H. J.; Angioni, E.; Kanibolotsky, A. L.; Findlay, N. J.; Coles, S. J.; Wilson, C.; Pitak, M. B.; Risko, C.; Coropceanu, V.; Brédas, J.-L.; Skabara, P. J. *Mater. Horiz.* **2016**, *3,* 333-339. (d) Raychev, D.; Guskova, O.; Seifert, G.; Sommer, J.-U. *Comput. Mater. Sci.* **2017**, *126*, 287-298.

[15] For experimental studies that employ non-covalent interactions as conformational locks in conjugated materials, see: (a) Huang, H.; Chen, Z.; Ortiz, R. P.; Newman, C.; Usta, H.; Lou, S.; Youn, J.; Noh, Y.-Y.; Baeg, K.-J.; Chen, L. X.; Facchetti, A.; Marks, T. *J. Am. Chem. Soc.* **2012**, *134*, 10966-10973. (b) Lei, T.; Dou, J.-H.; Cao, X.-Y.; Wang, J.-Y.; Pei, J. *J. Am. Chem. Soc.* **2013**, *135*, 12168-12171. (c) Lei, T.; Xia, X.; Wang, J.-Y.; Liu, C.-J.; Pei, J. *J. Am. Chem. Soc.* **2014,** *136,* 2135-2141. (d) Uddin, M. A.; Lee, T. H.; Xu, S.; Park, S. Y.; Kim, T.; Song, S.; Nguyen, T. L.; Ko, S.; Hwang, S.; Kim, J. Y.; Woo, H. Y. *Chem. Mater.* **2015**, *27,* 5997-6007. (e) Cheng, Y.; Qi, Y.; Tang, Y.; Zheng, C.; Wan, Y.; Huang, W.; Chen, R. *J. Phys. Chem. Lett.* **2016**, *7*, 3609-3615. (f) Zhu, C.; Guo, Z.-H.; Mu, A. U.; Liu, Y.; Wheeler, S. E.; Fang, L. *J. Org. Chem.* **2016**, *81*, 4347-4352. (g) Liu, Y.; Zhang, Z.; Feng, S.; Li, M.; Wu, L.; Hou, R.; Xu, X.; Chen, X.; Bo, Z. *J. Am. Chem. Soc.* **2017**, *139*, 3356-3359. (h) Chen, X.-K.; Wang, T.; Brédas, J.-L. *Adv. Energy Mater.* **2017**, *7*, 1602713. (i) Yang, L.; Zhu, Y.; Jiao, Y.; Yang, D.; Chen, Y.; Wu, J.; Lu, Z.; Zhao, S.; Pu, X.; Huang, Y. *Dyes Pigm.* **2017**, *145*, 222-232.

[16] For select studies of transition-metal dyes in dye-sensitized solar cells, see: (a) Nazeeruddin, M. K.; Péchy, P.; Renouard, T.; Zakeeruddin, S. M.; Humphry-Baker, R.; Comte, P.; Liska, P.; Cevey, L.; Costa, E.; Shklover, V.; Spiccia, L.; Deacon, G. B.; Bignozzi, C. A.; Grätzel, M. *J. Am. Chem. Soc.* **2001**, *123,* 1613-1624. (b) Altobello, S.; Argazzi, R.; Caramori, S.; Contado, C.; Fré, S. D.; Rubino, P.; Choné, C.; Larramona, G.; Bignozzi, C. A. *J. Am. Chem. Soc.* **2005**, *127,* 15342-15343. (c) Chen, C.-Y.; Wang, M.; Li, J.-Y.; Pootrakulchote, N.; Alibabaei, L.; Ngoc-le, C.-h.; Decoppet, J.-D.; Tsai, J.-H.; Grätzel, C.; Wu, C.-G.; Zakeeruddin, S. M.; Grätzel, M. *ACS Nano* **2009**, *3,* 3103-3109. (d) Mukherjee, S.; Bowman, D. N.; Jakubikova, E. *Inorg. Chem.* **2015***, 54,* 560-569. (e) Housecroft, C. E.; Constable, E. C. *Chem. Soc. Rev.* **2015**, *44,* 8386-8398.

[17] For studies on subphthalocyanine derivatives, see: (a) Cnops, K.; Rand, B. P.; Cheyns, D.; Verreet, B.; Empl, M. A.; Heremans, P. *Nat. Commun.* **2014**, *5*, 3406. (b) Claessens, C. G.;

González-Rodríguez, D.; Rodríguez-Morgade, M. S.; Medina, A.; Torres, T. *Chem. Rev.* **2014**, *114*, 2192-2277.

[18] For studies on contorted hexabenzocornonene derivatives, see: (a) Zhang, Q.; Peng, H.; Zhang, G.; Lu, Q.; Chang, J.; Dong, Y.; Shi, X.; Wei, J. *J. Am. Chem. Soc.* **2014**, *136*, 5057-5064. (b) Ball, M.; Zhong, Y.; Wu, Y.; Schenck, C.; Ng, F.; Steigerwald, M.; Xiao, S.; Nuckolls, C. *Acc. Chem. Res.* **2015***, 48,* 267-276. (c) Davy, N. C.; Man, G.; Kerner, R. A.; Fusella, M. A.; Purdum, G. E.; Sezen, M.; Rand, B. P.; Kahn, A.; Loo, Y.-L. *Chem. Mater.* **2016***, 28,* 673-681.

[19] For studies on biphenyl, see: (a) Bastiansen, O. *Acta Chem. Scand.* **1949**, *3*, 408-414. (b) Trotter, J. *Acta Cryst.* **1961**, *14*, 1135-1140.

[20] For studies on bithiophene, see: (a) Almenningen, A.; Bastiansen, O.; Svendsas, P. *Acta Chem. Scand.* **1958**, *12*, 1671-1673. (b) Samdal, S.; Samuelsen, E. J.; Volden, H. V. *Synth. Met.* **1993**, *59,* 259-265. (c) Takayanagi, M.; Gejo, T.; Hanazaki, I. *J. Phys. Chem.* **1994***, 98*, 12893-12898.

[21] (a) Chaloner, P. A.; Gunatunga, S. R.; Hitchvock, P. B. *Acta Cryst. C* **1994**, *50*, 1941-1942. (b) Pelletier, M.; Brisse, F. *Acta Cryst. C* **1994**, *50,* 1942-1945. (c) Siegrist, T.; Kloc, C.; Laudise, R. A.; Katz, H. E.; Haddon, R. C. *Adv. Mater.* **1998**, *10*, 379-382. (d) Vujanovich, E. C.; Bloom, J. W. G.; Wheeler, S. E. *J. Phys. Chem. A* **2012**, *116*, 2997-3003.

[22] Zhang, L.; Colella, N. S.; Cherniawski, B. P.; Mannsfeld, S. C. B.; Briseno, A. L. *ACS Appl. Mater. Interfaces* **2014**, *6*, 5327-5343.

[23] For benchmarks on the use DFT functionals for organic materials, see: (a) Salzner, U.; Aydin, A. *J. Chem. Theory Comput.* **2011**, *7*, 2568− 2583. (b) Bloom, J. W. G.; Wheeler, S. E. *J. Chem. Theory Comput.* **2014**, *10*, 3647-3655. (c) Niskanen, M.; Hukka, T. I. *Phys. Chem. Chem. Phys.* **2014**, *16,* 13294-13305. (d) Wildman, J.; Repiščák, P.; Paterson, M. J.; Galbraith, I. *J. Chem. Theory Comput.* **2016**, *12,* 3813-3824.

[24] For work on focal point analysis, see: (a) Csaszar, A. G.; Allen, W. D.; Schaefer, H. F. *J. Chem. Phys.* **1998**, *108*, 9751-9763. (b) East, A. L. L.; Allen, W. D. *J. Chem. Phys.* **1993**, *99*, 4638-4650. (c) Dunning, T. H. *J. Chem. Phys.* **1989**, *90*, 1007-1023. (d) Feller, D. *J. Chem. Phys.* **1993**, *98*, 7059-7071. (e) Helgaker, T.; Klopper, W.; Koch, H.; Noga, J. *J. Chem. Phys.* **1997**, *106*, 9639-9646.

[25] For work on Weizmann-*n* methods, see: (a) Martin, J. M.; de Oliveira, G. *J. Chem. Phys.* **1999**, *111*, 1843-1856. (b) Boese, A. D.; Oren, M.; Atasoylu, O.; Martin, J. M.; Kallay, M.; Gauss, J. *J. Chem. Phys.* **2004**, *120*, 4129-4141. (c) Karton, A.; Rabinovich, E.; Martin, J. M.; Ruscic, B. *J. Chem. Phys.* **2006**, *125*, 144108.

[26] For work on the Feller-Peterson-Dixon approach, see: (a) Feller, D.; Peterson, K. A.; Dixon, D. A. *J. Chem. Phys.* **2008**, *129*, 204105. (b) Peterson, K. A.; Feller, D.; Dixon, D. A. *Theor. Chem. Acc.* **2012**, *131*, 1079.

[27] For early work on BTTTs, see: (a) McCulloch, I.; Heeney, M.; Bailey, C.; Genevicius, K.; MacDonald, I.; Shkunov, M.; Sparrowe, D.; Tierney, S.; Wagner, R.; Zhang, W.; Chabinyc, M. L.; Kline, R. J.; McGehee, M. D.; Toney, M. F. *Nat. Mater.* **2006**, *5*, 328-333. (b) Chabinyc, M. L.; Toney, M. F.; Kline, J.; McCulloch, I.; Heeney, M. *J. Am. Chem. Soc.* **2007**, *129,* 3226-3237. (c) Kline, R. J.; DeLongchamp, D. M.; Fischer, D. A.; Lin, E. K.; Heeney, M.; McCulloch, I.; Toney, M. F. *Appl. Phys. Lett.* **2007**, *90,* 062117.

[28] For examples of BTTTs in OFETs and OTFTs, see: (a) Rawcliffe, R.; Shkunov, M.; Heeney, M.; Tierney, S.; McCulloch, I.; Campbell, A. *Chem. Commun.* **2008**, 871-873. (b) Esenturk, O.; Kline, R. J.; DeLongchamp, D. M.; Heilweil, E. J. *J. Phys. Chem. C* **2008**, *112,* 10587-10590. (c) Jung, Y.; Kline, R. J.; Fischer, D. A.; Lin, E. K.; Heeney, M.; McCulloch, I.; DeLongchamp, D. M. *Adv. Funct. Mater.* **2008**, *18,* 742-750. (d) Wang, S.; Tang, J.-C.; Zhao, L.-H.; Png, R.-Q.; Wong, L.-Y.; Chia, P.-J.; Chan, H. S. O.; Ho, P. K.-H.; Chua, L.-L. *Appl. Phys. Lett.* **2008**, *93,* 162103. (e) Umeda, T.; Kumaki, D.; Tokito, S. *J. Appl. Phys.* **2009**, *105,* 024516. (f) Wang, S.;

Kiersnowski, A.; Pisula, W.; Müllen, K. *J. Am. Chem. Soc.* **2012**, *134*, 4015-4018. (g) Yu, S. H.; Cho, J.; Sim, K. M.; Ha, J. U.; Chung, D. S. *ACS Appl. Mater. Interfaces* **2016**, *8,* 6570-6576.

[29] For examples of BTTTs in OPVs, see: (a) Parmer, J. E.; Mayer, A. C.; Hardin, B. E.; Scully, S. R.; McGehee, M. D.; Heeney, M.; McCulloch, I. *Appl. Phys. Lett.* **2008**, *92,* 113309. (b) Hwang, I.-W.; Kim, J. Y.; Cho, S.; Yuen, J.; Coates, N.; Lee, K.; Heeney, M.; McCulloch, I.; Moses, D.; Heeger, A. J. *J. Phys. Chem. C* **2008**, *112*, 7853-7857. (c) Mayer, A. C.; Toney, M. F.; Scully, S. R.; Rivnay, J.; Brabec, C. J.; Scharber, M.; Koppe, M.; Heeney, M.; McCulloch, I.; McGehee, M. D. *Adv. Funct. Mater.* **2009**, *19*, 1173-1179. (d) Zhang, L.; Liu, F.; Diao, Y.; Marsh, H. S.; Colella, N. S.; Jayaraman, A.; Russell, T. P.; Mannsfeld, S. C. B.; Briseno, A. L. *J. Am. Chem. Soc.* **2014**, *136*, 18120-18130. (e) Gao, J.; Thomas, A. K.; Johnson, R.; Guo, H.; Grey, J. K. *Chem. Mater.* **2014**, *26,* 4395-4404.

[30] For computational studies of BTTTs, see: (a) Cho, E.; Risko, C.; Kim, D.; Gysel, R.; Miller, N. C.; Breiby, D. W.; McGehee, M. D.; Toney, M. F.; Kline, R. J.; Bredas, J.-L. *J. Am. Chem. Soc.* **2012**, *134,* 6177-6190. (b) Cherniawski, B. P.; Lopez, S. A.; Burnett, E. K.; Yavuz, I.; Zhang, L.; Parkin, S. R.; Houk, K. N.; Briseno, A. L. *J. Mater. Chem. C* **2017**, *5,* 582-588.

[31] Liu, Y.; Hong, Z.; Chen, Q.; Chen, H.; Chang, W.-H.; Yang, Y. (M.); Song, T.-B.; Yang, Y. *Adv. Mater.* **2016**, *28,* 440-446.

[32] Frisch, M. J.; Trucks, G. W.; Schlegel, H. B.; Scuseria, G. E.; Robb, M. A.; Cheeseman, J. R.; Scalmani, G.; Barone, V.; Mennucci, B.; Petersson, G. A.; Nakatsuji, H.; Caricato, M.; Li, X.; Hratchian, H. P.; Izmaylov, A. F.; Bloino, J.; Zheng, G.; Sonnenberg, J. L.; Hada, M.; Ehara, M.; Toyota, K.; Fukuda, R.; Hasegawa, J.; Ishida, M.; Nakajima, T.; Honda, Y.; Kitao, O.; Nakai, H.; Vreven, T.; Montgomery, J. A., Jr.; Peralta, J. E.; Ogliaro, F.; Bearpark, M.; Heyd, J. J.; Brothers, E.; Kudin, K. N.; Staroverov, V. N.; Kobayashi, R.; Normand, J.; Raghavachari, K.; Rendell, A.; Burant, J. C.; Iyengar, S. S.; Tomasi, J.; Cossi, M.; Rega, N.; Millam, N. J.; Klene, M.; Knox, J. E.; Cross, J. B.; Bakken, V.; Adamo, C.; Jaramillo, J.; Gomperts, R.; Stratmann, R.

E.; Yazyev, O.; Austin, A. J.; Cammi, R.; Pomelli, C.; Ochterski, J. W.; Martin, R. L.; Morokuma, K.; Zakrzewski, V. G.; Voth, G. A.; Salvador, P.; Dannenberg, J. J.; Dapprich, S.; Daniels, A. D.; Farkas, Ö.; Foresman, J. B.; Ortiz, J. V.; Cioslowski, J.; Fox, D. J. *Gaussian 09, Revision B.01*; Gaussian, Inc.: Wallingford, CT, 2009.

[33] Becke, A. D. *J. Chem. Phys.* **1993**, *98*, 5648−5652.

[34] Lee, C.; Yang, W.; Parr, R. G. *Phys. Rev. B* **1988**, *37*, 785−789.

[35] Stephens, P. J.; Devlin, F. J.; Chabalowski, C. F.; Frisch, M. J. *J. Phys. Chem.* **1994**, *98*, 11623−11627.

[36] Vosko, S. H.; Wilk, L.; Nusair, M. *Can. J. Phys.* **1980**, *58*, 1200−1211.

[37] Zhao, Y.; Truhlar, D. *Theor. Chem. Acc.* **2008**, *120*, 215−241.

[38] Zhao, Y.; Truhlar, D. G. *J. Chem. Phys.* **2006**, *125*, 194101.

[39] Grimme, S. *J. Comput. Chem.* **2006**, *27*, 1787−1799.

[40] Becke, A. Density-Functional Thermochemistry. V. *J. Chem. Phys.* **1997**, *107*, 8554−8560.

[41] Chai, J.-D.; Head-Gordon, M. *J. Chem. Phys.* **2008**, *128*, 084106−084115.

[42] Chai, J.-D.; Head-Gordon, M. *Phys. Chem. Chem. Phys.* **2008**, *10*, 6615−6620.

[43] Adamo, C.; Barone, V. *J. Chem. Phys.* **1999**, *110,* 6158-6169.

[44] Wheeler, S. E.; Houk, K. N. *J. Chem. Theory Comput*. **2010**, *6*, 395-404.

[45] Legault, C. Y. *CYLview, 1.0 b*; *Université de Sherbrooke* (http://www.cylview.org), 2009.

[46] Bastiansen, O.; Samdal, S. *J. Mol. Struc.* **1985**, *128*, 115-125.

[47] Johansson, M. P.; Olsen, J. *J. Chem. Theory Comput.* **2008**, *4*, 1460-1471.

[48] (a) Karpfen, A.; Choi, C. H.; Kertesz, M. *J. Phys. Chem. A* **1997**, *101*, 7426-7433. (b) Sancho-García, J. C.; Karpfen, A. *Chem. Phys. Lett.* **2005**, *411*, 321-326.

[49] For studies on the effect of fluorine substitution on polymer properties, see: (a) Stuart, A. C.; Tumbleston, J. R.; Zhou, H.; Li, W.; Liu, S.; Ade, H.; You, W. *J. Am. Chem. Soc.* **2013**, *135,* 1806-1815. (b) Fei, Z.; Boufflet, P.; Wood, S.; Wade, J.; Moriarty, J.; Gann, E.; Ratcliff, E. L.;

McNeill, C. R.; Sirringhaus, H.; Kim, J.-S.; Heeney, M. *J. Am. Chem. Soc.* **2015**, *137*, 6866-6879. (c) Boufflet, P.; Han, Y.; Fei, Z.; Treat, N. D.; Li, R.; Smilgies, D.-M.; Stingelin, N.; Anthopoulos, T. D.; Heeney, M. *Adv. Funct. Mater.* **2015**, *25,* 7038-7048. (d) Dou, J.-H.; Zheng, Y.-Q.; Yao, Z.-F.; Yu, Z.-A.; Lei, T.; Shen, X.; Luo, X.-Y.; Sun, J.; Zhang, S.-D.; Ding, Y.-F.; Han, G.; Yi, Y.; Wang, J.-Y.; Pei, J. *J. Am. Chem. Soc.* **2015**, *137*, 15947-15956. (e) Kawashima, K.; Fukuhara, T.; Suda, Y.; Suzuki, Y.; Koganezawa, T.; Yoshida, H.; Ohkita, H.; Osaka, I.; Takimiya, K. *J. Am. Chem. Soc.* **2016**, *138*, 10265-10275. (f) Zhang, W.; Shi, K.; Huang, J.; Gao, D.; Mao, Z.; Li, D.; Yu, G. *Macromolecules* **2016**, *49,* 2582-2591. (g) Hu, Z.; Haws, R. T.; Fei, Z.; Boufflet, P.; Heeney, M.; Rossky, P. J.; Bout, D. A. V. *PNAS* **2017**, *114*, 5113-5118. (h) Zhang, W.; Mao, Z.; Chen, Z.; Huang, J.; Wei, C.; Gao, D.; Lin, Z.; Li, H.; Wang, L.; Yu, G. *Polym. Chem.* **2017**, *8,* 879-889.

[50] Zhang, S.; Yang, B.; Liu, D.; Zhang, H.; Zhao, W.; Wang, Q.; He, C.; Hou, J. *Macromolecules* **2016**, *49*, 120-126.

[51] For studies on selenophene-based molecules in organic electronics, see: (a) Yang, R.; Tian, R.; Yan, J.; Zhang, Y.; Yang, J.; Hou, Q.; Yang, W.; Zhang, C.; Cao, Y. *Macromolecules* **2005**, *38,* 244-253. (b) Ballantyne, A. M.; Chen, L. C.; Nelson, J.; Bradley, D. D. C.; Astuti, Y.; Maurano, A.; Shuttle, C. G.; Durrant, J. R.; Heeney, M.; Duffy, W.; McCulloch, I. *Adv. Mater.* **2007**, *19*, 4544-4547. (c) Chen, Z.; Lemke, H.; Albert-Seifried, S.; Caironi, M.; Nielsen. M. M.; Heeney, M.; Zhang, W.; McCulloch, I.; Sirringhaus, H. *Adv. Mater.* **2010**, *22,* 2371-2375. (d) Haid, S.; Mishra, A.; Uhrich, C.; Pfeiffer, M.; Bäuerle, P. *Chem. Mater.* **2011***, 23*, 4435-4444. (e) Dou, L.; Chang, W.-H.; Gao, J.; Chen, C.-C.; You, J.; Yang, Y. *Adv. Funct. Mater.* **2012**, *25*, 825-831. (f) Rudenko, A. E.; Noh, S.; Thompson, B. C. **2013,** *24,* 484002.

[52] Westenhoff, S.; Beenken, W. J. D.; Yartsev, A.; Greenham, N. C. *J. Chem. Phys.* **2006**, *125*, 154903.

[53] Yao, H.; Ye, L.; Zhang, H.; Li, S.; Zhang, S.; Hou, J. *Chem. Rev.* **2016***, 116,* 7397-7457.

[54] For work on the distortion-interaction model, see: (a) Ess, D. H.; Houk, K. N. *J. Am. Chem. Soc.* **2007**, *129*, 10646-10647. (b) Ess, D. H.; Houk, K. N. *J. Am. Chem. Soc.* **2008**, *130*, 10187-10198. (c) Hayden, A. E.; Houk, K. N. *J. Am. Chem. Soc.* **2009**, *131*, 4084-4089.

[55] For work on the activation-strain model, see: (a) van Zeist, W.-J.; Bickelhaupt, F. M. *Org. Biomol. Chem.* **2010**, *8*, 3118-3127. (b) Fernandez, I.; Bickelhaupt, F. M. *Chem. Soc. Rev.* **2014**, *43*, 4953-4967.

[56] (a) Zade, S. S.; Bendikov, M. *Org. Lett.* **2006**, *8*, 5243-5246. (b) Zade, S. S.; Zamoshchik, N.; Bendikov, M. *Acc. Chem. Res.* **2011**, *44*, 14-24.

[57] (a) Raos, G.; Famulari, A.; Marcon, V. *Chem. Phys. Lett.* **2003,** *379*, 364-372. (b) Fabiano, E.; Sala, F. D. *Chem. Phys. Lett.* **2006**, *418*, 496-501. (c) Stendardo, E.; Ferrer, F. A.; Santoro, F.; Improta, R. *J. Chem. Theory Comput.* **2012**, *8*, 4483-4493.

[58] Yoon, M.-H.; Facchetti, A.; Stern, C. E.; Marks, T. J. *J. Am. Chem. Soc.* **2006**, *128*, 5792-5801.

[59] Ichikawa, M.; Kato, T.; Uchino, T.; Tsuzuki, T.; Inoue, M.; Jeon, H.-G.; Koyama, T.; Taniguchi, Y. *Org. Electron.* **2010**, *11*, 1549-1554.

[60] Oniwa, K.; Kanagasekaran, T.; Jin, T.; Akhtaruzzaman, M.; Yamamoto, Y.; Tamura, H.; Hamada, I.; Shimotani, H.; Asao, N.; Ikeda, S.; Tanigaki, K. *J. Mater. Chem. C* **2013**, *1*, 4163-4170.

[61] Sun, J.-P.; Hendsbee, A. D.; Eftaiha, A. F.; Macaulay, C.; Rutledge, L. R.; Welch, G. C.; Hill, I. G. *J. Mater. Chem. C* **2014**, *2*, 2612-2621.

[62] Ie, Y.; Nitani, M.; Uemura, T.; Tominari, Y.; Takeya, J.; Honsho, Y.; Saeki, A.; Seki, S.; Aso, Y. *J. Phys. Chem. C* **2009**, *113*, 17189–17193.

[63] (a) Fitzner, R.; Reinold, E.; Mishra, A.; Mena-Osteritz, E.; Ziehlke, H.; Körner, C.; Leo, K.; Riede, M.; Weil, M.; Tsaryova, O.; Weiss, A.; Uhrich, C.; Pfeiffer, M.; Baüerle, P. *Adv. Funct.*

Mater. **2011**, *21*, 897− 910. (b) Elschner, C.; Schrader, M.; Fitzner, R.; Levin, A. A.; Bäuerle, P.; Andrienko, D.; Leo, K.; Riede, M. *RSC Adv.* **2013**, *3*, 12117-12123.

[64] For examples of polymers and oligomers incorporating **3-Me**, **6-Me**, and **9**, see: (a) Lin, Y.; Zhao, F.; Wu, Y.; Chen, K.; Xia, Y.; Li, G.; Prasad, S. K. K.; Zhu, J.; Huo, L.; Bin, H.; Zhang, Z.-G.; Guo, X.; Zhang, M.; Sun, Y.; Gao, F.; Wei, Z.; Ma, W.; Wang, C.; Hodgkiss, J.; Bo, Z.; Inganäs, O.; Li, Y.; Zhan, X. *Adv. Mater*. **2017**, *29*, 1604155. (b) Wong, Y. Q.; Meng, H.-F.; Wong, H. Y.; Tan, C. S.; Wu, C.-Y.; Tsai, P.-T.; Chang, C.-Y.; Horng, S.-F.; Zan, H.-W. *Organic Electronics* **2017**, *43*, 196-206.

[65] For studies on thiophene-based hole transport materials, see: (a) Krishnamoorthy, T.; Kunwu, F.; Boix, P. P.; Li, H.; Koh, T. M.; Leong, W. L.; Powar, S.; Grimsdale, A.; Grätzel, M.; Mathews, N.; Mhaisalkar, S. G. *J. Mater. Chem. A* **2014***, 2,* 6305-6309. (b) Li, H.; Fu, K.; Boix, P. P.; Wong, L. H.; Hagfeldt, A.; Grätzel, M.; Mhaisalkar, S. G.; Grimsdale, A. C. *ChemSusChem* **2014**, *7*, 3420-3425. (c) Ma, S.; Zhang, H.; Zhao, N.; Cheng, Y.; Wang, M.; Shen, Y.; Tu, G. *J. Mater. Chem. A* **2015**, *3*, 12139-12144. (d) Das, J.; Siram, R. B. K.; Cahen, D.; Rytchinski, B.; Hodes, G. *J. Mater. Chem. A* **2015**, *3*, 20305-20312. (e) Ie, Y.; Tanaka, K.; Tashiro, A.; Lee, S. K.; Testai, H. R.; Yamada, R.; Tada, H.; Aso, Y. *J. Phys. Chem. Lett.* **2015**, *6,* 3754-3759. (f) Molina-Ontoria, A.; Zimmermann, I.; Garcia-Benito, I.; Gratia, P.; Roldán-Carmona, C.; Aghazada, S.; Graetzel, M.; Nazeeruddin, M. K.; Martín, N. *Angew. Chem. Int. Ed.* **2016**, *55*, 6270-6274. (g) Zimmermann, I.; Urieta-Mora, J.; Gratia, P.; Aragó, J.; Grancini, G.; Molina-Ontoria, A.; Ortí, E.; Martín, N.; Nazeeruddin, M. K. *Adv. Energy Mater.* **2017**, *7*, 1601674.

[66] For studies on high-dimensional charge transport in organic molecules, see: (a) Skabara, P. J.; Arlin, J.-B.; Geerts, Y. H. *Adv. Mater.* **2013**, *25*, 1948-1954. (b) Arumugam, S.; Wright, I. A.; Inigo, A. R.; Gambino, S.; Howells, C. T.; Kanibolotsky, A. L.; Skabara, P. J.; Samuel, I. D. W. *J. Mater. Chem. C*, **2014**, *2*, 34-39. (c) Calvo-Castro, J.; Morris, G.; Kennedy, A. R.; McHugh, C. J. *Cryst. Growth Des.* **2016**, *16*, 5385-5393.

[67] Takimiya, K.; Kunugi, Y.; Konda, Y.; Niihara, N.; Otsubo, T. *J. Am. Chem. Soc.* **2004**, *126*, 5084-5085.

[68] Goldfinger, M. B.; Crawford, K. B.; Swager, T. M. *J. Am. Chem. Soc.* **1997**, *119*, 4578-4593.

[69] (a) Zhao, Y.-H.; Pan, H.; Fu, G.-L.; Lin, J.-M.; Zhao, C.-H. *Tet. Lett.* **2011**, *52*, 3832-3835. (b) Li, S.; Shang, Y.; Wang, L.; Kwok, R. T. K.; Tang, B. Z. *J. Mater. Chem. C* **2016**, *4*, 5363-5369.

Chapter 2. Quantitative Prediction of Morphology and Electron Transport in Crystal and Disordered Organic Semiconductors

2.1 Background

Organic semiconductors have received renewed attention in their applications in organic electronics over the last two decades due to ease of fabrication, low cost, and light weight.[1] Organic semiconducting materials can be classified as p-type, n-type, or ambipolar. These materials can be utilized in modern organic electronics such as organic-field effect transistors (OFETs) or interfaced p/n organic electronic devices as in organic photovoltaics (OPVs) and organic LED (OLEDs).[2,3] While p-type materials have been well-studied, efforts to develop n-type materials in OFETs have been slower due to inherently unfavorable features, including high electron injection barrier, electron trapping at interfaces, instability, and high industrial costs instability.[3,4] Fullerenes are used the most widely as electron acceptors in the active layer of OPVs,[5] though the last few years have seen a dramatic increase in research involving non-fullerene n-type materials,[6] such as perylene-diimide[7] and other non-fullerene small molecules.[8]

Charge transport is an important parameter that affects the performance of many types of organic electronic devices, including organic field effect transistors (OFETs) and organic photovoltaics (OPVs).[9] Low mobilities limit the performance of OPVs by increasing the probability for charge recombination, which limits the charge separation yield. Many organic materials with p-type mobilities on the order of 10 $cm^2\ V^{-1}\ s^{-1}$ have been reported, but n-type mobilities are typically on the order 1 $cm^2\ V^{-1}\ s^{-1}$, suggesting that there is still room to improve n-type transporting materials. There are several factors that influence charge mobility in conjugated organic materials; at the molecular level, these include molecular packing and disorder.[10,11] Understanding structure–property relationships in bulk organic semiconductors will aid in the design of more effective materials. Morphology-related properties and measured PCEs of ~150 OPV devices

were quantified by Jackson et al., and their results suggest that morphological materials design is needed to rationally design new materials for OPV devices.[12]

Charge transport in organic semiconductors has been described by several theories.[13] Two main mechanisms of charge transport are band transport and hopping transport. Band transport is exhibited in crystalline solids that are highly ordered with delocalized excitations, which result in typically high mobilities ($\mu > 1$ cm^2 V^{-1} s^{-1}). Hopping transport is exhibited in polycrystalline materials containing disorder in the system. This results in localized excitations with longer inter-site distances (< 1 nm) and lower mobilities for these materials ($\mu > 0.02$ cm^2 V^{-1} s^{-1}). Hopping-type transport, which is often used to describe charge transport in organic thin-films, can be described using Marcus theory. Marcus theory is based on two major assumptions: charges are localized on each site and non-adiabatic charge transfer reaction occurs via a hopping mechanism. The rate of charge transfer from site *i* to *j* (k_{ij}) is described by:

$$k_{ij} = J_{ij}^2 \frac{2\pi /}{\sqrt{4\pi\lambda k_B T}} \exp\left[-\frac{(\Delta E_{ij} - \lambda)^2}{4\lambda k_B T} \right] \quad \text{(Equation 2.1)}$$

where J_{ij} is electronic coupling between sites *i* and *j*, λ is reorganization energy, k_B is the Boltzmann constant, T is temperature, and Δ*Eij* is the site energy difference. Charge transport properties depend strongly on electronic coupling, which is defined as the extent of wavefunction overlap between molecules. The magnitude of this interaction is defined by the matrix element tab $\langle \Psi_a | H | \Psi_b \rangle$, where *H* is the electronic Hamiltonian of the system and Ψ_a and Ψ_b are the wavefunctions of two charge-localized states (diabatic states).[14] Our methodology is based on Marcus theory and calculates hopping-type transport in organic semiconductor systems.

A comprehensive method was developed in the Houk group[15] to calculate charge transport properties of organic crystals and thin-films based on this established charge-hopping model and MD simulations (Figure 1).[16] This workflow has been validated with test sets of over

20 electron donor used in OFETs and OPVs for both single crystal and thin film morphologies, for which calculated hole mobilities were predicted within an order of magnitude.

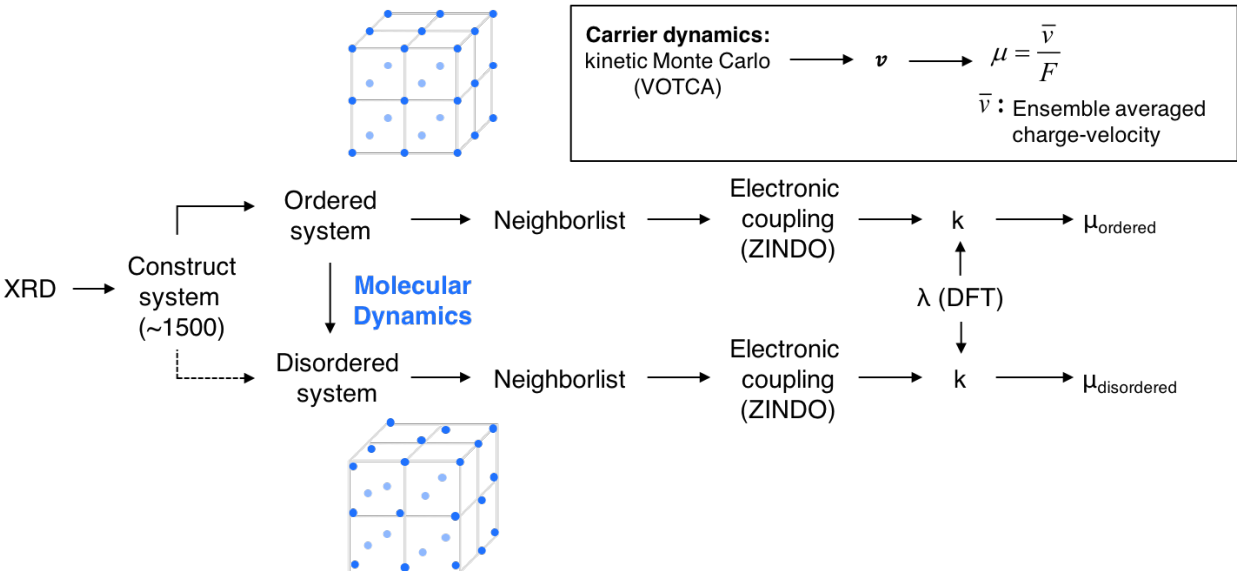

Figure 2.1. Workflow for methodology outlined in ref. 15 and applied in this work.

We now evaluate this methodology (discussed in detail in the next section) to compute electron mobilities for a diverse set of n-type organic materials, for which experimental crystal structures and electron mobilities are available. The first set consists of 20 organic materials fabricated as single-crystals (SCEM20), while the second set consists of 21 organic materials fabricated as thin-films (TFEM21), as shown in Scheme 2.1. These sets are comprised of acenes, perylenes, diimides, oligothiophenes, and fullerene derivatives. The electron mobilities for single-crystals are typically 10- to 1000-fold higher than those for thin-film morphologies, because they lack defects, impurities, and grain boundaries. The experimental electron mobilities in SCEM20 and TFEM21 sets range from 10^{-3}–10^{1} cm^2 V^{-1} s^{-1} and 10^{-6}–10 cm^2 V^{-1} s^{-1}, respectively. We present a benchmarking study on electron mobilities of these electron acceptors in both thin film and single crystal morphology.

Scheme 2.1. Chemical structures of the SCEM20 test set (top) and TFEM21 test set (bottom)

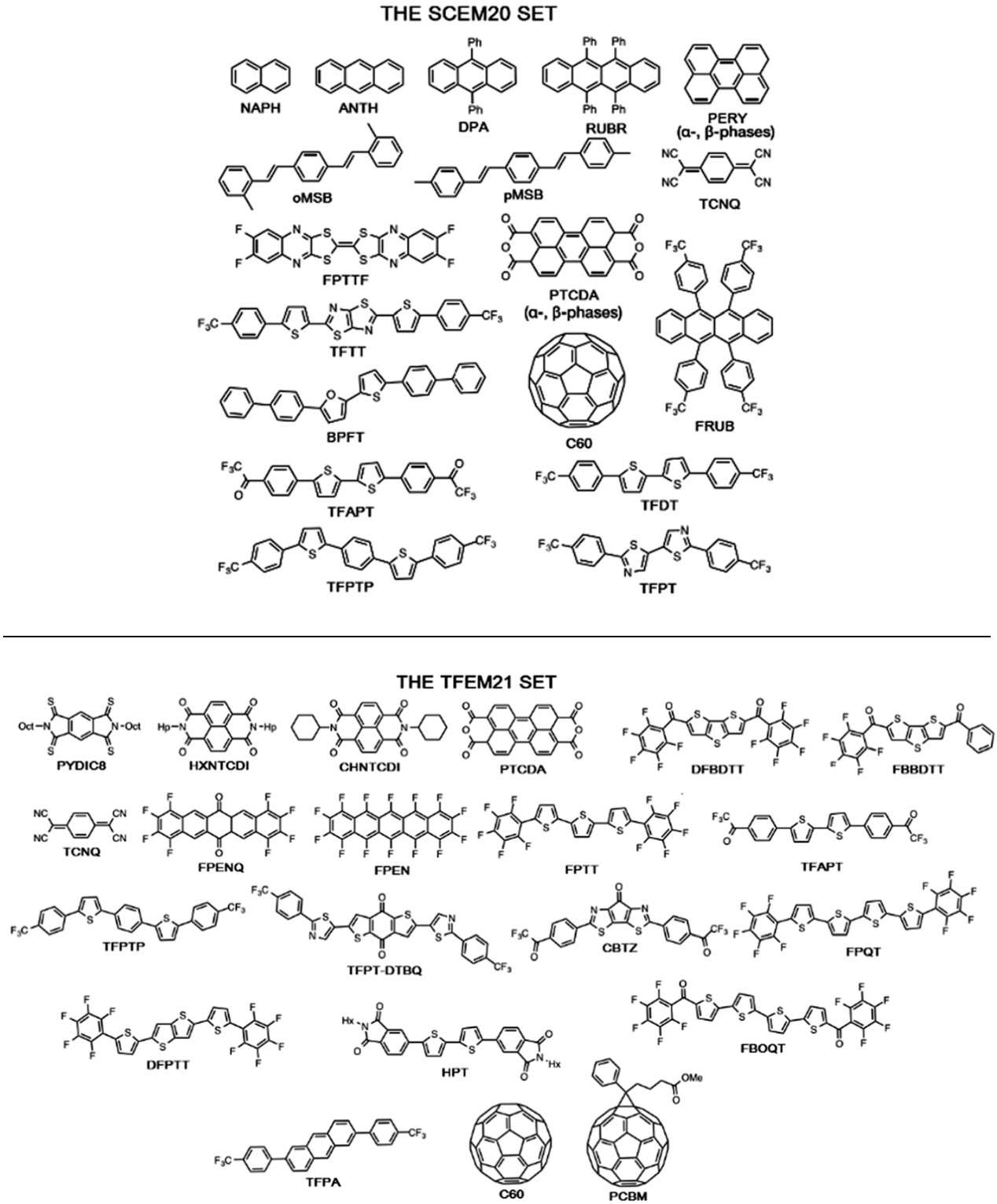

2.2 Methodology

Experimental crystal structure data for each DH molecule was obtained from references indicated in Table 2.1, which were used as starting structures for the calculations. Initial supercells containing ~1500 molecules were constructed with periodic boundary conditions (PBC). We considered two morphological phases: (1) crystal phase, with perfect positional order and (2) crystalline phase, with incorporation of positional disorder into XRD data. Single-crystal hole mobilities were computed based on perfect order morphology, and thin-film hole mobilities were modeled with the introduction of thermal and energetic disorder using atomistic MD simulations to predict mesoscale ordering.

MD simulations in an NPT ensemble were performed on these systems at 300K using the GPU version of Amber12.[17,18] GAFF force fields were used for molecular mechanics parameters.[19,20] Partial charges of ground-states were generated from B3LYP/6-311G(d,p)-optimized geometries via the Merz-Singh-Kollman scheme[21,22] using HF/6-31G(d), as implemented in Gaussian09.[23] Each supercell was first heated from 0K to 300 K for 2 ns and then NPT equilibrated for another 2 ns at 300 K while restraining heavy atom positions.[24] A final 20 ns production run was performed at 300 K and time-averaged pressure at 1 atm. Ten snapshots of the MD simulations were taken at various time points in order to obtain atomistic morphologies for subsequent charge transport calculations.

With the single-crystal and MD-equilibrated morphologies in hand, we performed charge-carrier dynamics simulations to calculate charge transfer rates using Marcus theory based on incoherent hopping events. Marcus theory relies on two assumptions: (1) charges are instantaneously localized on each site (or molecule, in the case of organic semiconductors)[25,26] and (2) a non-adiabatic charge transfer reaction occurs through a hopping-type mechanism. Electronic coupling elements, J_{ij}, of the charge-transfer were calculated for defined molecular pairs using the semi-empirical method ZINDO.[27,28] Pairs are defined as molecules with centroid

distances below 0.8 nm, each of which are added to a neighbor list, a compilation of all possible adjacent hopping sites. The reorganization energy λ of each molecule was calculated using the four-point rule with B3LYP/6-311G(d,p). Site energies were calculated self-consistently using Thole Model, which includes contributions from electrostatic interactions due to polarization and from an external electric field (see ref. 16 for details). In accordance with the method previously described for MD simulations, partial charges of neutral and charged states were generated via Merz-Singh-Kollman scheme,[29,30] using HF/6-31G(d) method based on B3LYP/6-311G(d,p)-optimized geometries. Isotropic atomic polarizabilities of the neutral and charged states were re-parameterized for each species to calibrate against molecular polarizabilities obtained using B3LYP/6-311G(d,p). Energetic disorders were extracted using the Gaussian Disorder Model (GDM), where the histogram of site energy differences (ΔE_{ij}) were fitted to the following Gaussian distribution and used to extract energetic disorder (σ).

Kinetic Monte Carlo (kMC) methods were used to predict charge transport of a charge carrier in an applied external electric field (m = v/F, where F = 10^7 V m^{-1} is field strength), as implemented in VOTCA, and hole mobilities were obtained using velocity-averaging.[16,31,32]

2.3 Benchmark

We computed mobilities for single-crystal and thin-film morphologies and compared them to experimental values (Figure 2.2). An error function of the form $\exp[n^{-1}\Sigma|\ln(\mu_{exp}/\mu_{theo})|]$ is employed to quantify the accuracy in our μ_e predictions. Our predictions of single-crystal μ typically deviate from experimental values by less than an order of magnitude. The error found in ref. 15 for single-crystal hole mobilities (μ_h) is 2.0. XRD measurements, according to paracrystal theory,[33,34,35] have shown that *g* is typically between 0–1% for single-crystals. This suggests that our model of a defect-free lattice is adequate for the single-crystal morphology in the SCEM20 set.

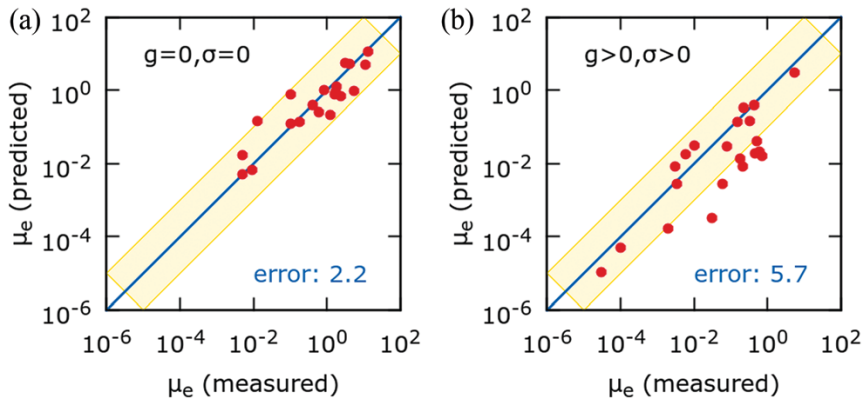

Figure 2.2. Correlation between predicted and experimental mobilities.
Relationship between the experimental (a) single-crystal SCEM20 and (b) thin-film TFEM21 electron mobilities (me) and their calculated electron mobilities based on (a) ideal-crystal (g = 0, σ = 0), and (b) disordered (g > 0, σ > 0) morphologies. The error function is defined in the text. μ_e is in units of $cm^2\ V^{-1}\ s^{-1}$ in all cases.

Figure 2.2b shows our μ_e predictions of disordered morphologies and the experimental measurements of TFEM21 set. Disordered μ_e is generally underestimated, but are within an order of magnitude of the experimental values. The error in thin-film μ_h predictions in ref. 15 is 3.6. Mobility is collectively controlled by various transport parameters (packing motif, electronic coupling *J*, electron-transfer reorganization energy λ_e, paracrystal-order parameter *g* and energetic-disorder σ). Based on our bench- marking for SCEM20 set (Figure 2.2a), the deviation is not an error in *J* and λ_e. Thus, to understand this apparent deviation we analyze *g* and σ reported in ref. 15 and this study. The average of *g* in ref. 15 is 2.8% and it is 3.0% for TFEM21 set. The average *g* is similar; the average σ in ref. 15 is 72 meV, while for TFEM21 set average σ is found to be 90 meV. Since energetic disorder is inversely related to mobility, the underestimated disordered μ_e is apparently due to relatively high predicted σ. We have tested the calculation of σ and μ_e using five different RESP methodologies (MK, MKUFF, CHelp, CHelpG, HLYGAt), and the results do not change dramatically.

Table 2.1 Single-crystal electron mobility (SCEM20) and thin-film electron mobility test sets (TFEM21)

SCEM20					TFEM21				
Name	Ref.A	Predicted μ_e (cm^2/Vs)	Expt μ_e (cm^2/Vs)	Ref. B	Name	Ref. A	Predicted μ_e (cm^2/Vs)	Expt μ_e (cm^2/Vs)	Ref. B
TFPT	36	1.2	1.83	36	**HPT**	37	8.4×10^{-3}	2.1×10^{-1}	37
FRUB	38	5.2	4.2	38	**CHNTCDI**	39	4.2×10^{-2}	1.1×10^{-1}-5.2×10^{-1}	40
TCNQ	41	7.5×10^{-1}	1.6	42	**TCNQ**	41	1.1×10^{-5}	3.0×10^{-5}	43
TFTT	44	2.2×10^{-1}	3×10^{-1}-1.2	44	**PTCDA**	75	4.9×10^{-5}	1.0×10^{-4}	45
TFDT	44	1.4×10^{-1}	1.8×10^{-1}	44	**FPQT**	46	4.0×10^{-1}	4.3×10^{-1}	47
RUB	48	1.03	8.1×10^{-1}	49	**TFPA**	50	2.8×10^{-3}	3.4×10^{-3}	50
NAPH	51	2.6×10^{-1}	~6×10^{-1}	52	**FPEN**	53	3.3×10^{-1}	2.2×10^{-1}	54
ANTH	55	9×10^{-1}	1.7	56	**C60**	68	3.1	5.3	57
PERY-α	58	9.5×10^{-1}	5.5	59	**DFBDTT**	60	1.7×10^{-4}	2.0×10^{-3}	60
PERY-β	61	4×10^{-1}	4×10^{-1}	62	**FBBDTT**	60	3.3×10^{-4}	3.0×10^{-2}	60
FPTTF	63	7.6×10^{-1}	1×10^{-1}	64	**CBTZ**	65	2.8×10^{-3}	6.0×10^{-2}	65
DPA	66	11.6	13	67	**FPTT**	47	8.4×10^{-3}	3.0×10^{-3}	47
C60	68	5.1	11	69	**TFAPT**	72	3.0×10^{-2}	8.0×10^{-2}	72
BPFT	70	1.5×10^{-1}	1.3×10^{-2}	70	**TFPT-DTBQ**	71	1.4×10^{-1}	1.5×10^{-1}	71
TFAPT	72	6.8×10^{-1}	2.4	72	**FPENQ**	73	1.4×10^{-2}	1.8×10^{-1}	73
TFPTP	74	5.66	3.1	74	**TFPTP**	74	2.1×10^{-2}	6×10^{-1}	74
PTCDA-α	75	1.7×10^{-2}	5×10^{-3}	76	**DFPTT**	77	1.5×10^{-1}	3.3×10^{-1}	77
PTCDA-	75	5×10^{-3}	5×10^{-3}	76	**FBOQT**	78	1.9×10^{-2}	4.5×10^{-1}	78
pMSB	79	1.2×10^{-1}	1×10^{-1}	79	**HXNTDCI**	80	1.7×10^{-2}	7×10^{-1}	80
oMSB	79	6.6×10^{-3}	9×10^{-1}	79	**PCBM**	81	3.1×10^{-2}	2.85×10^{-2}	82
					PYDIC8	83	1.8×10^{-2}	5.80×10^{-3}	83

Indicated references are for the measured XRD data (ref. A) and the measured electron mobility μ_e (ref. B) for each compound.

Experimentally, there is little known about the degree of short-range order (influencing the energetic disorder) and dispersivity (i.e., size-dependence), but these factors can influence transport efficiency dramatically depending on the fabrication conditions.[9] The degree of structural-order is often quantified using the paracrystal order parameter calculated by the line-profiles of the diffraction peaks from XRD patterns.[33–35] From a theoretical viewpoint, short-range

order in a simulation is controlled by simulation size (i.e., the number of sites, i.e. molecules, in the super-cell) prior to MD. The size-dependence of the simulated μ_e is evaluated for the disordered electron mobility of FPEN, FPTT and DFBDTT, representative examples. We systematically altered the number of molecules in the super-cell and calculated electron-mobility and preserved the periodic boundary conditions. Studies have shown that the predicted mobility could be dispersive (i.e., size-dependent) or non-dispersive (i.e., size-independent) depending on the degree of structural order of the material.[84,85] For FPEN, increasing system size results in a smooth four-fold increase in μ_e in the dispersive mobility region followed by saturation (Figure 2.3). For FPTT and DFBDTT, we observe an abrupt increase and then a 5–10 fold decrease in the dispersive mobility region and saturation. In all cases, computed electron mobilities saturate beyond roughly 750 molecules. Experimental μ_e values match with the theoretical value at N ≅ 250–300, which suggests dispersive mobilities for FPEN, FPTT and DFBDTT. We conclude that the theoretical mobility can be parametrized with a typical number of sites in order to improve the accuracy in the μ_e predictions.

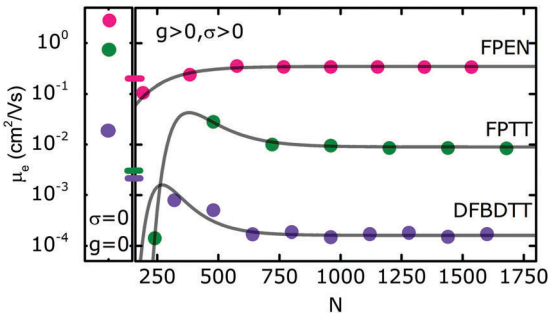

Figure 2.3. Scaling of system size.
Representative examples showing the scaling of the simulated disordered electron mobility, μ_e, with respect to the number of molecules N. PBC is preserved in all simulation cells. Dashes on the left vertical axis mark the corresponding experimental thin-film μ_e and solid lines are non-linear fits. The three points to the left of the y-axis are the simulated electron mobilities for ideal FPEN, FPTT and DFBDTT crystals μ_e ($\sigma = 0$, $g = 0$) results.

We also explored whether λ, g and σ correlate with μ_e. For SCEM20 set, when g and σ are set to zero, the remaining mobility-determining parameters are J and λ_e. Figure 2.4a shows

the relationship between ideal-crystal μ_e with λ_e for the SCEM20 set. We find no correlation from linear least-squares regression (LLSR) in the semi-log scale. Quite surprisingly, the variation disordered μ_e with g seems to exhibit some form of hetero- skedasticity. Standard LLSR results in no correlation as shown by the black dashed line in Figure 2.4b. Instead, we performed a weighted-LLSR method and obtained a correlation with an R^2 = 0.55. Figure 2.4c shows the relationship between μ_e with σ. We test both standard-LLSR and weighted-LLSR and observe that they both give very similar results (R^2 = 0.60). Thus, although both g and σ are weakly correlated with disordered electron-mobility μ_e, mobility dramatically decreases with increasing structural and energetic disorder.

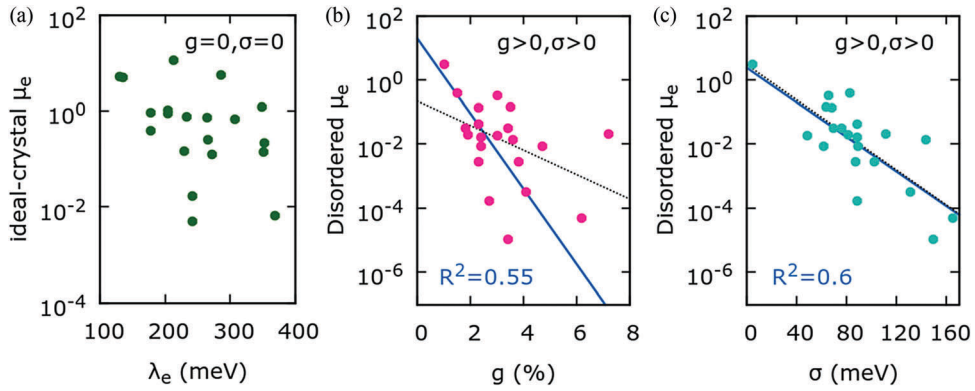

Figure 2.4. Mobility variation with reorganization, paracrystallinity, and energetic disorder.
(a) Variation of the calculated ideal-crystal (i.e., *g* = 0 and σ = 0) electron mobility of SCEM20 set with reorganization energy λ. (b and c) Variation of the calculated disordered (i.e., *g* > 0 and σ > 0) film electron mobility of TFEM21 set with paracrystal-order parameter *g* and energetic disorder σ. Dashed-black lines are the standard least-squares regression, while blue-solid lines are weighted least-squares regression, both in the semi-log scale. μ_e is in units of $cm^2\ V^{-1}\ s^{-1}$ in all cases.

2.4 Conclusions

Electron transport of a set of organic semiconductors has been explored for single crystal and thin-film morphologies. We utilized a combination of molecular dynamics and charge- carrier dynamics simulations to benchmark our computed electron-mobilities against the XRD-

determined SCEM20 and TFEM21 test sets. We benchmarked electron-mobility of SCEM20 based on the assumption of ideal-crystal morphology, and benchmarked electron-mobility of TFEM21 based on the assumption of disordered atomistic morphology obtained after molecular dynamics. For both SCEM20 and TFEM21 sets, electron mobilities are typically predicted within an order of magnitude of experiment. This methodology is a general way to compute the charge transport dynamics of p-type and n-type OSC materials.

2.5 References

[1] Arias, A. C.; MacKenzie, J. D.; McCulloch, I.; Rivnay, J.; Salleo, A. *Chem. Rev.* **2010**, *110*, 3–24.

[2] Wang, C.; Dong, H.; Hu, W.; Liu, Y.; Zhu, D. *Chem. Rev.* **2011**, *112*, 2208–2267.

[3] Cornil, J.; Brédas, J. L.; Zaumseil, J.; Sirringhaus, H. *Adv. Mater.* **2007**, *19*, 1791–1799.

[4] Nielsen, C. B.; Holliday, S.; Chen, H. Y.; Cryer, S. J.; McCulloch, I. *Acc. Chem. Res.* **2015**, *48*, 2803–2812.

[5] Acquah, S. F. A.; Penkova, A. V.; Markelov, D. A.; Semisalova, A. S.; Leonhardt, B. E.; Magi, J. M. ECS J. *Solid State Sci. Technol.* **2017**, *6*, M3155-M3162.

[6] Wadsworth, A.; Moser, M.; Marks, A.; Little, M. S.; Gasparini, N.; Brabec, C. J.; Baran, D.; McCulloch, I. *Chem. Soc. Rev.*, DOI: 10.1039/C7CS00892A.

[7] Zhong, Y.; Trinh, M. T.; Chen, R.; Wang, W.; Khlyabich, P. P.; Kumar, B.; Xu, Q.; Nam, C. Y.; Sfeir, M. Y.; Black, C.; Steigerwald, M. L. *J. Am. Chem. Soc.* **2014**, *136*, 15215–15221.

[8] Bin, H.; Zhang, Z.-G.; Gao, L.; Chen, S.; Zhong, L.; Xue, L.; Yang, C.; Li, Y. *J. Am. Chem. Soc.* **2016**, *138*, 4657–4664.

[9] Coropceanu, V.; Cornil, J.; da Silva Filho, D. A.; Olivier, Y.; Silbey, R.; Brédas, J.-L. *Chem. Rev.* **2007**, *107*, 926-952.

[10] Sokolov, A. N.; Atahan-Evrenk, S.; Mondal, R.; Akkerman, H. B.; Sánchez-Carrera, R. S.; Granados-Focil, S.; Schrier, J.; Mannsfeld, S. C. B.; Zoombelt, A. P.; Bao, Z.; Aspuru-Guzik, A. *Nat. Commun.* **2011**, *2*, 437.

[11] Nelson, J.; Kwiatkowski, J. J.; Kirkpatrick, J.; Frost, J. M. *Acc. Chem. Res.* **2009**, *42*, 1768–1778.

[12] Jackson, N. E.; Savoie, B. M.; Marks, T. J.; Chen, L. X.; Ratner, M. A. *J. Phys. Chem. Lett.* **2014**, *6*, 77–84.

[13] (a) Troisi, A. *Chem. Soc. Rev.* **2011**, *40*, 2347–2358. (b) Horowitz, G. *J. Mater. Res.* **2004**, *19*, 1946–1962. (c) Liu, C.; Huang, K.; Park, W.-T.; Li, M.; Yang, T.; Liu, X.; Liang, L.; Minari, T.; Noh, Y.-Y. *Mater. Horiz.* **2017**, *4,* 608–618. (d) Ciuchi, S.; Hatch, R. C.; Höchst, H.; Faber, C.; Blase, X.; Fratini, S. *Phys. Rev. Lett.* **2012**, *108*, 256401. (e) Venkateshvaran, D.; Nikolka, M.; Sadhanala, A.; Lemaur, V.; Zelazny, M.; Kepa, M.; Hurhangee, M.; Kronemeijer, A. J.; Pecunia, V.; Nasrallah, I.; Romanov, I.; Broch, D.; McCulloch, I.; Emin, D.; Olivier, Y.; Cornil, J.; Beljonne, D.; Sirringhaus, H. *Nature* **2014**, *515*, 384–388.

[14] Newton, M. D. *Chem. Rev.* **1991**, *91*, 767–792.

[15] Yavuz, I.; Martin, B. N.; Park, J.; Houk, K. N. *J. Am. Chem. Soc.,* **2015**, *137*, 2856–2866.

[16] Ruehle, V.; Lukyanov, A.; May, F.; Schrader, M.; Vehoff, T.; Kirkpatrick, J.; Baumeier, B.; Andrienko, D. *J. Chem. Theory Comput.* **2011**, *7*, 3335–3345.

[17] Case, D. A. *et al.* AMBER 12; University of California: San Francisco, CA, **2012**.

[18] Salomon-Ferrer, R.; Götz, A. W.; Poole, D.; Le Grand, S.; Walker, R. C. *J. Chem. Theory Comput.* **2013**, *9*, 3878–3888.

[19] Bayly, C. I.; Cieplak, P.; Cornell, W.; Kollman, P. A. *J. Phys. Chem.* **1993**, *97*, 10269–10280.

[20] Wang, J.; Wolf, R. M.; Caldwell, J. W.; Kollman, P. A.; Case, D. A. *J. Comput. Chem.* **2004**, *25*, 1157–1174.

[21] Singh, U. C.; Kollman, P. A. *J. Comput. Chem.* **1984**, *5*, 129–145.

[22] Besler, B. H.; Merz, K. M.; Kollman, P. A. *J. Comput. Chem.* **1990**, *11*, 431–439.

[23] Frisch, M. J.; Trucks, G. W.; Schlegel, H. B.; Scuseria, G. E.; Robb, M. A.; Cheeseman, J. R.; Scalmani, G.; Barone, V.; Mennucci, B.; Petersson, G. A.; Nakatsuji, H.; Caricato, M.; Li, X.; Hratchian, H. P.; Izmaylov, A. F.; Bloino, J.; Zheng, G.; Sonnenberg, J. L.; Hada, M.; Ehara, M.; Toyota, K.; Fukuda, R.; Hasegawa, J.; Ishida, M.; Nakajima, T.; Honda, Y.; Kitao, O.; Nakai, H.; Vreven, T.; Montgomery, J. A., Jr.; Peralta, J. E.; Ogliaro, F.; Bearpark, M.; Heyd, J. J.; Brothers, E.; Kudin, K. N.; Staroverov, V. N.; Kobayashi, R.; Normand, J.; Raghavachari, K.;

Rendell, A.; Burant, J. C.; Iyengar, S. S.; Tomasi, J.; Cossi, M.; Rega, N.; Millam, M. J.; Klene, M.; Knox, J. E.; Cross, J. B.; Bakken, V.; Adamo, C.; Jaramillo, J.; Gomperts, R.; Stratmann, R. E.; Yazyev, O.; Austin, A. J.; Cammi, R.; Pomelli, C.; Ochterski, J. W.; Martin, R. L.; Morokuma, K.; Zakrzewski, V. G.; Voth, G. A.; Salvador, P.; Dannenberg, J. J.; Dapprich, S.; Daniels, A. D.; Farkas, Ö.; Foresman, J. B.; Ortiz, J. V.; Cioslowski, J.; Fox, D. J. Gaussian 09, Revision D.01; Gaussian Inc: Wallingford, CT, **2009**.

[24] Allen, M. P.; Tildesley, D. J. *Computer Simulation of Liquids*; Oxford University Press: Oxford, U.K., **1989**.

[25] Stafström, S. *Chem. Soc. Rev.* **2010**, *39*, 2484–2499.

[26] Troisi, A. *Chem. Soc. Rev.* **2011**, *40*, 2347–2358.

[27] Kirkpatrick, J. *Int. J. Quantum Chem.* **2008**, *108*, 51-56.

[28] Brédas, J.-L.; Calbert, J. P.; da Silva Filho, D. A.; Cornil, J. *Proc. Natl. Acad. Sci.* **2002**, *99*, 5804–5809.

[29] Singh, U. C.; Kollman, P. A. **1984**, *5*, 129–145.

[30] Besler, B. H.; Merz, K. M.; Kollman, P. A. *J. Comput. Chem.* **1990**, *11*, 431–439.

[31] Brédas, J.-L.; Calbert, J. P.; da Silva Filho, D. A.; Cornil, J. *Proc. Natl. Acad. Sci.* **2002**, *99*, 5804–5809.

[32] Bässler, H. *Phys. Status Solidi* (*B*) **1993**, *175*, 15–56.

[33] Hindeleh, A. M.; Hosemann, R. *J. Phys. C: Solid State Phys.* **1988**, *21*, 4155–4170.

[34] Rivnay, J.; Noriega, R.; Kline, R. J.; Salleo, A.; Toney, M. F. *Phys. Rev. B: Condens. Matter Mater. Phys.* **2011**, *84*, 045203.

[35] Noriega, R.; Rivnay, J.; Vandewal, K.; Koch, F. P.; Stingelin, N.; Smith, P.; Toney, M. F.; Salleo, A. *Nat. Mater.* **2013**, *12*, 1038–1044.

[36] Ando, S.; Murakami, R.; Nishida, J.-I.; Tada, H.; Inoue, Y.; Tokito, S.; Yamashita, Y. *J. Am. Chem. Soc.* **2005**, *127*, 14996–14997.

[37] Sun, J.-P.; Hendsbee, A. D.; Eftaiha, A. F.; Macaulay, C.; Rutledge, L. R.; Welch, G. C.; Hill, I. G. *J. Mater. Chem. C* **2014**, *2,* 2612-2621.

[38] Xie, W.; Prabhumirashi, P. L.; Nakayama, Y.; McGarry, K. A.; Geier, M. L.; Uragami, Y.; Masei, K.; Douglas, C. J.; Ishii, H.; Hersam, M. C.; Frisbie, C. D. *ACS Nano* **2013**, *7*, 10245–10256.

[39] Shukla, D.; Rajeswaran, M. *Acta Crystallogr., Sect. E: Struc. Rep. Online* **2008**, *64,* 1735.

[40] Kakinuma, T.; Kojima, H.; Ashizawa, M.; Matsumotoa, H.; Mori, T. *J. Mater. Chem. C* **2013**, *1,* 5395-5401.

[41] Long, R. E.; Sparks, R. S.; Trueblood, K. N. *Acta Crystallogr.* **1965**, *18*, 932-939.

[42] Menard, E.; Podzorov, V.; Hur, S.-H.; Gaur, A.; Gershenson, M. E.; Rogers, J. A. *Adv. Mater.* **2004**, *16*, 2097-2101.

[43] Brown, A. R.; de Leeuw, D. M.; Lous, E. J.; Havinga, E. E. *Synth. Met.* **1994**, *66*, 257-261.

[44] Ando, S.; Nishida, J.; Tada, H.; Inoue, Y.; Tokito, S.; Yamashita, Y. *J. Am. Chem. Soc.* **2005**, *12*, 5336-5337.

[45] Ostrick, J. R.; Dodabalapur, A.; Torsi, L.; Lovinger, A. J.; Kwock, E. W.; Miller, T. M.; Galvin, M.; Berggren, M.; Katz, H. E. *J. Appl. Phys.* **1997**, *81*, 6804-6808.

[46] Facchetti, A.; Yoon, M.-H.; Stern, C. L.; Katz, H. E.; Marks, T. J. *Angew. Chem., Int. Ed.* **2003**, *42,* 3900-3903.

[47] Yoon, M.-H.; Facchetti, A.; Stern, C. E.; Katz, H. E.; Marks, T. J. *J. Am. Chem. Soc.* **2006**, *128,* 5792-5801.

[48] Jurchescu, O. D.; Meetsma, A.; Palstra, T. T. M. *Acta Crystallogr.* **2006**, *62*, 330-334.

[49] Bisri, S. Z.; Takenobu, T.; Takahashi, T.; Iwasa, Y. *Appl. Phys. Lett.* **2010**, *96*, 183304.

[50] Ando, S.; Nishida, J.; Fujiwara, E.; Tada, H.; Inoue, Y.; Tokito, S.; Yamashita, Y. *Chem. Mater.* **2005**, *17,* 1261-1264.

[51] Alt, H. C.; Kalus, J. *Acta Crystallogr.* **1982**, *1*, 2595-2600.

[52] (a) Warta, W.; Stehle, R.; Karl, N. *Appl. Phys. A: Mater. Sci. Process.* **1985**, *36*, 163-170. (b) Karl, N. *Synth. Met.* **2003**, *133*, 649-657.

[53] Sakamoto, Y.; Suzuki, T.; Kobayashi, M.; Gao, Y.; Fukai, Y.; Inoue, Y.; Sato, F.; Tokito, S. *J. Am. Chem. Soc.* **2004**, *126,* 8138-8140.

[54] Sakamoto, Y.; Suzuki, Y.; Kobayashi, M.; Gao, Y.; Inoue, Y.; Tokito, S. *Mol. Cryst. Liq. Cryst.* **2006**, *444*, 225-232.

[55] Brock, C. P.; Dunitz, J. D. *Acta Crystallogr.* **1990**, *46*, 795-806.

[56] Karl, N.; Marktanner, J. *Mol. Cryst. Liq. Cryst. Sci. Technol., Sect. A* **2001**, *355*, 149-173.

[57] Ito, Y.; Virkar, A. A.; Mannsfeld, S.; Oh, J. H.; Toney, M.; Locklin, J.; Bao, Z. *J. Am. Chem. Soc.* **2009**, *131,* 9396-9404.

[58] Ranganathan, A.; Kulkarni, G. U. *Proc. Indiana Acad. Sci.* **2003**, *115*, 637-647.

[59] Kim, S. H.; Yang, Y. S.; Lee, J. H.; Lee, J.-I.; Chu, H. Y. Lee, H.; Oh, J.; Do, L.-M.; Zyung, T. *Opt. Mater.* **2003**, *21*, 439-443.

[60] Chen, M.-C.; Chiang, Y.-J.; Kim, C.; Guo, Y.-J.; Chen, S.-Y.; Liang, Y.-J.; Huang, Y.-W.; Hu, T.-S.; Lee, G.-H.; Facchetti, A.; Marks, T. J. *Chem. Commun.* **2009**, 1846-1848.

[61] Näther, C.; Bock, H.; Havlas, Z.; Hauck, T. *Organometallics* **1998**, *17,* 4707-4715.

[62] Kotania, M.; Kakinuma, K.; Yoshimura, M.; Ishii, K.; Yamazaki, S.; Kobori, T.; Okuyama, H.; Kobayashi, H.; Tada, H. *Chem. Phys.* **2006**, *325*, 160-169.

[63] Nishida, J.-I.; Kumaki, D.; Tokito, S.; Yamashita, Y. *J. Am. Chem. Soc.* **2006**, *128,* 9598-9599.

[64] Nishida, J.-I.; Kumaki, D.; Tokito, S.; Yamashita, Y. *J. Am. Chem. Soc.* **2006**, *325*, 160-169.

[65] Ie, Y.; Nitani, M.; Karakawa, M.; Tada, H.; Aso, Y. *Adv. Funct. Mater.* **2010**, *20*, 907-913.

[66] Langer, V.; Becker, H.-D. *Z. Kristallogr.* **1992**, *199*, 313-315.

[67] Tripathi, A. K.; Heinrich, M.; Siegrist, T.; Pflaum, J. *Adv. Mater.* **2007**, *19,* 2097-2101.

[68] Dorset, D. L.; McCourt, M. P. *Acta Crystallogr.* **1994**, *50*, 344-351.

[69] Li, H.; Tee, B. C.-K.; Cha, J. J.; Cui, Y.; Chung, J. W.; Lee, S. Y.; Bao, Z. *J. Am. Chem. Soc.* **2012**, *134*, 2760-2765.

[70] Oniwa, K.; Kanagasekaran, T.; Jin, T.; Akhtaruzzaman, M.; Yamamoto, Y.; Tamura, H.; Hamada, I.; Shimotani, H.; Asao, N.; Ikeda, S.; Tanigaki, K. *J. Mater. Chem. C* **2013**, *1*, 4163-4170.

[71] Mamada, M.; Kumaki, D.; Nishida, J.; Tokito, S.; Yamashita, Y. *ACS Appl. Mater. Interfaces* **2010**, *2,* 1303-1307.

[72] Ie, Y.; Nitani, M.; Uemura, T.; Tominari, Y.; Takeya, J.; Honsho, Y.; Saeki, A.; Seki, S.; Aso, Y. *J. Phys. Chem. C* **2009**, *113*, 17189-17193.

[73] Liang, Z.; Tang, Q.; Liu, J.; Li, J.; Yan, F.; Miao, Q. *Chem. Mater.* **2010**, *22,* 6438-6443.

[74] Ichikawa, M.; Kato, T.; Uchino, T.; Tsuzuki, T.; Inoue, M.; Jeon, H.-G.; Koyama, T.; Taniguchi, Y. *Org. Electron.* **2010**, *11,* 1549-1554.

[75] Ogawa, T.; Kuwamoto, K.; Isoda, S.; Kobayashi, T.; Karl, N. *Acta Crystallogr., Sect. B: Struc. Sci.* **1999**, *55,* 123-130.

[76] Yamada, K.; Takeya, J.; Takenobu, T.; Iwasa, Y. *Appl. Phys. Lett.* **2008**, *92,* 253311.

[77] Youn, J. *et al. Adv. Electron. Mater.* **2015**, *1,* 1500098.

[78] Letizia, J. A.; Facchetti, A.; Stern, C. L.; Ratner, M. A.; Marks, T. J. *J. Am. Chem. Soc.* **2005***, 127,* 13476-13477.

[79] Kabe, R.; Nakanotani, H.; Sakanoue, T.; Yahiro, M.; Adachi, C. *Adv. Mater.* **2009**, *21*, 4034-4038.

[80] Shukla, D.; Nelson, S. F.; Freeman, D. C.; Rajeswaran, M.; Ahearn, W. G.; Meyer, D. M.; Carey, J. T. *Chem. Mater.* **2008**, *20,* 7486-7491.

[81] Rispens, M. T.; Meetsma, A.; Rittberger, R.; Brabec, C. J.; Sariciftci, N. S.; Hummelen, J. C. *Chem. Commun.* **2003**, 2116-2118.

[82] Yang, C.; Kim, J. Y.; Cho, S.; Lee, J. K.; Heeger, A. J.; Wudl, F. *J. Am. Chem. Soc.* **2008**, *130,* 6444-6450.

[83] Yang, T.-F.; Huang, S.-H.; Chiu, Y.-P.; Chen, B.-H.; Shih, Y.-W.; Chang, Y.-C.; Yao, J.-Y.; Lee, Y.-J.; Kuo, M.-Y. *Chem. Commun.* **2015**, *51,* 13773-13775.

[84] Borsenberger, P. M.; Pautmeier, L. T.; B¨assler, H. *Phys. Rev. B: Condens. Matter Mater. Phys.* **1992**, *46*, 12145.

[85] Lukyanov, A.; Andrienko, D. *Phys. Rev. B: Conden. Matter Mater. Phys.* **2010**, *82*, 193202.

Chapter 3. Impact of Morphology, Side-chain, and Crystallinity on Charge Transport Properties

3.1 Background

Polycyclic aromatic hydrocarbons (PAHs) have been of interest in the scientific community as organic semiconductors in field-effect transistors (FETs), light-emitting diodes (LEDs), and organic photovoltaics (OPVs). Most PAHs are two-dimensional, achiral materials that typically pack in a herringbone or lamellar manner. While these materials exhibit high mobilities and interesting optoelectronic properties, molecular ordering must be precisely controlled through functionalization of PAHs.[1,2,3] In the last 100 years, interest has evolved towards curved aromatic hydrocarbons, such as corannulenes and helicenes, that are three-dimensional and can be either chiral or achiral. Nuckolls advanced the idea of "contorted aromatics" as electronic materials years ago[4] and has since applied these materials as acceptor materials in OPVs[5,6,7] photodetectors,[8] and columnar-structured OFETs.[9] These materials usually pack in a columnar manner or with partial π-π stacking, which allows for close orbital contacts between molecules for high multi-dimensional charge transport.[10,11,12]

In particular, helical structures have been synthesized and studied for a variety of applications, including molecular recognition, asymmetric catalysis, and as conductive materials.[13] The molecular packing of these molecules can result in varying properties in the solid state, such as charge transport[14,15,16] and luminscence,[17,18] important parameters for the implementation of these materials in optoelectronic devices. Twisted two-dimensional aromatic compounds have found applications as one-dimensional photoconductors,[19] in small-molecule solar cells,[20] and as stackable molecules in thin-film transistors.[21] Spiro-fused materials are also important hole transport materials; for example, spiro-OMeTAD[22,23,24] is considered the state-of-the-art hole transport material and is used in both dye-sensitized[25,26] and perovskite solar cells.[27,28,29]

In 2015, Itami and coworkers reported the synthesis and characterization of π-extended double helicene **DH1** (Scheme 3.1), which combines the properties of planar [6]helicene and non-planar tribenzo[*b*,*n*,*pqr*]perylene (TBP).[30] Due to the chiral nature of the molecule, it packs in a contorted lamellar manner with π-π stacking and close π-π contacts in two directions. The Itami group published the synthesis and properties of alkylated **DH2** and dithia[6]helicene **DH3**.[31] Using DFT to calculate the FMOs of the double helicenes (DHs), the group found that the FMOs have a larger distribution on the TBP π-planes of **DH3** than the other variants. They also obtained a hole mobility of 3.3×10^{-2} cm^2 V^{-1} s^{-1} with an on/off ratio of greater than 10^5 for **DH3** from a top-contact/bottom-gate FET. The high hole mobility of **DH3**, coupled with the interesting packing properties of these helical molecules, indicate that these molecules are promising candidates as donor materials in organic electronic applications.[32] As a further probe into the factors the dictate the charge transport in these systems, we conducted a computational study on the effect of side-chain substitution and unique crystal packing on the charge transport of double helical molecules **DH1**, **DH2**, and **DH3**. Using the previously described method (Chapter 2.2) rooted in Marcus theory and kinetic Monte Carlo (kMC) simulations,[33] we calculate charge-transport properties and hole mobilities for perfect order and disordered DH systems. Crystal structure data were obtained from refs. 30 and 31.

Scheme 3.1. Double helical molecules of interest

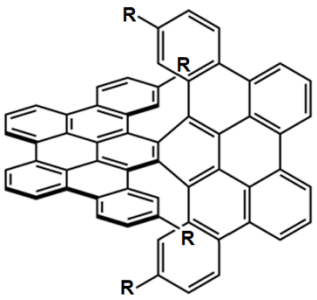

R=H DH1
R=nBu DH2

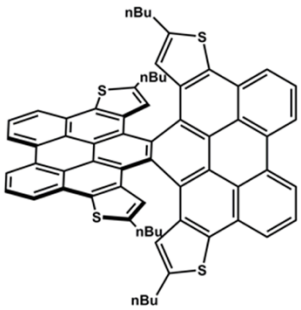

DH3

3.2 Molecular structure, packing, and morphology

We first discuss the packing of **DH1**, **DH2**, and **DH3** in the solid state. We then use three parameters to quantify the degree of structural change between the structures: (1) root-mean-square deviation (RMSD) of the structures, (2) dihedral angle between the TBP blades, and (3) paracrystallinity.

The impact of the side-chains in the crystallization and the packing motifs of the DH is dramatic. **DH1**, **DH2**, and **DH3** each exhibit 2D packing behavior, where π -blades form intrinsic slipped π-stacking (see Figure 3.1). For **DH1**, there are two types of interactions by the blades: a slipped π-π stacking interaction (Packing I) and an edge-to-edge interaction at the interface of the steroisomers (Packing II). For blades nearly perpendicular to the *a*-axis (parallel to the $(30\bar{1})$ plane), the TBP blades pack in a slipped, but relatively strong, π-π stacking manner. The blades that are nearly perpendicular to the *c*-axis (parallel to the $(\bar{1}02)$ plane) pack weakly, as only the edges of the TBPs are in contact. Packing is homochiral in the [100] and [001] directions (Packing I) and heterochiral in the [010] direction, in which different isomers are labeled with different colors (Packing II). For the **DH2** system, there is strong slipped π-π stacking of the TBPs along the [100] direction, and packing is heterochiral in both [100] and [010] directions. A similar packing arrangement is found in **DH3**, where there is strong and heterochiral π-π stacking of the π-blades along [001]. Finally, for alkylated derivatives **DH2** and **DH3**, the *n*-butyl side-chains interfere with lateral packing ([001] for DH2 and [100] for **DH3**).

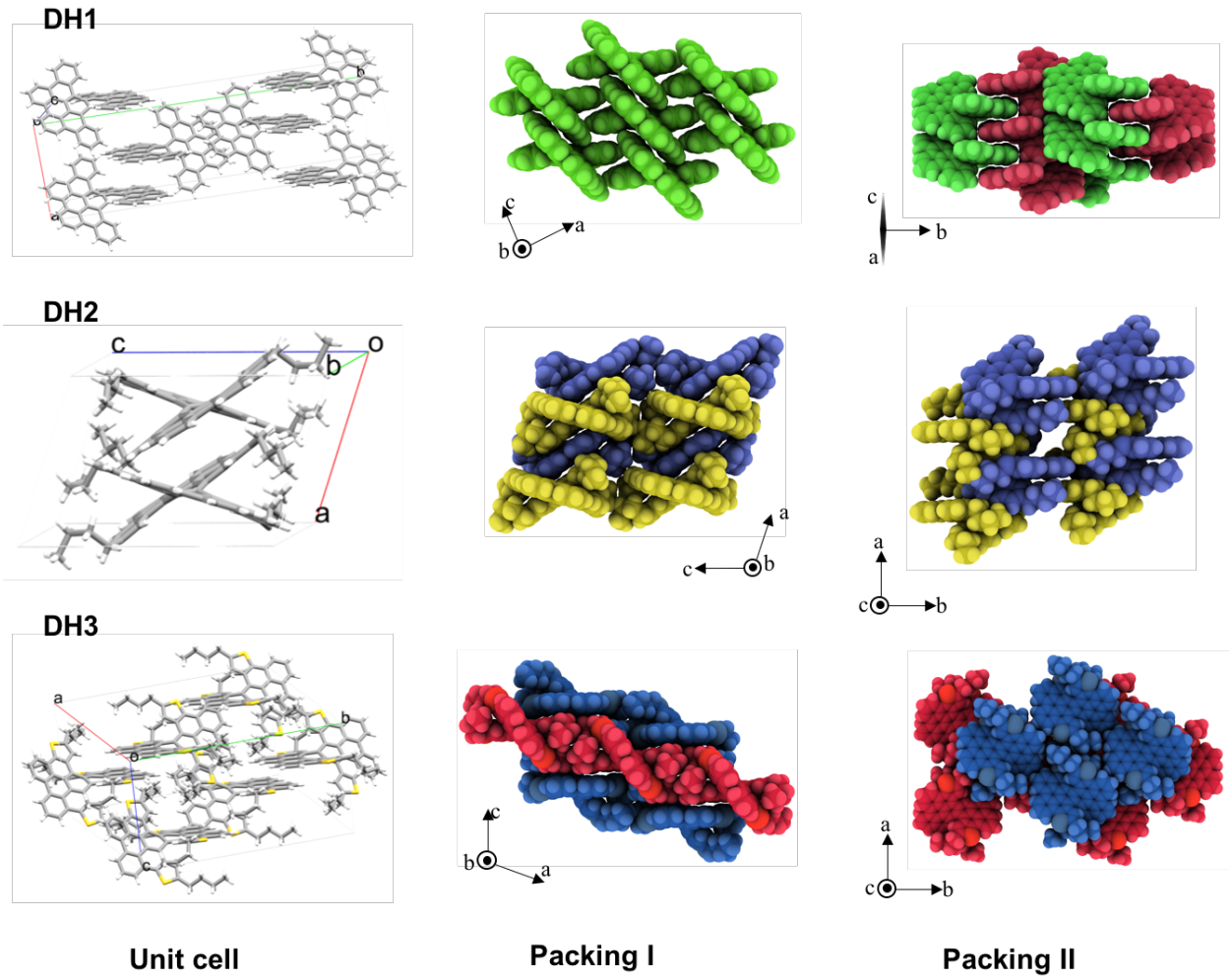

Figure 3.1. Packing of DHs.
Unit-cells and packing motifs from two angles. Heterochiral packing is indicated by the use of two different colors.

We compare the planarity of the π-blades in the solid state with DFT-optimized structures. XRD measurements reveal that the blades are planar in the crystal structures of all DHs, although DFT-optimized geometries indicate that the blades are slightly helical in the gas phase (Figure 3.2). The increased planarity in all three systems in the solid state is attributed to stabilizing non-bonding packing forces. These types of interactions are widely observed for conjugated materials such as biphenyl and bithiophene, which are non-planar in the gas phase[34,35] but exhibit low torsional disorder in the solid state when incorporated into oligomers and polymers.[36,37,38,39] For

the DHs, this change is beneficial in terms of charge-transport, as planarity increases the molecular overlap between molecules and enhances electronic-coupling between molecular pairs.

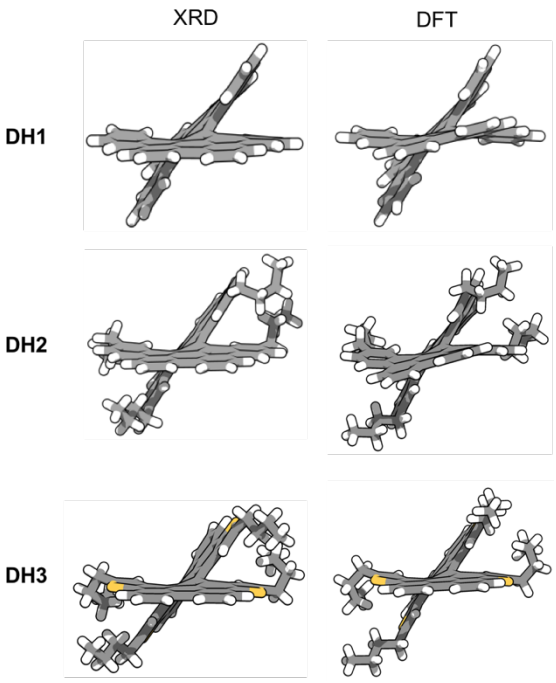

Figure 3.2. Structures of **DH1**, **DH2**, and **DH3** from X-ray measurements of solid-state structures and gas-phase B3LYP/6-311G(d,p) optimizations.

Room temperature MD simulations were performed to predict structural order in **DH1, DH2** and **DH3** in the solid state (Figure 3.3). In order to quantify the effect of temperature on the structures, the RMSD between each MD-disordered systems and its initial experimental supercell was calculated from a single MD snapshot at 300K. The RMSD values of **DH1**, **DH2**, and **DH3** are 0.73 Å, 1.28 Å, and 0.56 Å, respectively. To account for the influence of *n*-butyl side-chains, the RMSD of **DH2** with the exclusion of alkyl side-chains was calculated and found to be 0.88 Å, a value still higher than but closer to that of **DH1**. The average RMSD over individual molecules is ~0.2 Å for all DHs, indicating that the RMSD deviation can be largely attributed to relative orientations of the molecules and expansion of the supercells rather than changes in the DH molecules, highlighting the significance of the unique packing arrangements of the DHs.

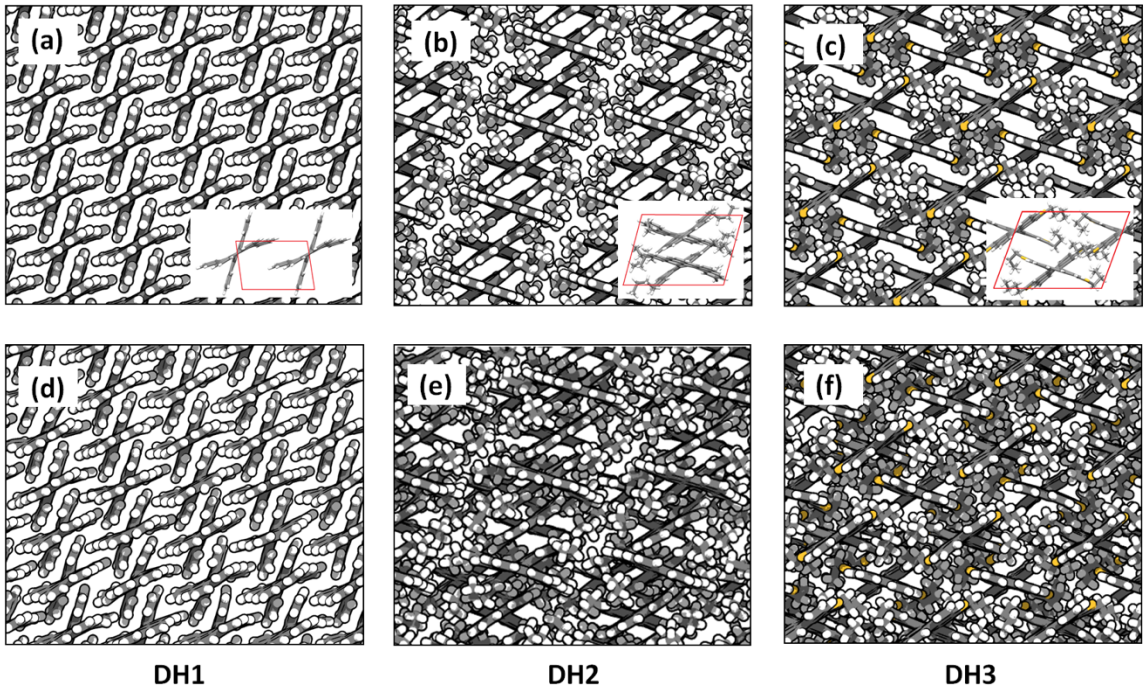

Figure 3.3. Ordered packing in supercells (a)-(c) and atomistic morphologies obtained from MD simulations at 300K (d)-(f).
For each case, packing in one crystallographic layer is shown for clarity.

Next, we analyzed the dihedral angle between the π-blades in the XRD, DFT-optimized, and MD-disordered structures. The experimental dihedral angles between the π-blades of **DH1, DH2** and **DH3** are 41°, 50° and 53° respectively.[30] The dihedrals between the π-planes in the optimized structures are similar (46°, 49° and 47° for **DH1, DH2** and **DH3**, respectively) to the experimental values with deviations of 1-6°, suggesting that side-chains have a negligible effect on DH core structures. Dihedral angle distributions from MD simulations are shown in Figure 3.4a. The averages of these distributions are 42°, 49° and 54° for **DH1, DH2** and **DH3**, respectively, which are consistent with the values from XRD and DFT structures. To quantify structural disorder in these systems, we calculated the standard deviations of these dihedral angle distributions, which are found to be similar (3.8°, 3.4° and 4.6° for **DH1**, **DH2** and **DH3**, respectively).

In order to quantify the positional disorder between neighboring molecules, we calculated paracrystallinity along the strong π-π stacking directions. Paracrystallinity is defined as $g = s/\langle d \rangle$,

where *d* is the distance between neighboring molecules exhibiting strong π-π stacking, *s* is the standard deviation of an ensemble of *d* distances and <…> represents an ensemble average.[40,41,42] A paracrystallinity value of ~0-1% corresponds to a nearly perfect order system, and a value of ~1-10% corresponds to crystalline order.[40] Paracrystallinity parameters for **DH1**, **DH2** and **DH3** are 1.7%, 2.2% and 1.3%, respectively, with **DH2** as the most structurally more disordered system and **DH3** least disordered, which is consistent with the RMSD analysis.

Our MD simulations reveal that the positional disorder of **DH2**, quantified by both RMSD and paracrystallinity, is higher than for **DH1**. In contrast, **DH3** has a smaller RMSD but disorder in the dihedral between the π-blades is larger. These observations cannot directly be attributed to the presence of side-chains since the presence of side-chains does not have strong influence on the molecular structure. Thus, the relative positional disorder is largely caused by the difference in packing arrangement. However, as we will describe later, high positional disorder does not always bode high charge transport in the crystalline phase.

3.3 Charge transport parameters

In order to probe the differences in charge transport, we calculate a number of relevant parameters, including hole-transfer reorganization energy, electronic coupling, and energetic disorder of **DH1, DH2** and **DH3**. We compare the charge-transport parameters to those of pentacene and rubrene, high-performing systems that were studied in our previous hole mobility benchmark.[33] The reorganization energy λ is an intrinsic property of the system that quantifies energetic changes due to structural variations between ground and excited state structures. We use gas phase optimizations of DHs to calculate λ according to the four-point rule based on the potential energy curves. Reorganization energies are very similar for **DH1, DH2** and **DH3** ($\lambda = 117$, 122 and 108 meV, respectively), indicating that addition of side-chains and/or heteroaromatic substitution has negligible influence on λ due to the inherently similar core structures. However, there is correlation between the degree of twisting in each π-blade and λ across the three

structures. As discussed in the previous section, the twisting in the π-blade is exhibited in the DFT-optimized structures but not in the crystal structure (Figure 3.2). The twisting is smallest in **DH3** and largest in **DH2**, which are in line with the calculated reorganization energies. These reorganization energies are also comparable to those of pentacene (100 meV) and rubrene (160 meV), both of which have shown highly efficient charge transport in organic semiconductors.

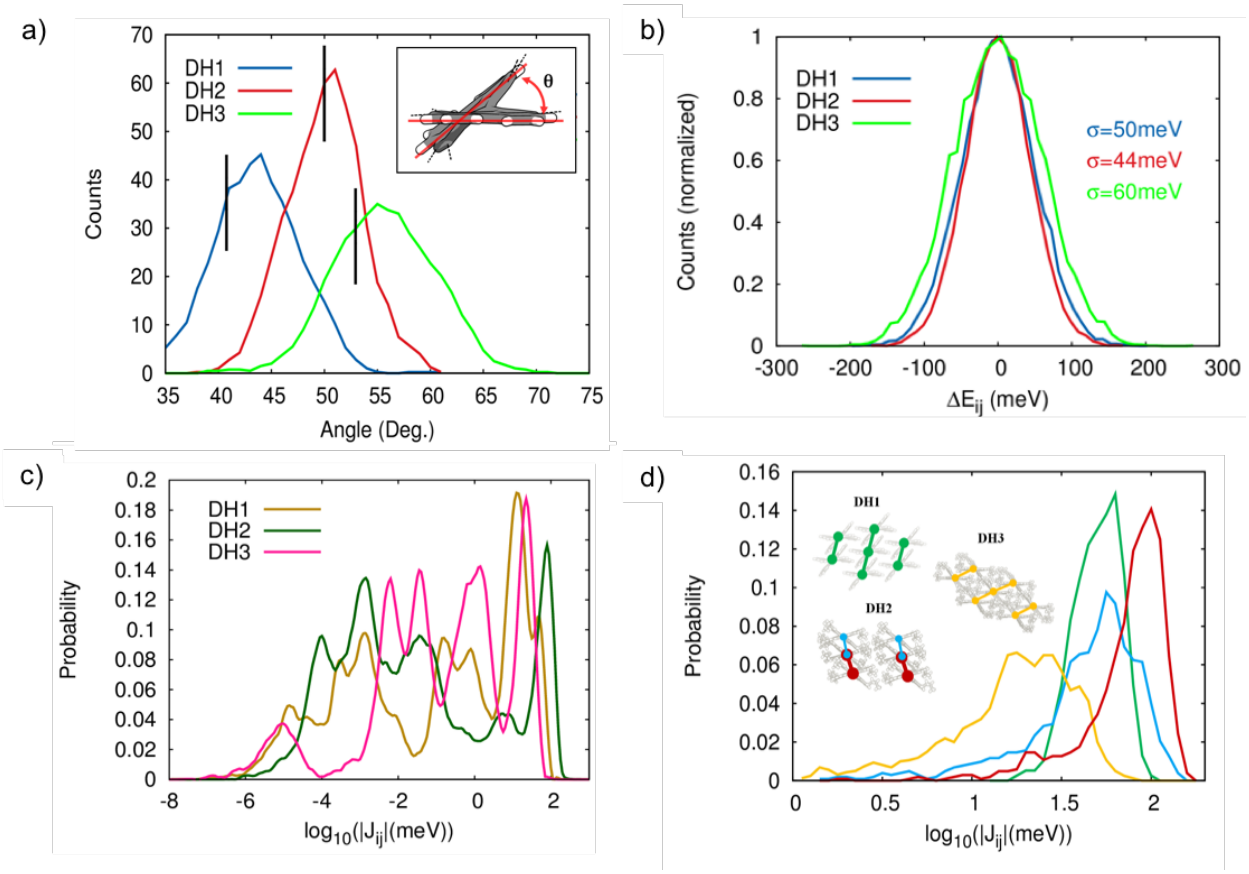

Figure 3.4. Charge transport parameters.
(a) Distributions of the angles between the plane of two π-blades of **DH1, DH2** and **DH3**. The vertical black lines represent values obtained from XRD measurements. Inset: Representative schematic illustrating the angle between two π-blades of DHs, where dashed lines indicate the fused portion of the molecule not pictured. (b) Site-energy difference distributions of **DH1, DH2** and **DH3**. Standard deviations, *i.e.* energetic disorders, are indicated. Electronic coupling distributions of the (c) overall packing and (d) π-π stacking arrangements.

Next, we looked at the variations in site-energy difference distributions in the equilibrated morphologies from MD, which have often been used as measures of energetic disorder σ.[43,44,45,46]

While the width of the site-energy difference distributions is similar for all DHs, the standard deviation, *i.e.* energetic disorder, of **DH1** (50 meV) is higher than that of **DH2** (44 meV) and energetic disorder of **DH3** is the highest (60 meV) (Figure 3.4b). **DH1** and **DH2** values are systematically lower than the typical σ values previously calculated for pentacene and rubrene using the same methodology (68 and 53 meV, respectively).[33] Energetically, **DH3** is less ordered but **DH1** and **DH2** are both ordered.

We then calculated the electronic coupling between neighboring molecules in crystal **DH1, DH2** and **DH3** using the ZINDO-based Molecular Orbital Overlap (MOO) methodology implemented in VOTCA (Figure 3.5). Electronic coupling values in the π-π stacking direction are high for both **DH1** (58 meV) and **DH2** (73 meV), while lower for **DH3** (37 meV). This is due to strong π-π stacking between the adjacent molecules, as described earlier. Electronic coupling values in the π-π stacking direction of pentacene and rubrene are ~60 and 80 meV, respectively.[33] Similar to the λ values, *J* values of both **DH1** and **DH2** are comparable to high-mobility pentacene and rubrene and indicative of high charge-transport performance. Electronic coupling determines charge-transport propensity; therefore, in single-crystal morphology, charge transport is predominantly one-dimensional for **DH1** and **DH3**, while it alternates for **DH2**.

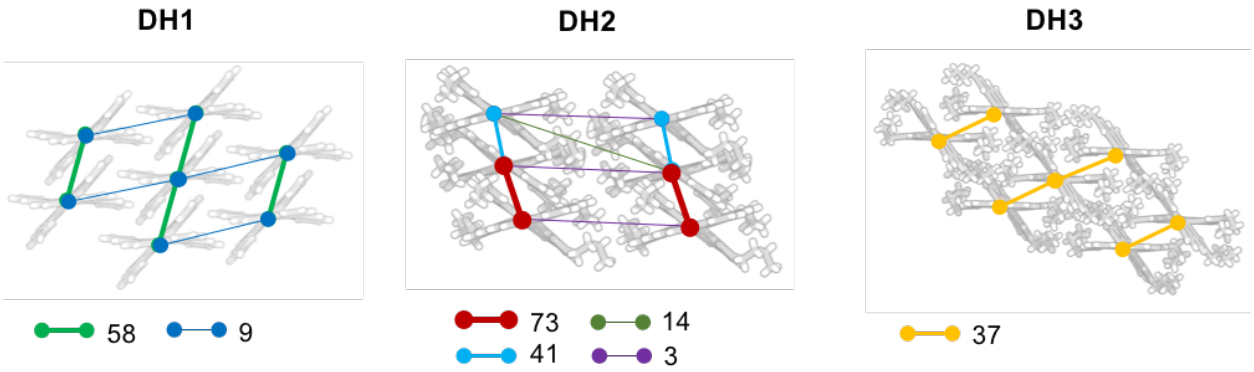

Figure 3.5. Electronic coupling pathways.
Crystal packing motifs and transport pathways of **DH1**, **DH2**, and **DH3**. The connections correspond to intermolecular electronic coupling, *J* (in meV). Thickness of each line is coherent

with the strength of the corresponding coupling. A *J* value of 38 meV in **DH3** along [110] direction (see Scheme 3.1) is not shown for clarity.

Analysis of the electronic coupling distribution of the disordered DH systems is shown in Figures 3.4c and 3.4d. Figure 3.4c shows the distribution of the overall electronic coupling in each of the systems, with peaks at various points due to multiple transport directions. There are two peaks in the strong electronic coupling region for **DH1**, corresponding to <*J*> = 10 meV and <*J*> = 49 meV, which correspond to weak and strong π-π stacking in **DH1**. For **DH2**, a combination of two strong couplings (49 and 75 meV*)* forms a single peak; these are the *J* values of the two π-π stacking interactions of **DH2**, which coexist alternatively along the charge-transport direction discussed earlier in the text. The maximum of the electronic-coupling distribution of **DH2** is higher than **DH1**, consistent with *J* values in perfect crystal morphologies. For **DH3**, coupling peaks at lower values than those of **DH1** and **DH2**, with an average value of 21 meV and corresponding to the π-π stacking of **DH3**. This value is considerably lower than electronic coupling value obtained for **DH3** in the crystal phase (37 meV). Figure 3.4d shows direction-resolved electronic coupling for the equilibrated atomistic morphologies. Electronic coupling distributions in both π-π stacking directions in **DH2** (blue and red) are broader than the one direction in **DH1** (green) and **DH3** (yellow). The standard deviation of each of these peaks (Σ) is low for **DH1** and **DH3** (13 meV for each) but much higher for the two peaks in **DH2** (26 and 29 meV). The broader *J*-distribution in the π-π stacking of **DH2** is attributed to the higher positional disorder, which arises from higher RMSD and paracrystallinity values compared to the other two systems.

3.4 Mobility

Finally, using the charge transport parameters calculated in the previous section, we calculated hole mobilities of the three molecules based on crystal and crystalline morphologies. The summary of prominent charge-transport parameters along with the hole mobilities of **DH1, DH2** and **DH3** are given in Table 3.1. We compared our results against those of high-mobility

pentacene and rubrene, where the parameters were calculated using the same method in ref. 33. We first calculated hole mobilities from the unit cells, *i.e.* hypothetically perfect order was considered (*i.e.* g = 0, σ = 0). As discussed earlier, reorganization energies of all systems are similar and the electronic coupling of **DH1** and **DH3** is weaker than **DH2**; however, the predicted hole mobility of **DH1** (8.6 cm^2/Vs) is higher than that of **DH2** (5.7 $cm^2\ V^{-1}\ s^{-1}$), which is surprising since the charge-transfer rate is proportional to J^2 (Equation 3.1). In **DH1**, pentacene, and rubrene, charge transfer is confined to a single direction, while the transfer travels in two directions for **DH2**. In a defect-free crystal, an alternating pattern in charge transport results in a decrease in the charge-carrier's net velocity, which is related to the lower hole mobility. If a charge-carrier is formed in a hopping site where transfer to the surrounding sites is unfavorable, the probability for the carrier to oscillate in the site and remain stagnant increases, causing an overall decrease in hole mobility. Therefore, for these systems, heterochiral transport is less favorable than homochiral transport in an ordered phase. The hole mobility of **DH3** is lower than **DH1** but same as **DH2**, which is, in our case, expected considering the lower J values for the homochiral transport.

The situation is dramatically different for the case of crystalline morphologies. Starting supercells were equilibrated using MD simulations, resulting in slight positional disorder. As expected, the added positional and energetic disorder results in decreased hole mobilities. While the hole mobility of **DH1** decreases roughly by a factor of four relative to its ordered hole mobility, the hole mobility of **DH2** is only slightly affected by disorder. Moreover, while the ordered hole mobility of **DH2** is the lowest of all molecules in Table 3.1, the crystalline hole mobility is the highest, close to its crystal value. With disorder, the hole-mobility of **DH3** decreases more than an order of magnitude from 5.7 to 0.4 $cm^2\ V^{-1}\ s^{-1}$. Fujikawa *et al.*[31] obtained the experimental hole-mobility of **DH3** in an OFET configuration and obtained a value of 0.033 cm^2/Vs, which is nearly an order of magnitude lower than our prediction. As the experimental mobility has not been

optimized,[47] the discrepancy between our prediction and the experimental results can be attributed to the polycrystalline nature of the thin-film transistor, which creates grain boundaries that impair charge-transport. We believe our value of 0.4 $cm^2 V^{-1} s^{-1}$ is the theoretical upper limit for mobility that **DH3** could obtain upon optimization of device processing.[48,49] We make mention that the experimental mobilities of DH1 and DH2 have not been achieved yet and thus no comparisons can be made.[47]

Table 3.1. Summary of charge-transport parameters for **DH1**, **DH2** and **DH3** and comparisons with benchmark materials

	Crystal					**Crystalline**				
	λ	$J_{\pi\text{-}\pi}$ (DFT)	$J_{\pi\text{-}\pi}$ (ZINDO)	μ (DFT)	μ (ZINDO)	g	$\langle J_{\pi\text{-}\pi} \rangle$	σ	μ	μ_{exp}
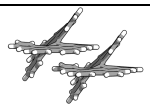 **DH1**	117	56	58	10.1	8.6	1.7	49	50	2.3	n/a
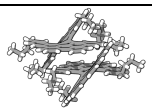 **DH2**	122	66	73	4.3	5.7	2.2	75	44	5.1	n/a
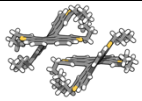 **DH3**	108	44	37	6.9	5.7	1.3	21	60	0.4	0.033[a]
 **pentacene***	95	42[§]	61	10.4	15.6	2.5	32	68	0.7	1.45[b]
 **rubrene***	160	106[§]	81	20.3	11.6	1.5	75	53	1.9	8.6[b]

Reorganization energy, λ, electronic-coupling, J, and energetic disorder, σ, are in units of meV. Paracrystallinity parameter, g, is % and hole-mobility, μ, is in units of cm^2/Vs. The average electronic coupling results (and, consequently, the hole mobilities) for crystalline morphologies are calculated by ZINDO. [a] ref. 31, [b] ref. [50]. *Reorganization energies and ZINDO calculations of pentacene and rubrene are taken from ref. 33, DFT based electronic coupling and mobilities are our work. [§]DFT calculated electronic coupling for the remaining directions were calculated to be 56 and 89 meV for pentacene and 18 meV for rubrene.

In order to understand the disproportionate changes in the predicted crystalline hole mobilities due to the presence of disorder, we plotted connectivity graphs showing the transport

networks in a single MD snapshot (Figure 3.6). The center-of-masses of the molecules are represented by spheres and strong electronic couplings between these sites (where J > 20 meV) are represented by the red lines. For **DH1**, strong coupling occurs mainly along the [001] direction (with some in the (110) plane), which results in mainly one-dimensional transport. On the other hand, the transport of **DH2** is largely two-dimensional, where the strong couplings occur along the [100] and [010] directions. Even though coupling is especially strong along one direction in **DH1** (<J> = 46±13 *meV*), the system is sensitive to charge-trapping due to positional disorder, which results in the hole mobility decreasing by a factor of 4 with the introduction of disorder (μ_{ideal} = 8.6 to μ_{disor} = 2.3 $cm^2\ V^{-1}\ s^{-1}$). On the other hand, the hole mobility of **DH2** is nearly maintained in the presence of disorder, as trap states can be bypassed due to the two-dimensional nature of electronic coupling in this system. In general, electronic coupling in the **DH3** system is lower than in the other two systems. For **DH3**, we do not observe many connections due to weak electronic coupling values (<20 meV), which impair charge transport and leads to traps. Moreover, the connectivity seems to be three-dimensional which is known to be destructive for charge-transport.[31] As a result, the mobility of **DH3** decreases from 5.7 to 0.4 $cm^2\ V^{-1}\ s^{-1}$, corresponding to a nearly 15-fold decrease in mobility.

Although the diverse connectivity in an ordered crystal of **DH2** is unfavorable for charge-transport, it becomes beneficial in its crystalline morphology for achieving high-mobility, as a charge-carrier can easily bypass a trap-state by following other favorable paths. In crystalline morphologies, having diverse pathways is favorable due to the increased probability of a charge carrier being able to bypass charge traps. Our findings are in line with previous studies on conjugated organic polymers. Noriega *et al.*[33] showed that the requirement for high mobility in conjugated polymers was the presence of interconnected aggregates rather than an increase in crystallinity. Molecular dynamics simulations by Jackson *et al.* [51] also indicate that conformationally disordered polymers can still result in efficient devices due to the ability of the

polymers to form local molecular ordering, which is of higher importance than long-range crystallinity. Similarly, although crystalline **DH2** shows high positional disorder, its ability to form interconnected hopping sites allow for high mobility despite disorder. **DH2** is a promising crystalline organic material and potentially may have one of the highest hole mobilities as an organic semiconductor that can readily be implemented in both single crystal and thin film technology.

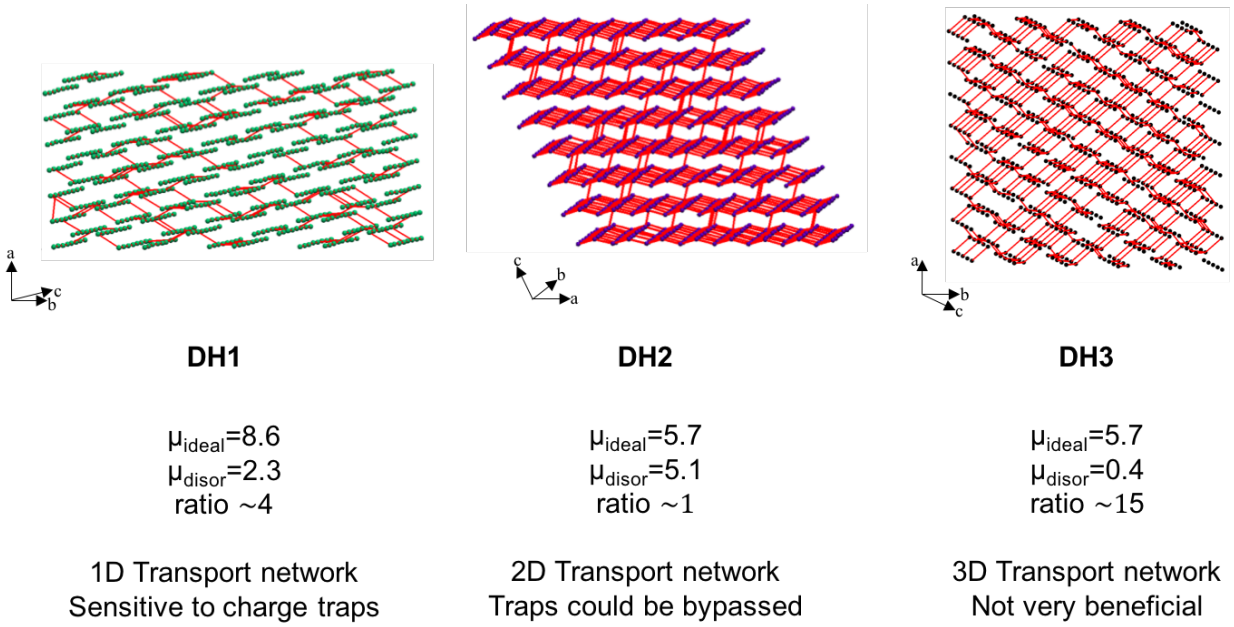

Figure 3.6. Transport networks in DH systems.
Connectivity graphs showing the transport networks of crystalline **DH1, DH2** and **DH3**. Green, blue and and black dots indicate central of masses of molecules and connections (red) represent electronic coupling values (where J > 20 meV) between neighboring pairs. Mobilities are in units of $cm^2\ V^{-1}\ s^{-1}$.

3.5 Conclusions

Atomistic morphologies and charge transport of unsubstituted and substituted π-extended double helicenes (**DH1** and **DH2**) and of a thiophene variant (**DH3**) are predicted. In the solid-state, each material exhibits a unique form of contorted packing and comprise both homochiral and heterochiral packing in the crystal structure. Using MD simulations, we examine the distributions of dihedral angles of π-blades and calculate RMSD and paracrystallinity parameters

in order to quantify structural disorder and understand the atomistic morphologies in the solid state. Our results reveal that **DH2** morphology is structurally more disordered compared to **DH1** and **DH3**. We then perform charge-transport simulations and calculated reorganization energies, electronic coupling and hole mobilities. The reorganization energies are similar, but the electronic coupling between π-π stacked neighboring pairs are different and highly dependent on the relative orientations of the DH molecules. Electronic coupling of **DH2** is stronger than that of **DH1** or **DH3**. These results reveal that, despite the dramatic influence on the packing arrangement, side-chain substitution has no direct impact on bulk features. Hole mobilities of **DH1**, **DH2**, and **DH3** were predicted based on ordered and crystalline morphologies, using kinetic Monte Carlo simulation methods. The hole mobility of ordered **DH2** is lower than for **DH1**, although the electronic coupling of **DH2** is stronger. This discrepancy is attributed to the alternating transport network of **DH2** due to heterochirality in the π-π stacking direction, which makes the system vulnerable to shallow charge-traps, even in an ordered morphology. **DH3** also comprises a somewhat three-dimensional transport network, but we observe that it is not beneficial for charge transport. We then predict hole mobilities in the crystalline order morphologies, in which positional and energetic disorders is incorporated into the systems. We find that the hole mobility of **DH2** is markedly higher than **DH1**, **DH3,** and benchmark high-mobility organic semiconductors rubrene and pentacene. Examination of electronic coupling within the disordered system reveals that although even in the presence of structural and positional disorder, there exists favorable electronic coupling in two directions. The 2D transport network in **DH2**, in which the system is susceptible to charge-trapping in crystal morphology, is favorable in disordered morphologies due to increased probability of bypassing charge trap states. This work provides fundamental understanding of the differences in charge transport in single crystal and thin film morphologies and serves as a foundation for understanding of other materials with multi-dimensional charge transport.

3.6 References

[1] Ostroverkhova, O. *Chem. Rev.* **2016**, *116*, 13279-13412.

[2] Wang, C.; Dong, H.; Jiang L.; Hu, W. *Chem. Soc. Rev.*, 2018, 47, 422-500.

[3] Yao, Z.-F.; Wang, J.-Y.; Pei, J. *Cryst. Growth Des.* **2018**, *18*, 7-15.

[4] For a review of contorted aromatics, see: Ball, M.; Zhong, Y.; Wu, Y.; Schenck, C.; Ng, F.; Steigerwald, M.; Xiao, S.; Nuckolls, C. *Acc. Chem. Res.* **2015**, *48,* 267-276.

[5] Ball, M.; Zhong, Y.; Fowler, B.; Zhang, B.; Li, P.; Etkin, G.; Paley, D. W.; Decatur, J.; Dalsania, A. K.; Li, H.; Xiao, S.; Ng, F.; Steigerwald, M. L.; Nuckolls, C. *J. Am. Chem. Soc.* **2016**, *138,* 12861-12867.

[6] Schuster, N. J.; Paley, D. W.; Jockusch, S.; Ng, F.; Steigerwald, M. L.; Nuckolls, C. *Angew. Chem. Int. Ed.* **2016**, *55,* 13519-13523.

[7] Sisto, T. J.; Zhong, Y.; Zhang, B.; Trinh, M. T.; Miyata, K.; Zhong, X.; Zhu, X.-Y.; Steigerwald, M. L.; Ng, F.; Nuckolls, C. *J. Am. Chem. Soc.* **2017**, *139,* 5648-5651.

[8] For work on helical nanoribbon photodetectors, see: Zhong, Y.; Sisto, T. J.; Zhang, B.; Miyata, K.; Zhu, X.-Y.; Steigerwald, M. L.; Ng, F.; Nuckolls, C. *J. Am. Chem. Soc.* **2017**, *139,* 5644-5647.

[9] For work by Nuckolls on using contorted hexabenzocoronenes in OFETs, see: Cohen, Y. S.; Xiao, S.; Steigerwald, M. L.; Nuckolls, C.; Kagan, C. R. *Nano Lett.* **2006**, *6*, 2838-2841.

[10] Skabara, P. J.; Arlin, J.-B.; Geerts, Y. H. *Adv. Mater.* **2013**, *25*, 1948-1954.

[11] Arumugam, S.; Wright, I. A.; Inigo, A. R.; Gambino, S.; Howells, C. T.; Kanibolotsky, A. L.; Skabara, P. J.; Samuel, I. D. W. *J. Mater. Chem. C* **2014**, *2*, 34-39.

[12] Calvo-Castro, J.; Morris, G.; Kennedy, A. R.; McHugh, C. J. *Cryst. Growth Des.* **2016**, *16*, 5385-5393.

[13] For a review of synthesis and applications of helicenes, see: Shen, Y.; Chen, C.-F. *Chem. Rev.* **2012**, *112*, 1463-1535.

[14] Kang, S. J.; Ahn, S.; Kim, J. B.; Schenck, C.; Hiszpanski, A. M.; Oh, S.; Schiros, T.; Loo, Y.-L.; Nuckolls, C. *J. Am. Chem. Soc.* **2013,** *135,* 2207-2212.

[15] Schiros, T.; Kladnik, G.; Prezzi, D.; Ferretti, A.; Olivieri, G.; Cossaro, A.; Floreano, L.; Verdini, A.; Schenck, C.; Cox, M.; Gorodetsky, A. A.; Plunkett, K.; Delongchamp, D.; Nuckolls, C.; Morgante, A.; Cvetko, D.; Kymissis, I. *Adv. Energy Mater.* **2013**, *3,* 894-902.

[16] Rice, B.; LeBlanc, L. M.; Otero-de-la-Roza, A.; Fuchter, M. J.; Johnson, E. R.; Nelson, J.; Jelfs, K. E. *Nanoscale* **2018**, *10*, 1865-1876.

[17] Zoppi, L.; Martin-Samos, L.; Baldridge, K. K. *J. Am. Chem. Soc.* **2011**, *133,* 14002-14009.

[18] Xiao, S.; Myers, M.; Miao, Q.; Sanaur, S.; Pang, K.; Steigerwald, M. L.; Nuckolls, C. *Angew. Chem., Int. Ed*. **2005**, *44*, 7390-7394.

[19] For select example of contorted aromatics in solar cells, see: Kang, S. J.; Kim, J. B.; Chiu, C.-Y.; Ahn, S.; Schiros, T.; Lee, S. S.; Yager, K. G.; Toney, M. F.; Loo, Y.-L.; Nuckolls, C. *Angew. Chem., Int. Ed.* **2012**, *51*, 8594-8597.

[20] For select example of contorted aromatics in thin-film transistors, see: Xiao, S.; Kang, S. J.; Zhong, Y.; Zhang, S.; Scott, A. M.; Moscatelli, A.; Turro, N. J.; Steigerwald, M. L.; Li, H.; Nuckolls, C. *Angew. Chem., Int. Ed.* **2013***, 52,* 4558-4562.

[21] For select example of tunability of contorted aromatics, see: Li, Y.; Jia, Z.; Xiao, S.; Liu, H.; Li, Y. *Nat. Commun.* **2015**, *7,* 11637-11647.

[22] For early work on the development of Spiro-OMeTAD, see: Salbeck, J.; Yu, N.; Bauer, J.; Weissörtel, F.; Bestgen, H. *Synth. Met.* **1997***, 91*, 209-215.

[23] For experimental work on the crystal structure and hole transport of Spiro-OMeTAD, see: Shi, D.; Qin, X.; Li, Y.; He, Y.; Zhong, C.; Pan, J.; Dong, H.; Xu, W.; Li, T.; Hu, W.; Brédas, J.-L.; Bakr, O. M. *Sci. Adv.* **2016**, *2*, e1501491.

[24] For calculations of hole transport of Spiro-OMeTAD, see: Yavuz, I.; Houk, K. N. *J. Phys. Chem. C*, **2017**, *121*, 993-999.

[25] For pioneering work on the application of Spiro-OMeTAD in dye-sensitized solar cells, see: Bach, U.; Lupo, D.; Comte, P.; Moser, J. E.; Weissörtel, F.; Salbeck, J.; Spreitzer, H.; Grätzel, M. *Nature* **1998***, 395,* 583-585.

[26] For a recent example on the application of Spiro-OMeTAD in dye-sensitized solar cells, see: Jang, S.-R.; Zhu, K.; Ko, M. J.; Kim, K.; Kim, C.; Park, N.-G.; Frank, A. J. *ACS Nano* **2011**, *5*, 8267-8274.

[27] For early work on the application of Spiro-OMeTAD in perovskite solar cells, see: Kim, H.-S.; Lee, C.-R.; Im, J.-H.; Lee, K.-B.; Moehl, T.; Marchioro, A.; Moon, S.-J.; Humphry-Baker, R.; Yum, J.-H.; Moser, J. E.; Grätzel, M.; Park, N.-G. *Sci. Rep.* **2012***, 2*, 591.

[28] For early work on the application of Spiro-OMeTAD in perovskite solar cells, see: Burschka, J; Pellet, N; Moon, S.-J.; Humphry-Baker, R.; Gao, P.; Nazeeruddin, M. K.; Grätzel, M. *Nature* **2013**, *499*, 316-319.

[29] For a recent review of Spiro-OMeTAD as a hole transport material in perovskite solar cells, see: Hawash, Z.; Ono, L. K.; Qi, Y. *Adv. Mater. Interfaces* **2017**, 1700623.

[30] Fujikawa, T.; Segawa, Y.; Itami, K. *J. Am. Chem. Soc.* **2015**, *137,* 7763-7768.

[31] Fujikawa, T.; Mitoma, N.; Wakamiya, A.; Saeki, A.; Segawa, Y.; Itami, K. *Org. Biomol. Chem.* **2017**, *15*, 4697-4703.

[32] Kiel, G. R.; Patel, S. C., Smith, P. W.; Levine, D. S.; Tilley, T. D. *J. Am. Chem. Soc.* **2017**, *139*, 18456-18459.

[33] Yavuz, I.; Martin, B. N.; Park, J.; Houk, K. N. *J. Am. Chem. Soc.* **2015**, *137*, 2856-2866, and references therein.

[34] Bastiansen, O. *Acta Chem. Scand.* **1949**, *3*, 408-414.

[35] Takayanagi, M.; Gejo, T.; Hanazaki, I. *J. Phys. Chem.* **1994***, 98*, 12893-12898.

[36] Pelletier, M.; Brisse, F. *Acta Cryst. C* **1994**, *50,* 1942-1945.

[37] Chaloner, P. A.; Gunatunga, S. R.; Hitchvock, P. B. *Acta Cryst. C* **1994**, *50*, 1941-1942.

[38] Siegrist, T.; Kloc, C.; Laudise, R. A.; Katz, H. E.; Haddon, R. C. *Adv. Mater.* **1998**, *10*, 379-382.

[39] Vujanovich, E. C.; Bloom, J. W. G.; Wheeler, S. E. *J. Phys. Chem. A* **2012**, *116*, 2997-3003.

[40] Hindeleh, A.; Hosemann, R. *J. Phys. C* **1988**, *21*, 4155-4170.

[41] Rivnay, J.; Noriega, R.; Kline, R. J.; Salleo, A.; Toney, M. F. *Phys. Rev. B*, **2011**, *84*, 045203.

[42] Noriega, R.; Rivnay, J.; Vandewal, K.; Koch, F. P.; Stingelin, N.; Smith, P.; Toney, M. F.; Salleo, A. *Nat. Mater.* **2013**, *12*, 1038-1044.

[43] Kwiatkowski, J. J.; Nelson, J.; Li, H.; Bredas, J. L.; Wenzel, W.; Lennartz, C. *Phys. Chem. Chem. Phys.* **2008**, *10*, 1852-1858.

[44] Martinelli, N. G.; Savini, M.; Muccioli, L.; Olivier, Y.; Castet, F.; Zannoni, C.; Beljonne, D.; Cornil, J. *Adv. Func. Mater.* **2009**, *19*, 3254-3261.

[45] Tummala, N. R.; Zheng, Z.; Aziz, S. G.; Coropceanu, V.; Brédas, J. L. *J. Phys. Chem. Lett.* **2015**, *6*, 3657-3662.

[46] Steiner, F.; Foster, S.; Losquin, A.; Labram, J.; Anthopoulos, T. D.; Frost, J. M.; Nelson, J. *Mater. Horiz.* **2015**, *2*, 113-119.

[47] Private communication with the Itami group, 2018.

[48] Sokolov, A. N.; Atahan-Evrenk, S.; Mondal, R.; Akkerman, H. B.; Sánchez-Carrera, R. S.; Granados-Focil, S.; Schrier, J.; Mannsfeld, S. C. B.; Zoombelt, A.; Bao, Z.; Aspuru-Guzik, A. *Nature Comm.,* 2011, **2**, 437.

[49] Vehoff, T.; Baumeier, B.; Troisi, A.; Andrienko, D. *J. Am. Chem. Soc.* **2010**, *132*, 11702–11708.

[50] Troisi, A. *Chem. Soc. Rev.* 2011, **40**, 2347–2358.

[51] Jackson, N. E.; Kohlstedt, K. L.; Savoie, B. M.; de la Cruz, M. O.; Schatz, G. C.; Chen, L. X.; Ratner, M. A. *J. Am. Chem. Soc.* **2015**, *137*, 6254-6262.

Chapter 4. Conjugated Trimeric Scaffolds Accessible From Indolyne Cyclotrimerizations: Synthesis, Structures, and Electronic Properties

4.1 Background

Novel conjugated small molecules are highly sought after due to potential applications in organic electronics: light-emitting diodes (OLEDs),[1] field-effect transistors (OFETs),[2] and organic photovoltaic devices (OPVs).[3] Most conjugated materials used in such applications rely on two-directional electron-rich fragments, (e.g., 2,5-disubstituted thiophenes). In contrast, tri-directional conjugated compounds are much less well studied, in part due to limitations in chemical synthesis. Perhaps the most well studied conjugated trimer is triphenylene (**1**) first prepared in 1880[4] (Figure 4.1). Although the synthesis of triphenylene has since been improved, yields are still modest at best. In general, symmetrical and unsymmetrical derivatives of functionalized triphenylene are found in the literature. More recently, indole-based variants **2** and **3** have also been reported.[5] Collectively, **1**–**3** and their functionalized derivatives have been used in two-photon absorption spectroscopy,[6] discotic liquid crystals,[7,8] solar cells,[9,10] OLEDs,[11] and more recently supercapacitors,[12] thus highlighting the importance of these types of trimeric scaffolds. Of particular synthetic and materials interest to our groups is triazatruxene **2**, which serves as donor and hole transport materials in organic and inorganic solar cells,[10] though typical syntheses are lengthy, involving several coupling steps.[13]

Table 4.1. Optimization of Cyclotrimerization

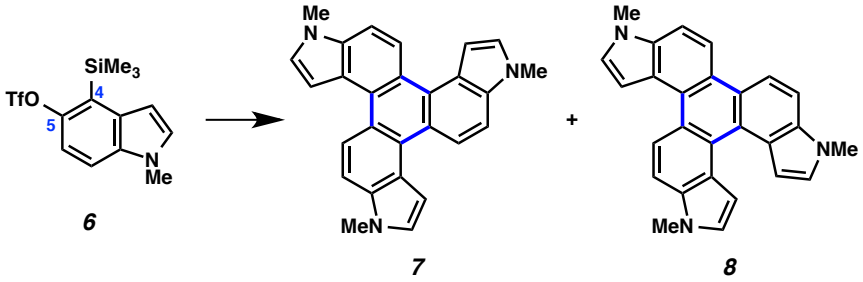

6 *7* *8*

Entry	*Conditions*	*Yield*[a]	*Ratio of 7 to 8*
1	CsF (3 equiv) $Pd(PPh_3)_4$ (20 mol%) MeCN (0.2 M), 35 °C	*34%*	*1 : 2.1*
2	CsF (3 equiv) $Pd(PPh_3)_4$ (20 mol%) MeCN (0.2 M), 50 °C	*46%*	*1 : 2.2*
3	CsF (3 equiv) $Pd(PPh_3)_4$ (20 mol%) MeCN (0.2 M), 65 °C	*39%*	*1 : 2.2*
4	CsF (3 equiv) $Pd(PPh_3)_4$ (20 mol%) MeCN (0.5 M), 50 °C	*85%*[b]	*1 : 2.1*
5	CsF (3 equiv) $Pd(PPh_3)_4$ (20 mol%) MeCN (1.0 M), 50 °C	*48%*	*1 : 2.0*
6	CsF (3 equiv) $Pd(Pt\text{-}Bu_3)_2$ (20 mol%) MeCN (0.5 M), 50 °C	*< 5%*	*N/A*
7	CsF (3 equiv) $Pd(dba)_2$ (10 mol%) BINAP (20 mol%) MeCN (0.5 M), 50 °C	*93%*[b]	*1 : 2.0*

[a] Yield determined by ^1H NMR analysis using 1,3,5-trimethoxybenzene as an external standard. [b] Isolated yields.

With the ultimate goal of accessing a series of hetaromatic trimeric scaffolds using uncommon synthetic transformations, we targeted a new class of indole-based trimers, as suggested by structure **4**. This structure, and isomers that vary by positioning of the pyrrole unit, have never been accessed previously. The Garg lab hypothesized that such motifs could be directly synthesized using an unconventional approach, namely, using the transition metal-

catalyzed trimerization of highly reactive hetarynes[14] (e.g., 4,5-indolyne **5**).[15,16] Though hetaryne chemistry has served as a powerful tool in the synthesis of complex natural products, transition metal-catalyzed reactions of indolynes have not been described previously and, to our knowledge, no examples of hetaryne trimerizations have been reported. We show here the successful trimerization of three isomeric indolynes, which, in turn, permits access to six new bent aromatic indole trimers that display photophysical properties derived from the monomeric building block *N*-methylindole. Excited state calculations were employed to characterize the high-intensity electronic transitions that lead to the observed spectra and to correlate them with the symmetry of the trimers. The extensive use of indolynes in synthetic chemistry will allow for further methodology development to attain easily functionalized trimers previously unattainable through conventional synthetic methods.

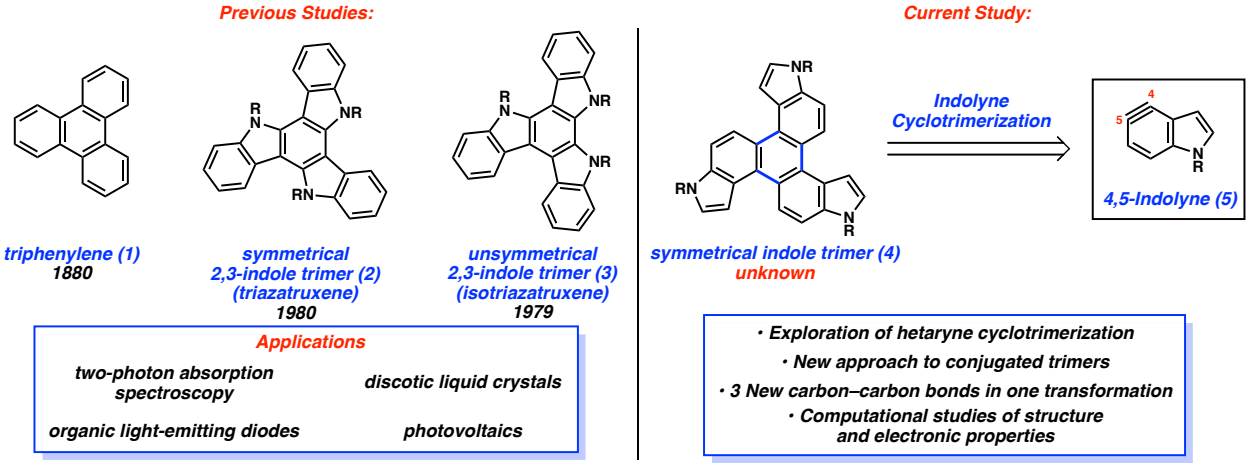

Figure 4.1. Previously studied conjugated trimers 1–3 and indole trimer 4 (present study).

4.2 Synthetic work by the Garg group

Although prior studies have established the feasibility of benzyne trimerization,[17] the corresponding metal-catalyzed union of hetarynes was unknown, as noted above. Thus, our first objective was to elucidate reaction conditions that allow for the trimerization of indolynes to take place. We elected to initially perform trimerization studies using an *in situ*-generated 4,5-indolyne.

As shown in Table 4.1, 4,5-indolyne precursor **6** was subjected to Pd-based conditions to effect trimerization. Initial studies involved the use of $Pd(PPh_3)_4$ as the catalyst, in the presence of CsF in acetonitrile. At 35°C, we were delighted to find that symmetrical trimer **7** and unsymmetrical trimer **8** were obtained in 34% yield, in a 1 : 2.1 ratio, respectively (entry 1), which is very close to the statistical ratio of 1 : 2. Increasing the temperature to 50 °C led to an improvement in yield (entry 2), whereas heating to 65 °C led to only modest change (entry 3). By performing the trimerization at 50 °C and at a concentration of 0.5 M, the yield increased to 85% (entry 4). The use of higher concentrations was less productive (entry 5), as was the use of $Pd(P\textit{t}\text{-}Bu_3)_2$ (entry 6). Finally, by maintaining the optimal temperature and concentration (i.e., 50 °C and 0.5 M), but switching to the use of Pd_2dba_3 and BINAP, isomers **7** and **8** were obtained in 93% yield (entry 7, 1:2 ratio, respectively). It should be noted that the trimerization allows for the formation of three new C–C bonds with excellent efficiency.

Having achieved the trimerization of a 4,5-indolyne, we attempted the corresponding transformation using 5,6- and 6,7-indolyne precursors **9** and **12**, respectively (Figure 2).[15,18] In both cases, the use of $Pd(PPh_3)_4$ gave the most promising results. 5,6-indolyne precursor **9** underwent trimerization to give a 1 : 3 ratio of isomers **10** and **11**, respectively, in 80% yield. The corresponding trimerization of 6,7-indolyne precursor **12** proved much more difficult. Nonetheless, the two desired trimers, **13** and **14**, could be accessed in a 1:1 ratio, albeit in modest yield. The fact that products **13** and **14** are formed to any extent, despite severe steric crowding, highlights the power of indolyne and aryne methodology for the synthesis of highly congested scaffolds.

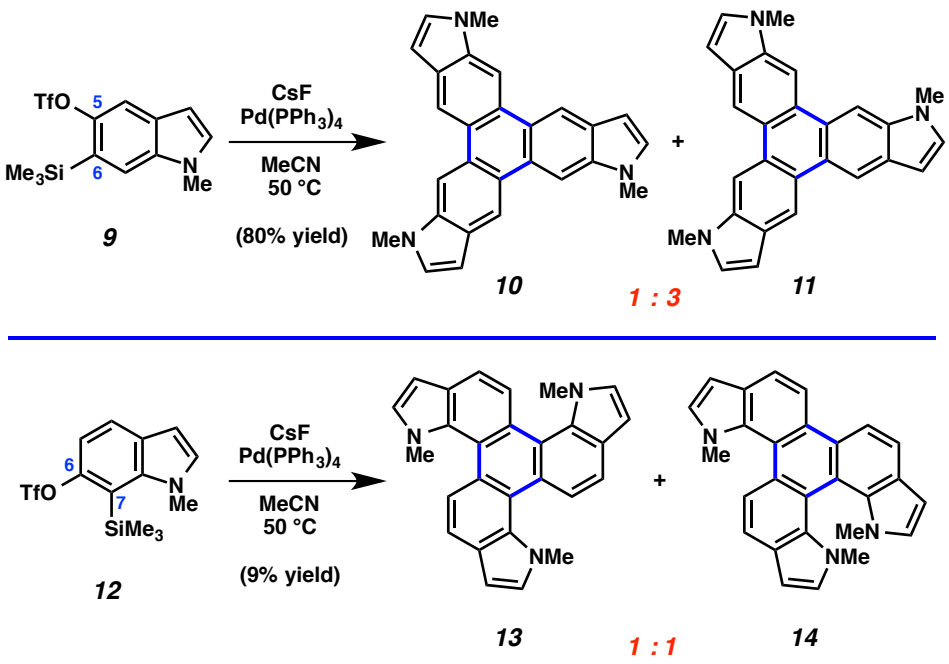

Figure 4.2. Trimerization of indolyne precursors 9 and 12.

4.3 Analysis of computational structures and electronic properties

The novel trimers were inspected by quantum mechanical calculations. The ground state geometry of each compound, **7**, **8**, **10**, **11**, **13**, and **14**, was minimized using density functional theory (DFT) with ωB97X-D[19]/6-31+G(d,p). The lowest energy conformer for each is shown in Figure 4.3, although conformational searches showed that a higher-energy conformer exists for each non-planar trimer (**7'**, **8'**, **13'**, and **14'**). Interestingly, both trimers **7** and **8** arising from 4,5-indolyne are non-planar. In the case of the symmetrical trimer **7**, all three branches are twisted out of planarity (–11, 21, and 21°). For the unsymmetrical trimer **8**, the two symmetrical branches lie largely in the plane of the central arene (only –7° out of plane); however, the unsymmetrical branch is twisted –17 and 30° out of planarity. In both cases, the twisting occurs to relieve steric repulsion between neighboring (*peri*) C–H bonds; a similar distortion is found in the experimental crystal structure of triphenyelene.[20] On the other hand, trimers **10** and **11** derived from the 5,6-indolyne are completely flat, with **10** retaining propeller-like C_3 symmetry, much like the calculated[11b] and experimental[12d] structures of triindole cores in functionalized triazatruxene

derivatives. The most unusual of the trimers are **13** and **14**, derived from the 6,7-indolyne. Both isomers are plagued by severe steric repulsion, due to the trajectory of the *N*-Me substituents. For symmetrical isomer **13**, out of plane twisting helps to alleviate interactions between the *N*-Me substituents and aryl C–H bonds. Trimer **13** twists in a symmetrical manner, where each dihedral is twisted 18° out of plane in the same direction; the unidirectional twisting, unseen in the other non-planar symmetrical trimer **7**, maintains the C_3 symmetry of the molecule. In the case of unsymmetrical isomer **14**, twisting relieves two types of steric interactions: those between two *N*-Me substituents (of neighboring indoles) and interactions between one *N*-Me substituent and proximal aryl C–H bonds. Trimer **14** has the greatest amount of torsional strain, with its dihedrals twisted 37, –17, and -10° out of plane. To our knowledge, **14** is one of the most bent fused heteroaromatic compounds known to date.[21] Although the nitrogens in **7**, **8**, **10**, and **11** are planar, those in **13** and **14** are slightly pyrimidalized, indicating that significant twisting in the structures results in less π-orbital overlap.

The distorted nature of the trimers correlates with the relative free energies of the molecules. Due to the steric repulsion, trimers **7** and **8** are 5.2 and 5.5 kcal mol^{-1} higher in energy compared to planar trimer **10**. The unsymmetrical counterpart to **10**, **11**, is only slightly higher in energy (0.8 kcal mol^{-1}). Lastly, the extremely distorted 6,7 indolyne trimers **13** and **14** are significantly higher in energy compared to **10**, with relative free energies of 20.0 and 15.8 kcal mol^{-1}, respectively. These relative energies may be corrected to be strain energies with respect to **10**.

An analysis of the electronic properties of the trimers was performed by analysis of the frontier molecular orbitals (FMOs) of each trimer. The energy levels for the highest occupied molecular orbital (HOMO) and lowest unoccupied molecular orbital (LUMO) are given in Figure 4.3. The HOMO energy levels of each trimer are approximately equal (–6.8 to –6.7 eV), while the LUMO energy levels vary. For the 4,5- and 5,6-trimers, the HOMO level of the symmetrical trimer

(0.8 and 0.9 eV for **7** and **10**, respectively) is higher in energy than the HOMO level of its corresponding unsymmetrical counterpart (0.6 and 0.8 eV for **8** and **11**, respectively). Interestingly, though **13** and **14** are highly distorted out of planarity, the LUMO energy levels for each are 0.5 eV. The lower HOMO-LUMO gaps of the 6,7-trimers are surprising, since visual inspection of plotted orbitals shows that the LUMOs are delocalized approximately to the same degree for each trimer.

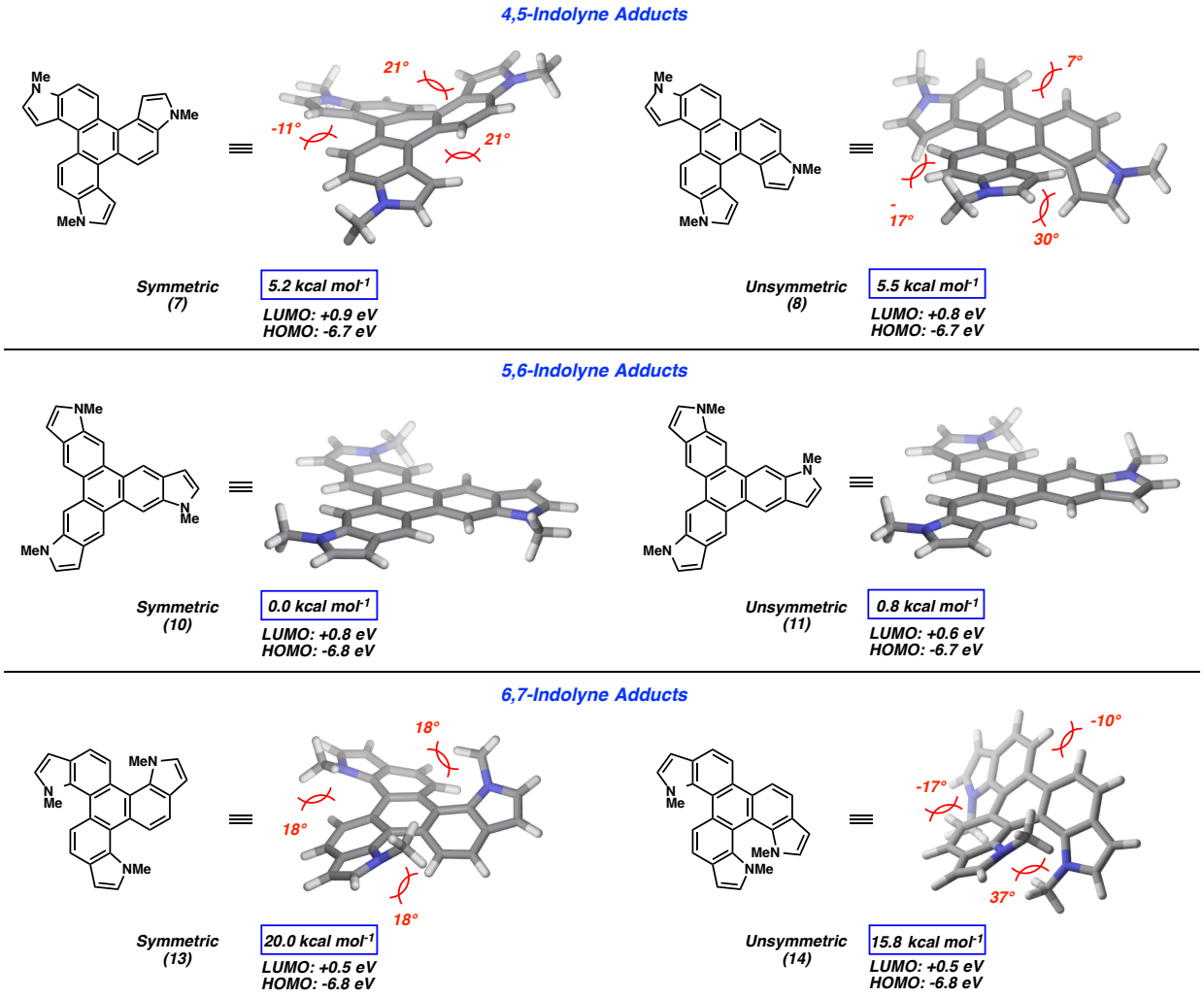

Figure 4.3. Geometry-optimized structures and computed properties.
Energies in boxes are relative free energies. HOMO and LUMO energy levels are given in eV.

4.4 Photophysical properties of trimers

With the six new indole trimers in hand, we performed measurements of various photophysical properties in order to investigate the potential of these planar and non-planar molecules in optoelectronic applications. Figure 4.4 highlights UV-Vis absorption and fluorescence emission data. Compared to the absorption of parent triphenylene, which absorbs from 240 to 340 nm,[22] the absorbance of the trimers is broader and λ_{max} is red-shifted to longer wavelength, absorbing from 200 to 400 nm, which is similar to the absorption of the 2,3-analog *N*-methyl-triazatruxene.[10b] While the λ_{max} for both absorption and fluorescence curves vary slightly between trimers, in general the molecules absorb in a characteristic manner, exhibiting two strong bands with varying vibronic structure. The first band ranges from around 280 to 330 nm, with a shoulder at longer wavelength, and the second sharper peak ranges from 200 to 250 nm. This absorption pattern is matched in computed UV-Vis spectra, which will be discussed in the next section.

The optical behavior of **7** and **8** are similar; each absorbs strongly to give two peaks (310 and 233 nm, 298 and 229, respectively). Trimers **10** and **11** also each exhibit two dominant peaks at similar wavelengths (292 nm and 225 nm, 280 and 239 nm, respectively). The differences in shape and oscillator strength of these two pairs of trimers are heavily influenced by vibrational structure, related to differences in symmetry and planarity. On the other hand, the spectra of **13** and **14** are similar in shape and intensity, and both exhibit strongest absorbance at 321 and 328 nm, respectively. At 217 and 220 nm, both trimers exhibit a peak of lesser intensity. Although **13** is C_3-symmetric while **14** is unsymmetrical, the optical properties of the two closely resemble each other. The red-shift of the maximum absorption peaks of **13** and **14** is in line with the lower computed HOMO-LUMO gaps. The data suggest that while the electronic properties of the six regioisomers vary with different connectivity, they involve similar transitions characteristic of the indole π-systems.

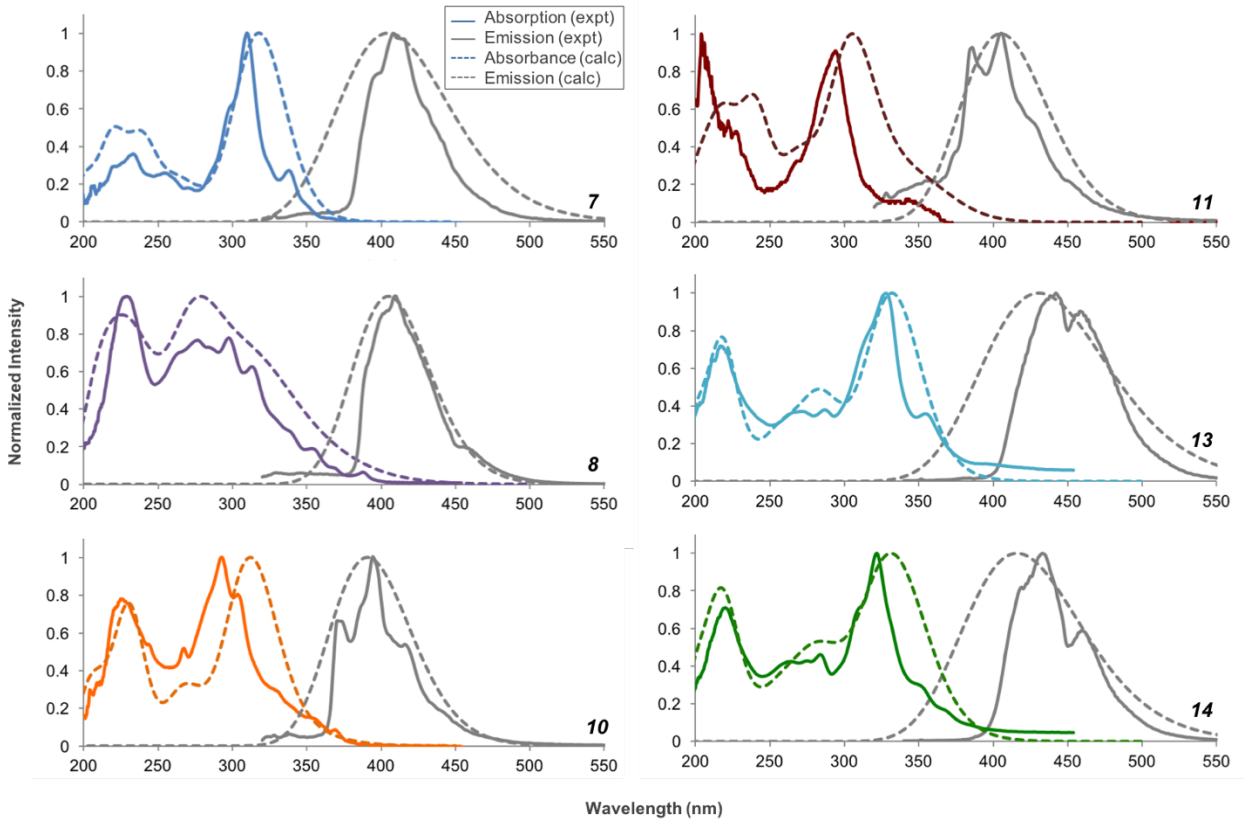

Figure 4.4. UV-Vis absorption and fluorescence emission spectra for in methylcyclohexane.

Fluorescence emission band structures are also similar, with both **7** and **8** displaying an emission band at roughly 410 nm. Similar variations are seen when comparing the symmetrical and unsymmetrical trimers of the 5,6-indolyne with similar band shapes. The λ_{max} for the symmetrical isomer **10** is 291 nm, whereas the λ_{max} for unsymmetrical isomer **11** is 235 nm. Fluorescence emission bands are roughly 400 nm for each trimer derived from the 5,6-indolyne. Finally, the band shapes of both UV-Vis and fluorescence spectra match well for the two trimers derived from the 6,7-indolyne. Both isomers, **13** and **14**, display a λ_{max} of roughly 320 nm, along with fluorescence emissions bands around 433 nm. Again, the emission maxima for **13** and **14** are red-shifted compared to those of the other four trimers.

Surprisingly, the λ_{max} of both planar molecules **11** and **12** are not at longer wavelength than the other four trimers, all of which are torsionally distorted out of plane. Instead, **13** and **14,** structures that are most twisted out of plane, exhibit longer wavelength $\lambda_{max,}$ an indication that the LUMO is stabilized more than the HOMO, or the HOMO is destabilized more than the LUMO, by distortion. Except for **13** and **14**, absorbance spectra vary between the symmetrical and unsymmetrical trimer in each pair, while band shapes of emission spectra are similar for each pair.

4.5 Excited state calculations

Understanding the origin of optical properties is critical in the design of materials for optoelectronic applications, especially absorbance and photoluminescence, which are important properties in OPVs, OLEDs, photodiodes, and laser diodes. Thus, we embarked on a computational study using time-dependent density functional theory (TD-DFT) to form a quantitative link between the electronic structures and absorbance properties of the trimers. TD-DFT was also used recently by Thomas *et al.*[23] to compute the electronic spectrum of the triazatruxene radical cation. In this study, TD-DFT with B3LYP[24]/6-31+G(d,p) was employed to compute the first 100 lowest excitation energies and oscillator strengths of each trimer. Each peak was fit to a Gaussian function and summation of each Gaussian produced a spectral prediction, which shows good agreement with experimental data in terms of matched frequencies (Figure 4.3). Detailed analysis of the excitations shows that each trimer gives six major excitations with high oscillator strengths in the UV-Vis region of the spectrum. The six excitations occur in pairs of degenerate or non-degenerate states, depending on the symmetry of the molecule. For each C_3-symmetric conformer of the symmetric trimers (**7'**, **10**, and **13)**, there are three sets of doubly degenerate excitations, which are exactly equal in energy, in oscillator strength, and in amplitudes of orbital contributions to the transitions (Figure 4.5a). The unsymmetrical trimers give three sets of excitations that, although non-degenerate, also occur in pairs. As the symmetry of the molecule

decreases (i.e., conversion of **7'** to **7**), the degeneracy of the pairs also decreases. The set of degenerate transitions that is lowest in energy occurs in the 300-330 nm range (*1a* and *1b* in Fig. 5a). Equal contributions to the states from HOMO to LUMO+1 and HOMO-1 to LUMO transitions are consistent with the fact that HOMO and HOMO-1 orbitals are degenerate and LUMO and LUMO+1 orbitals are degenerate. Two additional higher energy degenerate transitions are also observed around 270-300 nm (*2a* and *2b*), and the final two degenerate transitions are seen between 220-230 nm (*3a* and *3b*). As expected, as the excited states increase in energy, the range of orbitals that contribute to the states expands due to delocalization of electron density within these conjugated structures.

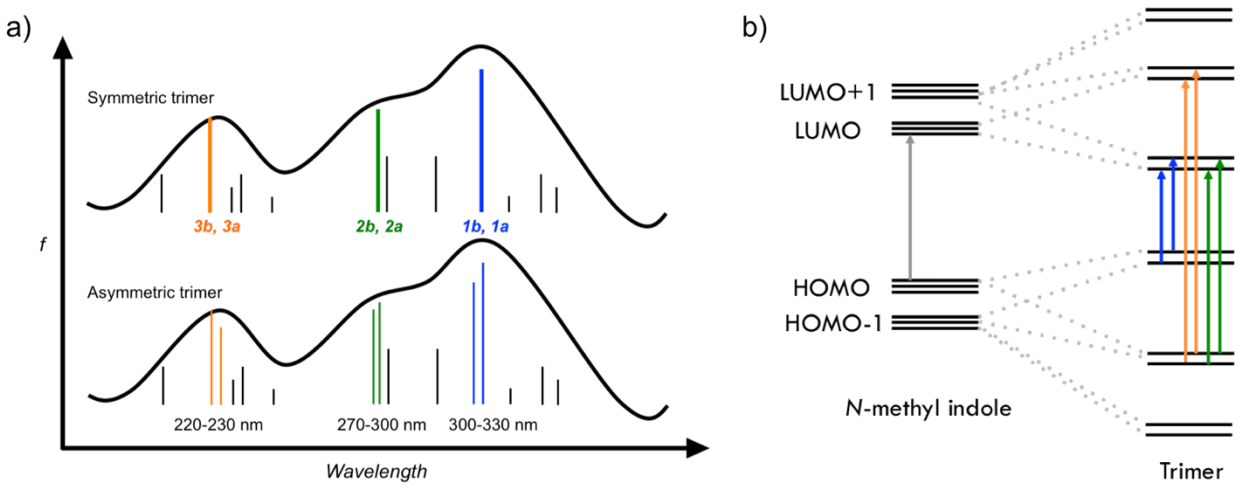

Figure 4.5. Absorption behaviour of trimers.
(a) Schematic of calculated excitations from a typical TD-DFT calculation plotted as oscillator strength vs. wavelength. Gaussian-fitted spectra in black. (b) Schematic of energy diagram depicting orbital splitting that results from trimerization of *N*-methylindole.

We further characterized the excited states *1a* and *2a* for each trimer using Natural Transition Orbital (NTO) analysis[25] in order to simplify the range of configurations obtained from TD-DFT to a physically significant and understandable description of the dominant electronic excitations. For excited states that are described by a large number of configurations with no single dominant component, NTO serves as a means to simplify the electronic transition density matrix to a compact orbital representation via diagonalization of the matrix and determination of

the natural orbitals that contribute to the transition. For the trimers, this resulted in a pair of transitions that give physical insight into the change in electron densities that occurs. Visualization of excited states by NTO analysis is useful for understanding the symmetry of a transition and charge transfer mechanisms, and has been employed in the study of absorbing properties of chromophores such as $[Ru(bpy)^3]^{2+}$ and stability of Pt catalysts.[26,27]

NTO analysis was performed on each of the six high intensity *1a* and *2a* peaks, showing that each peak arises from a mixture of HOMO to LUMO and HOMO-1 to LUMO+1 transitions. The two pairs of NTOs for *1a* are degenerate or nearly degenerate. In the case of **10**, HOMO to LUMO and HOMO-1 and LUMO+1 transitions give equal contributions of 0.48 to the excited state of highest intensity (306 nm, *f*=0.68). However, for its unsymmetrical counterpart, **11**, the contributions differ for its excitation of highest intensity (301 nm, *f*=0.51). The HOMO to LUMO transition contributes 0.66, and the HOMO-1 to LUMO+1 transition gives a value of 0.30. This pattern was found for each pair of trimers derived from the 4,5-, 5,6-, and 6-7-indolynes.

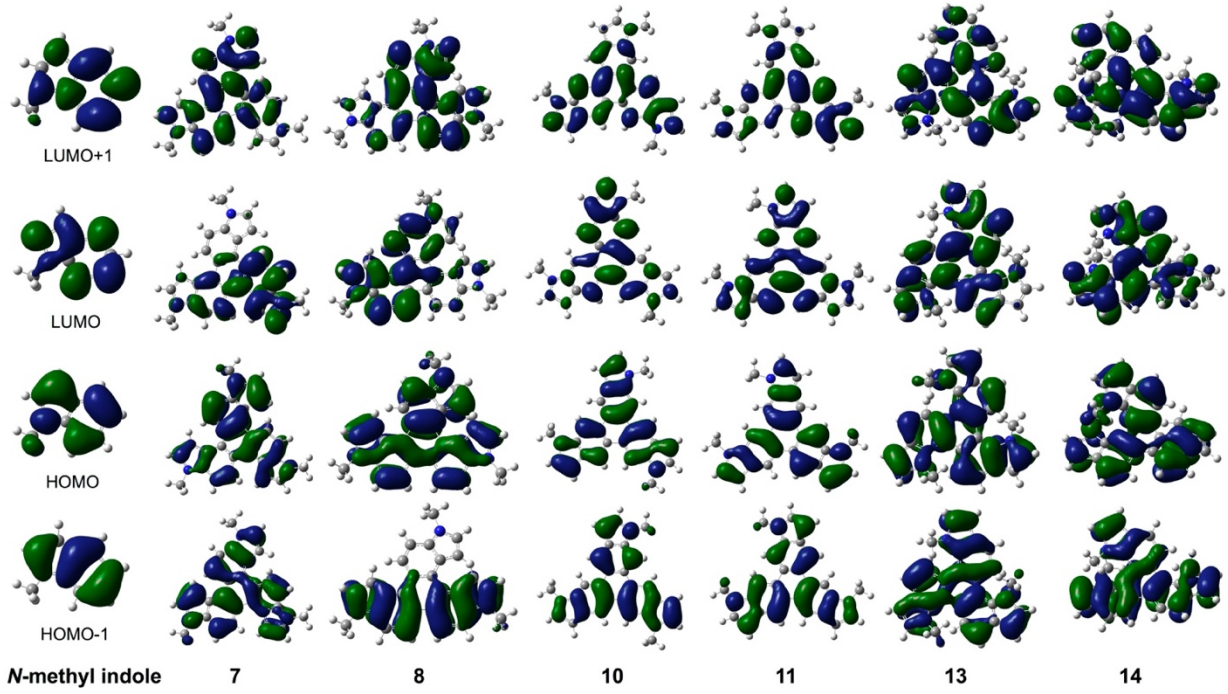

Figure 4.6. NTO orbitals of the orbitals of interest for excitation *1a* in 7, 8, 10, 11, 13, 14 and for analogous excitation in *N*-methylindole.

From NTO analysis, we determined that the HOMO and HOMO-1 orbitals in the trimers that are important in the optical transition are comprised of linear combinations of the HOMO and HOMO-1 orbitals of *N*-methylindole (Figure 4.6). Similarly, the LUMO and LUMO+1 orbitals in the trimers are made up of linear combinations of the LUMO and LUMO+1 orbitals of *N*-methylindole. These results show that the orbitals of interest for the high intensity transitions are additive from those in its building block. The HOMO to LUMO orbitals mix to form degenerate (or nearly degenerate, in the case of the asymmetric trimers) states in the trimers, and the FMOs of the trimers retain the nodal properties of the FMOs in *N*-methylindole due to a linear combination of the *N*-methylindole orbitals to form the trefoil core. Similar additivity is demonstrated with NTO analysis for excitation *2a*, which shows that the FMOs relevant in excitation *2a* are comprised of a different combination the FMOs of *N*-methylindole. From this analysis, we can infer that upon trimerization of *N*-methylindole, the three sets of indole FMOs mix to form orbitals of both higher and lower energy in the corresponding trimer, as depicted in Figure 4.5b.

Finally, we investigated the emissive properties of the trimers. As mentioned previously, the absorption and emission maxima of the 6,7-trimers (**13** and **14**) are noticeably red-shifted relative to the other trimers, a pattern that in line with the lower HOMO-LUMO gaps are shown in Figure 4.3. In order to probe the extent to which the excited states of **13** and **14** relax to give the greater red shift, TD-DFT was used to obtain relaxed geometries of the lowest excited state of each of the six trimers. The planarity of the excited state structures does not deviate much from the corresponding ground states (< 5° change in C-C-C-C dihedrals), though the bond length alternation pattern reverses. The bond lengths of the central benzene ring are denoted for the ground state and excited states for each trimer in Figure 4.7. In general, for each of the ground states, the newly forged C-C bond (in blue) has more single-bond character, while the other corresponding C-C bond (in black) has more double-bond character. Upon excitation, this bond length alternation (BLA) pattern reverses, and the blue bond has more double bond character

than the black bond. BLA can be defined as the average of the difference in length between adjacent carbon-carbon bonds in a hydrocarbon; BLA was calculated for the central benzene ring in each trimer and denoted in Figure 4.7. In general, each ground state exhibit higher BLA (0.3-0.4 Å) than the corresponding excited state (0.2-0.3 Å), indicating that delocalization of electrons increases in the excited state. The reversal of BLA (which is also seen in triphenylene) is consistent for each of the trimers regardless of the degree of planarity in the ground state, which indicates that the trimers behave in a similar manner upon excitation.

Finally, an energy calculation was performed in order to obtain the emission energy. Each lowest energy emission was fit to a Gaussian band and is shown in Figure 4.4, closely fitting experimental emission spectra. The band shapes of the calculated and experimental spectra vary due to fine vibrational structure, but the matching of the peaks is strong indication of the utility of TD-DFT in predicting the wavelength of maximum emission and broadening in fluorescence spectra for these types of materials.

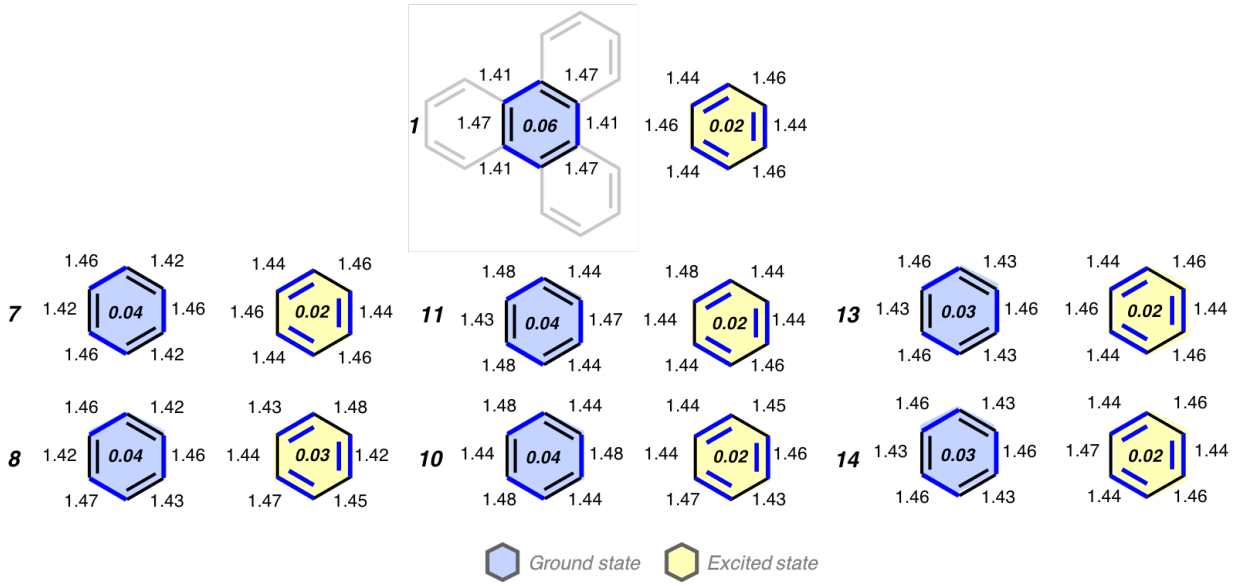

Figure 4.7. Bond length alternation in ground and excited states.
Bond length changes of the central benzene ring in the ground and excited states of triphenylene (**1**) and of each trimer. The complete structure of **1** is shown for clarity. Bond lengths of the newly forged C–C bond (blue) and the corresponding C–C bond derived from indolyne (black) are labelled, and BLA values are shown in the center of each ring (both are given in Å).

4.6 Conclusions

We have designed and synthesized a new class of indole-based conjugated trimers to be used as the core of electronic materials. Our approach to these unique scaffolds relies on the *in situ* generation of highly reactive indolyne intermediates, which undergo Pd-catalyzed cyclotrimerization. The process results in the formation of three new C–C bonds and has proven useful to prepare six previously unknown trimers. Several of the trimers are severly bent out of planarity to alleviate steric interactions, as shown by computational studies. The electronic and optical properties of these species are heavily influenced by structure; interestingly, the most distorted structures have low calculated HOMO-LUMO gaps, and absorb and emit at longer wavelengths. Excited state calculations show that the optical properties of the trimers are linked to the properties of the *N*-methylindole building block and behave in similar manners in the excited state. Interestingly, although **13** and **14** are highly bent molecules, the intrinsic HOMO-LUMO gaps are lower than the planar derivatives. Access to a new class of conjugated trimers, including several highly bent heteroaromatic compounds, through the first example of transition metal-catalyzed trimerization of indolynes is reported. Further investigations of the photophysical properties of the trimers are underway, and applications of substituted derivatives in organic electronics will be forthcoming.

4.7 References

[1] (a) Kulkarni, A. P.; Tonzola, C. J.; Babel A.; Jenekhe, S. A. *Chem. Mater.* **2004**, *16*, 4556–4573. (b) Duan, L.; Hou, L.; Lee, T.-W.; Qiao, J.; Zhang, D.; Dong, G.; Wang, L.; Qiu, Y. *J. Mater. Chem.* **2010**, *20*, 6392–6407. (c) Tao, Y.; Yang, C.; Qin, J. *Chem. Soc. Rev.* **2011**, *40*, 2943–2970. (d) Yu, T.; Liu, L; Xie, Z; Ma, Y. *Sci. China Chem.* **2015**, *58*, 907–915.

[2] (a) Mas-Torrent, M.; Rovira, C. *Chem. Soc. Rev.* **2008**, *37*, 827–838. (b) Allard, S.; Forster, M.; Souharce, B.; Thiem, H.; Scherf, U. *Angew. Chem., Int. Ed.* **2008**, *47*, 4070–4098. (c) Sirringhaus, H. *Adv. Mater.* **2014**, *26*, 1319–1335. (d) Back, J. Y.; Kim, Y.; An, T. K.; Kang, M. S.; Kwon, S.-K.; Park, C. E.; Kim, Y.-H. *Dyes Pigments* **2015**, *112*, 220–226.

[3] (a) Mishra, A.; Bäuerle, P. *Angew. Chem., Int. Ed.* **2012**, *51*, 2020–2067. (b) Lin, Y.; Li, Y.; Zhan, X. *Chem. Soc. Rev.* **2012**, *41*, 4245–4272. (c) Roncali, J.; Leriche, P.; Blanchard, P. *Adv. Mater.* **2014**, *26*, 3821–3838.

[4] Schmidt, H.; Schultz, G. *Justus Liebigs Ann. Chem.* **1880**, *203*, 118–137.

[5] (a) H. Muller, PhD thesis, University of Heidelberg, 1964. (b) Kaneko, T.; Matsuo, M. *Heterocycles* **1979**, *12*, 471–474. (c) Bergman, J.; Eklund, N. *Tetrahedron* **1980**, *36*, 1439–1443. (d) Bergman, J.; Eklund, N. *Tetrahedron* **1980**, *36*, 1445–1450.

[6] For studies on triazatruxene as two-photon absorption chromophores, see: (a) Ji, L.; Fang, Q.; Yuan, M.-s.; Liu, Z.-q.; Shen, Y.-x.; Chen, H.-f. *Org. Lett.* **2010**, *12*, 5192–5195. (b) Shao, J.; Guan, Z.; Yan, Y.; Jiao, C.; Xu, Q.-H.; Chi, C. *J. Org. Chem.* **2010**, *76*, 780–790.

[7] For a review on triphenylene-based discotic liquid crystals, see: Pal, S. K.; Setia, S.; Avinash, B. S.; Kumar, S. *Liq. Cryst.* **2013**, *40*, 1769–1816.

[8] For studies on triazatruxene-based discotic liquid crystals, see: (a) Gómez-Lor, B.; Alonso, B.; Omenat, A.; Serrano, J. L. *Chem. Commun.* **2006**, 5012–5014. (b) Talarico, M.; Termine, R.; García–Frutos, E. M.; Omenat, A.; Serrano, J. L.; Gómez-Lor, B.; Golemme, A. *Chem. Mater.* **2008**, *20*, 6589–6591. (c) García–Frutos, E. M.; Gómez-Lor, B. *J. Am Chem. Soc.* **2008**, *130*,

9173-9177. (d) García–Frutos, E. M.; Gutierrez-Puebla, E.; Monge, M. A.; Ramírez, R.; de Andrés, P.; de Andrés, A.; Ramírez, R.; Gómez-Lor, B. *Org. Electron.* **2009**, *10*, 643–652. (e) García–Frutos, E. M.; Hennrich, G.; Gutierrez, E.; Monge, A.; Gómez-Lor, B. *J. Org. Chem.* **2010**, *75*, 1070-1076. (f) Zhao, B.; Liu, B.; Png, R. Q.; Zhang, K.; Lim, K. A.; Luo, J.; Shao, J.; Ho, P. K. H.; Chi, C.; Wu, J. *Chem. Mater.* **2010**, *22*, 435–449. (g) Ye, Q.; Chang, J.; Chi, C. *J. Mater. Chem.* **2012**, *22,* 13180-13186.

[9] For recent studies on triphenylene based solar cells, see: (a) KR Pat., KR20110098302, 2011. (b) WO Pat., WO2012048781, 2012. (c) Bajpai, M.; Yadav, N.; Kumar, S.; Srivastava, R. Dhar, R. *Liq. Cryst.* **2016**, *43*, 928-936.

[10] For studies on triazatruxene based solar cells, see: (a) Bura, T.; Leclerc, N.; Fall, S.; Lévêque, P. Heiser, T.; Ziessel, R. *Org. Lett.* **2011**, *13*, 6030–6033. (b) Shelton, S. W.; Chen, T. L.; Barclay, D. E.; Ma, B. *ACS Appl. Mater. Interfaces* **2012**, *4*, 2534–2540. (c) Kulshreshtha, C.; Kim, G. W.; Lampande, R.; Huh, D. H.; Chae, M.; Kwon, J. H. *J. Mater. Chem. A* **2013**, *1,* 4077-4082. (d) Qian, X.; Zhu, Y.-Z.; Song, J.; Gao, X.-P.; Zheng, J.-Y. *Org. Lett.* **2013**, *15,* 6034-6037. (e) Rakstys, K.; Abate, A.; Dar, M. I.; Gao, P.; Jankauskas, V.; Jacopin, G.; Kamarauskas, E.; Kazim, S.; Ahmad, S.; Grätzel, S.; Nazeeruddin, M. K. *J. Am. Chem. Soc.* **2015**, *137*, 16172–16178. (f) Ramo, F. J.; Rakstys, K.; Kazim, S.; Grätzel, M.; Nazeeruddin, M. K.; Ahmad, S. *RSC Adv.* **2015**, *5,* 53426-3432. (g) Li, X.-C.; Wang, C.-Y.; Lai, W.-Y.; Huang, W. *J. Mater. Chem. C* **2016**, *4*, 10574-10587. (h) Calió, L.; Kazim, S.; Grätzel, M.; Ahmad, S. *Angew. Chem., Int. Ed.* **2016**, *55,* 14522-14545. (i) Su, P.-Y.; Huang, L.-B.; Liu, J.-M.; Chen, Y.-F.; Xiao, L.-M.; Kuang, D.-B.; Mayor, M.; Su, C.-Y. *J. Mater. Chem. A.* **2017**, *5*, 1913–1918.

[11] For a study on triazatruxene-based materials for organic light-emitting diodes, see: (a) Levermore, P. A.; Xia, R.; Lai, W.; Wang, X. H.; Huang, W.; Bradley, D. D. C. *J. Phys. D: Appl. Phys.* **2007**, *40,* 1896-1901. (b) Lai, W.-Y.; He, Q.-Y.; Zhu, R.; Chen, Q.-Q.; Huang, W. *Adv. Funct. Mater.* **2008**, *18*, 265–276. (c) Zhang, Z.-L.; Zou, L.-Y.; Ren, A.-M.; Liu, Y.-F.; Feng, J.-

K.; Sun, C.-C. *Dyes and Pigments* **2013**, *96,* 349–363. (d) Kim, G. W.; Lampande, R.; Choe, D. C.; Bae, H. W.; Kwon, J. H. *Thin Solid Films* **2015**, *589*, 105–110.

[12] For study on triazatruxene based supercapacitors, see: Li, X.-C.; Zhang, Y.; Wang, C.-Y.; Wan, Y.; Lai, W.-Y.; Pang, H.; Huang, W. *Chem. Sci.* **2017**, *8*, 2959–2965.

[13] For synthetic studies of triazatruxene, isotriazatruxene, and their functionalized derivatives, see: (a) Bergman, J.; Eklund, N. *Tetrahedron* **1980***, 36*, 1439–1443. (b) Bergman, J.; Eklund, N. *Tetrahedron* **1980***, 36,* 1445–1450. (c) Eissenstat, M. A.; Bell, M. R.; D'Ambra, T. E.; Alexander, E. J.; Daum, S. J.; Ackerman, J. H.; Gruett, M. D.; Kumar, V.; Estep, K. G.; Olefirowicz, E. M.; Wetzel, J. R.; Alexander, M. D.; Weaver, J. D.; Haycock, D. A.; Luttinger, D. A.; Casiano, F. M.; Chippari, S. M.; Kuster, J. E.; Stevenson, J. I.; Ward, S. J. *J. Med. Chem.* **1995***, 38,* 3094–3105. (d) Robertson, N.; Parsons, S.; MacLean, E. J.; Coxall, R. A.; Mount, A. R. *J. Mater. Chem.* **2000***, 10*, 2043–2047.

[14] For reviews of arynes and hetarynes, see: (a) Kauffmann, T. *Angew. Chem., Int. Ed. Engl.* **1965**, *4*, 543–618. (b) Reinecke, M. G. *Tetrahedron* **1982**, *38*, 427–498. (c) Pellissier, H.; Santelli, M. *Tetrahedron* **2003**, *59*, 701–730. (d) Wenk, H. H.; Winkler, M.; Sander, W. *Angew. Chem., Int. Ed.* **2003**, *42*, 502–528. (e) Sanz, R. *Org. Prep. Proced. Int.* **2008**, *40*, 215–291. (f) Bronner, S. M.; Goetz, A. E.; Garg, N. K. *Synlett* **2011**, 2599–2604. (g) Tadross, P. M.; Stoltz, B. M. *Chem. Rev.* **2012**, *112*, 3550–3557. (h) Gampe, C. M.; Carreira, E. M. *Angew. Chem., Int. Ed.* **2012**, *51*, 3766–3778. (i) Bhunia, A.; Yetra, S. R.; Biju, A. T. *Chem. Soc. Rev.* **2012**, *41*, 3140–3152. (j) Yoshida, H.; Takaki, K. *Synlett* **2012**, 1725–1732. (k) Dubrovskiy, A. V.; Markina, N. A.; Larock, R. C. *Org. Biomol. Chem.* **2013**, *11*, 191–218. (l) Wu, C.; Shi, F. *Asian J. Org. Chem.* **2013**, *2*, 116–125. (m) Goetz, A. E.; Garg, N. K. *J. Org. Chem.* **2014**, *79*, 846–851. (n) Goetz, A. E.; Shah, T. K.; Garg, N. K. *Chem. Commun*. **2015**, *51*, 34–45.

[15] For seminal studies on indolynes, see: (a) Julia, M.; Goffic, F. L.; Igolen, J.; Baillarge, M. *C. R. Acad. Sci., Ser. C* **1967**, *264*, 118–120. (b) Julia, M.; Huang, Y.; Igolen, J. *C. R. Acad. Sci., Ser.*

C **1967**, *265*, 110–112. (c) Igolen, J.; Kolb, A. *C. R. Acad. Sci., Ser. C* **1969**, *269*, 54–56. (d) Julia, M.; Igolen, J.; Kolb, M. *C. R. Acad. Sci., Ser. C* **1971**, *273*, 1776–1777.

[16] For select studies involving indolynes, see: (a) Buszek, K. R.; Luo, D.; Kondrashov, M.; Brown, N. VanderVelde, D. *Org. Lett.* **2007**, *9*, 4135–4137. (b) Brown, N.; Luo, D.; VanderVelde, D.; Yang, S.; Brassfield, A.; Buszek, K. R. *Tetrahedron Lett.* **2009**, *50*, 63–65. (c) Bronner, S. M.; Bahnck, K. B.; Garg, N. K. *Org. Lett.* **2009**, *11*, 1007–1010. (d) Garr, A. N.; Luo, D.; Brown, N.; Cramer, C. J.; Buszek K. R.; VanderVelde, D. *Org. Lett.* **2010**, *12*, 96–99. (e) Cheong, P. H.-Y.; Paton, R. S.; Bronner, S. M.; Im, G.-Y. J.; Garg, N. K.; Houk, K. N. *J. Am. Chem. Soc.* **2010**, *132*, 1267–1269. (f) Im, G.-Y. J.; Bronner, S. M.; Goetz, A. E.; Paton, R. S.; Cheong, P. H.-Y.; Houk, K. N.; Garg, N. K. *J. Am. Chem. Soc.* **2010**, *132*, 17933–17944. (g) Thornton, P. D.; Brown, N.; Hill, D.; Neuenswander, B.; Lushington, G. H.; Santini, C.; Buszek, K. R. *ACS Comb. Sci.* **2011**, *13*, 443–448. (h) Candito, D. A.; Dobrovolsky, D.; Lautens, M. *J. Am. Chem. Soc.* **2012**, *134*, 15572–15580. (i) Nerurkar, A.; Chandrasoma, N.; Maina, L.; Brassfield, A.; Luo, D.; Brown, N. Buszek, K. R. *Synthesis* **2013**, *45*, 1843–1852. (j) Picazo, E.; Houk, K. N.; Garg, N. K. *Tetrahedron Lett.* **2015**, *56*, 3511–3514.

[17] (a) Peña, D.; Escudero, S.; Pérez, D.; Guitián, E.; Castedo, L. *Angew. Chem., Int. Ed.* **1998**, *37*, 2659–2661. (b) Peña, D.; Pérez, D.; Guitián, E.; Castedo, L. *J. Am. Chem. Soc.* **1999**, *121*, 5827–5828. (c) Peña, D.; Pérez, D.; Guitián, E.; Castedo, L. *Org. Lett.* **1999**, *1*, 1555–1557. (d) Peña, D.; Cobas, A.; Pérez, D.; Guitián, E. Castedo, L. *Org. Lett.* **2000**, *2*, 1629–1632. (e) Peña, D.; Cobas, A.; Pérez, D.; Guitián, E.; Castedo, L. *Org. Lett.* **2003**, *5*, 1863–1866. (f) Iglesias, B.; Cobas, A.; Pérez, D.; Guitián, E.; *Org. Lett.* **2004**, *6*, 3557–3560. (g) Romero, C.; Peña, D.; Pérez, D.; Guitián, E. *Chem. Eur. J.* **2006**, *12*, 5677–5684. (h) Wang, Y.; Stretton, A. D.; McConnell, M. C.; Wood, P. A.; Parsons, S.; Henry, J. B.; Mount, A. R.; Galow, T. H. *J. Am. Chem. Soc.* **2007**, *129*, 13193–13200. (i) Peña, D.; Pérez, D.; Guitián, E. *Chem. Rec.* **2007**, *7*, 326–333. (j) Romero, C.; Peña, D.; Pérez, D.; Guitián, E. *J. Org. Chem.* **2008**, *73*, 7996–8000.

(k) Yin, J.; Qu, H.; Zhang, K.; Luo, J.; Zhang, X.; Chi, C.; Wu, J. *Org. Lett.* **2009**, *11*, 3028–3031. (l) Lynett, P. T.; Maly, K. E.; *Org. Lett.* **2009**, *11*, 3726–3729. (m) Peña, D.; Pérez, D.; Guitián, E. *Org. Biomol. Chem.* **2010**, *8*, 3386–3388. (n) Alonso, J. M.; Díaz-Álvarez, A. E.; Criado, A.; Pérez, D.; Peña, D. Guitián, E. *Angew. Chem., Int. Ed.* **2012**, *51*, 173–177. (o) García-López, J.-A.; Greaney, M. F. *Org. Lett.* **2014**, *16*, 2338–2341. (p) Chen, L.; Zhang, C.; Wen, C.; Zhang, K.; Liu, W.; Chen, Q. *Catal. Commun.* **2015**, *65*, 81–84. (q) Dong, Y.; Li, Y.; Wei, Y.-L.; Wang, J.-C.; Ma, J.-P.; Ji, J.; Yao, B.-J.; Dong, Y.-B. *Chem. Commun.* **2016**, *52*, 10505–10508.

[18] The 2,3-indolyne has yet to be accessed synthetically. For pertinent studies, see: (a) Conway, S. C.; Gribble, G. W. *Heterocycles* **1992**, *34*, 2095–2108. (b) Goetz, A. E.; Bronner, S. M.; Cisneros, J. D.; Melamed, J. M.; Paton, R. S.; Houk, K. N.; Garg, N. K. *Angew. Chem. Int. Ed.* **2012**, *51*, 2758-2762.

[19] Chai, J.-D.; Head-Gordon, M. *Phys. Chem. Chem. Phys.* **2008**, *10*, 6615−6620.

[20] Ahmed, F. R.; Trotter, J. *Acta Cryst.* **1963***, 16*, 503–508.

[21] Non-planar aromatic compounds are currently being sought after for new opportunities in materials chemistry. For recent examples, see: (a) Zhang, Q.; Peng, H.; Zhang, G.; Lu, Q.; Chang, J.; Dong, Y.; Shi, X.; Wei, J. *J. Am. Chem. Soc.* **2014**, *136*, 5057-5064. (b) Ball, M.; Zhong, Y.; Wu, Y.; Schenck, C.; Ng, F.; Steigerwald, M.; Xiao, S.; Nuckolls, C. *Acc. Chem. Res.* **2015***, 48,* 267-276. (c) Fujikawa, T.; Segawa, Y.; Itami, K. *J. Am. Chem. Soc.* **2015**, *137*, 7763–7768. (d) Fujikawa, T.; Segawa, Y.; Itami, K. *J. Am. Chem. Soc.* **2016**, *138*, 3587–3595. (e) Davy, N. C.; Man, G.; Kerner, R. A.; Fusella, M. A.; Purdum, G. E.; Sezen, M.; Rand, B. P.; Kahn, A.; Loo, Y.-L. *Chem. Mater.* **2016***, 28,* 673-681. (f) Fujikawa, T.; Mitoma, N.; Wakamiya, A.; Saeki, A.; Segawa, Y.; Itami, K. *Org. Biomol. Chem.* **2017**, DOI: 10.1039/C7OB00987A.

[22] National Institute of Standards & Technology Chemistry Webook. http://webbook.nist.gov (accessed May 18, 2017).

[23] Thomas, T. G.; Shekar, S. C.; Swathi, R. S.; Gopidas, K. R. *RSC Adv.* **2017**, *7,* 821-825.

[24] (a) Becke, A. D. *J. Chem. Phys.* **1993**, *98*, 5648−5652. (b) Lee, C.; Yang, W.; Parr, R. G. *Phys. Rev. B* **1988**, *37*, 785−789. (c) Stephens, P. J.; Devlin, F. J.; Chabalowski, C. F.; Frisch, M. J. *J. Phys. Chem.* **1994**, *98*, 11623−11627. (d) Vosko, S. H.; Wilk, L.; Nusair, M. Can. *J. Phys.* **1980**, *58*, 1200−1211.

[25] Martin, R. L. *J. Chem. Phys.* **2003**, *118*, 4775–4777.

[26] Clark, A. E.; Martin, R. L.; Hay, P. J.; Green, J. C.; Jantunen, K. C.; Kiplinger, J. L. *J. Phys. Chem. A* **2005**, *109*, 5481–5491.

[27] Roy, L. E.; Scalmani, G.; Kobayashi, R.; Batista, E. R. *Dalton Trans.* **2009**, 6719–6721.

Chapter 5. Mechanistic Studies of Degradation Pathways of Rubrene and Its Derivatives

5.1 Background

Organic semiconductors have attracted interest in large-area devices due to their mechanical flexibility, solution processability, and performance that rivals that of amorphous silicon.[1,2,3,4,5] Although these materials appear as attractive candidates for next-generation semiconductor materials, their propensity to degrade under ambient conditions has hindered their commercial use. Even the benchmark organic semiconductor, rubrene, one of the best performing materials,[6,7,8,9] has been shown to readily oxidize in both solution and amorphous thin films.[10,11,12,13,14,15,16] The photooxidation of rubrene has been well documented,[16,17] involving the photosensitized formation of singlet oxygen and subsequent formation of the *endo*-peroxide Diels–Alder adduct (Scheme 5.1, Stage 1).[18]

Scheme 5.1 Photocatalyzed oxidation of rubrene to rubrene-Ox1 (stage 1) and further acid-catalyzed oxidation to rubrene-Ox2 (stage 2)

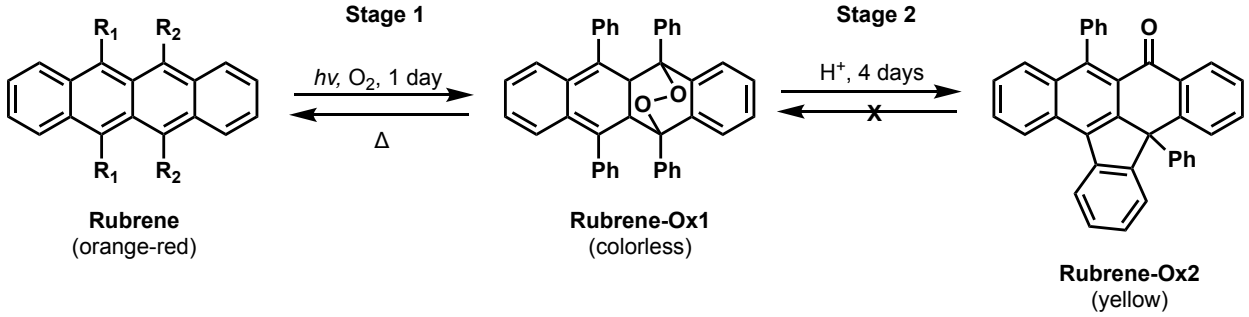

In collaboration with the Briseno lab at the University of Massachusetts Amherst, we embarked on a computational study to clarify the photo-oxidation of rubrene. In course of the Briseno lab's efforts to monitor and clarify the photo-oxidation of rubrene[11,17,19,20] and its thermal cycloreversion,[21] an irreversible second stage oxidation product, **Rubrene-Ox2**, was observed (Scheme 5.1, Stage 2). This oxidation is an acid-catalyzed process that irreversibly destroys the active transport layer and leads to permanent degradation of device performance. Using computations, we explored the mechanism of the formation of **Rubrene-Ox2**. In addition, we

explore the regioselectivity of various rubrene derivatives to understand how these functional groups influence the susceptibility of these structures to oxidation to form an analogous *endo*-peroxide.

5.2 Rearrangement of rubrene

The Briseno group has found that **Rubrene** undergoes photochemical oxidation to **Rubrene-Ox1** which, in the presence of acid from solvent impurities, undergoes further oxidation to **Rubrene-Ox2** with prolonged reaction time.[22] The Stage 1 oxidation is thermally reversible whereas the Stage 2 oxidation is irreversible due to loss of phenol. The reversibility of the Stage 1 oxidation was demonstrated both in solution and devices, where organic field effect transistors were fabricated and the reversibility of the oxidation was demonstrated via restoration of high mobility in the devices. On the other hand, the formation of **Rubrene-Ox2** was found to be irreversible, indicating acid impurities in solution-processed devices could affect device performance. We thus embarked on a computational study to study the mechanism by which **Rubrene-Ox2** could be formed. Further experimental details can be found in ref. 22.

Scheme 5.2 Mechanistic pathway studied computationally

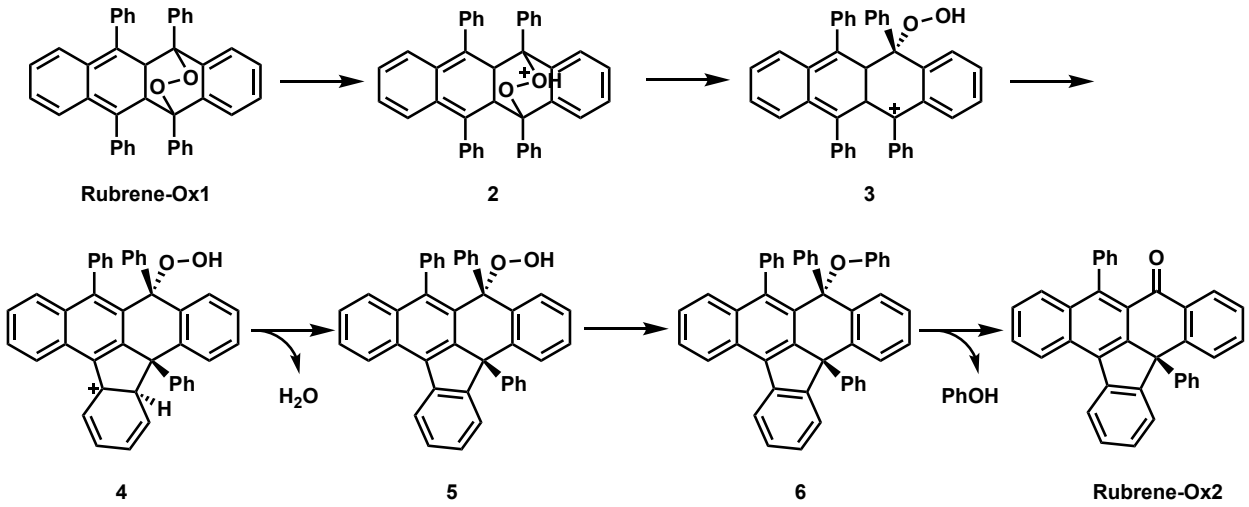

Scheme 5.2 shows the proposed acid-catalyzed mechanism for rubrene endo-peroxide rearrangement to **Rubrene-Ox2**. Chloroform is known to contain acidic impurities (HCl).[23]

Structures were optimized with M06-2X using the 6-31+G(d,p) basis set and polarizable continuum solvent model (IEFPCM, solvent: chloroform). Single-point energies were obtained using M06-2X with the 6-311+G(d,p) basis set and the same solvent model. The following discussion is based on the computed free energies relative to rubrene and $^3O_2$.

The first step in this pathway is the protonation of *endo*-peroxide **rubrene-Ox1** by model acid H_3O^+, forming cation **2** (Figure 5.1). The protonated *endo*-peroxide then undergoes a ring opening to afford the stabilized carbocation **3**, which is 27.2 kcal mol^{-1} lower in energy than **2**. Attack of the cation at C5 produces Wheland intermediate **4**, which is higher in energy than **3** by 5.4 kcal mol^{-1}. Subsequent deprotonation of **4** by H_2O gives **5**, which rearranges via a [1,2]-Ph shift and dehydration to give **6**. Finally, **6** loses PhOH to afford observed product **Rubrene-Ox2**.

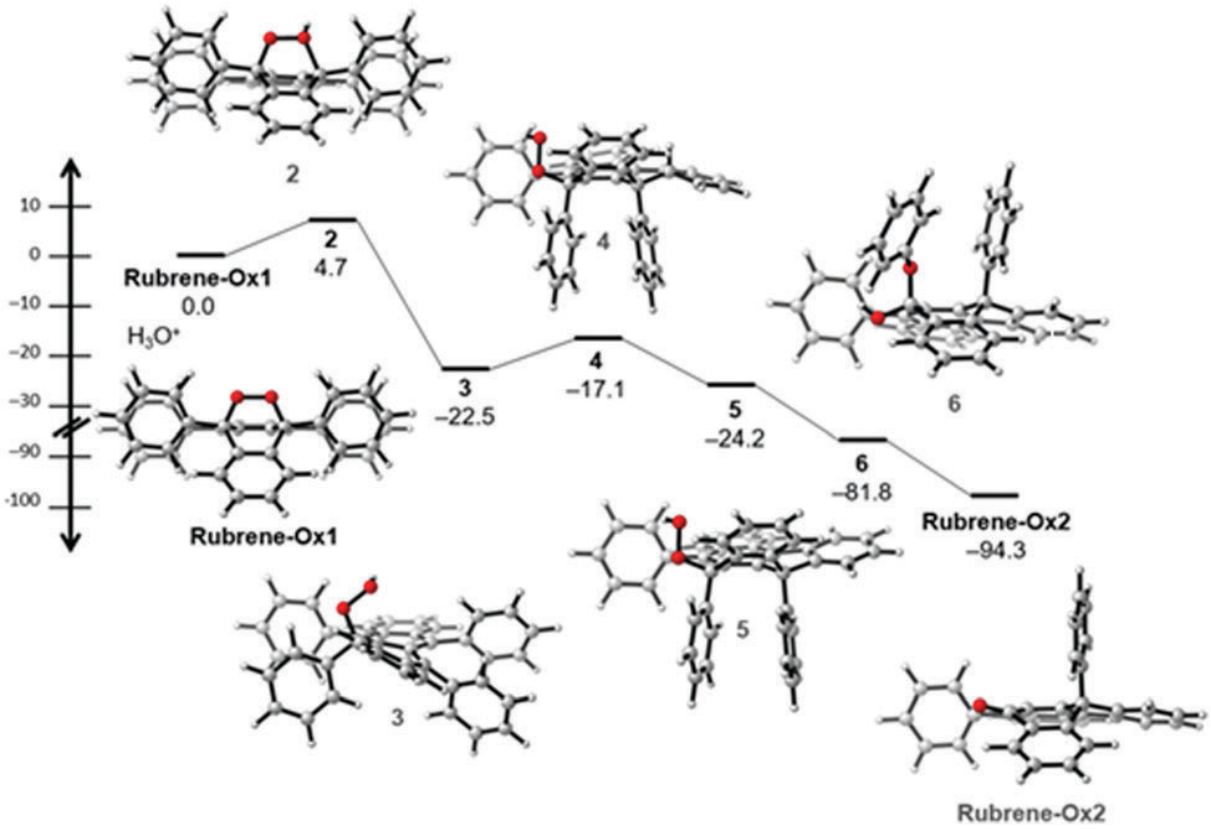

Figure 5.1. Free energy diagram of proposed mechanism of the rearrangement of rubrene-Ox1 to rubrene Ox2.
Values are free energies in kcal mol^{-1}.

5.3 Oxidation of rubrene derivatives

We also embarked on a computational study in order to investigate the oxidation of various functionalized tetracenes, or rubrene analogues. These materials and their corresponding stabilities are of interest due to the application of (poly)acenes and their functionalized derivatives in organic electronics. The Briseno group has found that rubrene analogues undergo oxidation by singlet oxygen to form *endo*-peroxides (Figure 5.2). For unsymmetric structures **Ru-2-5**, this oxidation is regioselective, forming only the *endo*-peroxide depicted.

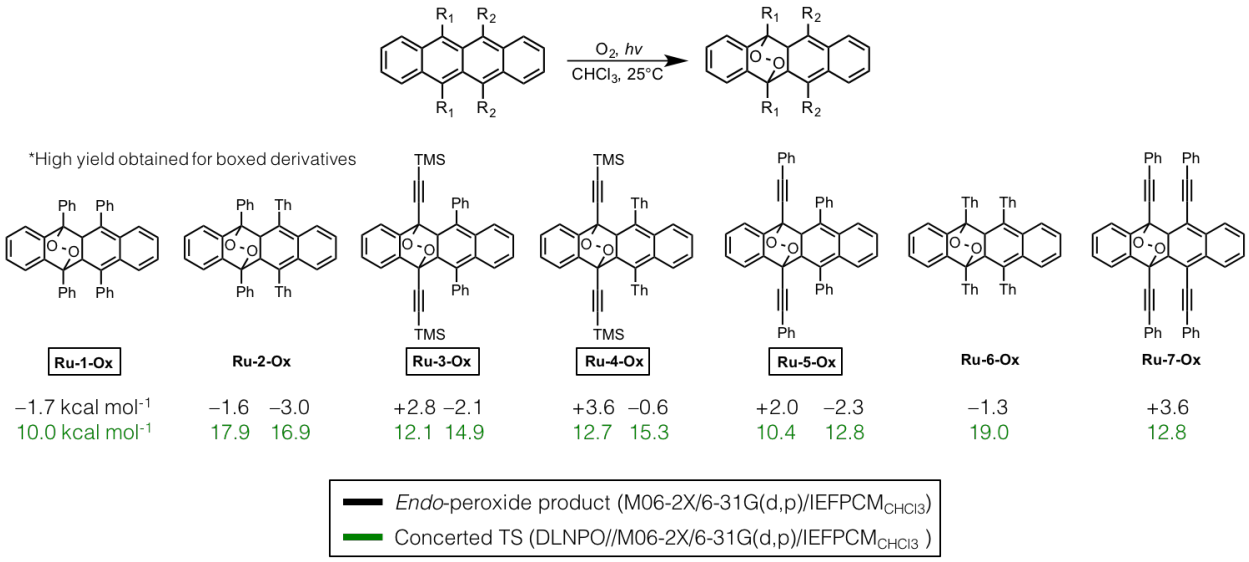

Figure 5.2. Energetics of oxidation of rubrene derivatives.
Product energies relative to the separated reactants are shown in black, and reaction barriers of the concerted O_2 addition are shown in green.

We used M06-2X/6-31G(d,p) to obtain relative energies of the *endo*-peroxides relative to the separated reactants (energies in black). Although oxidation can result in thermodynamically favorable products, the observed regioisomer is the less stable product. We thus sought to probe the kinetics of the oxidation by calculating the concerted transition states. We used M062-X/6-31G(d,p) to compute the transition structures of the concerted O_2 addition and obtained high-accuracy barriers with an energy calculation using DLNPO methods (energies in green). For **Ru-3**, **Ru-4**, and **Ru-5**, the free energy barrier to formation of the observed regioisomer is 2.4 to 2.7

kcal mol^{-1} lower in energy than that of the unobserved (but thermodynamically more favorable) regioisomer. For **Ru-2**, the free energy barrier to formation of the unobserved regioisomer is 1.0 kcal mol^{-1} lower in energy than the observed product. The regioselectivity of the oxidation is driven kinetically, and these barriers generally correspond with experimental half-lives (Table 5.1). From our calculations, we find that alkenyl groups influence the regioselectivity by stabilizing the transition state (i.e., **Ru-3**, **Ru-4**, and **Ru-5**). Flanking thiophene groups increase the stability of the molecule (**Ru-4**, **Ru-2**, and **Ru-6**).

Table 5.1. Half-life and calculated activation barrier to concerted oxidation for each rubrene

	Ru-1	**Ru-3**	**Ru-5**	**Ru-7**	**Ru-4**	**Ru-2**	**Ru-6**
Half-life (min)	17	22	22.5	635	795	>2400	Very stable
$\Delta G^{\neq}$ (kcal mol^{-1})	10.0	12.1	10.4	12.8	12.7	16.9	19.0

5.4 Conclusions

In the course of studying the formation and thermally activated cycloreversion of **Rubrene-Ox1** to pristine rubrene, we observed an irreversible, second stage oxidation product **Rubrene-Ox2**. It was found that acid impurities in chlorinated solvents lead to a pyramidalized ketone derivative, which is inactive in organic transistors. Using DFT calculations, we identify the acid-catalyzed pathway to this irreversible product. Such impurities present in solution-processed rubrene devices will detrimentally impact device performance and cannot be remediated through the application of heat to reform the parent acene. Devices from pure, thermally treated **Rubrene-Ox1** did in fact yield high carrier mobilities in both thin films and single crystal transistors. We also employed DFT calculations to understand the effect of varying flanking R groups on the stability and regioselectivity of rubrene analogues. Understanding the formation of these oxidation products will help us design more chemically robust rubrene derivatives.

5.5 References

[1] Li, Y.; Ji, D.; Liu, J.; Yao, Y.; Fu, X.; Zhu, W.; Xu, C.; Dong, H.; Li, J.; Hu, W. *Sci. Rep.* **2015**, *5*, 13195.

[2] Briseno, A. L.; Tseng, R. J.; Ling, M. M.; Falcao, E. H. L.; Yang, Y.; Wudl, F.; Bao, Z. *Adv. Mater.* **2006**, *18*, 2320–2324.

[3] Yi, H. T.; Payne, M. M.; Anthony, J. E.; Podzorov, V. *Nat. Commun.* **2012**, *3*, 1259.

[4] Reyes-Martinez, M. A.; Crosby, A. J.; Briseno, A. L. *Nat. Commun.* **2015**, *6*, 6948.

[5] Sekitani, T.; Zschieschang, U.; Klauk, H.; Someya, T. *Nat. Mater.* **2010**, *9*, 1015–1022.

[6] Qian, X.; Wang, T.; Yan, D. *Appl. Phys. Lett.* **2013**, *103*, 6–10.

[7] Takeya, J.; Yamagishi, M.; Tominari, Y.; Hirahara, R.; Nakazawa, Y.; Nishikawa, T.; Kawase, T.; Shimoda, T.; Ogawa, S. *Appl. Phys. Lett.* **2007**, *90*, 2005–2008.

[8] Podzorov, V.; Sysoev, S. E.; Loginova, E.; Pudalov, V. M.; Gershenson, M. E. *Appl. Phys. Lett.* **2003**, *83*, 3504–3506.

[9] Sundar, V. C.; Zaumseil, J.; Podzorov, V.; Menard, E.; Willett, R. L.; Someya, T.; Gershenson, M. E.; Rogers, J. A. *Science* **2004**, *303*, 1644–1646.

[10] Kytka, M.; Gerlach, A.; Schreiber, F.; Kováč, J. *Appl. Phys. Lett.* **2007**, *90*, 18–21.

[11] Sinha, S.; Wang, C. H.; Mukherjee, M.; Mukherjee, T.; Yang, Y. W. *Langmuir* **2014**, *30*, 15433–15441.

[12] Fumagalli, E.; Raimondo, L.; Silvestri, L.; Moret, M.; Sassella, A.; Campione, M. *Chem. Mater.* **2011**, *23*, 3246–3253.

[13] Najafov, H.; Mastrogiovanni, D.; Garfunkel, E.; Feldman, L. C.; Podzorov, V. *Adv. Mater.* **2011**, *23*, 981–985.

[14] Uttiya, S.; Raimondo, L.; Campione, M.; Miozzo, L.; Yassar, A.; Moret, M.; Fumagalli, E.; Borghesi, A.; Sassella, A. *Synth. Met.* **2012**, *161*, 2603–2606.

[15] Force, U. S. A.; Wilson, T. *J. Am. Chem. Soc.* **1966**, *23*, 2898–2902.

[16] Williams, A. H. *Trans. Faraday Soc.* **1939**, *35*, 765–771.

[17] Hochstrasser, R. M.; Ritchie, M. *Trans. Faraday Soc.* **1956**, *52*, 1363.

[18] Maliakal, A. J.; Chen, J. Y. C.; So, W. Y.; Jockusch, S.; Kim, B.; Ottaviani, M. F.; Modelli, A.; Turro, N. J.; Nuckolls, C.; Ramirez, A. P. *Chem. Mater.* **2009**, *21*, 5519–5526.

[19] Leach, A. G.; Houk, K. N. *Chem. Commun.* **2002**, 1243–1255.

[20] Käfer, D.; Witte, G. *Phys. Chem. Chem. Phys.* **2005**, *7*, 2850–2853.

[21] Aubry, J.-M.; Pierlot, C.; Rigaudy, J.; Schmidt, R. *Acc. Chem. Res.* **2003**, *36*, 668–675.

[22] Ly, J. T.; Lopez, S. A.; Lin, J. B.; Kim, J. J.; Lee, H.; Burnett, E. K.; Zhang, L.; Aspuru-Guzik, A.; Houk, K. N.; Briseno, A. L. *J. Mater. Chem. C* **2018**, *6,* 3757.

[23] Margolin, Z.; Long, F. A. *J. Am. Chem. Soc.* **1973**, *2438*, 2757–2762.

Chapter 6. Hopf 6π Electrocyclization of Polydiacetylene Precursors to Form Graphene Nanoribbons

6.1 Background

While graphene displays a number of remarkable properties, its zero bandgap makes it unsuitable for most semiconductor applications.[1] However, graphene nanoribbons (GNRs), which are narrow strips of graphene with widths below 10 nm, display defined bandgaps in addition to ballistic charge transport, thanks to the lateral confinement of charge carriers.[2] Not surprisingly, the designed synthesis of GNRs has quickly gained prominence in recent years.

Graphene nanoribbons are classified as either armchair, zigzag, or chiral, depending on the topology of the repeating units within their long edges.[3] Armchair graphene nanoribbons (AGNRs),[4] which are the most interesting type of GNR in terms of semiconductor applications, can be divided into three classes defined by the number of carbon atoms within their width. These classes comprise 3p, 3p + 1, and 3p + 2 carbon atoms, where p is in an integer. Armchair GNRs that fall into the 3p or 3p + 1 classes (e.g., [6] and [7]AGNRs) are predicted to be semiconducting, with a bandgap that increases as ribbon width decreases, while the 3p + 2 class (e.g., [8]AGNR) is predicted to have a significantly narrower bandgap.[5] The smallest member of the 3p + 2 class, [5]AGNR, was first synthesized using on-surface chemistry, and subsequently, in-solution.[6,7,8,9] Since then, many GNRs of the other classes have been synthesized, although the next smallest member of the 3p + 2 class, [8]AGNR, has yet to be reported via either solution or surface chemistry.

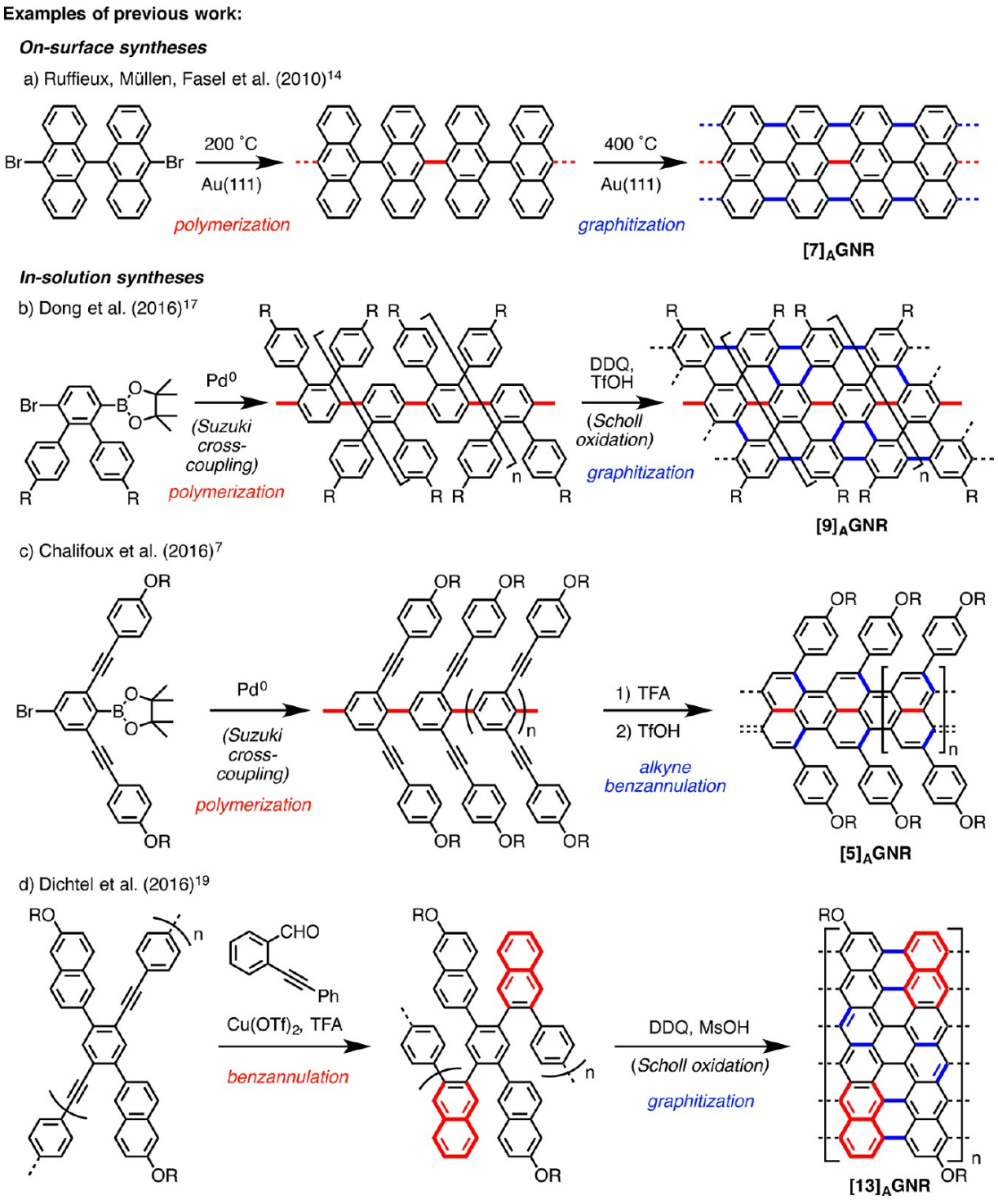

Figure 6.1. Examples of bottom-up syntheses of GNRs.
(a,b) Most approaches take advantage of the metal-catalyzed polymerization of arene monomers, either on-surface or in-solution, and subsequent oxidation of the ensuing polymers to the corresponding GNRs. (c,d) By contrast, Dichtel and Chalifoux have developed ingenious new benzannulation strategies to access GNRs.

Although GNRs are quickly gaining importance, there are only a limited number of methods to generate them. These methods fall either into “top-down” or “bottom-up” strategies.[10] Top-down strategies include cutting a large piece of graphene with an electron beam, unzipping of carbon nanotubes, or sonochemical tearing of graphene sheets.[11,12,13] A major limitation of the top-down strategies is that they do not provide homogeneous ultranarrow ribbon widths (<10 nm) or atomically precise edges. By contrast, bottom-up strategies rely on the precision and control afforded by synthetic chemistry to construct ribbons molecule-by-molecule. Until recently, only two marginally differing bottom-up approaches had been described: (1) surface-assisted coupling and cyclodehydrogenation of dihalo polycyclic arenes or (2) metal-catalyzed solution-phase polymerization of similar precursors, including alkynylarenes, to form polyarylene backbone polymers, followed by their subsequent, typically oxidative, aromatization to GNRs (Figure 6.1).[7,14,15,16,17,18] More recently, the groups of Dichtel and Chalifoux have described key strategic innovations in this area. Both approaches utilize benzannulation reactions performed after metal-catalyzed polymerization.[7,19]

In the conceptual elaboration of the project, the Rubin group identified that diphenyl polydiacetylene polymers should produce [8]AGNR if they could be triggered to undergo internal backbone cyclization and cyclodehydrogenation (Figure 6.2). While the broad bandgap semiconducting polydiacetylene polymers (PDAs) have a rich history of synthetic design, spectroscopy, and applications in materials science, with a more recent focus on their thermochromic properties,[20,21,22] synthetic strategies that directly utilize the polyenyne backbone functionality for further synthetic transformations are still rare.[23,24,25] Following initial studies seeking the formation of nanotubular PDAs through topochemical polymerization of [24]dehydroannulenes,[26,27] our approach to GNRs originated from the intriguing prospect of exploiting the rehybridization energy of sp carbons within the alkyne units of aryl-substituted polydiacetylenes. By coercing them to expand their coordination using known thermal reactions

involving the aryl substituents, the rehybridization and aromatization energies gained from each cyclizing alkyne unit should be energetically favorable and give polycyclic aromatic structures. This strategy was first exploited by the Rubin group to target the synthesis of [12]AGNRs from naphthyl-substituted PDAs.[28] Here, the group has extended this strategy to access [8]AGNRs for the first time. This novel approach to GNRs exploits the power of crystal engineering and solid-state reactions by targeting very large organic structures through programmed chemical transformations.

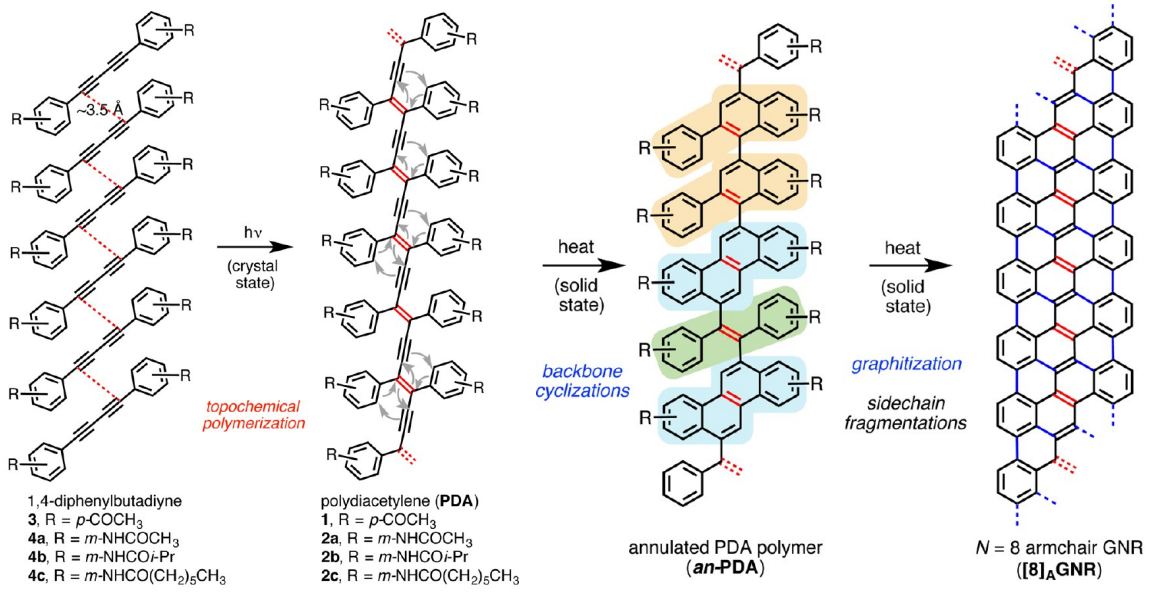

Figure 6.2. Synthetic approach by the Rubin group to [8]AGNR from substituted 1,4-diphenylbutadiynes.
This occurs via the crystalline-state topochemical polymerization of the latter, followed by a separate solid-state thermal aromatization and fragmentation of side-chains. Likely steps in the series of random Hopf cyclizations include the formation of 2- phenylnaphthalene units (orange shaded areas) as well as chrysene (cyan) and 1,2-diphenylethene units (green).

As demonstrated below, the diphenyl polydiacetylene motif has proven itself to be an ideal platform to access these GNRs. Experiments by the Rubin group show that four differently substituted diphenyl PDA polymers with either para- or meta-substituents (PDAs **1** and **2a−c**) all produce pristine [8]AGNRs quantitatively via simple heating. This process is readily applicable to bulk synthesis thanks to the inherent ease with which solid-state transformations can be scaled

up. This operationally simple, two- step synthesis of [8]AGNRs does not require any external reagents or solvents and should be applicable to a range of device manufacturing techniques. Furthermore, these transformations are not limited by edge substituents and should ultimately provide access to a variety of different edges and widths, including the incorporation of heteroatoms.

Scheme 6.1. Generations of model systems studied computationally

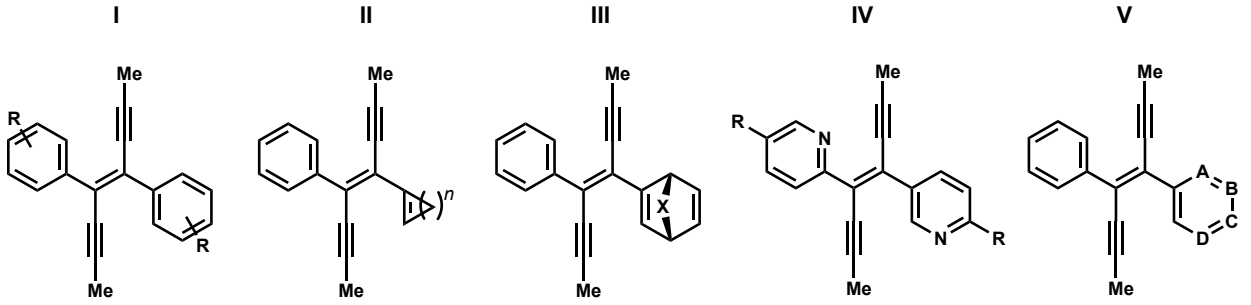

5, **R** = *p*-COMe
6, **R** = *m*-NHCOMe

7, *n* = 1
8, *n* = 2
9, *n* = 3
10, *n* = 4

11, **X** = O
12, **X** = CH_2
13, **X** = C=O
14, **X** = NMe

15, **R** = NHCOMe
16, **R** = H

17, **A** = N, **B**,**C**,**D** = C
18, **B** = N, **A**,**C**,**D** = C
19, **C** = N, **A**,**B**,**D** = C
20, **D** = N, **A**,**B**,**C** = C
21, **A**,**B** = N, **C**,**D** = C
22, **A**,**C** = N, **B**,**D** = C
23, **A**,**D** = N, **B**,**C** = C
24, **A**,**B**,**C** = N, **D** = C

Computations were employed to understand the cyclization process, the regioselectivity of the reaction, and to further design new systems that would allow for lower reaction temperatures and added functionality. This chapter will detail a number of studies towards understanding Hopf cyclizations of a number of systems depicted in Scheme 6.1: all-carbon PDAs (Generation I), strained cycloalkanes (Generation II), strained norbornadiene systems (Generation III), and azines (Generations IV and V).

6.2 Experimental work

The Rubin group at UCLA has demonstrated a highly efficient thermal conversion of four differently substituted polydiacetylenes (PDAs **1** and **2a−c**) into virtually indistinguishable N = 8 armchair graphene nanoribbons ([8]AGNR). PDAs **1** and **2a−c** are themselves easily accessed

through photochemically initiated topochemical polymerization of diynes **3** and **4a−c** in the crystal. The clean, quantitative transformation of PDAs **1** and **2a−c** into [8]AGNR occurs via a series of Hopf pericyclic reactions, followed by aromatization reactions of the annulated polycyclic aromatic intermediates, as well as homolytic bond fragmentation of the edge functional groups upon heating up to 600°C under an inert atmosphere. The conversion steps have been investigated in great detail using complementary spectroscopic techniques (CP/MAS 13C NMR, Raman, FT-IR, and XPS) as well as high-resolution transmission electron microscopy (HRTEM). Details of experiments including synthesis and characterization can be found in ref. 29.

6.3 Computational methods

All geometries were fully optimized at the B3LYP/6-31G(d) level of theory in the gas phase.[30,31,32,33] All optimized geometries were verified by frequency computations as minima (no imaginary frequencies) or transition structures (one imaginary frequency). For systems **5** and **6** (Generation I), frequency analysis was performed at 623.15 K, and frequency values discussed in the text were scaled using a factor 0.98.[34,35] The energetic trends were found not to differ greatly with this correction, so the this correction was not applied in subsequent calculations (Generations II-V). Free energy corrections were calculated using Truhlar's quasiharmonic approximation, which sets all the real vibrational frequencies that are lower than 100 cm^{-1} to 100 cm^{-1} to correct entropies for the breakdown of the harmonic oscillator approximation.[36,37] Subsequent single-point energy calculations on the optimized structures were performed using the M06-2X/6-311+G(d,p) level of theory.[38] The thermal corrections calculated from the scaled vibrational frequencies at the B3LYP/6-31G(d) level on the optimized geometries were then added to the M06-2X/6-311+G(d,p) electronic energies to obtain the Gibbs free energies. All quantum chemical computations were performed using Gaussian 09.[39] All graphics on optimized structures were generated with CYLview.[40]

Conformational searches were carried out with *MacroModel* from *Schrödinger* using OPLS_2005 and an energy window of 10.0 kcal mol^{-1}.[41] A redundant conformer elimination was performed using an energy window of 10.0 kcal mol^{-1} and a maximum atom deviation cutoff of 0.5 Å. The lowest energy conformers were optimized with B3LYP/6-31G(d) to locate the global minimum for each reaction.

6.4 Regioselectivity of PDA system

To generate [8]AGNRs, we postulated that the phenyl substituents on the PDA backbone would engage their adjacent trans-dienyne moieties into a series of Hopf pericyclic reactions to provide annulated polycyclic aromatic intermediates (*an*-PDA, Figure 6.2).[42, 43] Full cyclodehydrogenation of the resulting adjacent polycyclic aromatic rings, which would initially be a random mix of 2-phenylnaphthalene, chrysene, 1,2-diphenylethene units, or larger, would ultimately fully aromatize to 8- armchair graphene nanoribbons. Hopf cyclizations have been experimentally shown to take place via three distinct mechanisms dependent on the reaction temperature: (1) 6π- electrocyclization, (2) rearrangement of the alkyne to a vinylidene carbene followed by aryl C−H insertion, and (3) cyclization via initial radical addition to the alkyne.[44] It was shown that electrocyclization is the predominant mechanism for a gas-phase reaction below 550 °C. All polymers discussed here undergo backbone cyclization below 500°C in the solid state; therefore, it is most likely that the backbone cyclization process occurs via a 6π-electrocyclization pathway.

Scheme 6.2. Mechanistic pathway of Hopf cyclization of dienyne precursors

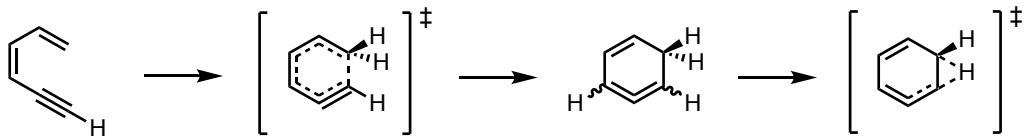

To model the energetics of the Hopf cyclization stage for PDAs 1 and 2a, we performed DFT calculations on the *trans*-enediynes **5** and **6** as model systems for the keto and amido

functionalized PDAs **1** and **2a**, respectively (Figure 6.2, Table 6.1). We based our mechanistic study on previous work by Hopf et al.,[43] in which the thermal cycloisomerization pathway of cis-hexa-1,3-dien-5-yne was explored computationally. As noted above, the authors established that the Hopf cyclization proceeds through the initial 6π-electrocyclization (***cycl***) that generates an annulated intermediate (***annul***), which is followed by two consecutive [1,2]-H shifts, with the first H-shift being the rate-determining step (***H-shift***) (Scheme 6.2). Structures were optimized in the gas phase using B3LYP/6-31G(d),[45] and single-point calculations were performed using M06-2X/6-311+G(d,p)[46] to obtain the free energy values shown in Figure 6.3. Transition-state geometries of the Hopf cyclization (**5-*cycl***, **6-*o-cycl***, **6-*p-cycl***) and first H-shift (**5-*H-shift***, **6-*o-H-shift***, **6-*p-H-shift***) steps are also shown in Figure 6.3.

Table 6.1. Computed energetics in kcal mol^{-1} relative to PDAs 5 and 6

	5		**6**			
			ortho		*para*	
	$\Delta H/\Delta H^{\neq}$	$\Delta G/\Delta G^{\neq}$	$\Delta H/\Delta H^{\neq}$	$\Delta G/\Delta G^{\neq}$	$\Delta H/\Delta H^{\neq}$	$\Delta G/\Delta G^{\neq}$
cycl	47.5	52.6	50.5	55.4	48.2	52.5
annul	41.6	45.5	37.8	41.5	38.6	42.0
H-shift	52.9	58.4	58.8	64.3	52.3	57.5

The activation free energies are 52.6 and 58.4 kcal mol^{-1} for **5-*cycl*** and **5-*H-shift***, respectively. Similar reaction barriers of 52.5 and 57.5 kcal mol^{-1} are found for the meta-amide model system undergoing cyclization para to its amide side chain (**6-*p-cycl***, **6-*p-H-shift***). The barriers to ortho cyclization (**6-*o-cycl***, **6-*o-H-shift***) are higher than for para cyclization by 2.9 and 6.8 kcal mol^{-1}, respectively. In all cases, the barriers for the first H-shift are higher than that for the Hopf cyclization, a finding that is in line with the work of Hopf et al.[43]

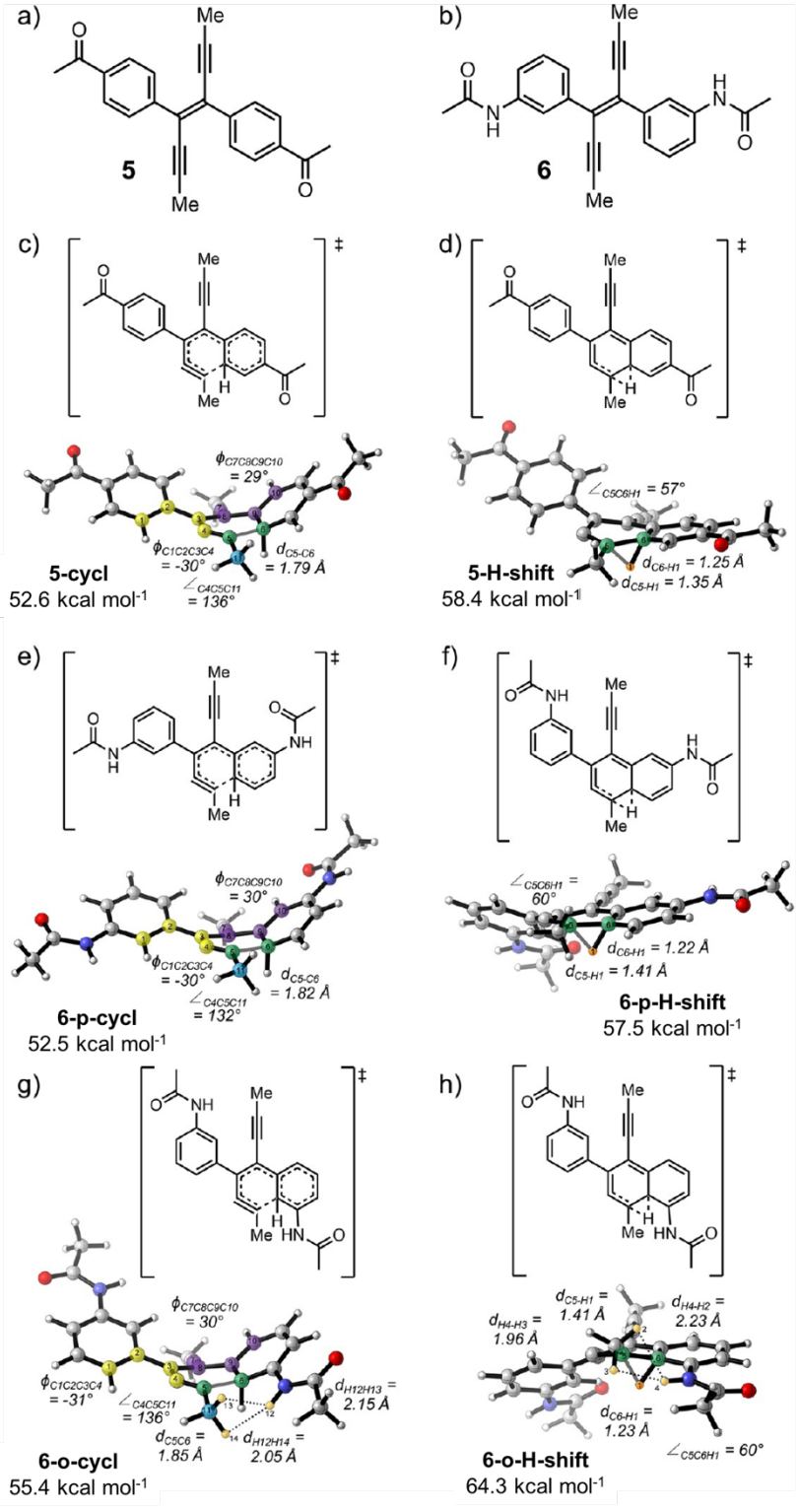

Figure 6.3. Transition-state geometries and activation free energies of the 6π-electrocyclization and subsequent H-shift for model systems 5 and 6.

The geometries of each of the transition structures are similar. The π-system of the alkynes is planar in each of the Hopf cyclization transition states, while the flanking aryl groups are out of plane by approximately 30°. In the H-shift step, the forming naphthyl ring is planar, and the C6−H1 bond stretches to about 1.22−1.25 Å from its normal C−H bond length of 1.09 Å (Figure 6.3d,f,h). In both ortho transition states **6-*o-cycl*** and **6-*o-H-shift***, the close proximity of the amide and methyl groups at the forming C−C bond leads to higher barriers. This results in an intrinsic preference for the para pathway over the ortho pathway by 6.8 kcal mol^{-1}.

For both models **5** and **6**, the reaction barriers of the rate-determining H-shift are >14 kcal mol^{-1} higher than that of *cis*-hexa-1,3-dien-5-yne. This increase in reaction barrier can be attributed to the benzannulation within the π-systems of **5** and **6** compared to *cis*-hexa-1,3-dien-5-yne, which requires disrupting the aromatic π-system in the transition state (discussed in the next section). In addition, while these gas-phase energies are useful for understanding the intrinsic barriers to cyclization, we acknowledge the limit of these simple models in accounting for the solid-state behavior and polymer conformational influence on the large scale graphitization process within PDAs **1** and **2a**.

6.5 Computations on model system

We explored a set of four test structures **A**-**D**, the former two in order to validate our method compared to calculations by Prall *et al*. and the latter two to probe the effect of π-extension of **A** on reaction barriers (Scheme 6.3). We computed the reaction barriers to **A-*cycl*** and **A-*H-shift***, which are 40.2 and 44.0 kcal mol^{-1}, respectively (Table 6.2). For the benzannulated system **B**, the barriers for **B-*cycl*** and **B-*H-shift*** increase to 46.6 and 51.1 kcal mol^{-1}, respectively, as would be expected to due to the breaking of aromaticity necessary for cyclization to occur. Enthalpies of rate-determining barriers for **A** and **B** are within 3 kcal mol^{-1} of those calculated by Prall *et al*.

Scheme 6.3. Model systems studied

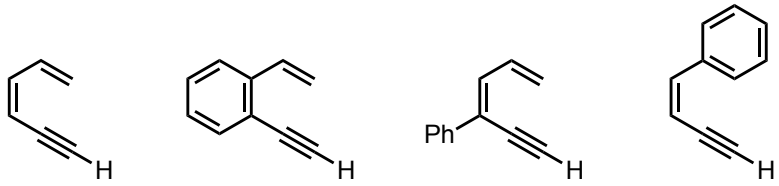

A **B** **C** **D**

Next, we explored the effect of extending the π-system, as in the PDAs. Phenylation at the 4-position of hexa-1,3-dien-5-yne (**C**) does not affect the reaction barriers, which stay approximately the same as those for **A** (37.6 and 46.3 kcal mol^{-1} for **C-*cycl*** and **C-*H-shift***, respectively). However, enynylbenzene **D** has much high reaction barriers of 54.1 and 58.4 kcal mol^{-1} for **D-*cycl*** and **D-*H-shift***, respectively. The increases in the energetic barriers of the rate-determining steps of **B** and **D** are due to the necessity to interrupt the aromaticity of the benzene ring.

Table 6.2. Computed energetics of model systems in kcal mol^{-1} relative to starting enyne

	A			B			C		D	
	$\Delta H/\Delta H^{\neq}$ [a]	$\Delta H/\Delta H^{\neq}$	$\Delta G/\Delta G^{\neq}$	$\Delta H/\Delta H^{\neq}$ [a]	$\Delta H/\Delta H^{\neq}$	$\Delta G/\Delta G^{\neq}$	$\Delta H/\Delta H^{\neq}$	$\Delta G/\Delta G^{\neq}$	$\Delta H/\Delta H^{\neq}$	$\Delta G/\Delta G^{\neq}$
cycl	31.7	34.5	40.2	36.4	41.3	46.6	32.4	37.6	48.9	54.1
annul	7.9	11.8	17.5	25.5	32.9	37.6	34.0	39.3	44.7	48.4
H-shift	39.4	36.7	44.0	46.0	44.4	51.1	39.7	46.3	52.7	58.4

[a]Computed by Prall et al.[43] using BCCD(T)/cc-pVDZ//BLYP/6-31G(d)

6.6 Strained systems

We have used computations to explore the regioselectivity and energetics of the PDA systems (Scheme 6.3, Generation I). We now turn our attention to a series of strained cyclic systems (Generation II) as a means to lower the barriers of cyclization and 1,2-shift. This type of reactivity has been explored by our group for Diels-Alder cycloadditions.[47] With these cyclic enynes, the barriers to the first cyclization are similar, ranging from 37.4 to 41.0 kcal mol^{-1} (Table 6.3), which is consistent with barriers for simple dienyne systems. However, with increasing ring

size, we see a decrease in the barrier of the 1,2-shift from 61.1 to 39.8 kcal mol^{-1}, a trend also seen for the allenic intermediate. This indicates that with increased strain in the system (due to smaller ring size), the tendency to undergo the 1,2-shift increases as well.

Table 6.3. Calculated free energies for generation III (**7**-**10**) and V (**11**-**14**)

	7 (*n* = 1)	**8** (*n* = 2)	**9** (*n* = 3)	**10** (*n* = 4)	**11** (**X** = O)	**12** (**X** = CH_2)	**13** (**X** = C=O)	**14** (**X** = NMe)
cycl	38.5	37.4	37.9	41.0	31.5	32.3	36.1	29.8
annul	28.0	21.4	16.9	17.9	4.2	3.5	10.4	1.4
H-shift	61.1	47.3	39.8	41.4	36.9	39.9	42.2	37.2

All energies are in kcal mol^{-1}.

The barriers for the unbridged cyclohexene system are 41.0 kcal mol^{-1} for the cyclization and 41.4 kcal mol^{-1} for the 1,2-shift. The ~20 kcal mol^{-1} decrease in the barrier of the rate-limiting step suggests that this hexadiene system would be promising in lowering the barrier towards GNR formation. With this in mind, we studied the effect of various norbornadiene moieties (Generation III). The barrier of the initial cyclization is further reduced, ranging from 29.8 to 36.1 kcal mol^{-1}, and the barriers for the 1,2-shift remain similar to the hexadiene system, ranging from 36.9 to 42.2 kcal mol^{-1}. These results indicate that these norbornadiene systems cause almost a 30 kcal mol^{-1} lowering of the rate-limiting step compared to the Generation I PDA system. In particular, the oxanorbornadiene system is an attractive target system, as subsequent deoxygenation and rearomatization can be easily achieved. Experimental studies are underway to validate these predictions.

6.7 *N*-PDA system

Nitrogen doping is an effective way to tailor the properties of graphene for various applications.[48] The Rubin lab has found that analogous pyridyl systems **1i** and **1h** can undergo topochemical polymerization to form PDAs **2i** and **2h**, which could potentially undergo further

graphitization upon heating and furnish nitrogen-doped GNRs (*N*-GNRs) (Figure 6.4). If cyclization occurs at the 2-position of the pyridine ring, then the armchair GNR obtained would potentially have interesting redox properties that could be harnessed for interesting applications (**[8]$_A$N2-GNR**). Alternatively, if cyclization occurs at the 4-position, then the formed pyridyl nitrogen would be on the peripheral positions of the *N*-GNR and would not possess these redox characteristics (edge-**[8]$_A$N2-GNR**).

To investigate the preferred cyclization pathway, we investigated a pyridyl system analogous to PDA **6**. We envisioned that **15** (Generation IV, Scheme 6.1) would regioselectively cyclize. We hypothesized that cyclization at the 2-position would be preferred over the 4-position due to the steric bulk of the amide group at the 5-position. The geometries of the transition state for the first cyclization (***cycl***), the annulated allenic intermediate (***annul***), and the 1,2-shift (***H-shift***) were computed. Like the PDAs, the 1,2-H-shift is the rate-limiting step, and we find that cyclization at the 2-position (*para* to the amide group, 54.7 kcal mol^{-1}) is preferred over cyclization at the 4-position (*ortho* to the amide group, 60.0 kcal mol^{-1}) (Figure 6.5). Calculations for the unsubstituted variant **16** were also computed to probe the intrinsic preference for the 2-position. The barrier 1,2-shift for the unsubstituted system is 53.7 and 55.7 kcal mol^{-1} for the 2- and 4-positions, respectively. The increased preference for the 2-position with the substituted is likely due to the unfavorable steric interactions that occur in the transition states for the 4-position. Preliminary experiments suggest that cyclization is indeed occurring at the 2-position to give the desired *N*-GNR.

Desired cyclization pathway:

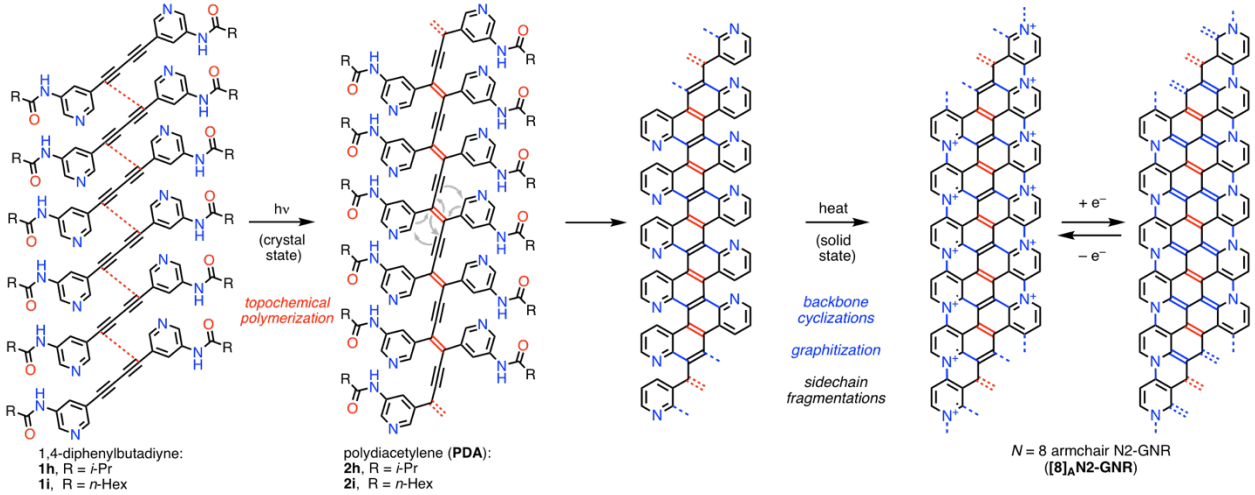

Undesired cyclization pathway:

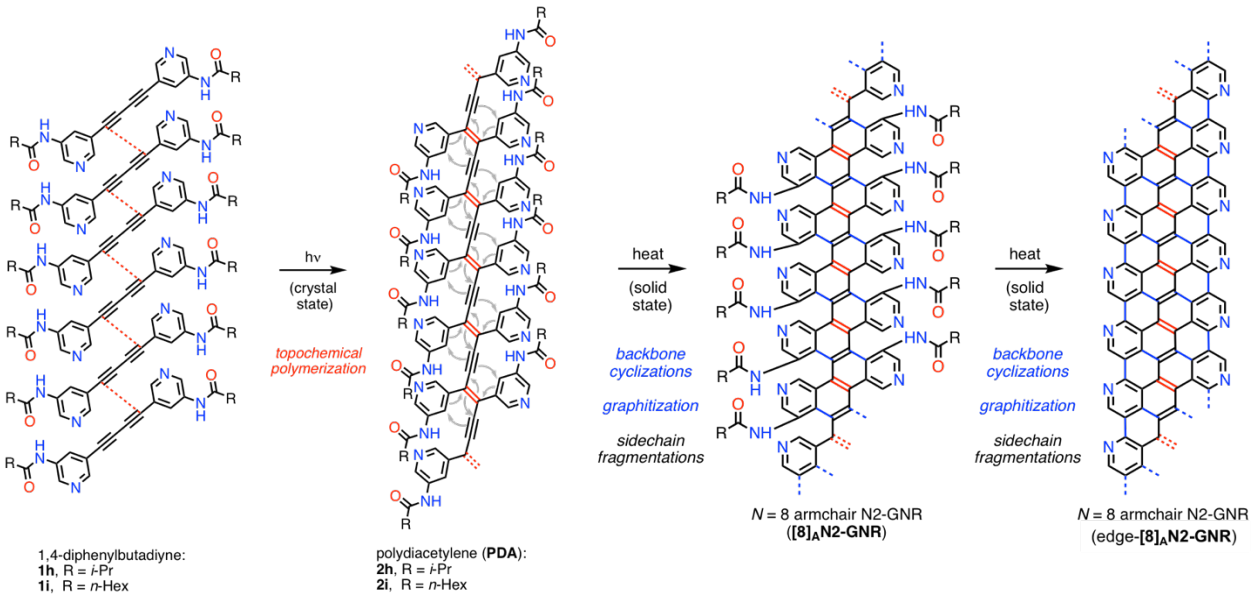

Figure 6.4. Desired (top) and undesired (bottom) cyclization pathways of pyridyl PDA systems towards redox-active $[8]_A$N2-GNR and edge-functionalized edge-$[8]_A$N2-GNR.

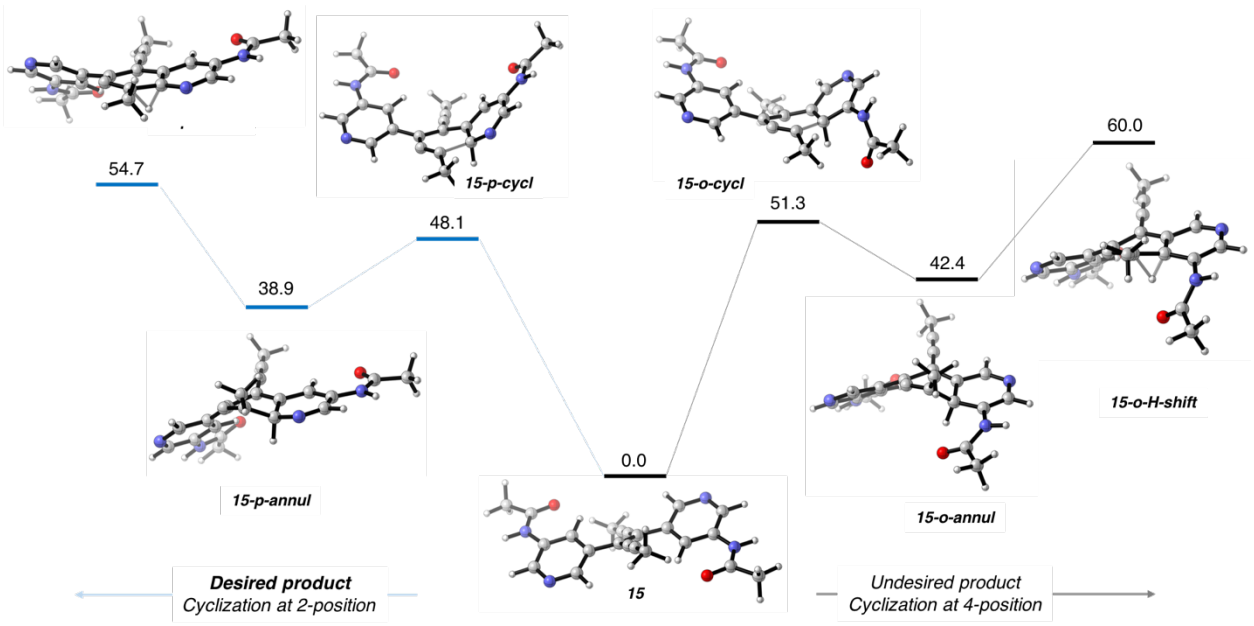

Figure 6.5. Free energy surface of pathways to desired product (left) and undesired product (right) relative to starting structure 15.
Energies are free energies in kcal mol^{-1}.

Scheme 6.4. Energetics for Generation V systems

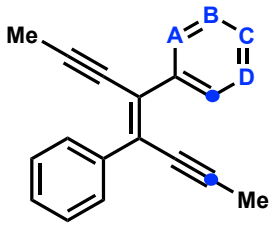

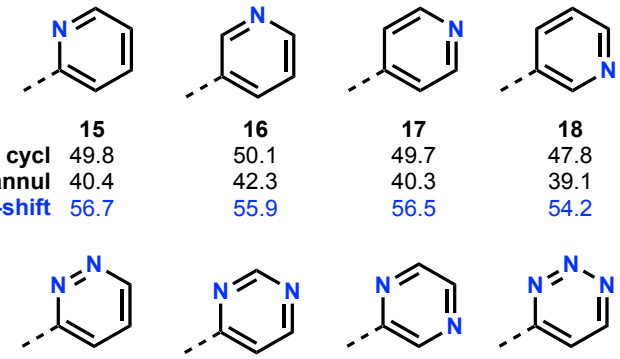

	15	**16**	**17**	**18**
cycl	49.8	50.1	49.7	47.8
annul	40.4	42.3	40.3	39.1
H-shift	56.7	55.9	56.5	54.2

19	**20**	**21**	**22**
47.4	51.1	49.7	47.6
43.0	39.1	38.3	36.1
59.4	58.6	56.5	58.7

We further sought to make predictions on the feasibility of other nitrogen-based systems with varying substitution. We computed the transition states for cyclization and 1,2-shift for a series of azines (Generation V, Scheme 6.4). In general, the barriers do not change very much with varying substitution and the barrier of the parent pyridine system is lowest. Electrostatic

potential maps of the geometries of the 1,2-shift indicate that the electron density is localized on the nitrogens, though the electron density of the carbons involved in the 1,2-shift are similar across all the systems (Figure 6.6).

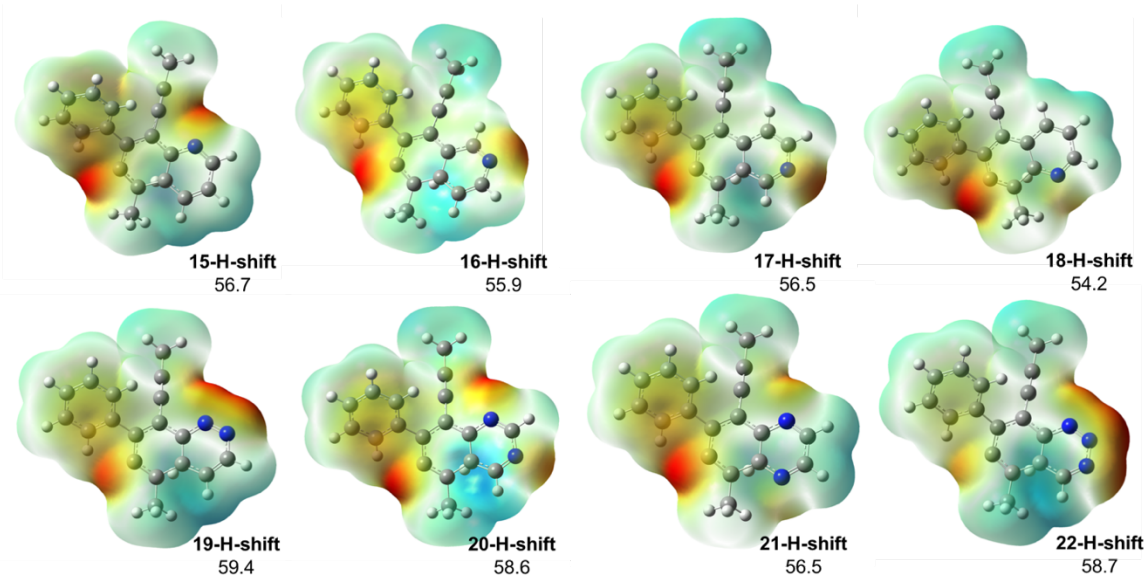

Figure 6.6. Electrostatic potential surfaces of the 1,2-shift transition state for nitrogen-based systems.

6.8 Conclusions

The Rubin group has demonstrated the cyclization of polydiacetylene (PDA) polymers in solid state to form graphene nanoribbons at high temperatures ranging from 350-500°C. This transformation proceeds through a Hopf cyclization, where the dienyne precursor undergoes initial cyclization, forms an allene intermediate, and undergoes a rate-limiting 1,2-H-shift. In collaboration with the Rubin lab, we first studied a series of model systems (Generation I) and found the barrier for this rate-limiting step to range between ~57 to 64 kcal mol^{-1} with various R groups. Towards the goal of lowering the barrier of these reactions to allow for this transformation to occur at lower temperatures, we pursued a series of strained cyclic systems (Generation II and III). We find that the barrier of the 1,2-shift can be lowered with cyclohexene systems and addition of a bridged moiety allows for further decrease in the reaction barriers of both cyclization and 1,2-

shift. We have identified that the oxanorbornadiene system is a promising system for lower barriers to GNR formation and can serve as an attractive precursor for subsequent rearomatization. We also studied pyridyl and other *N*-substituted systems (Generation IV and V), could which lead to doped GNRs that would carry interesting redox activities. We probed the effect of the degree of *N*-substitution on reaction rate, but unfortunately, heteroarenes with a variety of substitution patterns had little effect on the barrier of the 1,2-shift, which were consistently ~54 to 59 kcal mol^{-1}.

6.9 References

[1] Allen, M. J.; Tung, V. C.; Kaner, R. B. *Chem. Rev.* **2010**, *110*, 132−145.

[2] Nakada, K.; Fujita, M.; Dresselhaus, G.; Dresselhaus, M. S. *Phys. Rev. B: Condens. Matter Mater. Phys.* **1996**, *54*, 17954−17961.

[3] Dutta, S.; Pati, S. K. *J. Mater. Chem.* **2010**, *20*, 8207−8223.

[4] We are proposing the use of a modified nomenclature for the armchair (A) or zigzag (Z) topologies of GNRs, in which the A or Z letters are subscripted in front of the GNR acronym. The established convention for GNR width, indicated by the number of carbons within the GNR width, is placed in between brackets at the front of the AGNR or ZGNR terms. Thus, N = 8 armchair graphene nanoribbons are designated as [8]AGNR rather than the current designation (8- AGNR), while N = 12 zigzag GNRs would be designated as [12]ZGNR (instead of 12-ZGNR). However, the current nomenclature for GNRs with 2D "chirality" can be retained, as it is defined by the [n,m] numerals (n = zigzag edge repeat carbons, m = armchair edge repeat carbons) in front of the GNR abbreviation.

[5] Yang, L.; Park, C.-H.; Son, Y.-W.; Cohen, M. L.; Louie, S. G. *Phys. Rev. Lett.* **2007**, *99*, 186801.

[6] Kimouche, A.; Ervasi, M. M.; Drost, R.; Halonen, S.; Harju, A.; Joensuu, P. M.; Sainio, J.; Liljeroth, P. *Nat. Commun.* **2015**, *6*, 10177.

[7] Yang, W.; Lucotti, A.; Tommasini, M.; Chalifoux, W. A. *J. Am. Chem. Soc.* **2016**, *138*, 9137−9144.

[8] Jañsch,D.; Ivanov,I.; Zagranyarski,Y.; Duznovic,I.; Baumgarten, M.; Turchinovich, D.; Li, C.; Bonn, M.; Müllen, K. *Chem. - Eur. J.* **2017**, *23*, 4870−4875.

[9] Zhang, H.; Lin, H.; Sun, K.; Chen, L.; Zagranyarski, Y.; Aghdassi, N.; Duhm, S.; Li, Q.; Zhong, D.; Li, Y.; Müllen, K.; Fuchs, H.; Chi, L. *J. Am. Chem. Soc.* **2015**, *137*, 4022−4025.

[10] Tour, J. M. *Chem. Mater.* **2014**, *26*, 163−171.

[11] Sommer, B.; Sonntag, J.; Ganczarczyk, A.; Braam, D.; Prinz, G.; Lorke, A.; Geller, M. *Sci. Rep.* **2015**, *5*, 7781.

[12] Kosynkin, D. V.; Higginbotham, A. L.; Sinitskii, A.; Lomeda, J. R.; Dimiev, A.; Price, B. K.; Tour, J. M. *Nature* **2009**, *458*, 872−876.

[13] Li, X.; Wang, X.; Zhang, L.; Lee, S.; Dai, H. *Science* **2008**, *319*, 1229−1232.

[14] Cai, J.; Ruffieux, P.; Jaafar, R.; Bieri, M.; Braun, T.; Blankenburg, S.; Muoth, M.; Seitsonin, A. P.; Saleh, M.; Feng, X.; Müllen, K.; Fasel, R. *Nature* **2010**, *466*, 470−473.

[15] Ruffieux, P.; Wang, S.; Yang, B.;Sańchez-Sańchez, C.; Liu, J.; Dienel, T.; Talirz, L.; Shinde, P.; Pignedoli, C. A.; Passerone, D.; Dumslaff, T.; Feng, X.; Müllen, K.; Fasel, R. *Nature* **2016**, *531*, 489− 492.

[16] Yang, X.; Dou, X.; Rouhanipour, A.; Zhi, L.; Raẗder, J.; Müllen, K. *J. Am. Chem. Soc.* **2008**, *130*, 4216−4217.

[17] Li, G.; Yoon, K.-Y.; Zhong, X.; Zhu, X.; Dong, G. *Chem. - Eur. J.* **2016**, *22*, 9116−9120.

[18] Narita, A.; Verzhbitskiy, I. A.; Frederickx, W.; Mali, K. S.; Jensen, S. A.; Hansen, M. R.; Bonn, M.; De Feyter, S.; Casiraghi, C.; Feng, X.; Müllen, K. *ACS Nano* **2014**, *8*, 11622−11630.

[19] Gao, J.; Uribe-Romo, F. J.; Saathoff, J. D.; Arslan, H.; Crick, C. R.; Hein, S. J.; Itin, B.; Clancy, P.; Dichtel, W. R.; Loo, Y.-L. *ACS Nano* **2016**, *10*, 4847−4856.

[20] Park, I. S.; Park, H. J.; Kim, J.-M. ACS Appl. Mater. Interfaces 2013, 5, 8805−8812.

[21] Lauher, J. W.; Fowler, F. W.; Goroff, N. S. *Acc. Chem. Res.* **2008**, *41*, 1215−1229.

[22] Ishijima, Y.; Okaniwa, M.; Oaki, Y.; Imai, H. *Chem. Sci.* **2017**, *8*, 647−653.

[23] Luo, L.; Wilhelm, C.; Young, C. N.; Grey, C. P.; Halada, G. P.; Xiao, K.; Ivanov, I. N.; Howe, J. Y.; Geohegan, D. B.; Goroff, N. S. *Macromolecules* **2011**, *44*, 2626−2631.

[24] Luo, L.; Resch, D.; Wilhelm, C.; Young, C. N.; Halada, G. P.; Gambino, R. J.; Grey, C. P.; Goroff, N. S. *J. Am. Chem. Soc.* **2011**, *133*, 19274−19277.

[25] Levesque,I.;Neábo,J.R.;Rondeau-Gagne,́S.;Vigier-Carrieѐ, C.; Diagle, M.; Morin, J.-F. *Chem. Sci.* **2014**, *5*, 831−836.

[26] Suzuki, M.; Comito, A.; Khan, S. I.; Rubin, Y. *Org. Lett.* **2010**, *12*, 2346−2349.

[27] Suzuki, M.; Khosrowabadi Kotyk, J. F.; Khan, S. I.; Rubin, Y. *J. Am. Chem. Soc.* **2016**, *138*, 5939−5956.

[28] Jordan, R. S.; Wang, Y.; McCurdy, R. D.; Yeung, M. T.; Marsh, K. L.; Khan, S. I.; Kaner, R. B.; Rubin, Y. *Chem.* **2016**, *1*, 78−90.

[29] Jordan, R. S.; Li, Y. L.; Lin, C.-W.; McCurdy, R. D.; Lin, J. B.; Brosmer, J. L.; Marsh, K. L.; Khan, S. I.; Houk, K. N.; Kaner, R. B.; Rubin, Y. Synthesis of N = 8 Armchair Graphene Nanoribbons from Four Distinct Polydiacetylenes. *J. Am. Chem. Soc.* **2017**, *139*, 15878-15890.

[30] Becke, A. D. *J. Chem. Phys.* **1993**, *98*, 5648−5652.

[31] Lee, C.; Yang, W.; Parr, R. G. *Phys. Rev. B* **1988**, *37*, 785−789.

[32] Stephens, P. J.; Devlin, F. J.; Chabalowski, C. F.; Frisch, M. J. *J. Phys. Chem.* **1994**, *98*, 11623−11627.

[33] Vosko, S. H.; Wilk, L.; Nusair, M. *Can. J. Phys.* **1980**, *58*, 1200−1211.

[34] Bauschlicher, C. W., Jr.; Partridge, H. *J. Chem. Phys.* **1995**, *103,* 1788-1791.

[35] Wong, M. W. *Chem. Phys. Lett.* **1996**, *256*, 391-399.

[36] Zhao, Y.; Truhlar, D. G. *Phys. Chem. Chem. Phys.* **2008**, *10*, 2813-2818.

[37] Ribeiro, R. F.; Marenich, A. V.; Cramer, C. J.; Truhlar, D. G. *J. Phys. Chem. B* **2011**, *115*, 14556-14562.

[38] Zhao, Y.; Truhlar, D. G. *Theor. Chem. Acc.* **2008**, *120*, 215.

[39] Frisch, M. J.; Trucks, G. W.; Schlegel, H. B.; Scuseria, G. E.; Robb, M. A.; Cheeseman, J. R.; Scalmani, G.; Barone, V.; Mennucci, B.; Petersson, G. A.; Nakatsuji, H.; Caricato, M.; Li, X.; Hratchian, H. P.; Izmaylov, A. F.; Bloino, J.; Zheng, G.; Sonnenberg, J. L.; Hada, M.; Ehara, M.; Toyota, K.; Fukuda, R.; Hasegawa, J.; Ishida, M.; Nakajima, T.; Honda, Y.; Kitao, O.; Nakai, H.;

Vreven, T.; Montgomery, J. A., Jr.; Peralta, J. E.; Ogliaro, F.; Bearpark, M.; Heyd, J. J.; Brothers, E.; Kudin, K. N.; Staroverov, V. N.; Kobayashi, R.; Normand, J.; Raghavachari, K.; Rendell, A.; Burant, J. C.; Iyengar, S. S.; Tomasi, J.; Cossi, M.; Rega, N.; Millam, N. J.; Klene, M.; Knox, J. E.; Cross, J. B.; Bakken, V.; Adamo, C.; Jaramillo, J.; Gomperts, R.; Stratmann, R. E.; Yazyev, O.; Austin, A. J.; Cammi, R.; Pomelli, C.; Ochterski, J. W.; Martin, R. L.; Morokuma, K.; Zakrzewski, V. G.; Voth, G. A.; Salvador, P.; Dannenberg, J. J.; Dapprich, S.; Daniels, A. D.; Farkas, Ö.; Foresman, J. B.; Ortiz, J. V.; Cioslowski, J.; Fox, D. J. *Gaussian 09, Revision B.01*; Gaussian, Inc.: Wallingford, CT, 2009.

[40] Legault, C. Y. *CYLview, 1.0 b*; *Université de Sherbrooke* (http://www.cylview.org), 2009.

[41] Watts, K. S.; Dalal, P.; Tebben, A. J.; Cheney, D. L.; Shelley, J. C. *J. Chem. Inf. Model.* **2014**, *54*, 2680.

[42] Jordan, R. S.; Wang, Y.; McCurdy, R. D.; Yeung, M. T.; Marsh, K. L.; Khan, S. I.; Kaner, R. B.; Rubin, Y. *Chem.* **2016**, *1*, 78−90.

[43] Prall, M.; Krüger, A.; Shreiner, P. R.; Hopf, H. *Chem. - Eur. J.* **2001**, *7*, 4386−4394.

[44] Zimmermann, G. Eur. *J. Org. Chem.* **2001**, *2001*, 457−471.

[45] (a) Becke, A. D. *J. Chem. Phys.* **1993**, *98*, 5648−5652. (b) Lee, C.; Yang, W.; Parr, R. G. Phys. Rev. B: *Condens. Matter Mater. Phys.* **1988**, *37*, 785−789. (c) Stephens, P. J.; Devlin, F. J.; Chabalowski, C. F.; Frisch, M. J. *J. Phys. Chem.* **1994**, *98*, 11623−11627. (d) Vosko, S. H.; Wilk, L.; Nusair, M. *Can. J. Phys.* **1980**, *58*, 1200−1211.

[46] Vosko, S. H.; Wilk, L.; Nusair, M. *Can. J. Phys.* **1980**, *58*, 1200−1211.

[47] Liu, F.; Paton, R. S.; Kim, S.; Liang, Y.; Houk, K. N. *J. Am. Chem. Soc.* **2013**, *135*, 15642-15649

[48] Wang, H.; Maiyalagan, T.; Wang, X. *ACS Catalysis* **2012**, *2*, 781-794.

Chapter 7. Design of a Stable *E*-Selective Olefin Metathesis Catalyst

7.1 Background

Since the advent of olefin metathesis, stereoselective olefin metathesis catalysts have been sought for use in academic and industrial applications. Traditional metathesis catalysts provide olefinic products in thermodynamic ratios, which typically favor the *E* isomer.[1,2,3,4] There have been extensive efforts by the Schrock and Hoveyda groups[5] and the Grubbs group[6] to develop *Z*-selective olefin metathesis catalysts. In particular, there has been extensive work on a ruthenium-based catalyst featuring a bidentate catechothiolate ligand that catalyzes Z-selective olefin metathesis through stereoretention (Figure 7.1, **I**).[7,8,9,10,11] This ruthenium complex has been shown to be especially useful in ring-opening metathesis polymerization and ring-opening cross metathesis. The large aryl groups on the N-heterocyclic carbene (NHC) ligand force the substituents at the α-positions of the metallacyclobutane (mcb) to point downwards, as depicted in Figure 7.1. This class of catalysts is also stereoretentive for *E*-olefins, as the catalysts feature an open pocket above the β-position of the metallacyclobutane that allows for the β-substituent to point up and promotes this selectivity. Although manipulations to the catalytic scaffold have enhanced the reactivity of the stereoretention, no kinetic *E*-selectivity has been directly imparted by the catalyst. Computations by the Houk group suggest that the bulk of the dithiolate ligand resides away from the metallacycle, therefore not providing much effect on the stereochemistry of the metallacycle.

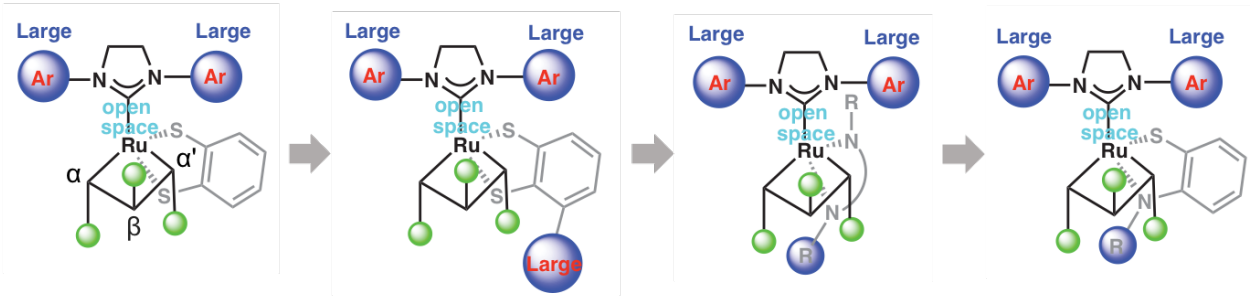

I
Dithiolate ligand

II
Dithiolate ligand with large aryl groups

III
Diamide ligand

IV
Thioamide ligand

Figure 7.1. Progress towards an *E*-selective catalyst.
Generations of anionic ligands with varying heteroatom substitution.

Towards the realization of a kinetically *E*-selective catalyst, the Houk and Grubbs group have studied several classes of ligands with bulky groups aimed to force the β-substituent up to allow for a *E*-to-*E* selective pathway. Unfortunately, even with extended conjugated ligands positioned *ortho* to the sulfur, as shown in **II**, there is no effect of the stereochemistry of the metallacycle compared with **I**.[12] Our groups next investigated a number of new diamide ligands which might be able to impart selectivity to the metallacycle via a bulky *N*-group (**III**). Our preliminary calculations on these new diamide ligands predict that the proper stereochemical arrangement favoring a kinetically *E*-selective pathway is preferred; however, these diamides were unable to be ligated to the metal center in experiments. We have since started exploring another class of thioamide (S,N) type catalysts (**IV**) that might allow for better coordination to ruthenium than the diamide ligands while still imposing steric bulk via the *N*-group .

In this chapter, I will describe computational studies of a new class of thioamide ligands designed by the Grubbs group that are expected to be highly *E*-selective (Scheme 7.1). These ligands are likely to be less basic than their diamide counterparts, as well as easier to synthesize and ligate successfully. Catalysts **1a** and **1b** have been synthesized and tested experimentally, and catalysts **1c**, **1d**, and **1e** are new predictions. This work serves as grounds for understanding

the reactivity and selectivity of this new class of Ru-complexes and we propose design principles for further development of these catalysts for academic and industrial use.

Scheme 7.1. Thioamide catalysts of interest

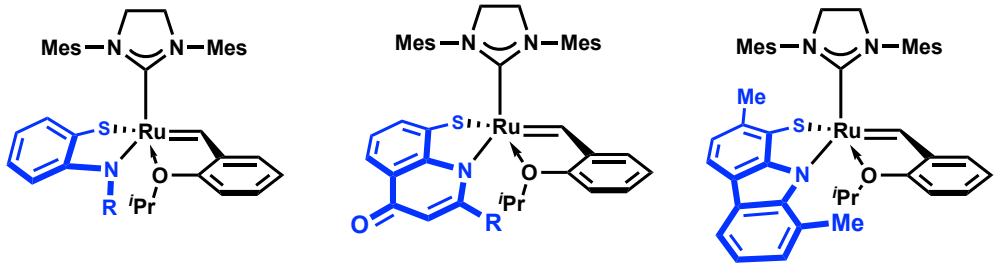

1a, **R** = Ms
1b, **R** = Boc

1c, **R** = Me
1d, **R** = Ph

1e

7.2 Experimental studies

The Grubbs group has achieved the synthesis of S,N catalysts **1a** and **1b** with anionic thioamide ligands that are *N*-functionalized with mesyl and tert-butyloxycarbonyl (Boc) groups, respectively. A crystal structure of **1a** has been obtained and shows the preferred conformation of the isopropoxy ligand, where the ether oxygen is facing away from the Ru center (Figure 7.2). This is different than the *O*-ligated conformation that is typically observed in dithiolate catalysts. The group has attempted to use this complex for metathesis (Table 7.1), though studies shows that the catalyst is not metathesis active, affording zero yield of **DE** and **9C18** and instead returns starting material **MO**. **1b** was also synthesized, but this complex was unfortunately unstable and underwent decomposition via C-H activation of the *ipso* methyl C-H of the NHC, similar to decomposition pathways of *Z*-selective Ru metathesis catalysts that have been observed previously.[13] Computations were employed to understand the lack of reactivity of these catalysts, as well as elucidate structural properties of the ligands to design new ligands that will allow for an active and selective metathesis catalyst.

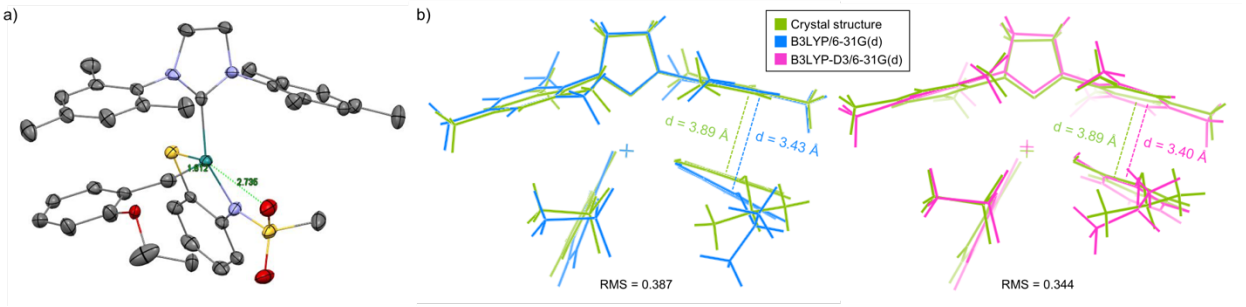

Figure 7.2. Structures of 1a.
(a) Crystal structure of **1a** (b) Overlay of crystal structure (green) with DFT-calculated geometries using B3LYP (blue) and B3LYP-D3.

Table 7.1. Metathesis activity studies of 1a

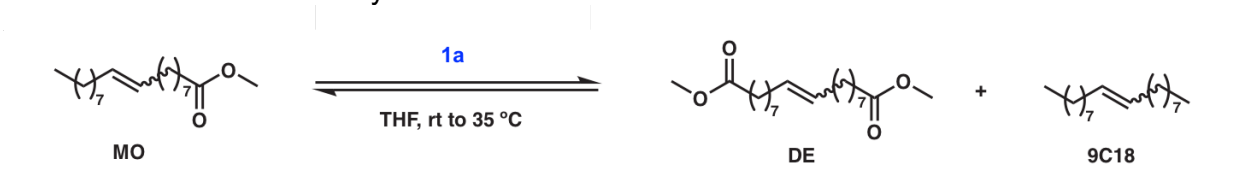

T	mol %	MO	time (h)	% MO (Z/E)	% DE (Z/E)	% 9C18 (Z/E)
rt	10 mol %	>99% Z	6 h	100% (12/1)	0	0
			20 h	100% (12/1)	0	0
rt	10 mol %	>99% E	6h	100% (1/43)	0	0
			20 h	100% (1/36)	0	0

7.3 Computational methods

All DFT computations were performed with Gaussian 09.[14] Ground state structures were optimized at the B3LYP level of theory using LANL2DZ for ruthenium and 6-31G(d) for other atoms.[15,16,17,18] Vibrational analysis was used to confirm all stationary points as minima (no imaginary frequencies) or transition structures (one imaginary frequency). Free energy corrections were calculated using Truhlar's quasiharmonic approximation, which sets all the real vibrational frequencies that are lower than 100 cm^{-1} to 100 cm^{-1} to correct entropies for the breakdown of the harmonic oscillator approximation.[19,20] Subsequent single-point energy calculations on the optimized structures were performed using at the M06 level of theory using SDD for ruthenium and 6-311+G(d,p) for all other atoms with the SMD continuum solvent model

for THF.[21,22] The thermal corrections calculated from the scaled vibrational frequencies at the B3LYP level on the optimized geometries were then added to the M06 electronic energies to obtain the Gibbs free energies. All graphics on optimized structures were generated with CYLview.[23]

In our studies on bottom-bound versus side-bound pathways, we also explored the effect of Grimme's dispersion correction on the optimized geometry.[24] While the geometries do differ slightly, with tighter π-stacking between aryl moieties in the complex, we find that the overall energies are similar. The inclusion of dispersion results in higher Δ*G* values, though ΔΔ*G* trends remain similar. A comparison of the calculated geometry of **1a** using B3LYP and B3LYP-D3 against the crystal structure is shown in Figure 7.2.

7.4 Computational results of S,N-mesyl catalyst 1a

The mechanistic pathway that this study follows is delineated in Scheme 7.2 and is similar to previous studies. We use *trans*-2-butene as a model olefin. The pathway starts with catalyst initiation via ligand exchange (Scheme 7.2A). Once the ethylidene **et** has been generated, it can undergo two different metathesis pathways, a side-bound pathway, where the olefin approaches orthogonal to the NHC ligand, (Scheme 7.2B, left) and a bottom-bound pathway, where the olefin approaches trans to the NHC (Scheme 7.2B, right). Ground state structures are depicted in the catalytic cycle (Scheme 7.2B) and transition states are depicted in Scheme 7.2C. The steps in the pathways are analogous, starting with olefin coordination to give **3**, which then undergoes metathesis (**4**) to give the four-membered metallacyclobutane (**5**) (we will focus on these structures). Cycloreversion (**6**) releases the olefin product and the ethylidene, which then can go through the cycle again.

Scheme 7.2. Metathesis pathway for representative S,N-catalyst

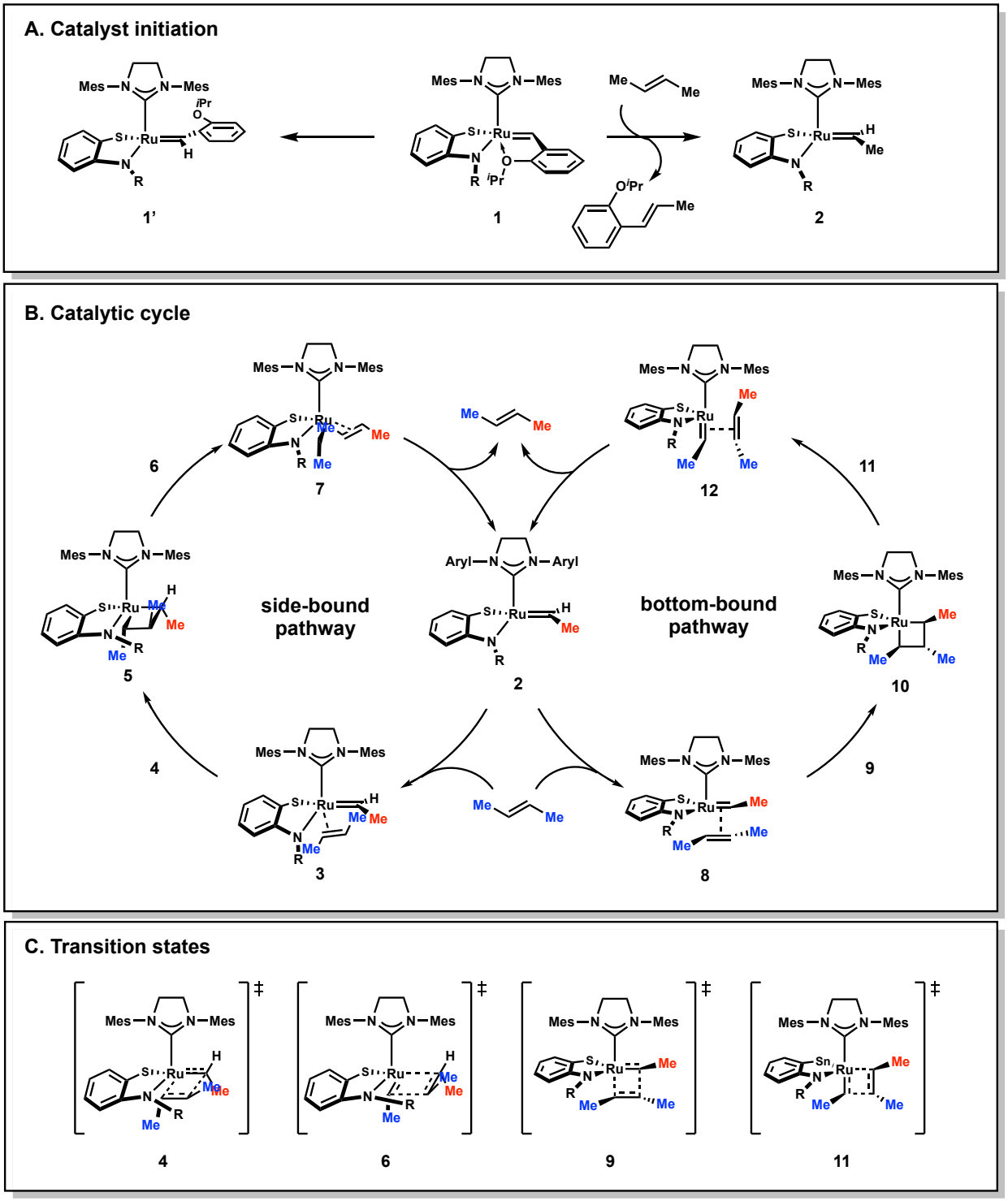

Initiation

We begin by computing the energies of catalyst initiation. For most benzylidene-based olefin metathesis catalysts, the resting state typically prefers to adopt a bound conformation as in **1**, where the ether oxygen is coordinated to the ruthenium center, over an unbound conformation, as in **2**, where the ether points away from the metal center. Initiation from its resting state occurs to generate the active catalyst, ethylidene **2**, by undergoing ligand exchange with free olefin to liberate the *o*-alkoxystyrene derivative. It is a challenge to ascertain the exact mechanism by which the catalyst is activated and undergoes ligand exchange to form the corresponding alkylidene, as this can proceed through a dissociation, association, or interchange mechanism.[25]

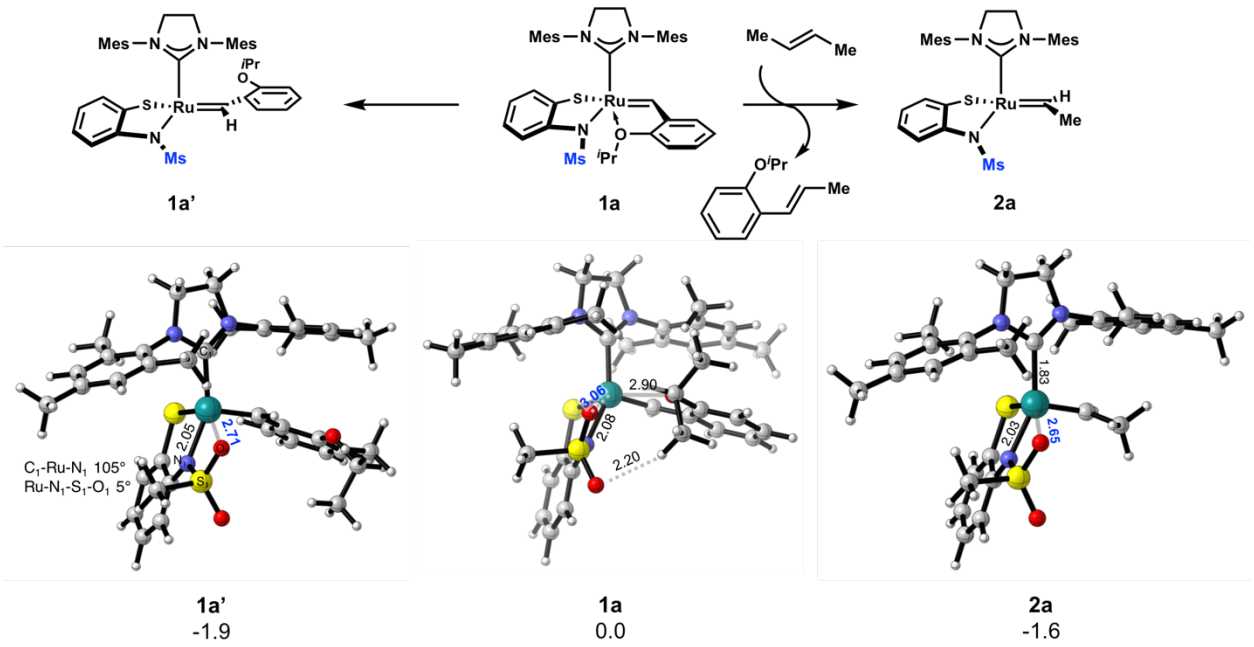

Figure 7.3. Estimation of initiation barriers.
DFT-optimized structures of structures involved in estimating catalyst initiation rate. Values below structure names are free energies in kcal mol^{-1} relative to chelated catalyst **1a**. Labels on structure images are bond distances in angstroms (Å) unless otherwise indicated.

A method has been developed to estimate the rate of initiation of second-generation Ru olefin metathesis catalysts by a measure of Ru-O bond strength.[26,27] This method has been extensively benchmarked by the Grubbs, Houk, and Liu groups with good correlation for benzylidene-containing catalysts. Following this model, we estimate the reactivity of **1a** by (1)

comparing the reaction energy to go from **1** to **1'** and (2) comparing the reaction energy to form the active form **2** from the full benzylidene **1**. We make mention that this method may not be an ideal fit for these new systems but nevertheless helps paint a qualitative picture of the reactivity of these catalysts.

The catalyst prefers the conformation of **1a'** over the *O*-chelated conformation of **1a** by 1.9 kcal mol^{-1} (Figure 7.3). This is different than benzylidene catalysts with dithiolate groups, where the benzylidene ligand prefers to be *O*-chelated. This preference can be explained by the stabilizing Ru-O interaction that occurs in **1a'** with the *N*-mesyl group, which is disrupted in **1a**. The Ru-O interaction in **1a'** (Ru-O 2.71 Å) is stronger than the interaction in **1a** (Ru-O 3.06 Å), thus providing more stabilization for the complex overall. Similar energies were computed for **1b**, where the **1b'** is more stable by 1.1 kcal mol^{-1}. This allows us to extrapolate an initiation rate of k_{est} = 3.4–4.4 10^5 s^{-1} based on our previous work.[26,27]

We now turn to looking at the reaction energy for formation of the active state of the catalyst (**2a**). The reaction energy for this ligand exchange process is exergonic by −1.6 kcal mol^{-1}, which in turn gives an estimated value of 8.7 × 10^3 for k_{est}. The geometry of the ethylidene is similar to that of the unchelated full catalyst, where there is a strong Ru-O interaction (2.65 Å). To rotate the N-mesyl group costs energy, as this motion breaks the Ru-O interaction. Rotation about that bond in the clockwise and counterclockwise direction incurs an energetic penalty of 7.0 and 11.5 kcal mol^{-1}, respectively. This Ru-O interaction is an important factor in the overall reactivity of the catalyst and will be further discussed in the context of the metathesis pathway.

Table 7.2. Energies for olefin coordination, metathesis barrier, and metallacyclobutane formation

		Side-bound			Bottom-bound	
		3	**4**	**5**	**9**	**10**
1a	*E*-to-*E*	16.6	24.7	20.3	34.5	9.5
	E-to-*Z*	17.0	32.4	29.2	34.8	13.5
1c	*E*-to-*E*	19.8	31.2	27.6	32.4	11.2
	E-to-*Z*	17.7	38.1	33.3	33.5	16.7
	Z-to-*Z*	-	43.0	36.3	38.4	15.0
	Z-to-*E*	-	40.4	18.9	-	14.0
1d	*E*-to-*E*	22.4	31.6	28.0	-	15.5
	E-to-*Z*	-	32.7	28.5	-	18.2
1e	*E*-to-*E*	-	31.8	27.2	34.4	9.7
	E-to-*Z*	-	36.0	33.6	34.4	17.4

Values are free energies in kcal mol^{-1}.

Olefin coordination

We next computed the energies of olefin complexation (**3a**) (Table 7.2, Figure 7.4). It has been established that the preferred pathway is through a side-bound pathway where the olefin approaches the complex from the side rather than the bottom, so we will focus on the side-bound pathway first.[7] Typical complexation energies for dithiolate catalysts via this side-bound pathway are ~2.5-3.3 kcal kcal mol^{-1} (the detailed energies will be discussed in the succeeding chapter). For this catalyst, this complexation is endergonic for both *E*-to-*E* and *E*-to-*Z* pathways (16.6 and 17.0 kcal mol^{-1}, respectively) due to the necessity to distort ligand sphere. In the coordinated complex, there is a loss of the Ru-O interaction and lengthened Ru-N bond (~0.2 Å increase) that occurs in order to accommodate the olefin. Compared to **2a**, there is also an increase in C_1-Ru-N_1 bond angle from 151° to ~161°. This disruption of the ligand sphere accounts for the large complexation barrier, which likely plays in a role in rendering the catalyst inactive.

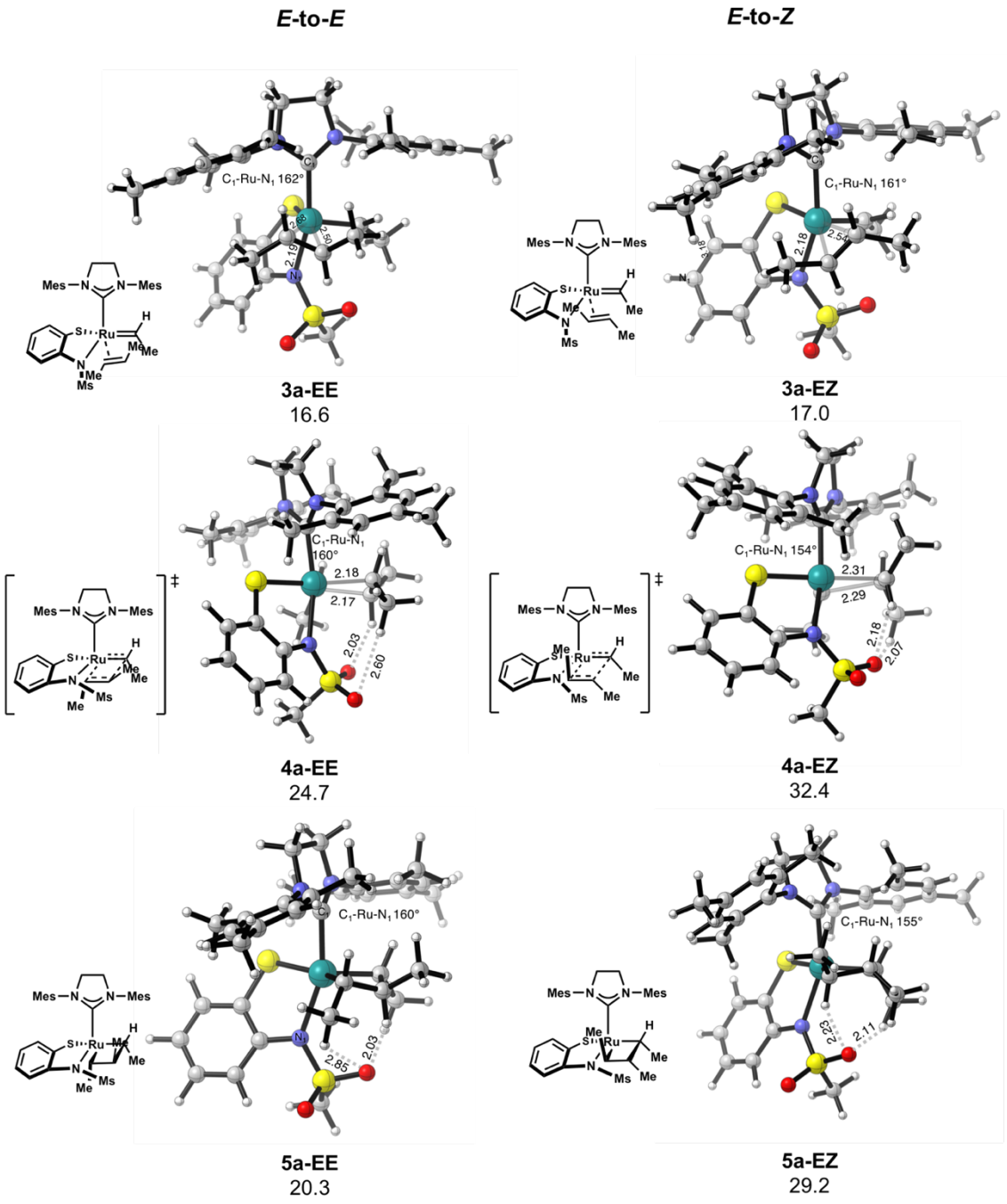

Figure 7.4. Structures for catalyst 1a.
Structures of side-bound olefin-coordinated complexes (**3a**), metathesis transition state (**4a**), and metallacyclobutane (**5a**) for the *E*-to-*E* and *E*-to-*Z* pathways with the ligand **a**. Values are free energies in kcal mol^{-1} relative to separated **2a** and *trans*-2-butene. Labels on structure images are bond distances in angstroms (Å) unless otherwise indicated.

With these structures in hand, we can make conclusions about the factors that dictate the selectivity. For both **4a-EE** and **4a-EZ** structures, the substituent that is pointing up prefers to

reside in the open pocket between the two NHC aryl groups, following the established stereochemical model for stereorententive dithiolate catalysts. In **4a-EE**, the β-substituent is pointing upwards and can be cradled between the NHC aryl groups with change to the ligand sphere and the α-substituent pointing down is far from the *N*-Ms group. In **4a-EZ**, the α-substituent is pointing upwards and in order to adopt this conformation, the NHC must rotate to accommodate the methyl group in this open pocket. This forces the α-methyl pointing down close to the *N*-Ms group, making this transition state less favorable. The selectivity for the *E*-to-*E* metathesis transition state is dictated by the preference for the group pointing upwards to be pocketed between the NHC aryl groups.

The preference for the **5a-EE** is dictated by other factors. Regardless of whether the β-substituent pointing upwards is methyl or hydrogen, the β-group prefers to be in the open pocket. The substituent that is pointing upward (whether in the α- or β-position) interacts with the NHC ligand and causes the C_{NHC}-Ru-C angle of that position to open, forcing the group downward, closer to the *N*-Ms group, and twisting the mcb overall. This effect is more pronounced when the β-methyl is pointing downward, as in **5a-EZ**, as the methyl group interacts with the N-Ms group. In **5a-EE**, the β-substituent pointing downward is hydrogen and has less steric interactions with N-Ms. The α-methyl group pointing downward is far enough away from the N-Ms group to not have a great steric impact, making the **5a-EE** more favorable. In the **5a** structures, the selectivity is dictated by whether the β-substituent is pointing downward or upward.

It has been established and accepted in the community that dithiolate catalysts proceed via a side-bound pathway, but we were curious as to whether this was applicable to this new class of thioamide catalysts as well. The bottom-bound metallacyclobutanes **10a-EE** and **10a-EZ** were computed (Scheme 7.2A, right), which are significantly lower in energy than the analogous side-bound structures. **10a-EE** is 9.5 kcal mol^{-1} and **10a-EZ** is 13.5 kcal mol^{-1}, with a preference for the *E*-to-*E* mcb by 4.0 kcal mol^{-1}. The barriers to mcb formation are 34.5 for 34.8 kcal mol^{-1},

respectively. The mcb energies are lower for the bottom-bound pathway, likely due to the stabilizing π-π interactions between the aryl group of the S,N ligand and the *N*-mesityl group on the NHC. However, there is a significant kinetic preference of almost 10 kcal mol^{-1} for the side-bound pathway, ruling out the possibility of the bottom-bound pathway for this catalyst.

7.5 Predictions of other S,N catalysts

The prospect that this new class of S,N-type catalysts could realize a truly kinetically *E*-selective catalyst is exciting; however, **1a** is not metathesis active experimentally. Based on our calculations, we surmise that the chelation of the *N*-Ms group stabilizes the ethylidene, resulting in high barriers to olefin coordination and metallacyclobutane formation. With this in mind, the Grubbs group designed other π-conjugated S,N catalysts **1c**, **1d**, and **1e**. The design of the ligand was driven by reducing the basicity of the nitrogen with extended conjugation, imparting stereocontrol via R group substitution, and locking the ligand into place with a rigid structure. Computations were employed to make predictions on the reactivity and selectivity of these newly-designed catalysts. The energies for olefin coordination, metathesis barrier, and metallacyclobutane formation are shown in Table 7.2.

The structures of **2c**-**e** are shown in Figure 7.5. The geometry of these ethylidene structures are similar, with the sulfur bound to the metal center orthogonal to the NHC (N_{NHC}-Ru-S_L ~91−93°) and the nitrogen bound in a trans-like manner to the NHC. Due to the structural constraints of the bidentate S,N ligand, the nitrogen is not completely trans and the N_{NHC}-Ru-N_L angle is 149-153°. Like **2a**, ethylidenes **2c** and **2d** also have high olefin coordination energies. To accommodate for the incoming olefin, the ligand sphere must be distorted, opening up the N_{NHC}-Ru-N_L angle to ~162−163° for **3c** and ~157° for **3d** and increasing the Ru-N_L bond length from ~2.04−2.09 to 2.21−2.24 Å, resulting in a weakly coordinated ligand. This results in high energies of ~17−22 kcal mol^{-1}, making it unlikely for metathesis to be feasible without harsh reaction conditions.

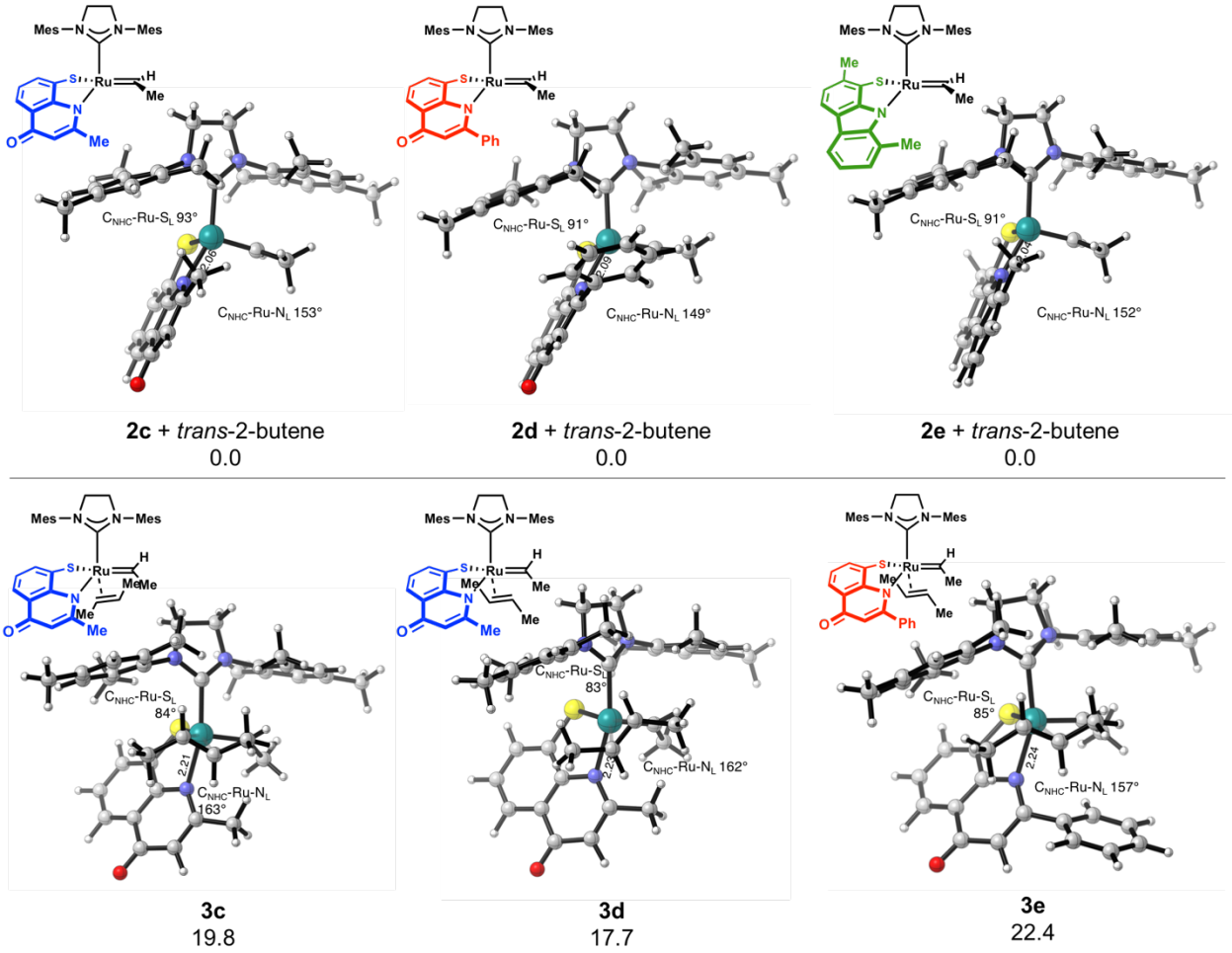

Figure 7.5. Ethylidene 2 and olefin coordination structures 3 of ligands c-e. Values are free energies in kcal mol^{-1} relative to separated **2** and *trans*-2-butene for each system. Labels on structure images are bond distances in angstroms (Å) unless otherwise indicated.

For ligand **c**, the side-bound *E*-to-*E* pathway is favored over the *E*-to-*Z* pathway, although these energies are relatively high (31.2 and 27.6 kcal mol^{-1} for **4c-EE** and **5c-EE**, respectively) (Figure 7.6). This pathway is also in direct competition with the analogous bottom-bound pathway; while the side-bound pathway is slightly more favorable kinetically by 1.2 kcal mol^{-1}, **5c-EE** is 16.4 kcal mol^{-1} higher in energy than the **10c-EE** (refer to Table 7.2 for energies). Both pathways are have high barriers and we are unable to make concrete conclusions about which pathway is favored. However, we can take a look at these calculated structures in the side-bound pathway (however unfavorable they may be) to draw conclusions about the origin of selectivity.

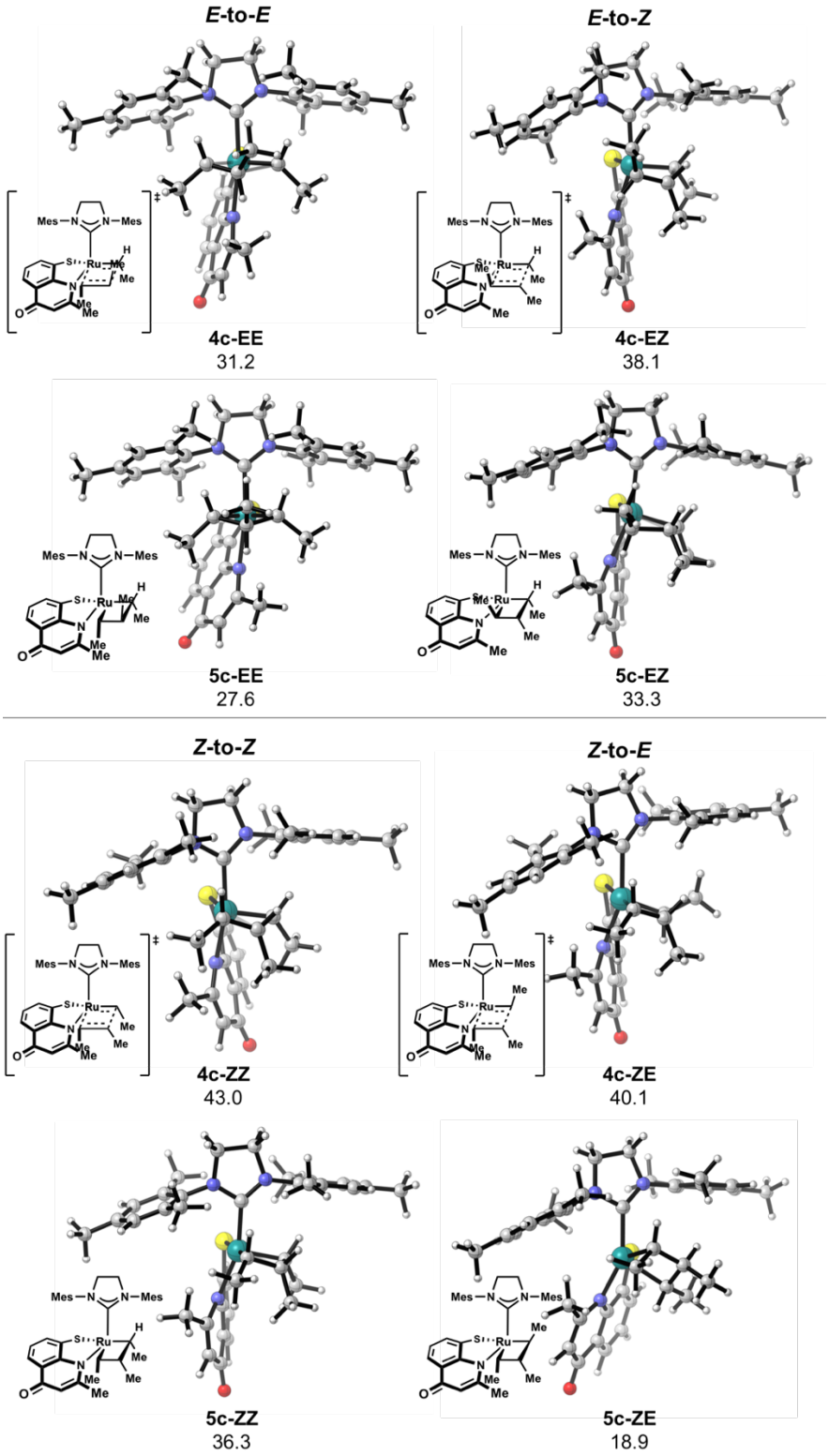

Figure 7.6. Metathesis transition states and mcb structures for catalyst 1c.
Metathesis transition state and metallacyclobutane structures in the *E*-to-*E, E*-to-*Z, Z*-to-*Z, and Z*-to-*E* pathways for ligand **c**. Values are free energies in kcal mol^{-1} relative to **2c** and *trans*-2-butene.

The selectivity for both **4c-EE** and **5c-EE** seem to be dictated by the NHC aryl groups, which is in alignment with the stereochemical model for stereoretentive dithiolate catalysts. Regardless of whether it is in the α- or β-position, the group that point upwards prefers to reside in the open pocket between the NHC aryl groups. In **5c-EE**, the *N*-Me group resides in the empty space below the β-position of the mcb, whereas in **5c-EZ** pathway, the ligand sphere must reorient so that the *N*-Me group can reside below the α-position of the mcb, making this pathway less favorable. The structures for the *Z*-to-*Z* and *Z*-to-*E* pathways were also computed, which are even higher in energy. In both **5c-ZZ** and **5c-ZE**, the methyl group pointing downward towards the *N*-Me group forces the ligand to twist in order to orient the methyl away from the mcb.

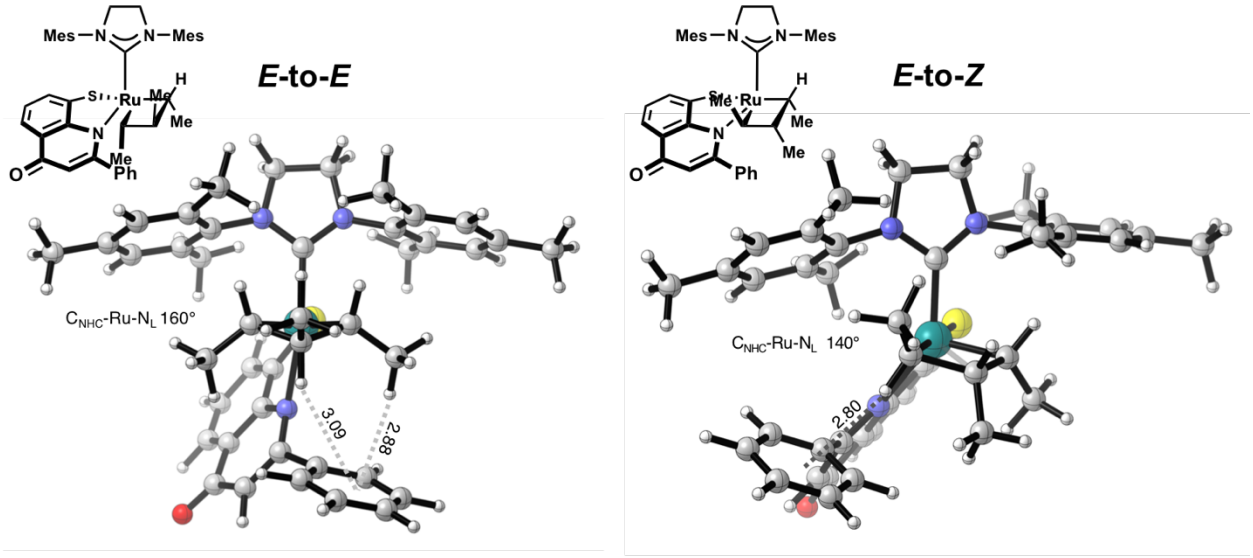

5d-EE
28.0

5d-EZ
28.5

Figure 7.7. Metallacyclobutane structures 5d-EE and 5d-EZ
Values are free energies in kcal mol^{-1} relative to **2d** and *trans*-2-butene.

Catalyst **1d** is less selective than its analogous methyl-substituted catalyst **1c**. The mcb structures **5d-EE** and **5d-EZ** are shown in Figure 7.7. The structures and energies of **5d-EE** and **5c-EE** are similar, where the β-substituent pointing up is located in between the NHC aryl groups. The C_{NHC}-Ru-N_L bond angle in **5d-EE** is almost linear (160°), keeping the phenyl group away from

the mcb. The structure of **5d-EZ** is also similar to that of **5c-EZ**, where the α-substituent resides in the open pocket between the NHC aryl groups. However, **5d-EZ** is about the same energy as **5d-EE** and therefore the catalyst is not selective. This may be attributed to a stabilizing CH-π interaction in 5d-EZ that is not found in the analogous methyl-substituted **5c-EZ**. The lack of selectivity is reflected in the metathesis transition state barriers as well (31.6 and 32.7 for **4d-EE** and **4d-EZ**, respectively).

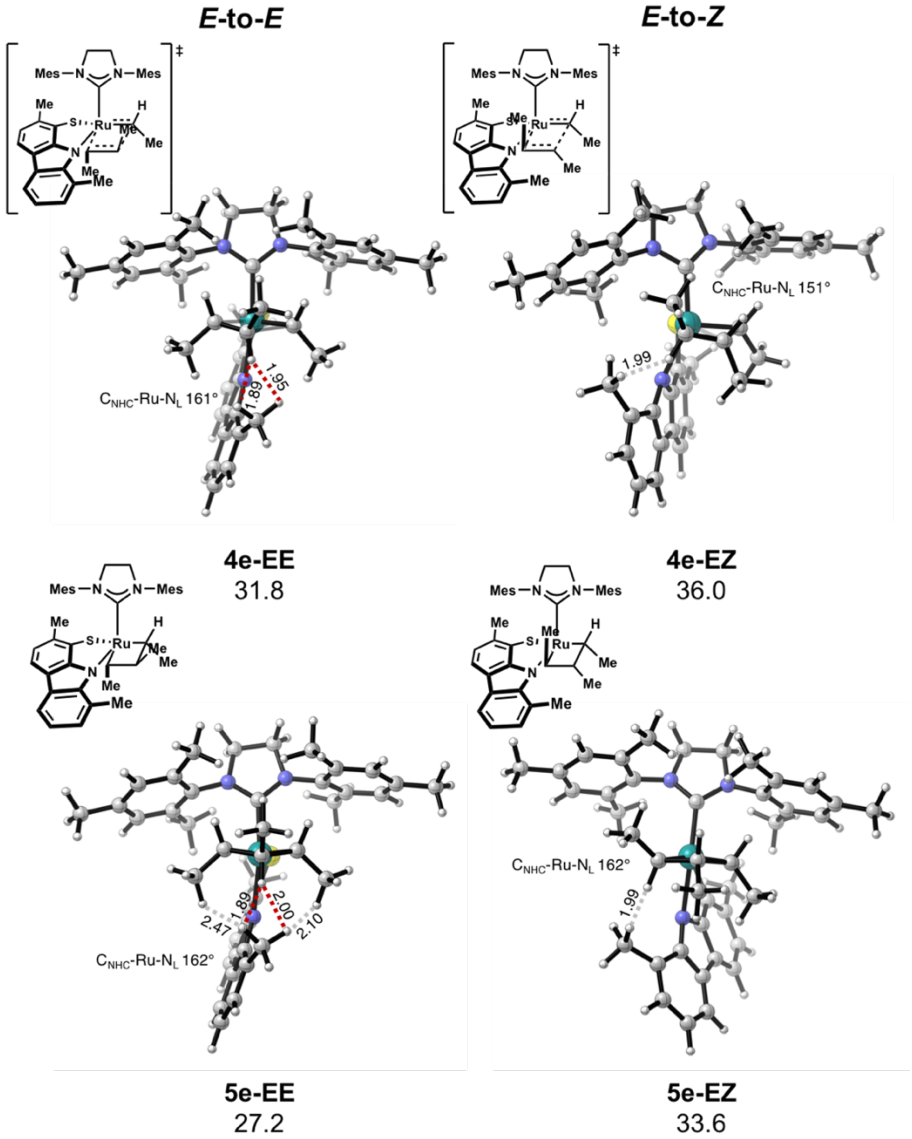

Figure 7.8. Metathesis transition state 4e and metallacyclobutane 5e structures for the *E*-to-*E* and *E*-to-*Z* pathways for ligand e.
Values are free energies in kcal mol^{-1} relative to **2e** and *trans*-2-butene.

Structures for catalyst **1e** are shown in Figure 7.8. Metathesis with **1e** likely proceeds through a side-bound mechanism and exhibits similar *E*-selectivity as in **1a**. In the transition state (**4e**), the substituent pointing up prefers to be in the open pocket. In **4e-EE**, this allows for the methyl group on the ligand to occupy the open space under the β-substituent, whereas in **4e-EZ**, this forces the methyl group on the ligand and the hydrogen on pointing downward in the α-position closer, resulting in unfavorable steric interactions. In the mcb structures (**5e-EE** and **5e-EZ**), the β-substituent pointing upward prefers to reside in the open pocket between the NHC aryl groups, resulting in unfavorable interactions between the methyl group and hydrogen α-substituent. Although **1e** is kinetically *E*-selective, the metathesis pathway is highly unfavorable due to distortion of the ligand sphere as the methyl group on the ligand must be forced out of the way for metathesis to occur; therefore, it is not a promising ligand. However, from these results, we are able to gain some insight into the ligand properties that may allow for useful, productive, and selective catalysts.

Table 7.3. Tuning energetics with substitution

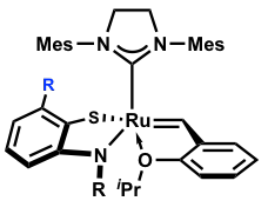

1a (R = H)
1f (R = NO_2)

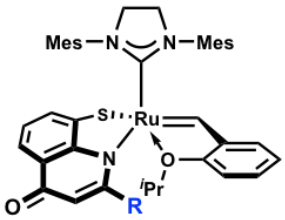

1c (R = Me)
1g (R = CF_3)

		Side-bound		Bottom-bound	
		4	**5**	**9**	**10**
1a	*E*-to-*E*	24.7	20.3	34.5	9.5
1f	*E*-to-*E*	23.4	19.5	31.5	8.8
1c	*E*-to-*E*	31.2	27.6	32.4	11.2
1g	*E*-to-*E*	31.6	27.4	30.0	11.6

Values are free energies in kcal mol^{-1} relative to **2** and *trans*-2-butene.

To attempt to lower the barrier to metathesis by functionalizing the ligands with electron-withdrawing groups, we performed computations on some theoretical models **1f** and **1g** to tune the energetics (Table 7.3). The energies remain very similar to the parent systems, indicating that the reactivity is largely dictated by steric and not electronic considerations.

7.6 Predictions of phosphorus-based catalyst

We hypothesized that changing the heteroatom from nitrogen to phosphorus would lessen the basicity of the ligand by another degree. With this in mind, the Grubbs group designed catalyst **1h** (inset, Figure 7.9). The structure of this S,P catalyst is similar to the **1a** structures, with reduced basicity due to substitution of nitrogen by phosphorus and steric control to be imparted by the phenyl group.

Preliminary calculations indicate the ligand **h** would not be *E*-selective. This ligand can ligate to the metal center in two ways either with the sulfur (**2h**) or phosphorus (**2h'**) trans to the NHC. The second conformation is the preferred binding mode, as this minimizes the steric repulsion of the *P*-phenyl group, which can be rotated away from the other ligands, as well as, unfortunately, the β-position of the metallacyclobutane and therefore would be able to impart no steric control.

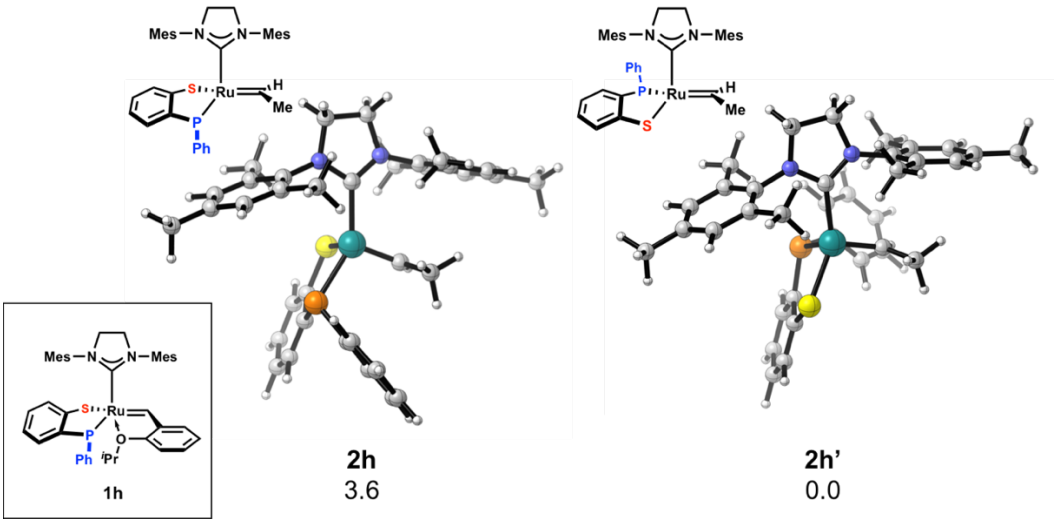

Figure 7.9. Ethylidene structures for two binding patterns of ligand h
Values are free energies in kcal mol^{-1}.

For completeness of this study and to ascertain whether this proposed stereochemical model is valid, we computed the selectivity of the catalyst if it were to adopt the first conformation in **2h**, where S binds trans to the NHC (Figure 7.10). In this less favorable conformation, the *P*-phenyl group can hinder the β-position of the mcb, favoring the *E*-to-*E* pathway. The *E*-to-*E* pathway is preferred over the *E*-to-*Z* pathway, and, interestingly, the *Z*-to-*Z* pathway over *Z*-to-*E*.

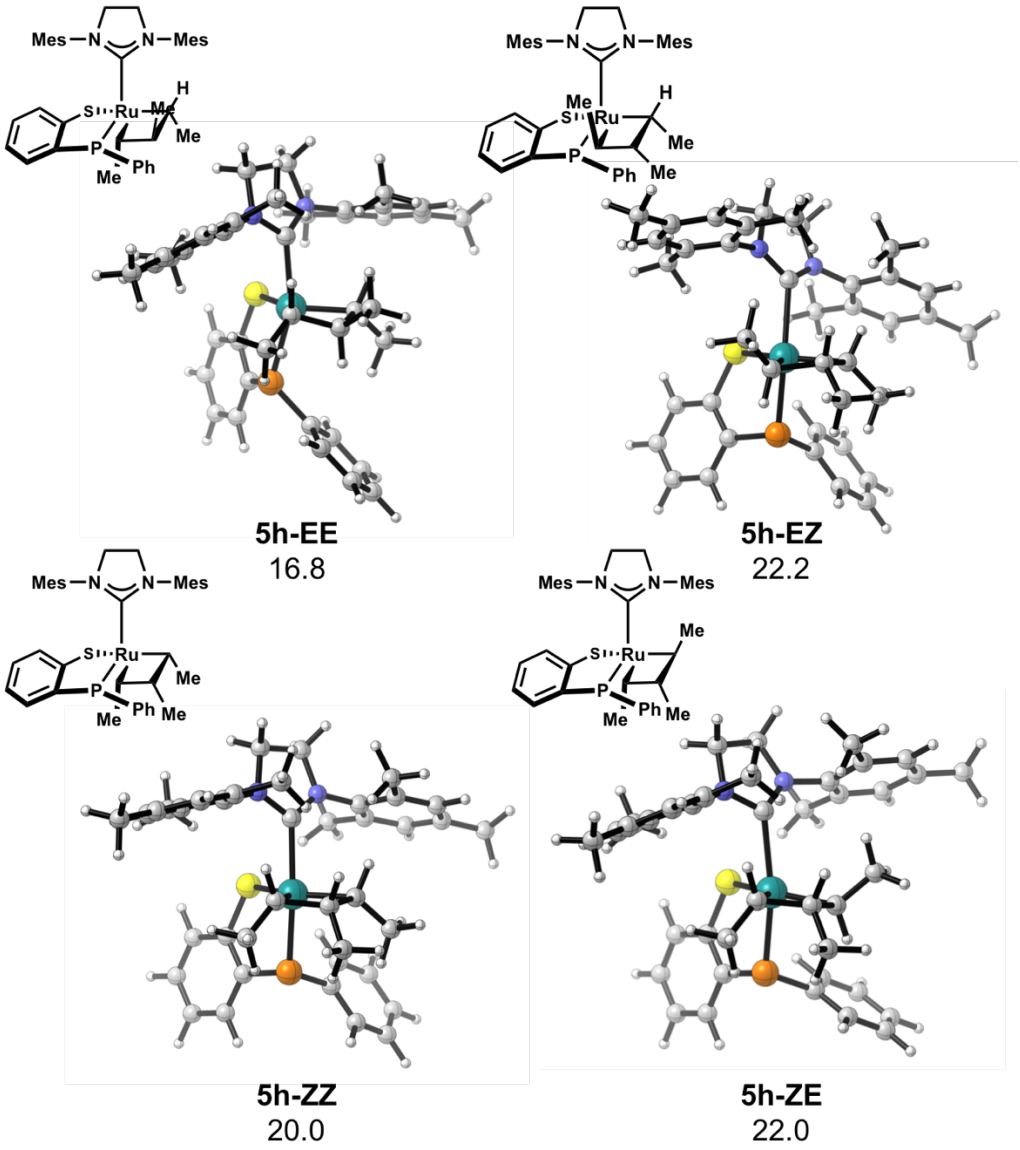

Figure 7.10. Metallacyclobutanes for all four pathways with ligand h
Values are free energies in kcal mol^{-1} relative to **2h** and *trans*-2-butene.

7.7 Conclusions and Outlook

We have shown that *E*-selective olefin metathesis can be achieved by ligand design. Using computations, we predict that by incorporating a sterically bulky group on a S,N-ligand, the selectivity can be governed. Unfortunately, this sterically bulky group results in high energy olefin complexation, which is necessary for olefin metathesis to occur. However, we believe that by fine-tuning the size and electronic nature of the R group, we can achieve a happy medium for a catalyst that imparts enough steric control for *E*-selectivity and low enough energies for olefin complexation.

7.8 References

[1] Couturier, J.-L.; Paillet, C.; Leconte, M.; Basset, J.-M.; Weiss, K. *Angew. Chem., Int. Ed. Engl.* **1992**, *31*, 628.

[2] Schrock, R. R.; Murdzek, J. S.; Bazan, G. C.; Robbins, J.; DiMare, M.; O'Regan, M. *J. Am. Chem. Soc.* **1990**, *112*, 3875.

[3] Scholl, M.; Ding, S.; Lee, C. W.; Grubbs, R. H. *Org. Lett.* **1999**, *1*, 953.

[4] Ritter, T.; Hejl, A.; Wenzel, A. G.; Funk, T. W.; Grubbs, R. H. *Organometallics* **2006**, *25*, 5740.

[5] For work on molybdenum and tungsten based *Z*-selective catalysts, see: (a) Ibrahem, I.; Yu, M.; Schrock, R. R.; Hoveyda, A. H. *J. Am. Chem. Soc.* **2009**, *131*, 3844. (b) Jiang, A. J.; Zhao, Y.; Schrock, R. R.; Hoveyda, A. H. *J. Am. Chem. Soc.* **2009**, *131*, 16630. (c) Flook, M. M.; Jiang, A. J.; Schrock, R. R.; Hoveyda, A. H. *J. Am. Chem. Soc.* **2009**, *131*, 7962. (d) Yu, M.; Wang, C.; Kyle, A. F.; Jakubec, P.; Dixon, D. J.; Schrock, R. R.; Hoveyda, A. H. *Nature* **2011**, *479*, 88. (e) Meek, S. J.; O'Brien, R. V.; Llaveria, J.; Schrock, R. R.; Hoveyda, A. H. *Nature* **2011**, *471*, 461. (f) Marinescu, S. C.; Levine, D. S.; Zhao, Y.; Schrock, R. R.; Hoveyda, A. H. *J. Am. Chem. Soc.* **2011**, *133*, 11512. (g) Yu, M.; Ibrahem, I.; Hasegawa, M.; Schrock, R. R.; Hoveyda, A. H. *J. Am. Chem. Soc.* **2012**, *134*, 2788. (h) Wang, C.; Haeffner, F.; Schrock, R. R.; Hoveyda, A. H. *Angew. Chem., Int. Ed.* **2013**, *52*, 1939. (i) Kiesewetter, E. T.; O'Brien, R. V.; Yu, E. C.; Meek, S. J.; Schrock, R. R.; Hoveyda, A. H. *J. Am. Chem. Soc.* **2013**, *135*, 6026. (j) Mann, T. J.; Speed, A. W. H.; Schrock, R. R.; Hoveyda, A. H. *Angew. Chem., Int. Ed.* **2013**, *52*, 8395.

[6] For work on ruthenium based *Z*-selective catalysts, see: (a) Herbert, M. B.; Grubbs, R. H. *Angew. Chem., Int. Ed.* **2015**, *54*, 5018. (b) Endo, K.; Grubbs, R. H. *J. Am. Chem. Soc.* **2011**, *133*, 8525. (c) Keitz, B. K.; Endo, K.; Herbert, M. B.; Grubbs, R. H. *J. Am. Chem. Soc.* **2011**, *133,* 9686. (d) Keitz, B. K.; Endo, K.; Patel, P. R.; Herbert, M. B.; Grubbs, R. H. *J. Am. Chem. Soc.* **2012**, *134*, 693. (e) Marx, V. M.; Herbert, M. B.; Keitz, B. K.; Grubbs, R. H. *J. Am. Chem.*

Soc. **2013**, *135*, 94. (f) Rosebrugh, L. E.; Herbert, M. B.; Marx, V. M.; Keitz, B. K.; Grubbs, R. H. *J. Am. Chem. Soc.* **2013**, *135*, 1276.

[7] Khan, R. K. M.; Torker, S.; Hoveyda, A. H. *J. Am. Chem. Soc.* **2013**, *135,* 10258-10261.

[8] Khan, R. K. M.; Torker, S.; Hoveyda, A. H. *J. Am. Chem. Soc.* **2014**, *136*, 14337-14340.

[9] Koh, M. J.; Khan, R. K. M.; Torker, S.; Hoveyda, A. H. *Angew. Chem. Int. Ed.* **2014**, *53,* 1968-1972.

[10] Koh, M. J.; Khan, R. K. M.; Torker, S.; Yu, M.; Mikus, M. S.; Hoveyda, A. H. *Nature* **2015**, *517*, 181-186.

[11] Grandner, J. M.; Shao, H.; Grubbs, R. H.; Liu, P.; Houk, K. N. *J. Org. Chem*. **2017**, *82*, 10595.

[12] Montgomery, T. P.; Grandner, J. M.; Houk, K. N.; Grubbs, R. H. *Organometallics* **2017**, *36,* 3940-3953.

[13] Herbert, M. B.; Lan, Y.; Keitz, B. K.; Liu, P.; Endo, K.; Day, M. W.; Houk, K. N.; Grubbs, R. H. *J. Am. Chem. Soc.* **2012**, *134,* 7861.

[14] Frisch, M. J.; Trucks, G. W.; Schlegel, H. B.; Scuseria, G. E.; Robb, M. A.; Cheeseman, J. R.; Scalmani, G.; Barone, V.; Mennucci, B.; Petersson, G. A.; Nakatsuji, H.; Caricato, M.; Li, X.; Hratchian, H. P.; Izmaylov, A. F.; Bloino, J.; Zheng, G.; Sonnenberg, J. L.; Hada, M.; Ehara, M.; Toyota, K.; Fukuda, R.; Hasegawa, J.; Ishida, M.; Nakajima, T.; Honda, Y.; Kitao, O.; Nakai, H.; Vreven, T.; Montgomery, J. A., Jr.; Peralta, J. E.; Ogliaro, F.; Bearpark, M.; Heyd, J. J.; Brothers, E.; Kudin, K. N.; Staroverov, V. N.; Kobayashi, R.; Normand, J.; Raghavachari, K.; Rendell, A.; Burant, J. C.; Iyengar, S. S.; Tomasi, J.; Cossi, M.; Rega, N.; Millam, N. J.; Klene, M.; Knox, J. E.; Cross, J. B.; Bakken, V.; Adamo, C.; Jaramillo, J.; Gomperts, R.; Stratmann, R. E.; Yazyev, O.; Austin, A. J.; Cammi, R.; Pomelli, C.; Ochterski, J. W.; Martin, R. L.; Morokuma, K.; Zakrzewski, V. G.; Voth, G. A.; Salvador, P.; Dannenberg, J. J.; Dapprich, S.; Daniels, A. D.; Farkas, Ö.; Foresman, J. B.; Ortiz, J. V.; Cioslowski, J.; Fox, D. J. *Gaussian 09, Revision B.01*; Gaussian, Inc.: Wallingford, CT, 2009.

[15] Becke, A. D. *J. Chem. Phys.* **1993**, *98*, 5648−5652.

[16] Lee, C.; Yang, W.; Parr, R. G. *Phys. Rev. B* **1988**, *37*, 785−789.

[17] Stephens, P. J.; Devlin, F. J.; Chabalowski, C. F.; Frisch, M. J. *J. Phys. Chem.* **1994**, *98*, 11623−11627.

[18] Vosko, S. H.; Wilk, L.; Nusair, M. *Can. J. Phys.* **1980**, *58*, 1200−1211.

[19] Zhao, Y.; Truhlar, D. G. *Phys. Chem. Chem. Phys.* **2008**, *10*, 2813-2818.

[20] Ribeiro, R. F.; Marenich, A. V.; Cramer, C. J.; Truhlar, D. G. *J. Phys. Chem. B* **2011**, *115*, 14556-14562.

[21] (a) Zhao,Y.; Truhlar, D. G. *Theor. Chem. Acc.* **2008**, *120*, 215-241. (b) Zhao, Y.; Truhlar, D. G. *Acc. Chem. Res.* **2008**, *41*, 157-167.

[22] Marenich, A. V.; Cramer, C. J.; Truhlar, D. G. *J. Phys. Chem. B* **2009**, *113*, 6378-6396.

[23] Legault, C. Y. *CYLview, 1.0 b*; *Université de Sherbrooke* (http://www.cylview.org), 2009.

[24] Grimme, S.; Antony, J.; Ehrlich, S.; Krieg, H. *J. Chem. Phys.* **2010**, *132,* 154104.

[25] For studies concerning the initiation of Hoveyda-Grubbs catalysts, see: (a) Vorfalt, T.; Wannowius, K. J.; Plenio, H. Angew. Chem., Int. Ed. 2010, 49, 5533−5536. (b) Thiel, V.; Hendann, M.; Wannowius, K. J.; Plenio, H. *J. Am. Chem. Soc.* **2012**, *134*, 1104−1114. (c) Nuñez-Zarur, F.; Solans-Monfort, X.; Rodríguez-Santiago, L.; Sodupe, M. *Organometallics* **2012**, *31*, 4203−4215. (d) Ashworth, I. W.; Hillier, I. H.; Nelson, D. J.; Percy, J. M.; Vincent, M. A. *ACS Catal.* **2013**, *3*, 1929−1939. (e) Bates, J. M.; Lummiss, J. A. M.; Bailey, G. A.; Fogg, D. E. *ACS Catal*. **2014**, *4*, 2387− 2394. (f) Nelson, D. J.; Manzini, S.; Urbina-Blanco, C. A.; Nolan, S. P. *Chem. Commun.* **2014**, *50*, 10355−10375. (g) Griffiths, J. R.; Keister, J. B.; Diver, S. T. *J. Am. Chem. Soc.* **2016**, *138*, 5380−5391.

[26] Engle, K. M.; Lu, G.; Luo, S.-X.; Henling, L. M.; Takase, M. K.; Liu, P.; Houk, K. N.; Grubbs, R. H. *J. Am. Chem. Soc*. **2015**, *137*, 5782

[27] Luo, S.-X.; Engle, K. M.; Dong, X.; Hejl, A.; Takase, M. K.; Henling, L. M.; Liu, P.; Houk, K. N.; Grubbs, R. H. *ACS Catal.* **2018**, *8*, 4600.

Chapter 8. Deactivation of Stereoretentive Dithiolate Catalysts via a 1,2-Sulfide Shift

8.1 Background

In 2013, Hoveyda and coworkers reported a Ru-based complex with a bidentate disulfide ligand,[1] which gave an efficient catalytic *Z*-selective olefin metathesis.[2] Reactions involving terminal alkenes are low-yielding for this class of catalysts due to the instability of the formed methylidene complex, which can undergo 1,2-shift of the electron-rich sulfur *trans* to the NHC to the neighboring electrophilic carbene carbon, a reaction that effectively deactivates the catalyst.[3] One strategy to circumvent this problem involves the use of a sacrificial olefin to avoid methylidene complex formation and which allowed for the activity of the catalyst to be retained.[4]

Scheme 8.1. Deactivation of Z-selective olefin metathesis via 1,2-shift

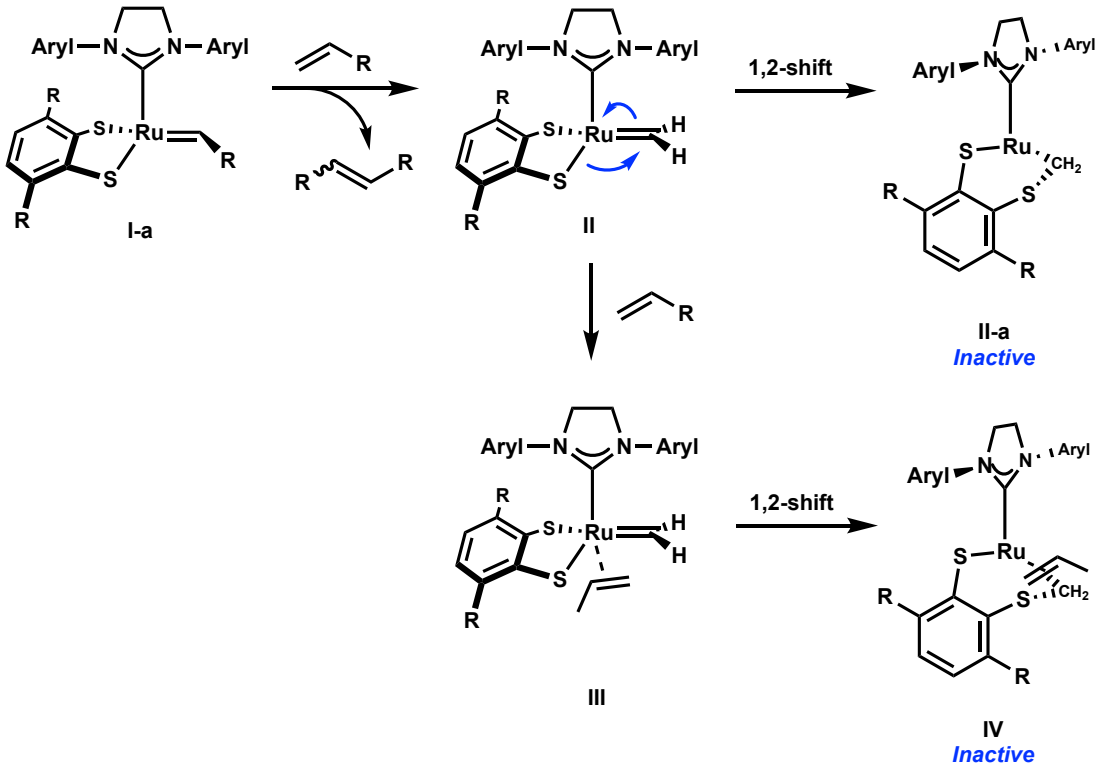

The Hoveyda group initially hypothesized that this deactivation proceeded via the ethylidene complex. They performed DFT calculations on the competition between deactivation

and metathesis for this species.[3] However, a further report[4] and control experiments by the Grubbs group have indicated that this transformation likely occurs through the methylidene species. Using computations, we sought to study the factors that dictate the reactivity of the methylidene, we hope to tune the dithiolate ligand to decrease its propensity to undergo deactivation. We envision the mechanistic pathway outlined in Scheme 8.1. Upon coupling with a terminal olefin, the alkylidene complex **I-a** generates methylidene **II**, which can proceed via: (1) 1,2-shift directly to **II-a** or (2) olefin coordination to form **III**, followed by 1,2-shift to generate inactive complex **IV**.

8.2 Computational methods

All DFT computations were performed with Gaussian 09.[5] Ground state structures were optimized at the B3LYP level of theory using LANL2DZ for ruthenium and 6-31G(d) for other atoms.[6,7,8,9] Vibrational analysis was used to confirm all stationary points as minima (no imaginary frequencies) or transition structures (one imaginary frequency). Free energy corrections were calculated using Truhlar's quasiharmonic approximation, which sets all the real vibrational frequencies that are lower than 100 cm^{-1} to 100 cm^{-1} to correct entropies for the breakdown of the harmonic oscillator approximation. [10,11] Subsequent single-point energy calculations on the optimized structures were performed at the M06 level of theory using SDD for ruthenium and 6-311+G(d,p) for all other atoms with the SMD continuum solvent model for THF.[12,13] The thermal corrections calculated from the scaled vibrational frequencies at the B3LYP level on the optimized geometries were then added to the M06 electronic energies to obtain the Gibbs free energies. Natural population analysis was performed using B3LYP/LANL2DZ/6-31G(d) and orbital occupations >10% were analyzed. Orbital energies discussed here were obtained from calculations using B3LYP/LANL2DZ/6-31G(d). All graphics on optimized structures were generated with CYLview.[14]

8.3 Results

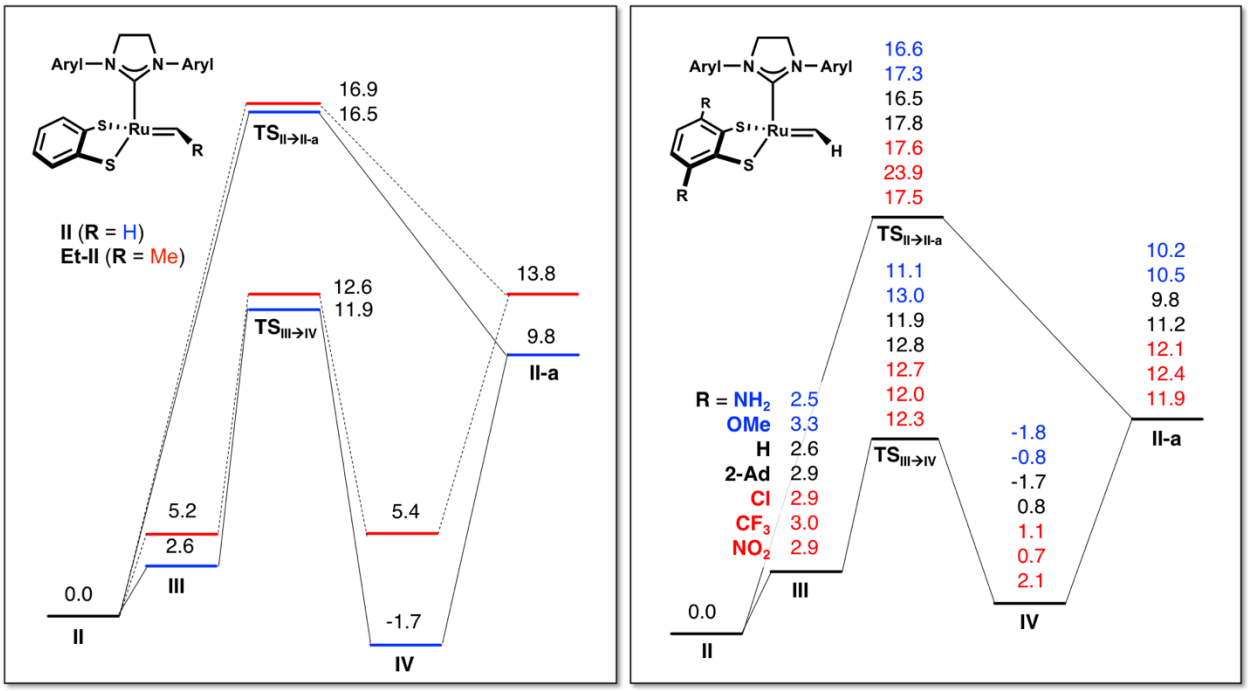

Figure 8.1. Reaction energetics of 1,2-shift of ethylidene vs. methylidene (left) and methylidene with varying R group substitution (right).
Groups in blue are electron-donating and groups in red are electron-withdrawing. Values are free energies in kcal mol^{-1}.

Methylidene vs. ethylidene

We first sought to develop an understanding the preferred pathway towards deactivation starting with parent compound **II** (Figure 8.1, left). The barrier for 1,2-shift ($\mathbf{TS_{II\rightarrow II\text{-}a}}$) is 16.5 kcal mol^{-1} and the forming deactivated complex **II-a** is 9.8 kcal mol^{-1}, indicating that this would be a highly endergonic process and unlikely to occur. This is likely due to the fact that the 16-electron count species (**II**) is forming a 14-electron count species (**II-a**) which would be unfavorable. The alternative pathway involving olefin coordination is much more feasible. The olefin coordinated complex **III** is a stable 18-electron count species and is 2.6 kcal mol^{-1} relative to separated **II** and propene. The barrier to 1,2-shift of complex III $\mathbf{TS_{III\rightarrow IV}}$ is only 11.9 kcal mol^{-1} (4.6 kcal mol^{-1} lower than $\mathbf{TS_{II\rightarrow II\text{-}a}}$), forming **IV**, which is −1.7 kcal mol^{-1}. This overall process is exergonic, and we can

conclude that the methylidene complex is likely to undergo deactivation via the olefin-coordinated pathway.

The analogous ethylidene pathway (**Et-II**) was also computed to probe the effect of alkylidene substitution on energetics. The barriers to 1,2-shift are similar with and without olefin coordination to the methylidene system (16.9 and 12.6 for $\mathbf{TS_{II \rightarrow II\text{-}a}}$ and $\mathbf{TS_{III \rightarrow IV}}$, respectively). With substitution on the carbene, the olefin complexation energy increases to 5.2 kcal mol^{-1}, which is approximately the same energy as IV (5.4 kcal mol^{-1}), making the two states isoenergetic. The ethylidene is therefore less likely to undergo deactivation than the methylidene.

Scheme 8.2. Isodesmic equations to probe methyl substitution stabilization

Equation 1: *Stabilization of ethylene by methyl is greater than for the Ru-carbene*

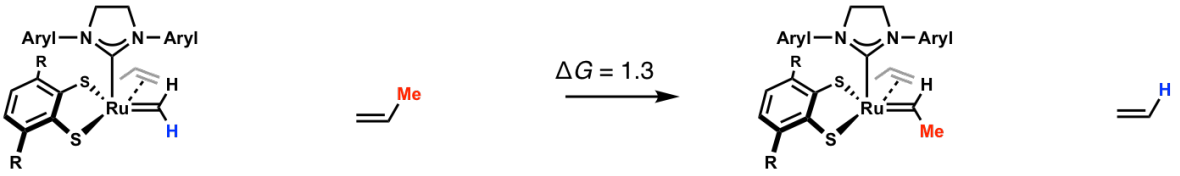

III Et-III

Equation 2: *Stabilization of alkylidene by methyl is greater than for 1,2-shift product*

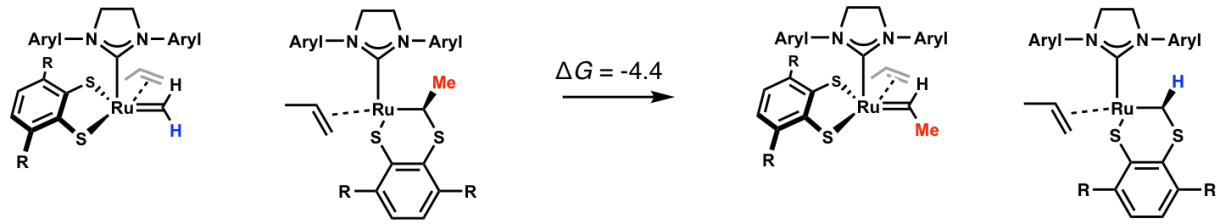

III Et-IV Et-III IV

Values are free energies in kcal mol^{-1}.

This effect was further probed using isodesmic equations to determine the effect of methyl substitution on complex stabilization (Scheme 8.2). Equation 1 is an isodesmic equation of the olefin-coordinated alkylidene III and free olefin, with methyl substitution either on the carbene or alkene. The stabilization of ethylidene by methyl is greater than for the ruthenium carbene, as indicated by the positive ΔG value (+1.3 kcal mol^{-1}). Equation 2 is an isodesmic equation of III

and inactive complex IV, where one carbene is substituted with methyl. The stabilization of the alkylidene by methyl is greater than for the 1,2-shift product, indicated by the negative Δ*G* value (−4.4 kcal mol^{-1}). From these equations, we can conclude that the 1,2-shift product is more facile without substitution at the carbon alpha to the metal center, and alkylidene **III** is more facile with more substitution at the carbene carbon. This is different than what we find in Equation 1, where methyl substitution is more important to the stabilization of the olefin than the carbene.

Olefin coordination

The effect of olefin coordination on the energetics on the 1,2-shift barrier can be explained upon analysis of the optimized geometries (Figure 8.2). Upon coordination of propene with **II** to form **III**, the olefin forces the alkylidene carbon and the shifting sulfur closer together ($C_{carbene}$−S_{trans} 1.85 Å) and decreases the S-Ru-C angle to 54°, contorting the geometry of the complex to be more similar to those of the 1,2-shift transition states $\mathbf{TS_{II\rightarrow II\text{-}a}}$ and $\mathbf{TS_{III\rightarrow IV}}$. In other words, olefin coordination pre-distorts the complex so that it is more likely to undergo 1,2-shift.

To understand the electronics of this deactivation process, we used natural population analysis to calculate the dominant contributors to the HOMO and LUMO of **II** and **III**. In **II**, the dominant orbital contributor to the HOMO is p orbital on the sulfur *trans* to the NHC (37%), while the dominant contributor to the LUMO is the d orbital on Ru (34%). In **III**, the dominant contributor to the HOMO is also the p orbital on the shifting sulfur (36%), whereas the dominant contributor to the LUMO is now the p orbital on the carbene carbon (46%), indicating an increase in the electrophilicity of this carbene upon coordination. Additionally, with olefin coordination, the LUMO level increases dramatically from −1.76 to −1.19 eV, while the HOMO level does not change significantly (−4.53 to −4.44 eV). This suggests the 1,2-shift is driven by the change in electrophilicity of the carbene rather than the nucleophilicity of the shifting sulfur.

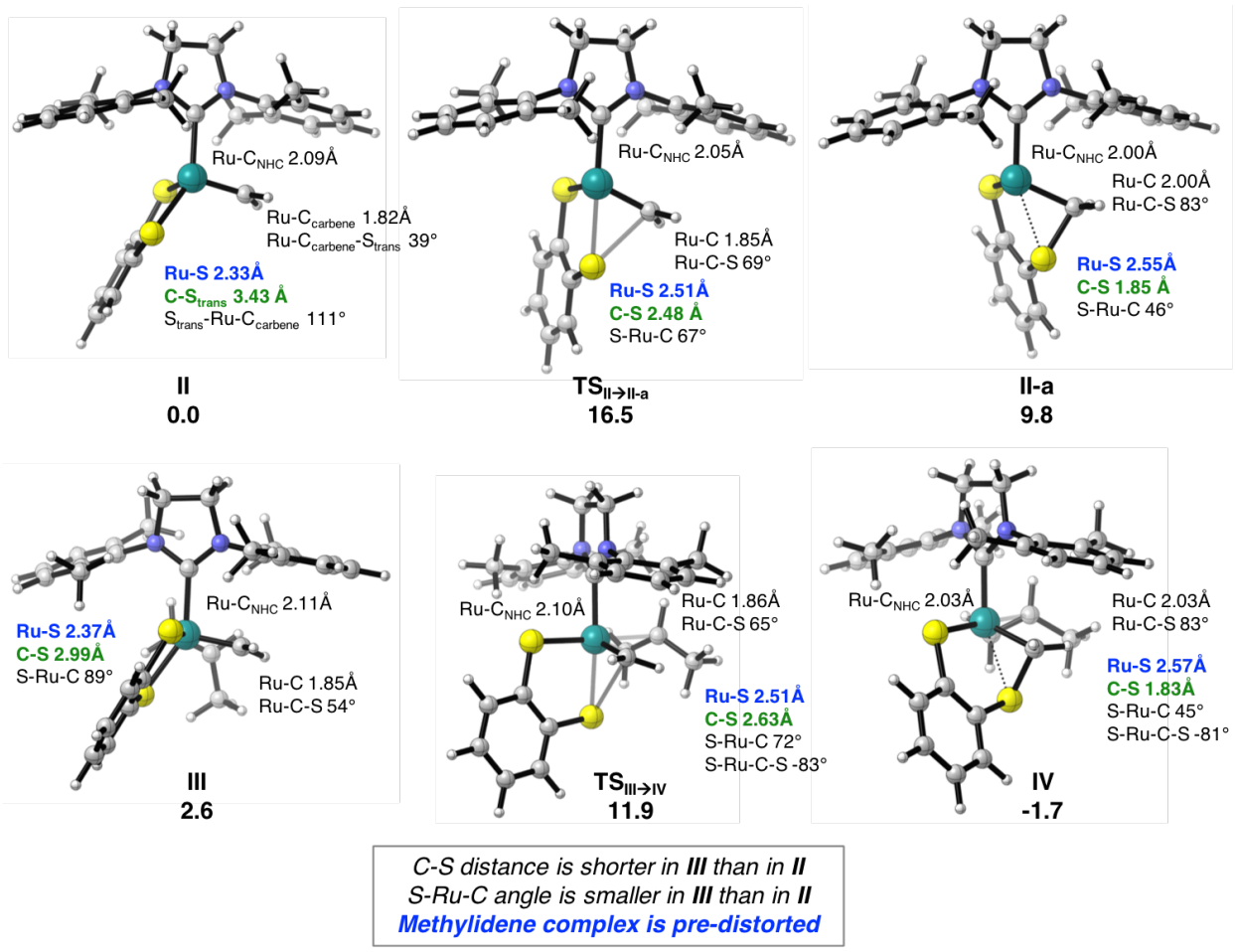

Figure 8.2. Geometries of parent methylidene system H-II.
Values are free energies in kcal mol^{-1}.

In order to determine how to slow the 1,2-shift, we sought to reduce the electron density of the shifting sulfur by functionalizing the ligand with various R groups *ortho* to sulfur (Figure 8.1, right). Although both electron-withdrawing and electron-donating groups, as well as a bulky 2-adamantyl group, were computed, the energetics did not vary greatly, with barriers ranging from 11.1 to 13.0 kcal mol^{-1} for **TS$_{III→IV}$**.

For the series of electron-withdrawing groups, we also compared the energies for metallacyclobutane (**V**) formation against energies of deactivation toward the 1,2-shift product **IV** (Figure 8.3). Across all of the systems, the energy of **V** is lower than the energy of **IV**, with a preference of 6.3 kcal mol^{-1} for the parent system and preferences of 1.1−1.2 kcal mol^{-1} for the

substituted systems. With substitution of electron-withdrawing groups, formation of the 1,2-shift product becomes more unfavorable, though metallacyclobutane formation also becomes more unfavorable. The barriers to metathesis $\mathbf{TS_{III\rightarrow V}}$ and to 1,2-shift $\mathbf{TS_{III\rightarrow IV}}$ were also computed. The parent system exhibits the greatest preference for metathesis (2.3 kcal mol^{-1}), and the trifluoromethyl-substituted system also prefers metathesis over deactivation slightly (1.4 kcal mol^{-1}). For the chloro- and nitro-substituted systems, the barriers to metathesis $\mathbf{TS_{III\rightarrow V}}$ and $\mathbf{TS_{III\rightarrow IV}}$ are similar (< 0.4 kcal mol^{-1} difference). While the energy difference between metathesis and deactivation differ somewhat with change in substitution, in general, these differences are not significant, and we can conclude that these two processes would be in competition in solution. Ultimately, the thermodynamically favorable 1,2-shift product would be preferred.

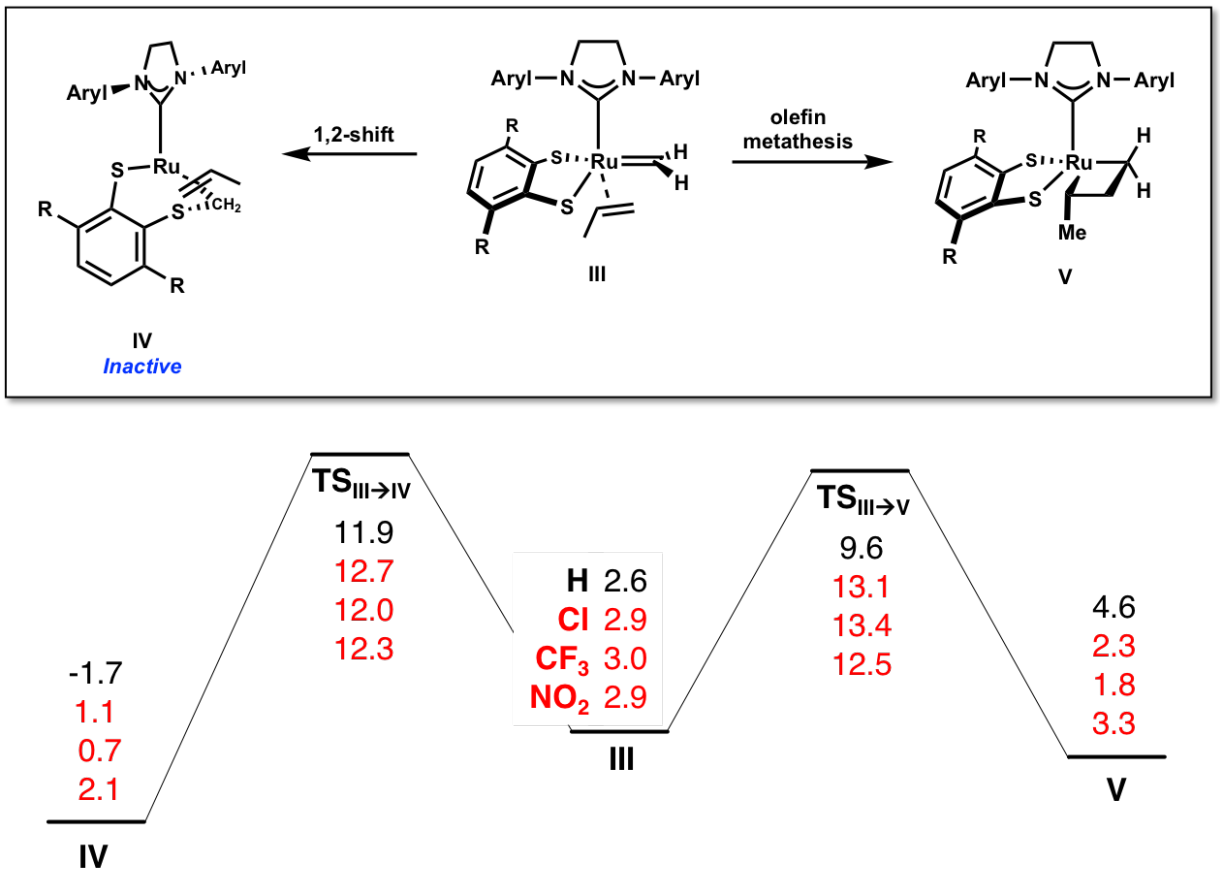

Figure 8.3. Comparison of 1,2-shift and metathesis barriers.
Values are free energies in kcal mol^{-1} relative to separated ethylidene **II** and propene.

We next probed the effect of varying heteroatom substitution on the ligand with other chalcogens (selenium and oxygen) (Figure 8.4). We expected that with more electronegative atoms like oxygen, the nucleophilicity of the shifting heteroatom could be tuned to disfavor the 1,2-shift. On the other hand, with the more electropositive selenium, the propensity for the 1,2-shift would increase.

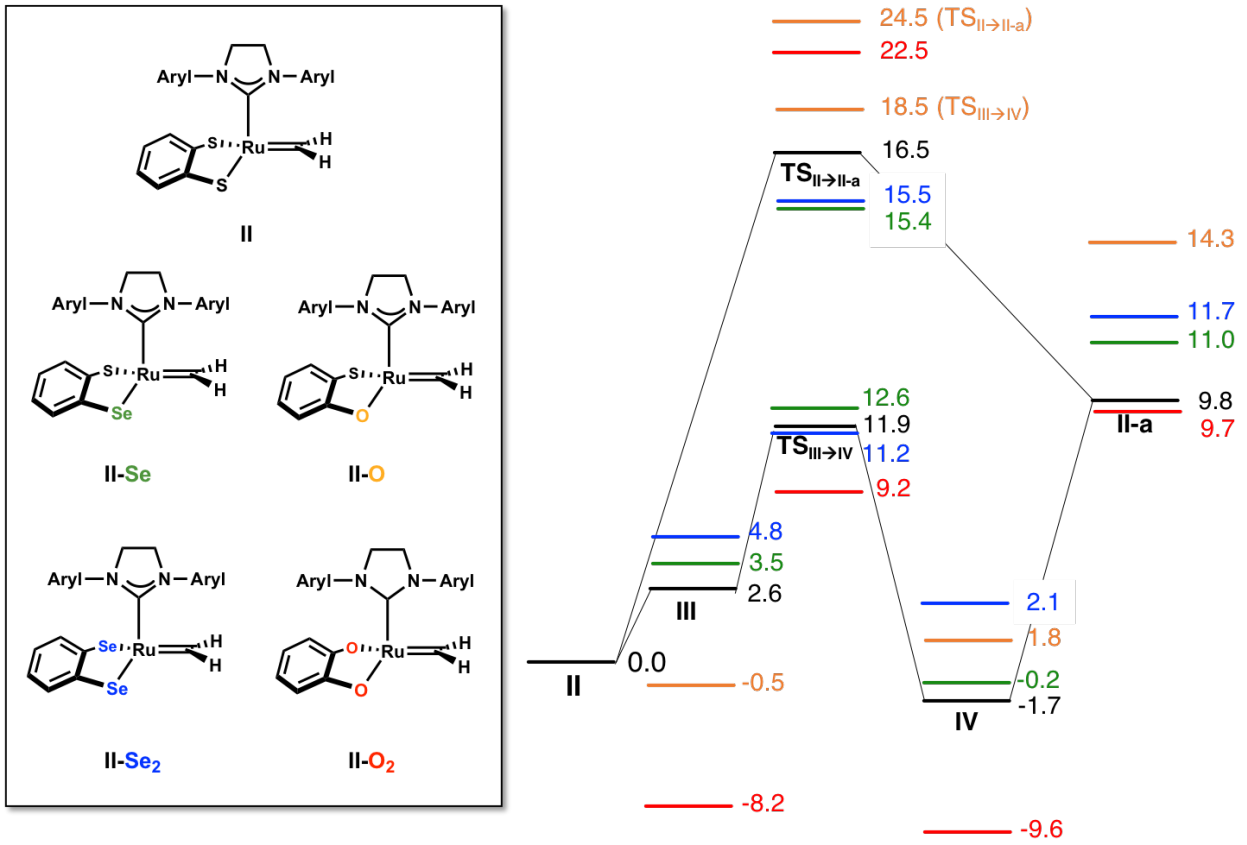

Figure 8.4. Effect of chalcogen substitution on energetics.
Values are free energies in kcal mol^{-1}.

Substituting the shifting sulfur with oxygen (as in **II-O**) makes complex **III-O** slightly favorable (−0.5 kcal mol^{-1}) and **IV-O** unfavorable (1.8 kcal mol^{-1}). Since oxygen is a weaker electron donor than sulfur, the metal center is electron-deficient and therefore olefin coordination is exergonic. This substitution increases the barriers of $\mathbf{TS_{III\rightarrow IV}}$ and $\mathbf{TS_{II\rightarrow II\text{-}a}}$ to 18.5 and 24.5 kcal mol^{-1}, respectively, which can be attributed to the weaker nucleophilicity of oxygen compared to sulfur. When the second sulfur is also substituted (as in $\mathbf{II\text{-}O_2}$), the complexation energy becomes

more exergonic (−8.2 kcal mol^{-1}), due to further loss of electron density at the ruthenium center. The barrier of $\mathbf{TS_{III\rightarrow IV}}$ for this dioxy system is 9.2 kcal mol^{-1} (19.0 kcal mol^{-1} relative to **III-O$_2$**), which is highly unfavorable, and the barrier of $\mathbf{TS_{II\rightarrow II\text{-}a}}$ is even higher (22.5 kcal mol^{-1}).

On the other hand, mono- and bi-functionalization with selenium renders olefin coordination energies slightly higher (3.5 and 4.8 kcal mol^{-1} for **III-Se** and **III-Se$_2$**, respectively) and lowers $\mathbf{TS_{II\rightarrow II\text{-}a}}$ to ~15.4 kcal mol^{-1}, though $\mathbf{TS_{III\rightarrow IV}}$ energies remain about the same. The energies for **IV-Se** and **IV-Se$_2$** are also lower, making the overall transformation exergonic. Compared to sulfur, selenium is a stronger electron donor to the metal center, making additional electron density from the olefin less favorable.

Table 8.1. Barriers to 1,2-shift for newly designed S,N catalysts

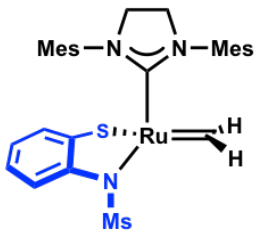

A-Ms-II

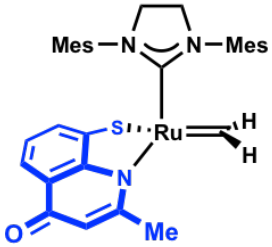

B-Me-II

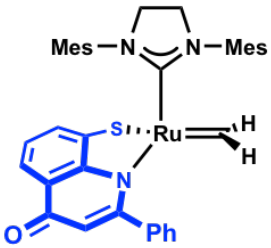

B-Ph-II

Ligand	$\mathbf{TS_{II\rightarrow II\text{-}a}}$	**II-a**	**III**	$\mathbf{TS_{III\rightarrow IV}}$	**IV**
A-Ms	24.9	12.6	13.4	28.2	4.5
B-Me	-	17.1	17.5	32.1	4.9
B-Ph	26.1	18.2	15.8	35.6	7.1

Values are free energies in kcal mol^{-1} relative to ethylidene **II** and propene.

New S,N ligands

In the preceding chapter, we discussed a series of new S,N ligands that could potentially allow for *E*-selective olefin metathesis. To ascertain the stability of these catalysts against this deactivation pathway, the barriers to 1,2-shift were computed (Table 8.1). The barriers to 1,2-shift

with and without olefin coordination are much higher than parent system **II**. Like the parent system, the barrier for $\mathbf{TS_{II \rightarrow II\text{-}a}}$ ranges from ~25−26 kcal mol^{-1}. The coordination energies are ~13−18 kcal mol^{-1}, and TSIII→IV have barriers to ~28−36 kcal mol^{-1}. The high coordination energies were discussed in the previous chapter, and these barriers support a conclusion that these catalysts would be highly unlikely to undergo this deactivation process. This is likely due to the close proximity of the bulky ligand with the carbene carbon (Figure 8.5), steric interactions that are not present in the various classes of dithiolate catalysts that were discussed previously.

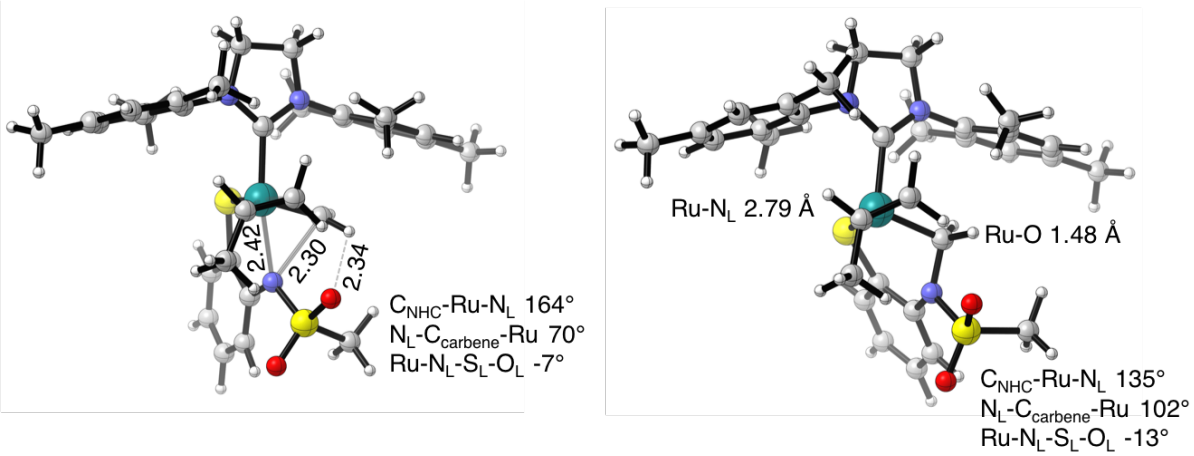

A-Ms-TS$_{III \rightarrow IV}$
24.9

A-Ms-IV
4.5

Figure 8.5. Geometries of TS$_{III \rightarrow IV}$ and IV with new S,N ligand A-Ms.
Values are free energies in kcal mol^{-1} relative to **A-Ms-II** and propene.

8.4 Conclusions

We have used computations to characterize the nature of the 1,2-sulfur shift that occurs onto the carbene carbon in a ruthenium methylidene complex. This transformation effectively deactivates the olefin metathesis activity of this class of ruthenium catalysts with bidentate dithiolate ligands. The deactivation proceeds more readily for methylidene than substituted carbenes, as the carbene is stabilized by alkyl substitution. The shift can be characterized as a nucleophilic attack of the sulfur *trans* to the NHC on the electrophilic carbene carbon, and likely occurs only after olefin coordination to the methylidene complex, as olefin coordination increases

the electrophilicity of the carbene carbon. Unfortunately, for this class of dithiolate catalysts, this process is in direct competition with olefin metathesis. We have shown that substituting the dithiolate ligand with a thioamide ligand, with an *N*-group that can impart steric interactions for selectivity, also increases the barriers to deactivation. This new class of S,N catalysts are therefore promising candidates for stable, selective olefin metathesis catalysts.

8.5 References

[1] Khan, R. K. M.; Torker, S.; Hoveyda, A. H. J. Am. Chem. Soc. 2013, 135, 10258−10261.

[2] Khan, R. K. M.; Torker, S.; Hoveyda, A. H. J. Am. Chem. Soc. 2014, 136, 14337−14340.

[3] Koh, M. J.; Khan, K. M.; Torker, S.; Yu, M.; Mikus, M. S.; Hoveyda, A. H. *Nature* **2015**, *517*, 181-186.

[4] Xu, C.; Shen, X.; Hoveyda, A. H. *J. Am. Chem. Soc.* **2017**, *139*, 10919-10928.

[5] Frisch, M. J.; Trucks, G. W.; Schlegel, H. B.; Scuseria, G. E.; Robb, M. A.; Cheeseman, J. R.; Scalmani, G.; Barone, V.; Mennucci, B.; Petersson, G. A.; Nakatsuji, H.; Caricato, M.; Li, X.; Hratchian, H. P.; Izmaylov, A. F.; Bloino, J.; Zheng, G.; Sonnenberg, J. L.; Hada, M.; Ehara, M.; Toyota, K.; Fukuda, R.; Hasegawa, J.; Ishida, M.; Nakajima, T.; Honda, Y.; Kitao, O.; Nakai, H.; Vreven, T.; Montgomery, J. A., Jr.; Peralta, J. E.; Ogliaro, F.; Bearpark, M.; Heyd, J. J.; Brothers, E.; Kudin, K. N.; Staroverov, V. N.; Kobayashi, R.; Normand, J.; Raghavachari, K.; Rendell, A.; Burant, J. C.; Iyengar, S. S.; Tomasi, J.; Cossi, M.; Rega, N.; Millam, N. J.; Klene, M.; Knox, J. E.; Cross, J. B.; Bakken, V.; Adamo, C.; Jaramillo, J.; Gomperts, R.; Stratmann, R. E.; Yazyev, O.; Austin, A. J.; Cammi, R.; Pomelli, C.; Ochterski, J. W.; Martin, R. L.; Morokuma, K.; Zakrzewski, V. G.; Voth, G. A.; Salvador, P.; Dannenberg, J. J.; Dapprich, S.; Daniels, A. D.; Farkas, Ö.; Foresman, J. B.; Ortiz, J. V.; Cioslowski, J.; Fox, D. J. *Gaussian 09, Revision B.01*; Gaussian, Inc.: Wallingford, CT, 2009.

[6] Becke, A. D. *J. Chem. Phys.* **1993**, *98*, 5648−5652.

[7] Lee, C.; Yang, W.; Parr, R. G. *Phys. Rev. B* **1988**, *37*, 785−789.

[8] Stephens, P. J.; Devlin, F. J.; Chabalowski, C. F.; Frisch, M. J. *J. Phys. Chem.* **1994**, *98*, 11623−11627.

[9] Vosko, S. H.; Wilk, L.; Nusair, M. *Can. J. Phys.* **1980**, *58*, 1200−1211.

[10] Zhao, Y.; Truhlar, D. G. *Phys. Chem. Chem. Phys.* **2008**, *10*, 2813-2818.

[11] Ribeiro, R. F.; Marenich, A. V.; Cramer, C. J.; Truhlar, D. G. *J. Phys. Chem. B* **2011**, *115*, 14556-14562.

[12] (a) Zhao,Y.; Truhlar, D. G. *Theor. Chem. Acc.* **2008**, *120*, 215-241. (b) Zhao, Y.; Truhlar, D. G. *Acc. Chem. Res.* **2008**, *41*, 157-167.

[13] Marenich, A. V.; Cramer, C. J.; Truhlar, D. G. *J. Phys. Chem. B* **2009**, *113*, 6378-6396.

[14] Legault, C. Y. *CYLview, 1.0 b*; *Université de Sherbrooke* (http://www.cylview.org), 2009.